A Numerical Study of Vortices and Turbulence in Quantum Fluids

George William Stagg

Thesis submitted for the degree of
Doctor of Philosophy

School of Mathematics & Statistics
Newcastle University
Newcastle upon Tyne
United Kingdom

June 2016

Acknowledgements

I would like to offer my appreciation to the many people who made my time at university an enjoyable experience. I will begin by thanking my PhD supervisors, Carlo Barenghi and Nick Parker, for their constant enthusiasm and for never having fear of exploring an interesting tangent. I also thank EPSRC for financially supporting this project.

Thanks to those who were there while I was studying for the MMath: Sam Hunter, Josie Kendall, Seb Mellor, Holly Moffat, Maz Phillips, Chris Slattery, Jack Sykes and more, for encouraging me to come out of my shell and making lectures more fun than they have any right to be. I particularly send my thanks to Becca Nicholson, who first convinced me to go for the PhD. I also thank the homeslices: Ben, Quinn, Bone, Chris, Ant, and Murray, for the many hours of fun both online and in real life.

Thanks to those I met through various NUTS events: Nige, Ben, Stevie, Gemma, Liz, Hep, Dan, Schwarz, Jacob, Esther, Chief, Duffy, Scott, Ash and many more, for all the good times, introducing me to live theatre and comedy, listening to me prattle on about physics, and for coming up with "Teggers".

Thanks to those who were there when I first started: Holly Ainsworth, Stacey Aston, Matt Buckley, Laura Cole, David Cushing, Tom Fisher, Fred Gent, Victoria Hardy, Sam James, Christian Lawson-Perfect, Nick Loughlin, Keith Newman, Jamie Owen, Rob Pattinson, Lucy Sherwin-Robson, Gavin Whitaker, and Nina Wilkinson, for being friendly, welcoming and supportive. Further thanks to those who later joined: Robbie Bickerton, Tom Bland, David Brown, Paolo Comaron, Liam Dobson, Can Evirgen, James Hollins, Yameng Ji, Ste Johnson, Sarah Jowett, Aamir Khan, Katie Marshall, Joe Matthews, David Pescod, Em Rickinson, David Robertson, Amit Seta and all the other PhD students, for the discussions, fun times, and for distracting me when I needed it most (or in the case of David Cushing, for distracting me when I needed it the least).

I thank Michael Beaty, Chris Graham, John Nicholson, and Anthony Youd, for keeping the network working smoothly and for patiently helping with anything computers.

Thanks to the superfluid group: Joy Allen, Andrew Baggaley, André Cidrim, Matthew Edmonds, Luca Galantucci, Donatello Gallucci, Fabrizio Larcher, Kean Loon Lee, Nick Proukakis, Angela White and more, for their ideas, constructive criticism, and vast knowledge and experience. I also thank Yuri Sergeev and Davide Proment for taking the time to examine the content of this thesis.

To my Mum and Dad, Peter, Cheryl, and Zoe: I thank you for all the love, Sunday dinners, computer problems, and for reminding me where my roots lie.

Finally, I give my deepest love and thanks to Hayley Moore, for her unending patience, kind support, and for always being able to make me laugh.

Abstract

Quantum fluids possess amazing properties of which two are particularly striking. Firstly they exhibit superfluid flow, with the total absence of viscosity. Secondly, there are no excitations when the fluid velocity (relative to some obstacle or surface) is slower than a critical value; above this velocity the flow becomes dissipative and macroscopic excitations are created in the form of quantised vortices with fixed circulation proportional to Planck's constant. In this thesis we numerically study the dynamics of quantum fluids in the vicinity of obstacles and surfaces, from the production of a single vortex pair to the complex and chaotic motion of turbulent vortex tangles. This approach provides quantitative predictions for atomic Bose-Einstein condensates (BEC) and qualitative insight for superfluid helium. We give detailed descriptions of the numerical schemes and present extensive numerical simulation of the Gross-Pitaevskii equation (GPE) and its variants at zero temperature and beyond, in both two and three dimensions.

We study the wake that forms behind obstacles in the presence of a superfluid flow, modelling atomic BEC experiments with moving laser-induced potentials, and explore the dependence on obstacle shape and size. We find that suitable obstacles produce classical-like wakes consisting of clusters of vortices of the same polarity. Remarkably, symmetric wakes resemble those observed in classical viscous flow at low Reynolds number, despite the constrained vorticity. The structures are unstable, forming time-dependent asymmetric wakes similar to a classical Bénard–von Kármán vortex street.

Motivated by the recent work of Kwon *et al.* (Phys. Rev. A **90**, 063627 (2014)), we model an atomic BEC experiment in which a trapped, oblate condensate is translated past a stationary, laser-induced obstacle. The critical velocity is exceeded and so vortices nucleate, forming a state of two-dimensional quantum turbulence. We explore the system at both zero-temperature and with thermal dissipation, modelled through a phenomenological term in the GPE. Our simulations provide insight into early stage evolution, not accessible experimentally, and into the decay of vortices by annihilation or passage out of the condensate.

We use classical field methods to simulate homogeneous Bose gases at finite temperature, from strongly non-equilibrium initial distributions to thermalised equilibrium states. We introduce a moving cylindrical potential and study how the thermal component of the gas affects vortex nucleation. We have found that the critical velocity decreases with increasing temperature and scales with the speed of sound of the condensate. Above the critical velocity, vortices are nucleated as irregular vortex lines, rings, or vortex tangles.

Finally we model the surfaces of walls and moving objects (such as wires, grids, propellers or spheres) in the presence of superfluid flow, using a real rough boundary obtained via atomic force microscopy. We find evidence pointing to the formation of a thin 'superfluid boundary layer' consisting of vortex loops and rings. As boundary layers usually arise from viscous forces, this is a surprising and intriguing result.

Contents

Part I

Introduction and Theory

Chapter 1

Introduction

In quantum mechanics there are two classes of particle: bosons and fermions. Fermionic particles (such as electrons) follow Fermi-Dirac statistics, have half-integer spin, and obey the Pauli exclusion principle. Bosonic particles (such as photons) have integer spin, follow Bose-Einstein statistics and, unlike fermions, any number are permitted to occupy the same quantum state. Under certain conditions, this latter property allows a large fraction of bosons to occupy the ground state macroscopically, a phenomenon known as Bose-Einstein condensation (BEC) [1, 2]. Bose-Einstein condensation is as diverse as it is astonishing, appearing in all manner of topics from atomic physics to condensed matter to astrophysics, manifesting as unexpected phenomena such as superfluidity, quantised circulation and superconductivity [3, 4]. These effects derive directly from quantum mechanics, and the fluids that exhibit them are known as "quantum fluids".

1.1 Bose-Einstein condensation

The roots of the original prediction of Bose-Einstein condensation lies with Indian scientist, Satyendra Nath Bose. In 1924 Bose re-derived Planck's law of black-body radiation, developing a theory of the statistical mechanics of photons by treating them as a collection of identical particles [5]. Albert Einstein helped Bose publish his work and went on to generalise his photon distribution law to an ideal gas of N non-interacting massive bosons [6]. This led to the Bose-Einstein distribution, $f(\epsilon_i)$, describing the statistical distribution of bosons over single particle energy states,

$$f(\epsilon_i) = \frac{1}{e^{(\epsilon_i - \mu)/k_B T} - 1}, \tag{1.1}$$

where ϵ_i is the energy of level i, μ is the chemical potential, k_B is the Boltzmann constant, and T is the temperature. The total number of particles in the system can be written as a

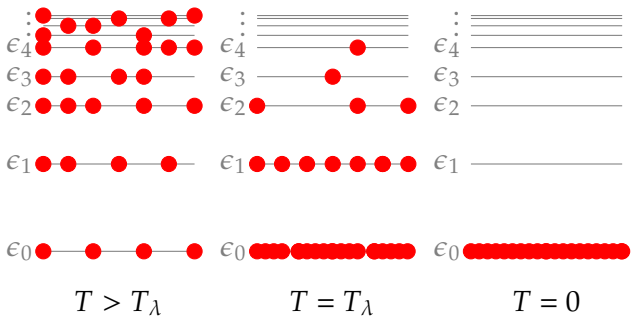

Figure 1.1: Schematic depiction of Bose-Einstein condensation. The ground state ϵ_0 becomes macroscopically occupied as the temperature is reduced to below the critical temperature for condensation. In the limit of $T = 0$ all bosons occupy the ground state.

sum over the mean occupation of each energy level,

$$N = \sum_i N_i = \sum_i g(\epsilon_i) f(\epsilon_i), \tag{1.2}$$

where N_i is the mean occupation of level i and $g(\epsilon_i)$ is the degeneracy of energy level i. Under the Bose-Einstein distribution the occupation of the ground state diverges in the limit of zero temperature, leading to the macroscopic occupation that defines the BEC. Schematically, Bose-Einstein condensation is shown in Figure 1.1. While it is impossible to reach the limit of $T = 0$ in reality, the macroscopic occupation occurs for temperatures less than a certain critical value $T < T_\lambda$.

Consider a gas of non-interacting bosons in thermal equilibrium at temperature T. The thermal de Broglie wavelength for each particle characterises the spatial extent of its localised wavepacket, and is conventionally defined by

$$\lambda_{\mathrm{dB}} = \sqrt{\frac{2\pi\hbar^2}{m k_{\mathrm{B}} T}}, \tag{1.3}$$

where m is the mass of the particle and $\hbar$ is the reduced Plank constant. The de Broglie wavelength is inversely proportional to the square root of the temperature T, so that at high temperatures the wavepacket of each particle is small compared to the average inter-particle distance. Here classical, particle-like behaviour dominates the dynamics of the gas and the particles approximately follow the classical Boltzmann distribution. As the temperature of the gas is reduced, the wavelength associated with the particles grows. At a critical temperature, T_λ, the wavelength for each particle becomes comparable to the average inter-particle distance and the individual characteristics of particles are no longer apparent. Here the particles become indistinguishable and the idea of a particle trajectory no longer makes sense. The particles behave in a truly quantum manner and

form a degenerate gas. The critical temperature for which this process occurs marks the onset of Bose-Einstein condensation.

For a gas of identical non-interacting Bosons in a three-dimensional system of volume D^3 and uniform number density $\rho = N/D^3$, Bose-Einstein condensation occurs when $\rho\lambda_{\mathrm{dB}}^3 \leq \zeta(3/2)$ [1, 7], where $\zeta(3/2) \approx 2.612$ is the Riemann zeta function evaluated at 3/2. By using this relation with Equation 1.3 one finds the critical temperature,

$$T_\lambda = \frac{2\pi\hbar^2}{mk_{\mathrm{B}}}\left(\frac{\rho}{\zeta(3/2)}\right)^{2/3}, \tag{1.4}$$

for the onset of Bose-Einstein condensation. The fraction of bosons condensed into the ground state, termed the condensate fraction, can then be calculated as a function of temperature,

$$\frac{N_0}{N} = 1 - \left(\frac{T}{T_\lambda}\right)^{3/2}. \tag{1.5}$$

These relations are derived in detail in Appendix A.1.

1.2 Superfluid helium

Many concepts relating to Bose-Einstein condensation and quantum gases were developed in the context of liquid ^{4}He. Liquid helium is interesting in that when cooled to very low temperatures, the liquid does not crystallise or solidify at atmospheric pressures. In fact a pressure of over 25 atmospheres is required to solidify ^{4}He, even at its lowest temperatures [1].

Around 1930, Keesom *et. al* [8, 9] observed that when cooling liquid ^{4}He, there exists a critical temperature known as the lambda point ($T_\lambda = 2.17$ K) at which the fluid undergoes a phase transition into a state known as helium II. It was later discovered by Kapitza [10], Allen and Misener [11] that helium II exhibits inviscid flow (one of several remarkable properties of helium II), and the fluid was named a "superfluid".

London [12, 13] was the first to interpret the properties of helium II as a manifestation of Bose-Einstein condensation of helium atoms, but the idea was not widely accepted at first. The strongly-interacting liquid of helium atoms is a world away from Einstein's non-interacting gas of bosons. Instead, the two-fluid model of Landau [14] was the first successful description of helium II hydrodynamics, wherein two fluids exist alongside one another with densities depending on the temperature: an inviscid superfluid component and a viscous normal fluid component. At $T = T_\lambda$, the normal fluid makes up the entire fluid and there is no superfluid component. As the temperature is decreased, the proportion of the normal fluid decreases and that of the superfluid increases, such that at $T = 0$ the fluid is entirely superfluid.

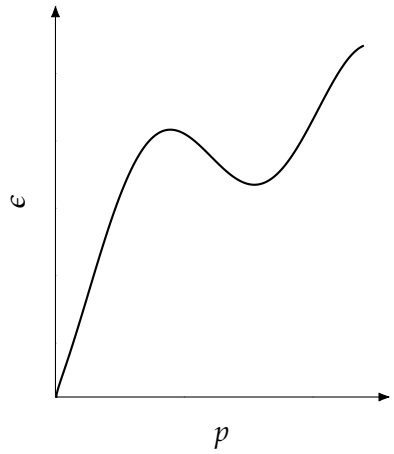

Figure 1.2: The dispersion relation for superfluid ^{4}He, demonstrating the spectrum of elementary excitations. The linear dispersion of phonons can be seen at low momenta and the roton minimum at higher momenta.

1.2.1 Dispersion relation and excitations

Landau showed that superfluid behaviour can be accounted for by a dispersion relation that is linear at low momenta [14]. Bogoliubov then showed that a weakly-interacting Bose gas supports exactly such a dispersion law [15]. This link between bosonic gases and helium II was a strong indicator that Bose-Einstein condensation was indeed the fundamental mechanism behind superfluidity, and finally gave traction to London's theory. Later, Onsager [16] and Feynman [17] predicted quantised circulation as an extension to London's work, by considering systems described by a wavefunction.

While Bose-Einstein condensation is now known to be the driving force behind helium II superfluidity, the strong interactions inherent in liquid helium restricts the condensed fraction of helium atoms to less than 10% [18] (even in the limit of zero temperature) and so a weakly-interacting Bose gas provides only a qualitative model of helium II superfluidity.

The dispersion relation for liquid helium ^{4}He is shown in Figure 1.2, its shape first predicted by Landau [19] in 1947. For small momenta the relation is indeed linear. The fundamental excitations associated with this part of the relation are sound waves, known as *phonons*. For larger momentum, however, $\epsilon(p)$ exhibits an approximately quadratic shaped dip and local minimum. The fundamental excitations of this part of the relation are known as *rotons*, with the centre of the dip corresponding to the smallest possible energy of a roton, the *roton minimum*. Rotons were first experimentally confirmed in 1957, using neutron scattering techniques, by Palevsky *et. al.* [20]. These measurements and others [21–23] confirmed that Landau's predicted dispersion relation was indeed correct.

1.3 Dilute weakly-interacting atomic gases

Gases of alkali atoms such as rubidium, sodium and lithium are ideal candidates for condensation: they are weakly-interacting, can be easily trapped magnetically, and readily cooled using lasers. When considering these gases, Einstein's ideal gas predictions provide a good estimate of the critical temperature for Bose-Einstein condensation. However, as the gas is cooled towards the critical temperature it is necessary to avoid the transition into a liquid or solid. This can be done by reducing the atomic density such that the gas is dilute enough that elastic binary collisions in the gas dominate over three-body collisions. The required atomic densities are around $n \sim 10^{14}$ cm^{-3} [1], and so by using Equation 1.4 one predicts that the ultra-low temperatures of $T \sim 10^{-6}$ K are required for the onset of Bose-Einstein condensation.

1.3.1 Experimental realisation

The requirement of such low temperatures delayed the realisation of a true atomic BEC until 1995, when advances in atom cooling and trapping [24–26] lead to the condensation in vapours of rubidium (^{87}Rb) by the group of Professors Carl Wieman and Eric Cornell at the University of Colorado [27], and sodium (^{23}Na) by the group of W. Ketterle at MIT [28]. Wieman, Cornell and Ketterle were awarded the 2001 Nobel Prize in Physics for "*the achievement of Bose-Einstein condensation in dilute gases of alkali atoms, and for early fundamental studies of the properties of the condensates*" [29].

A variety of cooling techniques, including laser [24–26] and evaporative [30] cooling, originally developed in the attempt to condense spin-polarised hydrogen [31–33], are used to reach the ultra-low temperatures required for atomic Bose-Einstein condensation [1, 34, 35]. A typical atomic condensate begins life as around 10^9 atoms which are cooled to around 1K by a Zeeman slower: a laser beam propagating opposite to the atom flow reduces the velocity of the atoms from around 800 m/s to 30 m/s. The atoms are transferred to a magneto-optical trap (MOT) formed by laser beams and magnetic fields and further cooled through Doppler cooling, where the Doppler effect is employed to reduce the momentum of atoms. A limit of this method is reached at around 1 μK [1] at which point evaporative cooling is required to cool the gas even further. Here the confining trap is carefully modified so that the high energy atoms escape the system. The remaining lower energy atoms rethermalise at a reduced temperature and lower density due to the loss of atoms. Using this technique, the gas can be cooled to the nK regime. The BEC then emerges marked by a very narrow velocity distribution for the atoms, indicating a macroscopic occupation of the ground state.

[1] Compare this to the density of dry air at room temperature and pressure, $n \sim 10^{19}$ cm^{-3}.

Since the first experiments in 1995, an explosion of ultra-cold atomic physics has followed. Many species of atom are now routinely condensed by over 100 experimental groups all over the world. The list grows continuously: many alkalis [27, 28, 36–41], calcium [42], dysprosium [43], strontium [44–47], ytterbium [48], chromium [49], spin-polarised hydrogen [50], metastable helium [51], quasi-equilibrium magnons [52], exciton-polaritons [53] and even mixtures of different species [54–57]. Each species expands the richness of the fascinating phenomena available to experimentalists, with their unique atomic properties and range of interactions.

The experimental advances of controlling the trapping potential has allowed for direct interaction with the condensate using time-dependent magnetic fields and lasers. Localised laser beams can punch a 'hole' in a condensate to create almost arbitrarily shaped obstacles [58]. Exotic trapping potentials such as ring traps [59, 60], uniform box traps [61, 62], optical lattices [63] and double-well [64] potentials can be realised with relative ease. The route has even opened to experimentation in reduced dimensionality [65–68]. By significantly trapping the gas along one dimension it is possible to make a disc shaped, effectively two dimensional condensate, useful [69, 70] for the study of vortex dynamics. A further trapping along a second dimension creates an elongated, effectively one dimensional condensate such that solitons, one-dimensional non-dispersive waves, become supported [71, 72].

1.3.2 Scattering length and interactions

The atomic binary collisions in ultra-cold dilute gases are characterised by the s-wave scattering length, a_s. This is because for low energy collisions, the scattering due to the s-wave term dominates over the higher energy p-wave and d-wave terms [1]. Geometrically, a positive a_s (as in a rubidium or sodium BEC) can be thought of as a measure of the effective radius of repulsive atoms. For gases with density in the region required, $n^{1/3}a_s \ll 1$, and so a_s is much smaller than the average inter-atomic distance. This implies that the gas is weakly-interacting and around 99% of the atoms can become Bose-condensed, resulting in a condensate fraction much greater than the theoretical maximum for helium II. This makes ultra-cold dilute atomic gases the purest form of BEC that can also be easily controlled and manipulated in the lab.

The scattering length may also be negative (as in a lithium BEC [36, 37]). In this case the atoms are attractive, rather than repulsive, and so without trapping the BEC is unstable to collapse. Three-dimensional harmonic trapping can stabilise the system, up to a certain atom number, with critical atom number dependent on the system dimensionality and trapping strength.

Importantly, it is possible to control the inter-atomic interaction, and therefore the scattering length, through the entire range of the parameter space using techniques such

as *Feshbach resonance* (theoretically laid out in [73] and experimentally demonstrated in [74, 75, 38]), providing further experimental control over the BEC.

With the unique level of purity and control available in the lab, weakly-interacting dilute atomic gases have become the ideal test-bed for studying Bose-Einstein condensation and for observation of quantum effects on a macroscopic scale.

1.4 Macroscopic nonlinear excitations: vortices and solitons

The rise of interest in Bose-Einstein condensation has led to a great amount of theoretical work. It can be argued that the greatest success in this area is the development of an effective mean-field theory which provides the so-called Gross-Pitaevskii equation (GPE) [1, 76–78], a classical evolution equation and a variant of the nonlinear-Schrödinger equation used in many areas of physics, including plasma physics [79] and non-linear optics [80, 81]. The GPE is much simpler than modelling a BEC using the full many-body Schrödinger equation, yet accurately captures the statics and dynamics [78, 82–88] of a BEC over a range of realistic experimental parameters. Section 2 describes the mean-field formulation in detail and formally derives the GPE from the starting point of the many-body Schrödinger equation.

The non-linearity in the GPE arises from atom-atom interactions and gives rise to a great deal of interesting effects, both from a mathematical standpoint and when modelling an atomic BEC. A selection of the interesting and experimentally relevant non-linear phenomena are described in this section.

1.4.1 Vortices

A family of non-linear excitations supported by the GPE are *quantum vortices*, which arise via topological defects in the wavefunction that parametrises the condensate. Solutions with quantum vortices contain structures identified by a localised density dip, the vortex core, masking a phase singularity in its centre. The phase singularity forms a velocity field such that fluid circulates around the vortex core.

Quantum vortices are carriers of vorticity in an irrotational superfluid system, and can arise both naturally during the formation of a BEC or by direct interaction with a condensate. A standard method of generating vortices, relevant to atomic condensates and helium II, is by rotation of the superfluid [89–93]. Superfluid rotation can be induced by rotation of the containing vessel for helium II, or in the case of atomic condensates methods such as stirring with laser beams can be used. At lower angular speeds the rotation has no effect, however, above a critical value the presence of vortices lowers the energy of the system [94, 95]. In this case, one or more vortices nucleate into the system, forming a lattice [89, 92] at the centre of rotation. Another example is the formation of vortices as a result

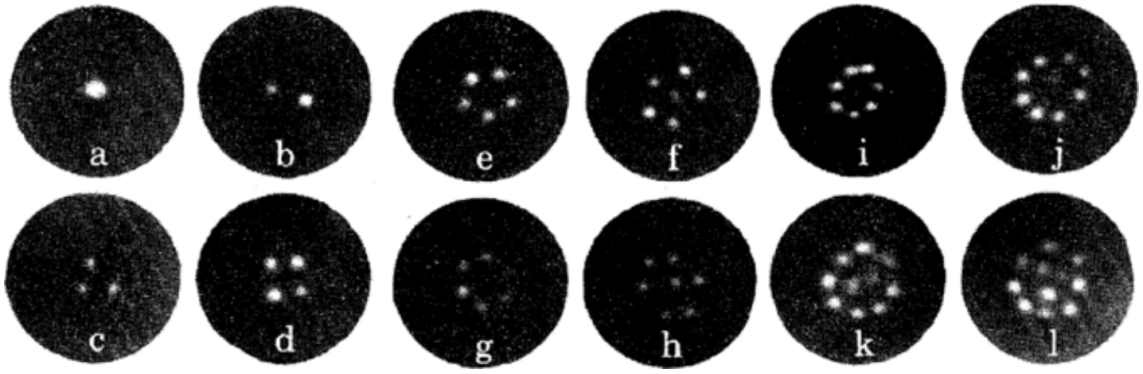

Figure 1.3: Results of the superfluid helium experiments of Packard [89], with (a-l) corresponding to increasing rotation velocities of the helium II container. Vortex line position is marked by the glowing dots.

of broken symmetry after a fast quench into the BEC regime. Through the Kibble-Zurek mechanism [96–98], pockets of phase coherence form, separated in space. As the phase coherence grows in the condensate, boundaries are created and discontinuities along these boundaries leads to the formation of vortex lines. Further methods of generating vortices include artificial phase imprinting [99–101] of the topological defect via laser light, or by stirring a BEC with a localised laser beam [90–92, 102–104].

Quantised vortices have much in common with the classical vortices observed in nature. However, while classical vortices can be created with any degree of fluid rotation, characterised by the circulation Γ, quantised vortices differ in that their circulation is constrained (as a direct consequence of quantum mechanics) to integer multiples of the *quantum of circulation*, κ, with a value dependent on the system.

Experimentally, quantum vortices have been observed in many different configurations and for various trap geometries. Quantised vortex lines [85], vortex rings [84], vortex tangles [105], quasi-two-dimensional turbulence [106], vortex lattices [90, 92, 107, 108], vortex dipoles [69], giant vortices [109], and multiply charged vortices [110] have all been realised in BECs. The condensate is observed via imaging of the atomic gas density, but the vortex core size is typically smaller than the imaging resolution. To overcome this the condensate is expanded by releasing it from the trap prior to imaging. The vortices then appear as localized regions of low density in the expanded condensate images.

Quantum vortices have also been observed in superfluid helium [111]. In 1979, the first clear and direct image of a quantised vortex lattice in rotating helium II was provided by Packard *et. al* [89]. Electrons were trapped inside vortex cores and accelerated towards a florescent screen to mark the position of the vortex. The resulting images are shown in Figure 1.3 for different rotation speeds. More recently, there has been a significant advance by Lathrop *et al* [112]. Here vortex lines were visualised and tracked in helium II by using tracer particles of frozen hydrogen.

1.4.2 Solitons

Solitons are non-linear localised excitations, supported by the one dimensional GPE. Soliton solutions contain localised propagating wavepackets that are self-reinforcing due to the non-linearity of the system balancing dispersive effects. When in a homogeneous medium they travel at zero or finite constant speed, and have the property that they undergo non-destructive collisions. There are two species of soliton, bright [113] and dark solitons [114]. Their behaviour in optics, leading to a bright collection or dark absence of light, is the origin of these names. Solitons are an active area of research in several diverse areas of non-linear mathematics and physics [71, 115], and are well known for their applications in optical and fluid systems [116]. For these reasons solitons have been of great interest [117, 118] since the first experimental realisation of atomic BECs.

In two and three-dimensional BECs, solitons take the form of solitonic waves, but are not solitons in the strict mathematical sense; the structures either collide inelastically or are unstable and proceed to decay [83, 119–121]. In weakly-interacting BECs with quasi-1D geometries, however, solitons are stable and have been observed with long lifetimes and with behaviour in agreement with numerical simulations [72].

Bright solitons

Bright solitons arise in interfacial fluid waves [122], plasma physics [79, 123], acoustics [124], and optical physics [125], and can be easily pictured by the classical example of a hump travelling along the surface of water, as first reported in 1845 [122]. The non-dispersal and destruction-less collision properties of bright solitons make them particularly important in applications for optical communications [126].

Bright solitons, which are supported in condensates for the case of effectively attractive interactions ($a_s < 0$) [113], were first generated and experimentally observed with lithium [127, 128] in quasi-one-dimensional traps.

Dark solitons

Generally throughout physics, dark solitons are less prevalent than the bright species, but are of particular interest in the context of weakly-interacting BECs as they are are formed in the case of repulsive interactions ($a_s > 0$) [114]. They consist of a density dip and phase slip [129] of varying size, depending on the speed of the soliton propagation. Dark solitons were first realised in 1987 in non-linear optics [130], followed by their creation in shallow liquids [131], as discrete mechanical standing waves [132], and in magnetic films [133].

More recently, dark solitons have been engineered in repulsive atomic BECs in a controlled manner through phase imprinting methods [82–84, 72] and by perturbing the condensate density. They have also been produced through dynamical processes [134, 135],

such as by sweeping a laser beam through the condensate [135].

Dark solitons that have been generated in higher than quasi-1D geometries have been observed to decay into vortex rings [84, 85, 136], due to their known instability to transverse excitations.

1.5 Turbulence

1.5.1 Classical Turbulence

Classical turbulence is a complicated flow regime characterised by chaotic and highly irregular flow and the appearance of unsteady vortices on many length scales interacting with one another. In classical turbulence, we expect to encounter several length scales at which eddys form, the largest of which are constrained by only the physical boundaries of the flow. This length scale is known as the *integral* length scale. Conversely, the size of the smallest measurable length scale is physically limited by the measurement device, a role also played by finite grid resolution in computational fluid dynamics.

For flows with high Reynolds number, as we consider eddy sizes of smaller and smaller length scale, the effect of viscous forces becomes increasingly large compared to inertial forces. The length scale at which these forces balance is known as the *Kolmogorov* length scale. At scales smaller than the Kolmogorov length scale viscosity causes energy to be dissipated from the flow.

For statistically steady-state turbulence, the energy dissipated by viscosity equals the energy supplied at the large scales. Over time, turbulent dynamics transports kinetic energy between the length scales, in a process known as *energy cascade*. In classical isotropic turbulence, most of the kinetic energy is contained in large-scale structures and is distributed across length scales following the famous Kolmogorov energy spectrum [137].

1.5.2 Quantum Turbulence

Quantum turbulence is a state dominated by an irregular tangle of quantised vortex lines. The quantised circulation and inviscid flow characteristics of superfluidity provides a simplified platform to study complicated vortex dynamics in general, and so the nature of turbulence in superfluids is the subject of much experimental and theoretical study [138–142].

The nature of quantum turbulence can be categorised based on the energy spectrum, where two regimes have been identified. In Vinen or ultra-quantum turbulence, vortex tangles are random and have only a single length scale: the average inter-vortex spacing. In Kolmogorov or quasi-classical turbulence, the energy spectrum follows Kolmogorov scaling, as in the classical regime [143–145]. Despite the fundamental differences between

superfluids and classical fluids, the observations of Kolmogorov energy spectra in superfluid turbulence are suggestive of a deep connection between them [141].

1.5.3 Turbulence in helium II

Quantum vortices are carriers of vorticity in superfluids and play an important role in the behaviour of the superfluid component of helium II. They have been experimentally and theoretically studied in helium II from around 1950 [18], but clearly visualising the three dimensional nature of individual vortex lines and vortex reconnections (the collision of two vortex lines such that there is a change of topology) remained a challenge until fairly recently [112, 146]: the large normal fluid component and a vortex core size of only a few Angströms limit visualisation techniques.

A large disordered collection of vortex lines is thought to be the driving force of the turbulence. However, within the tangle the vortex core size is small compared to the average inter-vortex spacing. For this reason the standard method of modelling of vortex dynamics at large-scales is handled by approximating the vortices as infinitesimally thin vortex filaments, with motion described by the Biot-Savart law [147]. The limitation of the vortex filament model is that all phenomena that occur on the length-scale of the vortex core (of which we are interested in) is lost. Features such as vortex reconnection can be manually introduced into this model [147], but the full microscopic description is lost.

On the other hand, the GPE model for a weakly-interacting Bose gas provides a microscopic model of helium II on a qualitative level. As already discussed, the strongly-interacting helium atoms, existence of high momenta rotons, and relatively low fraction of condensed helium atoms limit the accuracy of the model. Nevertheless, the GPE excels at describing the micro-scale phenomena such as vortex nucleation [148], reconnections [149, 150], sound emission [151, 152], and Kelvin wave excitation, and so we will use the GPE at various points throughout this thesis to model helium II dynamics.

Typically turbulence in helium II is generated using mechanical methods, creating turbulence with oscillating obstacles, including grids [153], wires [154–156], spheres [157] and others [158–162]. Methods without the use of oscillating structures have been also been devised, such as the use of heat flux [163] or container spin-down [164], to generate turbulence . A mutual friction [18] couples the normal fluid and superfluid components, and at finite temperature leads to a dissipation of the resulting turbulent vortex tangle. In the limit of very low temperatures the mutual friction tends to zero. It is expected that in this limit Kelvin wave excitations [151, 152] and vortex reconnections leads to dissipation via sound waves, but the entire mechanism is not yet fully understood [165].

1.5.4 Turbulence in BECs

Weakly interacting atomic BECs offer a key advantage for the experimental study of quantum turbulence. Although the spatial extent of BECs support much fewer vortices than for superfluid helium, the structure of individual vortices and their turbulent dynamics can be experimentally resolved much easier. This is due to the relatively large vortex core size, on the scale of a micron, available to atomic BECs and the fact that the state of the entire atomic gas can be readily visualised through imaging techniques. Expansion imaging has provided a technical leap in this area, allowing individual vortex cores and reconnection events to be directly observed [90, 103, 106]. Improved real time and non-destructive imaging of condensates is now possible [70] by out-coupling of a small representative fraction of the gas for each image, allowing for observation of quantum vortex trajectories. A further recent improvement in this area [166] has allowed for the imaging of vortex polarity as well as its location in space. These technical leaps in imaging have made atomic condensates an extremely attractive medium for exploring quantum vortex turbulence.

The range of length scales available to classical turbulence and superfluid helium turbulence far outshines those currently available to atomic BECs, and much theory of classical turbulence is defined by the distribution of kinetic energy over the large number of length scales available. Nevertheless, numerical studies show quantum turbulence can distribute the kinetic energy in an atomic condensate in agreement with Kolmogorov's 5/3 law [143–145].

1.6 Thesis overview

An outline of the structure of this thesis and a brief description of each chapter is given in this section. The thesis is split into three main parts. Part I introduces the formalism, models and numerical tools that we go on to use in part II to model quantum fluids and generate numerical results. Part III is a collection of appendices. The following publications partially feature the results shown in the thesis, and collaborative contributions are highlighted here.

- Quantum analogues of classical wakes in Bose-Einstein condensates
  G. W. Stagg, N. G. Parker and C. F. Barenghi, J Phys B: At. Mol. Opt. Phys. **47** 095304 (2014)

- Generation and decay of two-dimensional quantum turbulence in a trapped Bose-Einstein condensate
  G. W. Stagg, A. J. Allen, N. G. Parker and C. F. Barenghi, Phys. Rev. A **91**, 013612 (2015)

- Classical-like wakes past elliptical obstacles in atomic Bose-Einstein condensates
  G. W. Stagg, A. J. Allen, C. F. Barenghi, N. G. Parker, J. Phys.: Conf. Ser. **594** 012044 (2015)

- Critical velocity of a finite-temperature Bose gas
  G. W. Stagg, R. W. Pattinson, C. F. Barenghi, N. G. Parker, Phys. Rev. A **93**, 023640 (2016)
- A superfluid boundary layer
  G. W. Stagg, N. G. Parker, C. F. Barenghi, arXiv:1603.01165 (2016)
- Vortex scattering by impurities in a Bose-Einstein condensate
  A. Griffin, G. W. Stagg, N. P. Proukakis, and C. F. Barenghi, **in preparation**
- Ultra-quantum decay of strongly non-equilibrated BEC turbulence
  G. W. Stagg, N. G. Parker and C. F. Barenghi, **in preparation**

Part I - Introduction and Theory

Chapter 1 introduces the concept of Bose-Einstein condensation, superfluidity, and the nature of quantum turbulence in weakly interacting atomic condensates and superfluid liquid helium.

Chapter 2 describes the theoretical concepts and mean-field methodology that allows us to accurately model a dilute, weakly interacting atomic Bose gas. We describe the Gross-Pitaevskii equation (GPE), a non-linear Schrödinger equation used to model condensates at zero temperature, and go on to extend the GPE to take into account finite temperature effects through phenomenological damping or the classical-field method. We detail some of the consequences of the model, such as quantised circulation, and show various initial conditions and simple solutions of the GPE.

Chapter 3 describes the theory and implementation of various numerical procedures we use to generate the simulations and results shown in part II. Our numerical time-stepping GPE solver is described, followed by an extensive description of our vortex locating and tracking routines. Finally a method is described for the filtering of the thermal part of the field when using the classical-field method.

Part II - Numerical Studies

Part II consists of a selection of the numerical simulations we have performed, interpretations of the results and any applications to real experimental systems.

Chapter 4 extends recent studies of moving obstacles in superfluids, a system mimicking a well known problem in classical viscous flows. We present numerical simulations of classical-like wakes, consisting of vortex clusters, generated by the presence of elliptical obstacles.

Chapter 5 was motivated by the recent experimental work of Kwon *et al.* [106]. We model their experimental set up in which a trapped condensate is translated past an obstacle, and study the decay of the resulting 2D quantum turbulence and vortex annihilation

events. Communications with Y. Shin and A. Cidrim were helpful in the interpretation of the numerical simulations shown in this chapter.

Chapter 6 was motivated by further work of Kwon *et al.* [167], highlighting the need to extend the study of the critical velocity for vortex nucleation to finite temperatures. We use classical field methods to simulate finite temperature homogeneous Bose gases from a strongly non-equilibrium initial distribution, and classify the nature of the resulting turbulent vortex tangle. We introduce a cylindrical obstacle into equilibrium states for various temperatures, measure the critical velocity, and characterise the nature of the resulting vortex lines. The previous numerical work of A. J. Youd was helpful in the development of our classical-field code, used in this chapter.

Chapter 7 is inspired by recent experimental studies in helium II, generating turbulence with oscillating obstacles such as wires, spheres and grids [153–162]. We simulate a quantum fluid in the presence of a real rough boundary obtained via atomic force microscopy [168], with data kindly provided by C. R. Lawson. We find surprising evidence of the formation of a thin 'superfluid boundary layer' consisting of vortex loops and rings.

In Chapter 8 we briefly review the main conclusions of our work and discuss opportunities for further research in the area.

Part III - Appendix

Part III is a collection of appendices. Appendix A consists of various detailed derivations related to the theoretical modelling of an atomic BEC. Appendix B contains definitions of various quantities we refer to throughout the thesis. Appendix C is a collection of algorithms that we have used.

Chapter 2

Theoretical Modelling of Bose-Einstein Condensates

2.1 Mean-field description

We aim to accurately model the dynamics of a closed system containing a dilute, weakly interacting Bose gas of N atoms, at extremely low temperature. One could model the entire system by constructing a N-body quantum wavefunction, which would follow the Schrödinger equation, but the complexity of this method makes it extremely unwieldy to model the large number of particles used in Bose-Einstein condensate (BEC) experiments.

We instead model the system with a mean-field theory, described in Section 2.2, in which there are essentially two main approximations. First, justified by the dilute property of the gas, any binary interaction between particles at $\mathbf{r}$ and $\mathbf{r}'$ is assumed to be a contact interaction following a delta function of the form

$$V(\mathbf{r} - \mathbf{r}') = g\delta(\mathbf{r} - \mathbf{r}'),$$

where g is an interaction coefficient. Interactions involving a higher number of particles are ignored. Secondly, we assume that all particles in the condensate are macroscopically described by a single wavefunction, $\psi(\mathbf{r}, t)$, where $\mathbf{r}$ is position and t is time. As the particles all share the same phase and quantum state, $\psi(\mathbf{r}, t)$ is a classical field. This second approximation also assumes that there are no particles contributing to thermal or quantum fluctuations beyond the classical field, and so is only justified in general in the limit of zero temperature. Nevertheless, we go further and describe some finite-temperature based effects in Sections 2.11 and 2.12.

2.2 The Gross-Pitaevskii equation

The result of the mean-field methodology is the Gross-Pitaevskii equation (GPE),

$$i\hbar\frac{\partial\psi(\mathbf{r},t)}{\partial t} = \left(-\frac{\hbar^2}{2m}\nabla^2 + V(\mathbf{r},t) + g|\psi(\mathbf{r},t)|^2 - \mu\right)\psi(\mathbf{r},t), \tag{2.1}$$

where m is the mass of a single particle, μ is the chemical potential, and $V(\mathbf{r},t) = V_{\text{obj}}(\mathbf{r},t) + V_{\text{trap}}(\mathbf{r},t)$ is an external potential. In the case of no obstacles or surfaces the obstacle potential is $V_{\text{obj}}(\mathbf{r},t) = 0$, otherwise $V_{\text{obj}}(\mathbf{r},t)$ is defined using Gaussian or step functions, as shown in Section 2.15. In the homogeneous case the trapping potential is $V_{\text{trap}}(\mathbf{r},t) = 0$, otherwise harmonic trapping is used, such as $V_{\text{trap}}(\mathbf{r},t) = m\omega\mathbf{r}^2/2$ for a 3D spherically symmetric trap.

The GPE takes the form of a non-linear time-dependent Schrödinger equation, where the first two terms on the right hand side are the energy of a single particle in a potential field, and the third non-linear term describes the interactions between the multiple particles in the system, with a strength usually parametrised by $g = 4\pi\hbar^2 a_s/m$, where a_s is the s-wave scattering length. The wavefunction of the system is normalised so that the integrated density is equal to the number of atoms N,

$$\int |\psi|^2 \, \mathrm{d}^3\mathbf{r} = N. \tag{2.2}$$

Taking into account the fact that the GPE is only strictly valid at $T = 0$, it turns out the equation is surprisingly successful at quantitatively modelling ultra-cold gasses, even for finite temperature systems, providing the temperature of the system is small compared to the critical temperature for Bose-Einstein condensation [169]. The GPE also provides a qualitative model of BEC based effects in superfluids such as liquid helium II [170] and rotating neutron star cores [171].

A detailed explanation of the mean-field formulation of the model and the full derivation of the GPE is shown in Section A.3.

2.3 Time-independent Gross-Pitaevskii equation

We find a stationary version of the GPE by first fixing the potential, $V(\mathbf{r})$, so that it is constant in time, and then writing the wavefunction in the form $\psi(\mathbf{r},t) = \psi_0(\mathbf{r})$, where $\psi_0(\mathbf{r})$ is a stationary state. Equation 2.1 then becomes

$$0 = \left(-\frac{\hbar^2}{2m}\nabla^2 + V(\mathbf{r}) + g|\psi_0(\mathbf{r})|^2 - \mu\right)\psi_0(\mathbf{r}), \tag{2.3}$$

the time-independent GPE. In the absence of interactions, $g = 0$, this reduces to the standard time-independent Schrödinger equation, with the chemical potential μ reducing to the energy per particle. This version of the GPE can be used to find stationary solutions of the system, with the value of μ characterising the energy of the ground state.

2.4 The chemical potential

The chemical potential of the system, μ, can be thought of as the energy required to add a particle to a system with large N, or alternatively as a measure of the energy of a particle. The value of μ will vary for the specific species of bosons considered and provides a useful scale of energy.

The chemical potential can be found in terms of energies of the system by direct integration of Equation 2.3,

$$\mu = \left(E_{\text{kin}} + E_{\text{pot}} + 2E_{\text{int}}\right)/N, \tag{2.4}$$

where the quantities E_{kin}, E_{pot} and E_{int} are defined in Appendix B.1.

2.5 Quasi-two-dimensional Gross-Pitaevskii equation

For some condensate geometries it is useful to be able to simulate the condensate via a lower dimensional GPE. An example of this is a highly oblate condensate, in which the trapping potential is defined as

$$V_{\text{trap}}(x, y, z) = m\omega_{\perp}^2 \frac{\left(x^2 + y^2\right)}{2} + m\omega_z^2 \frac{z^2}{2}, \tag{2.5}$$

with trapping frequencies $\omega_z \gg \omega_{\perp}$ and under the condition $\hbar\omega_z \gg \mu$, where μ is the 3D chemical potential. Tight z confinement causes the dynamics to become essentially two dimensional (experimentally achieved in [65]) as the wavefunction along z becomes fixed into the time-independent harmonic oscillator ground state, $\psi_z(z)$, so that

$$\psi(\mathbf{r}, t) = \psi_{\perp}(x, y, t)\psi_z(z), \tag{2.6}$$

where $\int |\psi_{\perp}|^2 \, \mathrm{d}^2\mathbf{r} = N$ by convention. An expression for ψ_z is found by considering significant trapping in the z direction. In this case the kinetic and potential energy is large compared to the inter-atomic interactions. The solution along z then approaches the solution without interactions, leading to a Gaussian ground state,

$$\psi_z(z) = \pi^{-1/4} l_z^{-1/2} \exp\left(-z^2/2l_z^2\right), \tag{2.7}$$

where $l_z = \sqrt{\hbar/m\omega_z}$ and the $\psi_z(z)$ is normalised so that $\int |\psi_z|^2 \, \mathrm{d}z = 1$. This is known as the quasi-2D regime and when this form of ψ is substituted into Equation 2.1 it forms a 2D GPE that can be used to model the system with reduced dimensionality, with the modified interaction term $g_{2\mathrm{D}} = g/(\sqrt{2\pi}l_z)$ [172]. The 3D chemical potential μ is also modified as an extra term is absorbed, $\mu_{2\mathrm{D}} = \mu - \hbar\omega_z/2$, and all other three-dimensional properties become two-dimensional.

A similar process can be performed with 'cigar' quasi-1D geometries so that a 1D GPE can be used with a modified $g_{1\mathrm{D}}$ interaction term, and $\mu_{1\mathrm{D}}$ chemical potential. As before all 3D properties become 1D, however as we will not consider quasi-1D regimes in detail, the specifics are omitted from this thesis.

2.6 Hydrodynamic interpretation

Often it can be helpful to write the GPE, via the so called Madelung transformation, as a set of hydrodynamic equations. The transformation reinterprets the wavefunction ψ as a magnitude directly related to the fluid density and a phase which is directly related to the fluid velocity. We write the wavefunction in the form

$$\psi(\mathbf{r}, t) = R(\mathbf{r}, t) \exp(i\theta(\mathbf{r}, t)), \tag{2.8}$$

and identify the fluid density as $n = mR^2$ and the velocity as $\mathbf{v} = \hbar\nabla\theta/m$. In vector form we obtain a continuity equation

$$\frac{\partial n}{\partial t} + \nabla \cdot (n\mathbf{v}) = 0, \tag{2.9}$$

and an equation similar to the Euler equation for an inviscid fluid,

$$n\left(\frac{\partial \mathbf{v}}{\partial t} + (\mathbf{v} \cdot \nabla)\,\mathbf{v}\right) = -\nabla p - \nabla \mathbf{P} - n\nabla\left(\frac{V}{m}\right). \tag{2.10}$$

where $p = \frac{g}{2}(\frac{n}{m})^2$ is the pressure and $P_{jk} = -\frac{\hbar^2}{4m^2} n \frac{\partial^2 \ln n}{\partial x_j \partial x_k}$ is known as the quantum pressure. A detailed derivation of this result can be found in Appendix A.4.

2.7 Quantised circulation

An interesting feature of the GPE is that the fluid circulation must be quantised. We can see this by first writing the integrated change of phase along any closed curve C,

$$\Delta\theta = \oint_C \nabla\theta \cdot \mathrm{d}\mathbf{l}, \tag{2.11}$$

where d$\mathbf{l}$ is the line element along C. The wavefunction at the start and the end of the integration must be single valued, so

$$\exp(i\theta_0) = \exp(i\theta_0)\exp(i\Delta\theta), \tag{2.12}$$

for some θ_0. This is only satisfied when $\Delta\theta = 2\pi q$, with $q \in \mathbb{Z}$. Our local velocity is $\mathbf{v} = \hbar\nabla\theta/m$ and so we can write

$$\Gamma = \oint_C \mathbf{v}\cdot \mathrm{d}\mathbf{l} = \frac{2\pi\hbar}{m}q. \tag{2.13}$$

Notice that we are now taking the line integral of the velocity; we have a formula for the circulation. We find the circulation must be quantised in units of $\kappa = 2\pi\hbar/m$, the so called 'quantum of circulation'. This is in stark contrast to classical fluids where the circulation can take any real value. Also note that when the circulation is non-zero, a singularity is introduced into the velocity and phase. The fluid density must vanish at the centre of the resulting vortex, so as to avoid solutions with infinite energy density.

2.8 Dimensionless Gross-Pitaevskii equations

Systems which exhibit superfluidity due to the phenomenon of Bose-Einstein condensation can form at almost any scale, from ultra-cold atomic BECs formed at the micron scale, to containers of superfluid helium on the metre scale, to neutron stars, the cores of which are theorised to be superfluid on the kilometre scale [171].

A trapped atomic BEC in particular can be experimentally realised with a wide range of variable parameters and anisotropic geometries. Through creative use of magnetic or optical potentials, atomic BECs have been realised in toroidal ring [59, 60], box-like [61, 62], quasi-2D 'pancake' [69], and quasi-1D 'cigar' [83, 134] traps. Through laser 'painting', a method to produce arbitrary and dynamic trapping potentials has even been demonstrated [58]. Adding an additional dimension to the parameter space, Feshbach resonances can be used to realise atomic condensates over a wide range of both attractive and repulsive atom-atom interactions [74].

For these reasons it is desirable to rescale the quantities used in the GPE so that any of the calculations performed can be easily reformulated into any scale and parameter regime desired. We make this process easier by doing all calculations with dimensionless parameters. Another advantage of the dimensionless formulation is that the size of the values involved are all normalised on the scale of unity, reducing the chance of errors in numerical computation due to the floating point representation used by modern computer architectures. We present two methods of making the GPE dimensionless, the specific scaling used is chosen by the needs of the simulation and is usually apparent (such as by

whether a trapping potential is involved).

2.8.1 Homogeneous GPE

Consider an infinite and homogeneous system with repulsive interactions and where $V_{\text{trap}} = 0$. In this system's ground state, ψ does not depend on $\mathbf{r}$ or t, and so we can set the time and spatial derivatives in the GPE to zero,

$$0 = \left(g|\psi(\mathbf{r}, t)|^2 - \mu\right)\psi(\mathbf{r}, t). \tag{2.14}$$

By rearranging, we can easily find the natural homogeneous density of the system: $n(\mathbf{r}) = |\psi(\mathbf{r})|^2 = \mu/g$. We then choose to rescale the wavefunction using this value, so that $\bar{\psi} = \psi/\sqrt{\rho}$, where $\rho = \mu/g$.

By dimensional arguments (see Appendix B.3 for details), the length scale of space is the healing length $\xi = \hbar/\sqrt{mg\rho}$ and the length scale of time is $\tau = \hbar/(g\rho)$, where we have used $n(\mathbf{r}) = \rho$ as the homogeneous uniform density. The scale of velocity in the system is the speed of sound, $c = \sqrt{\rho g/m}$ (see Appendix B.4 for details). These units are often called the 'natural units'. We define the rescaled dimensionless quantities as

$$\bar{t} = \frac{t}{\tau}, \quad \bar{r} = \frac{r}{\xi}, \quad \bar{\varepsilon} = \frac{\varepsilon}{\mu}, \tag{2.15}$$

for time, length, and energy respectively, where a overbar denotes a dimensionless quantity. Substituting the dimensionless quantities into Equation 2.1 and setting $V_{\text{trap}}(\mathbf{r}, t) = 0$ leads to the homogeneous GPE,

$$i\frac{\partial\bar{\psi}(\bar{\mathbf{r}}, \bar{t})}{\partial\bar{t}} = \left(-\frac{1}{2}\bar{\nabla}^2 + |\bar{\psi}(\bar{\mathbf{r}}, \bar{t})|^2 + \bar{V}_{\text{obj}}(\bar{\mathbf{r}}, \bar{t}) - 1\right)\bar{\psi}(\bar{\mathbf{r}}, \bar{t}). \tag{2.16}$$

The resulting normalisation condition for $\bar{\psi}$ is

$$\int |\bar{\psi}|^2 \, \mathrm{d}^3\bar{\mathbf{r}} = 1. \tag{2.17}$$

2.8.2 Trapped GPE

When considering a harmonically trapped condensate it is convenient to work with a wavefunction scaled so that the normalisation condition is similar to Equation (2.17). We denote the scaled wavefunction for a harmonically trapped condensate $\tilde{\psi}$ and write

$$\int |\tilde{\psi}|^2 \, \mathrm{d}^3\mathbf{r} = 1. \tag{2.18}$$

We introduce the harmonic oscillator length, $l_r = \sqrt{\hbar/(m\omega)}$, where ω is a trap frequency. This leads to the dimensionless rescalings,

$$\tilde{t} = t\omega, \quad \tilde{r} = \frac{r}{l_r}, \quad \tilde{\varepsilon} = \frac{\varepsilon}{\hbar\omega}, \tag{2.19}$$

for time, length, and energy respectively, where an tilde denotes a dimensionless quantity. We rewrite Equation 2.2 with dimensionless length to find,

$$\int |\psi|^2 \, \mathrm{d}^3\mathbf{r} = N \Rightarrow \int |\psi|^2 N^{-1} l_r^3 \, \mathrm{d}^3\tilde{\mathbf{r}} = 1, \tag{2.20}$$

and so we rescale the wavefunction to satisfy Equation 2.18,

$$|\tilde{\psi}|^2 = |\psi|^2 N^{-1} l_r^3 \Rightarrow \tilde{\psi} = \psi N^{-\frac{1}{2}} l_r^{\frac{3}{2}}. \tag{2.21}$$

Substituting the new rescaled quantities into Equation 2.1 leads us to the trapped GPE,

$$i\frac{\partial\tilde{\psi}(\tilde{\mathbf{r}},\tilde{t})}{\partial\tilde{t}} = \left(-\frac{1}{2}\tilde{\nabla}^2 + \tilde{g}|\tilde{\psi}(\tilde{\mathbf{r}},\tilde{t})|^2 + \tilde{V}(\tilde{\mathbf{r}},\tilde{t}) - \tilde{\mu}\right)\tilde{\psi}(\tilde{\mathbf{r}},\tilde{t}). \tag{2.22}$$

where

$$\tilde{g} = \frac{gN}{\hbar\omega l_r^3}. \tag{2.23}$$

2.9 The imaginary time propagation method

Many numerical explorations of quantum systems, particularly those associated with magnetic or optical trapping, involve calculating the ground-state as either the final result or as a stepping stone for further calculations. While often there exists analytic solutions for a condensate ground state, this problem is often solved numerically using so called eigensolvers. Numerically finding the ground state becomes practically necessary if a simulation requires complicated potential fields.

There are several methods available for implementing a numerical eigensolver: inverse iteration and Lanczos methods [173], systematic variational techniques [174], boundary eigenvalue methods [175], conjugate gradient techniques [176] and imaginary time propagation [177]. We choose to use the last of these methods due to its relative simplicity at the expense of computational time.

The imaginary time method revolves around moving from real to imaginary time using the substitution $t_i = -it$. This transforms the GPE into a form similar to a diffusion equation. As a result, a local equilibrium can be found by propagating in time. This can be understood by considering a solution of the form $\psi(\mathbf{r},t) = \sum_n \psi_n(\mathbf{r})\exp(-iE_n t/\hbar)$, where $\psi(\mathbf{r},t)$ is a superposition of eigenfunctions $\psi_n(\mathbf{r})$ with eigenvalues E_n. Under propagation

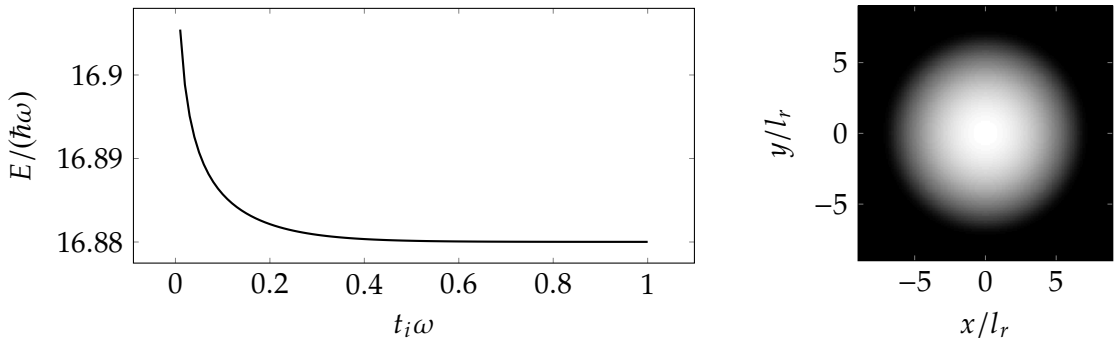

Figure 2.1: An example of the use of the imaginary time propagation method for finding the condensate ground state for a condensate with interaction energy $\tilde{g} = 2000$ and $\tilde{\mu} = 25.27$, with the Thomas-Fermi solution as the initial state. The density of the final ground state solution is shown (right) along with the energy of the solution as the method propagates through imaginary time (left).

of the GPE in imaginary time, the wavefunction exponentially decays,

$$\psi(\mathbf{r}, t_i) = \sum_n \psi_n(\mathbf{r}) \exp\left(\frac{-E_n t}{\hbar}\right).$$

In particular, the decay rate is directly related to the size of the eigenvalues E_n, so that the contributions from higher energy eigenfunctions decay the fastest. The final ingredient is to inhibit the overall decay of the wavefunction by renormalising during propagation. After a sufficient transient time the contributions from higher energy eigenfunctions become negligible, forcing the wavefunction to tend towards the ground state.

The imaginary time propagation method converges on the ground state solution very slowly and so we must perform many numerical steps to prepare an initial state. A silver lining of this drawback is that the method can be used to prepare almost any viable initial state. For example, an initial condition consisting of a Thomas-Fermi profile with many vortices can be made more accurate with this method by imposing the phase during imaginary time propagation. The result is a less violent start to condensate dynamics; minimal sound is produced due to the difference between the approximate initial condition and a true solution of the GPE.

The energy can be used as a way to gauge the solution convergence. An example ground state solution for a 2D condensate in a harmonic trap is found using the imaginary time method and is shown with the energy in Figure 2.1. For $t_i > 0.6/\omega$ the computed ground state energy does not significantly change, a good indicator that the ground state has been found to sufficient accuracy.

2.10 Transforming the reference frame

2.10.1 Linearly translating frame to simulate flow

The GPE is transformed into the translating reference frame via the linear momentum operator. In quantum mechanics the momentum operator is defined in position space as $\hat{P} = -i\hbar\nabla$. In most cases we wish to translate the frame in order to simulate a flow and so the operator is rewritten so that the momentum is along a single axis (usually the x axis),

$$\hat{P}_x = -i\hbar\frac{\partial}{\partial x}.$$

This term can be added to the right hand side of the GPE to modify it such that it is in the reference frame moving along x. For example, the GPE in the frame translating along the x direction with velocity v is written,

$$i\hbar\frac{\partial\psi(\mathbf{r},t)}{\partial t} = \left(-\frac{\hbar^2}{2m}\nabla^2 + V(\mathbf{r},t) + g|\psi(\mathbf{r},t)|^2 - \mu - vi\hbar\frac{\partial}{\partial x}\right)\psi(\mathbf{r},t). \tag{2.24}$$

2.10.2 Rotating frame

The GPE is transformed into the rotating reference frame via the angular momentum operator. Recall that in classical mechanics the angular momentum is defined as a vector product of the position $\mathbf{r}$ and the momentum $\mathbf{p}$,

$$\mathbf{L} = \mathbf{r}\times\mathbf{p} = \begin{vmatrix} \underline{i} & \underline{j} & \underline{k} \\ x & y & z \\ p_x & p_y & p_z \end{vmatrix}.$$

In quantum mechanics the corresponding position and momentum *operators* are defined as $\hat{R} = \mathbf{r}$ and $\hat{P} = -i\hbar\nabla$, and so we can define a similar angular momentum *operator*,

$$\hat{L} = \hat{R}\times\hat{P}. \tag{2.25}$$

Components of equation 2.25 can also be written as differential operators,

$$\hat{L}_x = -i\hbar\left(y\frac{\partial}{\partial z} - z\frac{\partial}{\partial y}\right), \quad \hat{L}_y = -i\hbar\left(z\frac{\partial}{\partial x} - x\frac{\partial}{\partial z}\right), \quad \hat{L}_z = -i\hbar\left(x\frac{\partial}{\partial y} - y\frac{\partial}{\partial x}\right), \tag{2.26}$$

which can then be added to the right hand side of the GPE to modify it such that it is in the rotating reference frame. For example, the GPE in the frame rotating about the z axis

with angular momentum Ω is written,

$$i\hbar\frac{\partial\psi(\mathbf{r},t)}{\partial t} = \left(-\frac{\hbar^2}{2m}\nabla^2 + V(\mathbf{r},t) + g|\psi(\mathbf{r},t)|^2 - \mu - i\hbar\Omega\left[x\frac{\partial}{\partial y} - y\frac{\partial}{\partial x}\right]\right)\psi(\mathbf{r},t), \quad (2.27)$$

2.11 The dissipative Gross-Pitaevskii equation

Equation 2.1 does not include any form of damping or dissipation. In fact, up to numerical accuracy, the GPE conserves both the particle number and the total energy of the system. In physical reality, due to the effects of finite-temperature, all excitations are damped over time. Whist in some experiments (at temperatures $T \ll T_c$) this damping is minimal over experimental timescales, in some other cases the effects of this damping must be considered. The dissipative Gross-Pitaevskii equation (DGPE) attempts to introduce a simple-minded way of modelling finite-temperature damping by introducing a phenomenological dissipation into the GPE. The procedure was introduced by Pitaevskii [178] and refined by others [179–181]. The derivation of the DGPE presented here closely follows the arguments shown previously by these authors.

We would like to extend the GPE such that a damping process is introduced, so that dynamics approach an equilibrium state over time. Such an equilibrium state can be described by Equation 2.3. The equation of motion for our wavefunction ψ is then written

$$i\hbar\frac{\partial\psi}{\partial t} = \hat{Q}\psi, \quad (2.28)$$

where $\hat{Q}$ is a non-Hermitian operator (so that we have a relaxation process). At equilibrium the anti-Hermitian part of $\hat{Q}\psi$ must be zero. We force this by writing the anti-Hermitian part of $\hat{Q}\psi$ in the form,

$$i\Gamma\left(-\frac{\hbar^2}{2m}\nabla^2 + V(\mathbf{r}) + g|\psi(\mathbf{r})|^2 - \mu\right)\psi(\mathbf{r}),$$

which will be forced to zero at equilibrium by satisfaction of Equation 2.3. Here Γ is a dimensionless value parametrising the relaxation.

Another property we require is that when $\Gamma = 0$ the $T = 0$ behaviour of the GPE is recovered. This forces us to write $\hat{Q}\psi$ as

$$\hat{Q}\psi = (1 + i\Gamma)\left(-\frac{\hbar^2}{2m}\nabla^2 + V(\mathbf{r}) + g|\psi(\mathbf{r})|^2 - \mu\right)\psi(\mathbf{r}),$$

and the equation of motion becomes the DGPE,

$$i\hbar\frac{\partial\psi(\mathbf{r})}{\partial t} = (1+i\Gamma)\left(-\frac{\hbar^2}{2m}\nabla^2 + V(\mathbf{r}) + g|\psi(\mathbf{r})|^2 - \mu\right)\psi(\mathbf{r}), \tag{2.29}$$

where $\Gamma < 0$ for damping.

Equation 2.29 describes the evolution of an exited condensate ψ towards equilibrium. The process can be understood by considering ψ to be made up of a ground state ψ_0 and an excitation δ,

$$\psi = e^{-i\mu t}(\psi_0 + \delta).$$

The value of δ will approach zero as the wavefunction is evolved via 2.29. The parameter Γ will control the speed of the relaxation and the exact value will change depending on the system. For instance the thermal component of the fluid will largely affect the damping time-scales and so Γ will depend largely on temperature. A microscopic justification for the model is found in [182, 183]; by studying the growth of a condensate in the presence of a rotating thermal cloud an expression for Γ was found.

$$\Gamma = \frac{4m g_c a^2 k_B T}{\pi\hbar^2}, \tag{2.30}$$

where k_B is Boltzmann's constant and $g_c = 3$ is a factor used for correction.

For an arbitrary wavefunction ψ (that is preferably close to a true solution of the GPE), evolution will indeed approach an equilibrium state. However it is important to note that since now the equation of motion is non-Hermitian, the evolution does not conserve total energy or total atom number. For a fixed chemical potential μ and interaction strength g, the final equilibrium state may no longer satisfy the normalisation condition, Equation 2.2). The resulting equilibrium state may be different from the ground state as found by imaginary time propagation or other eigensolvers. It is therefore necessary to force consistency by either renormalising the wavefunction every time step so that the particle number is constant, or by carefully choosing the value of the chemical potential so that the equilibrium state approached using the DGPE matches the true ground state with correct atom number. The latter of these two methods is perhaps preferred as it is less artificial in nature, and so a numerical technique for finding the 'correct' μ for a given value of g is presented in Algorithm 1.

Some authors [180, 181] write the DGPE in a similar but different way,

$$(i-\gamma)\hbar\frac{\partial\psi}{\partial t} = \left(-\frac{\hbar^2}{2m}\nabla^2 + V(\mathbf{r}) + g|\psi|^2(\mathbf{r}) - \mu\right)\psi(\mathbf{r}), \tag{2.31}$$

where $\gamma > 0$ for damping. Following these authors, this is the form of the DGPE used in numerical simulations in this thesis. Simple algebra shows that while not exactly equal

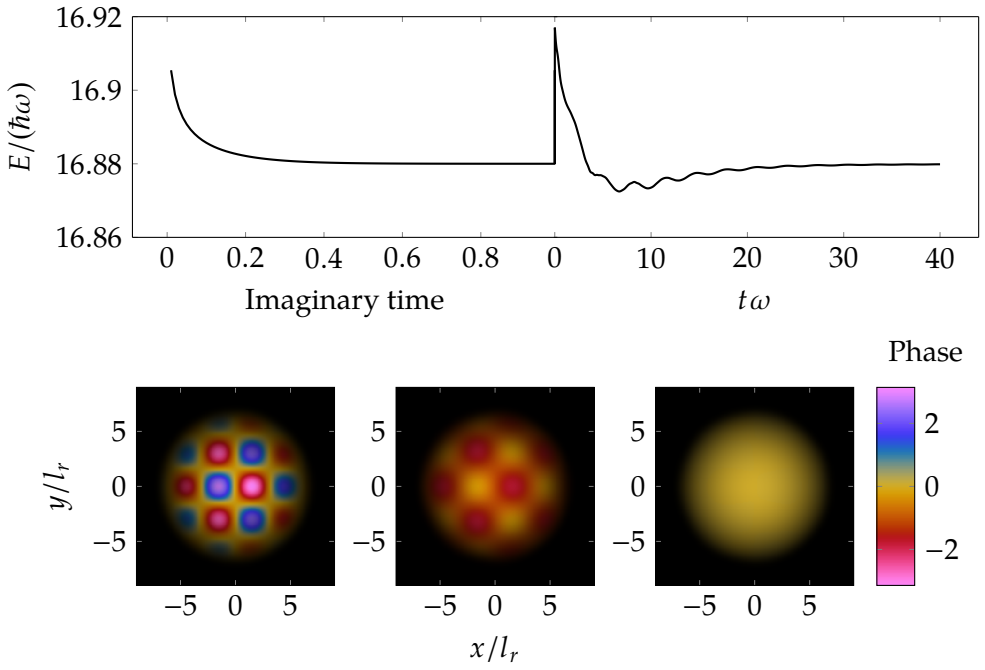

Figure 2.2: Simulated DGPE for a condensate with interaction energy $\tilde{g} = 2000$, $\tilde{\mu} = 25.27$ and $\gamma = 0.01$. The total energy (upper) is shown during both imaginary and real time. At $t = 0$ an excitation is added to the condensate [$\tilde{\psi} \rightarrow \tilde{\psi} + \sin(x/l_r)\cos(y/l_r)$]. The ground state is then reapproached through dissipation. Density and phase are shown (below) at time $t = 0$ (left), $t = 1/\omega$ (center), and $t = 40/\omega$ (right).

to Equation 2.29, the difference is only in a factor of γ^2. When $\gamma \ll 1$, which is in most cases, this difference is negligible and makes no difference to qualitative behaviours. An example evolution using Equation 2.31 is shown in Figure 2.2, also demonstrating the method of carefully choosing a value of μ using Algorithm 1, so that the equilibrium state approached using the DGPE matches the true ground state.

2.12 Finite temperature homogeneous condensate using the classical field method

A common method of simulating finite temperature Bose gases is the classical-field method, also referred to as c-field method. The classical-field method used in this thesis is investigated and laid out in [184]. The advantage of the method is that the numerics are no more complicated than simulations of the zero-temperature GPE, instead the meaning of the field ψ is reinterpreted.

An analysis of the kinetics of a weakly interacting bosonic field was undertaken in [185] and it was demonstrated that under the assumption that the occupation numbers are large, the system evolves as an ensemble of classical fields with corresponding classical-action.

In the case of a highly disordered and weakly interacting Bose gas, the state can be viewed as a mixture of coherent modes, each of which evolves (to leading order) along the classical trajectory described by Equation 2.1. The initial condition for numerical simulations of this system must reflect the highly occupied and non-equilibration nature of the Bose gas, and is described in Section 2.14.3.

We emphasise that the requirements of large occupation numbers and weak interactions are essential. Without these requirements quantum modes exist that are coupled to the rest of the system and with occupation number of order unity, and the classical field description breaks down. All Bose gases discussed in this thesis will be of the dilute and weakly interacting form, so this caveat poses no future trouble. Further discussion and analysis of a highly non-equilibrium Bose gas and the classical-field method can be found in [184].

2.13 A selection of simple solutions

Due to the nonlinearity of the GPE fully analytical solutions are rare. However, there are a selection of solutions available for simple cases that allow us to gain insight into the behaviour of a fluid governed by the GPE in more complicated scenarios.

2.13.1 Density near a wall

Consider a stationary ($\partial\psi/\partial t = 0$) solution of the 1D GPE with no trapping potential ($V(x,t) = 0$) and boundary conditions $\psi(0) = 0$ (representing a hard wall boundary at $x = 0$) and $\psi(x) = \sqrt{\mu/g}$ as $x \to \infty$. The 1D GPE becomes

$$-\frac{\hbar^2}{2m}\frac{\partial^2}{\partial x^2}\psi + g\psi|\psi|^2 - \mu\psi = 0, \tag{2.32}$$

which is solved by,

$$\psi(x) = \sqrt{\frac{\mu}{g}}\tanh\left(\frac{x}{\xi}\right). \tag{2.33}$$

This solution is shown in Figure 2.3. We gain insight through this analytical solution for how a fluid governed by the GPE 'heals' near areas of low density. There is clearly a natural minimum distance, related to ξ, over which the wavefunction can change from a density of zero to its homogeneous value. This behaviour appears many times in the context of superfluids, from solitons and solitary waves in low dimensional systems, to the fluid behaviour near impurities and vortex lines and tubes in fully 3D systems.

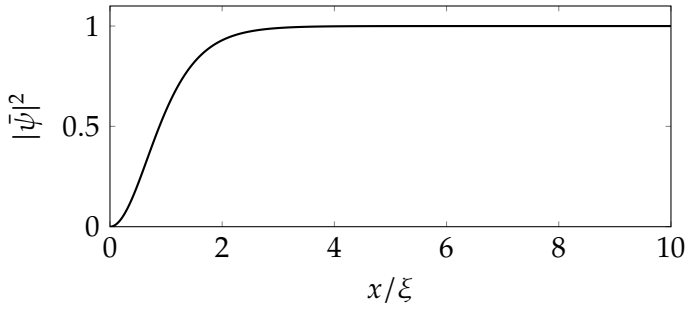

Figure 2.3: A fluid governed by the homogenous GPE healing at a hard wall at $x = 0$.

2.13.2 Soliton solutions

Due to its nonlinear nature, solutions of the GPE can support localised non-dispersive waves packets known as solitons. Two flavours of solitons can form in 1D, so called bright or dark solitons. Bright solitons form when interactions between particles are attractive ($g < 0$), however, as no physically relevant simulations in this thesis occur in this range we do not focus on these solitons. Dark solitons form when the interaction term is repulsive ($g > 0$) and physically consist of a dip in the density along with a phase slip of up to a value of π. When the density dips to zero, the phase slip is equal to π and the velocity of the soliton is $v = 0$. Dark solitons with $v > 0$ have a density dip that does not quite reach zero and a smaller valued, smooth phase slip. The 1D dark soliton solutions, derived in the 70s [186, 187], take the general form,

$$\psi(x,t) = \sqrt{\rho}\exp\left(-\frac{i\mu}{\hbar}t\right)\left\{\sqrt{1-\frac{v^2}{c^2}}\tanh\left[\sqrt{1-\frac{v^2}{c^2}}\frac{(x-vt)}{\xi}\right]+\frac{iv}{c}\right\}, \tag{2.34}$$

where v is the velocity of the soliton and $c = \sqrt{\rho g/m}$ is the speed of sound. Examples of dark solitons are seen in Figures 2.4 and 2.5.

Solitonic waves can exist in higher dimensional systems, but these are not solitons

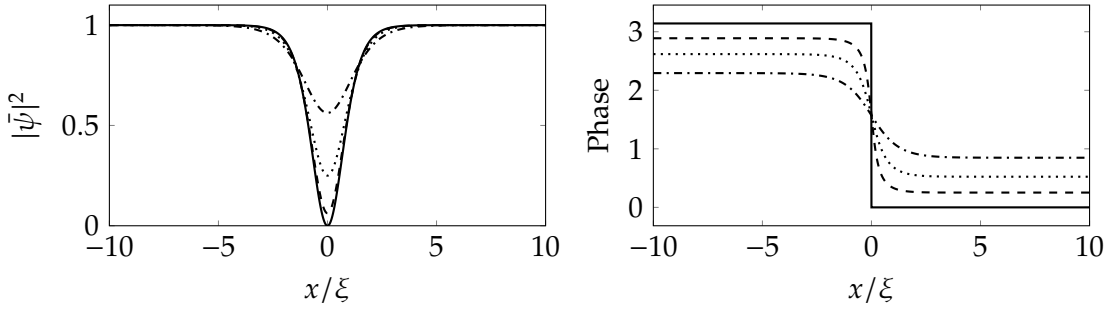

Figure 2.4: Density (left) and phase (right) of solitons in a 1D homogeneous system moving at speed $v = 0\ c$ (solid),$v = 0.25\ c$ (dashed), $v = 0.5\ c$ (dotted) and $v = 0.75\ c$ (dash-dotted).

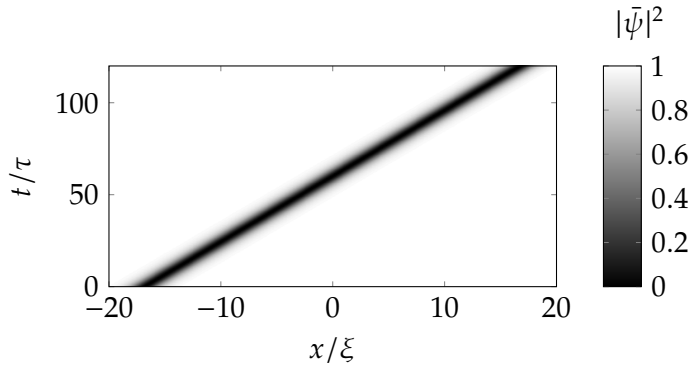

Figure 2.5: Density over time of a 1D fluid containing a soliton with speed $v = 0.25c$, confirming the non-dispersal nature of the wavepacket.

in the strict mathematical sense; the structures are unstable, and decay due to the snake instability [84, 85]. Nevertheless, long living stable solitary waves can exist, particularly in quasi-1D geometries [119].

2.13.3 Quantised vortices

We have already seen in section 2.7 that rotation in a fluid governed by the GPE must be quantised. Both two and three-dimensional solutions of the GPE can support vortices and vortex lines as carriers of quantised vorticity. They are defined by a singularity in the phase, along with a corresponding dip in density. This density dip masks the phase singularity, which is related to the fluid velocity, and so avoids solutions with infinite energy density.

The 2D quantised vortex core solution (or equivalently the solution in the plane perpendicular to a straight line 3D vortex) is circularly symmetric and can be written in polar coordinates as

$$\psi(r, \varphi) = f_v(r)\sqrt{\rho}\exp(ni\varphi), \tag{2.35}$$

where $n \in \mathbb{Z}$ is the charge or winding number of the vortex. Vortex solutions can be found numerically using the imaginary time propagation method outlined in Section 2.9 and an example 2D solution with $n = 1$ is shown in Figure 2.6.

No analytic form exists for the shape of the vortex core, $f_v(r)$, and it must be approximated or calculated numerically. A useful approximation for the shape of the core when $n = 1$ is the Padé approximation,

$$f_v(r) = \sqrt{\frac{0.6874(r/\xi)^2 + 0.1144(r/\xi)^4}{1 + 0.6666(r/\xi)^2 + 0.1144(r/\xi)^4}}. \tag{2.36}$$

which takes the values $f_v(0) = 0$ and $f_v(r) = 1$ as $r \to \infty$, and is close to the true vortex core shape everywhere [188]. A comparison of the Padé approximation and the true ($n = 1$)

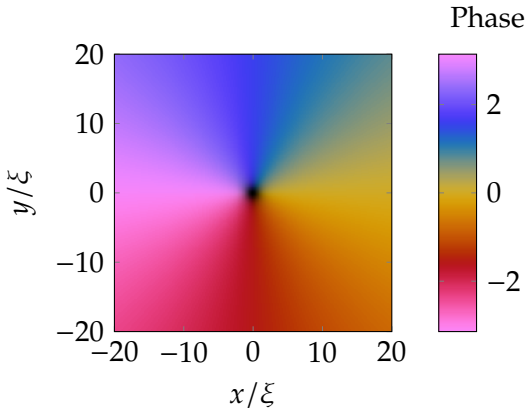

Figure 2.6: Density and phase of a vortex at $(x, y) = (0, 0)$ with $n = 1$, found numerically with the GPE in imaginary time. Note how the density dip at the vortex centre masks the phase singularity from the fluid.

vortex solution is shown in Figure 2.7 (a). Note that the density dip heals over a radius on the order of 5ξ. While the density heals over a short area around the vortex, the presence of a vortex changes the phase in the entirety of the fluid; vortices are a truly non-local phenomenon and multiple vortices can interact even when separated much further than the size of their density cores.

Figure 2.7 (b) shows the velocity field near a vortex. As seen in Section 2.6, the velocity of the fluid can be written $\mathbf{v} = \frac{h}{m}\nabla\theta$, where θ is the phase. We can use this with Equation 2.35 to find the velocity around a vortex,

$$\mathbf{v}(r, \varphi) = \frac{n\hbar}{mr}\hat{\boldsymbol{\varphi}}, \tag{2.37}$$

where $\hat{\boldsymbol{\varphi}}$ is the azimuthal unit vector. Note that Equation 2.37 demonstrates a $v \propto 1/r$

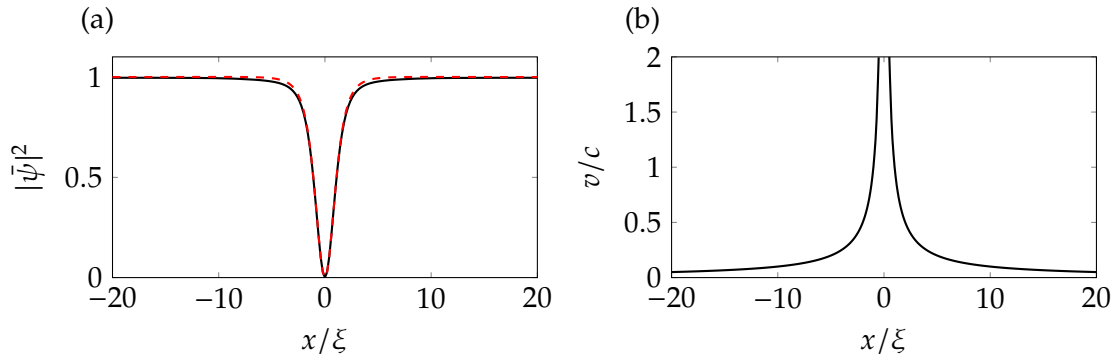

Figure 2.7: (a) A comparison of the true vortex solution (black solid line) at $x = 0$, found by numerically propagating the GPE in imaginary time, and the Padé approximation (red dashed line) for a vortex core with a charge of $n = 1$. (b) Fluid velocity in the vicinity of a vortex at $x = 0$ with charge $n = 1$.

dependence in the speed of the fluid around the vortex.

2.14 Initial conditions

When numerically solving the GPE, an initial condition must be chosen. Correct choice of initial condition is important for accurate simulation of dynamics. If an unstable initial condition is chosen far from the ground state solution, noise and other excitations such as solitary waves and vortices may be generated that interfere with any measurements and studies undertaken at later times in the numerical computation. A selection of appropriate non-violent initial conditions are outlined in this section.

2.14.1 Homogeneous initial condition

When the potential term $V = 0$, the condensate ground state becomes homogeneous with density $\rho = \mu/g$. In this case, a stationary solution of the GPE is as simple as setting the ground state density everywhere,

$$\psi = \sqrt{\frac{\mu}{g}}. \tag{2.38}$$

2.14.2 Thomas-Fermi profile of a trapped condensate

Consider an initial condition that is stationary in time, but has a non-zero potential and so varies in space. Such a condition will necessarily satisfy 2.3, the time-independent GPE. Let us assume that the potential term V varies slowly in space, and that the atom interactions are repulsive ($g > 0$) and large enough so that $\nabla^2\psi$ is negligible compared to the strength of the atom-atom interactions. In this case we can neglect the kinetic energy term in the solution and write

$$\mu\psi(\mathbf{r}) = \left(V(\mathbf{r}) + g|\psi(\mathbf{r})|^2\right)\psi(\mathbf{r}), \tag{2.39}$$

which can be simplified as,

$$|\psi(\mathbf{r})|^2 = \frac{\mu - V(\mathbf{r})}{g}. \tag{2.40}$$

From this result, we then construct an approximate solution,

$$\psi(\mathbf{r}) = \begin{cases} \sqrt{\frac{\mu - V(\mathbf{r})}{g}} & \text{if } \mu \geq V(\mathbf{r}), \\ 0 & \text{otherwise.} \end{cases} \tag{2.41}$$

This is known as the Thomas-Fermi (TF) profile and is extremely useful as an approximate initial condition for modelling a trapped atomic condensate. In the case of a harmonic trap,

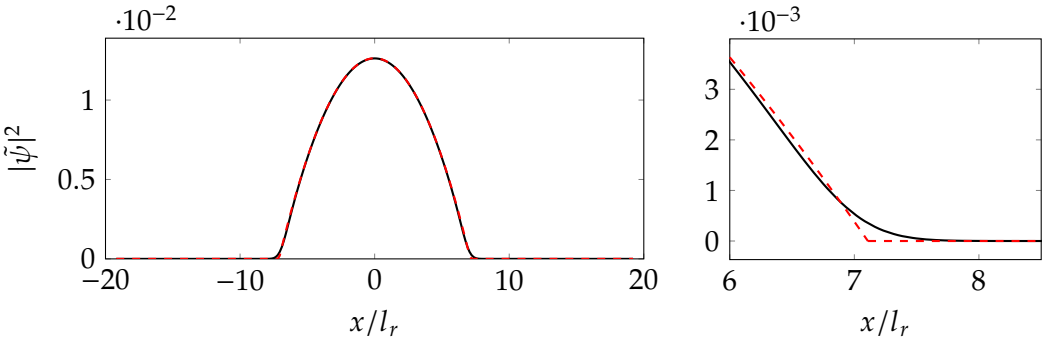

Figure 2.8: Comparison of the TF profile (red dashed line) and the true trapped ground state (black solid line) for a condensate in a harmonic trap, as found by numerical solution of the GPE in imaginary time. The TF profile fits extremely well over most of the condensate density (left), however fails at capturing the smooth tails of the density distribution (right). Here the TF radius is approximately $R_{\mathrm{TF}} = 7.1\, l_r$ and can be identified as a kink in the TF profile.

the approximation is accurate near the centre of the condensate but fails near the condensate edge, where the tails of the true density distribution are not captured. Nevertheless Figure 2.8 demonstrates the high accuracy of the approximation. Due to the discrepancy at the tails of the condensate density, it is often the case that the TF profile is used as an initial guess for numerical eigensolvers, which then find a time-independent numerical solution to be used as the true initial condition.

The TF solution provides a useful analytic approximation for the size of a condensate. The perimeter of the fluid occurs approximately when $\mu = V(\mathbf{r})$, and so the approximate Thomas-Fermi radius of the condensate is,

$$R_{\mathrm{TF}} = \sqrt{\frac{2\mu}{m\omega_r^2}}. \tag{2.42}$$

The TF radius is a useful indicator of length scales when working with analytical descriptions of condensate behaviours in a trapped system.

2.14.3 Classical field initial condition

In numerical simulation of a finite temperature Bose gas, we begin with a highly non-equilibrium state, so that the low-lying coherent modes of the system are all highly occupied. The corresponding initial condition is

$$\psi_{\mathrm{neq}}(\mathbf{r}) = \sum_{\mathbf{k}}^{k<k_{\mathrm{max}}} a_{\mathbf{k}} \exp(\mathrm{i}\mathbf{k}\cdot\mathbf{r}), \tag{2.43}$$

where the complex Fourier amplitudes $a_{\mathbf{k}}$ are related to the occupation numbers $n_{\mathbf{k}}$ through $\langle a_{\mathbf{k}} a^*_{\mathbf{k}'} \rangle = n_{\mathbf{k}} \delta_{\mathbf{k}\mathbf{k}'}$. The phase of the complex amplitudes $a_{\mathbf{k}}$ are distributed uniformly on $[0, 2\pi]$ while the value of $|a_{\mathbf{k}}|$ is fixed for all $\mathbf{k}$. It has been found that using different distributions of $|a_{\mathbf{k}}|$, with the same number density, N/V, and kinetic energy density, E_{kin}/V, leads to the same qualitative turbulent evolution [184]. The choice of N/V and E_{kin}/V uniquely determines the condensate fraction, and therefore the temperature for the equilibrium state of the Bose gas. A momentum cutoff, $k < k_{\text{max}}$, is introduced to limit the momentum of the low lying modes, and in harmonic systems can be imposed as an energy-cutoff during evolution using the projected GPE [189]. However, in the case of homogeneous finite temperature simulations the momentum cut-off arises naturally as a consequence of the discretisation of the system; for a 3D finite temperature simulation in a periodic box with uniform grid spacing Δ, $k_{\text{max}} = \sqrt{3}\pi/\Delta$.

The numerical initial condition used in our simulations, $\psi(\mathbf{r}, t_0)$, is determined by renormalisation of $\psi_{\text{neq}}(\mathbf{r})$, setting the number density and kinetic energy density as a way of varying temperature at equilibrium.

2.15 Modelling obstacles and surfaces

In atomic BEC experiments, adding obstacles can be achieved by using laser beams. A red-detuned laser beam can create areas of attraction, and conversely, blue-detuned laser beams can create areas of repulsion. Should a blue-detuned laser beam be bright enough, a localised 'hole' in the condensate forms. Similarly, in superfluid helium experiments, there are examples where the fluid can feel the presence of obstacles, including grids [153, 190], wires [154–156], forks [158, 159], propellers [191, 161], spheres [157] and other objects [162].

These effects are replicated in the GPE model through the use of two and three-dimensional potentials. In atomic BEC simulations the profile of the potential matches that of the intensity of the laser beam, typically a cylindrical beam with a Gaussian profile. In superfluid helium simulations, smooth or hard wall potentials are used with an amplitude large compared to the chemical potential.

2.15.1 Three-dimensional elliptical Gaussian

In our 3D simulations the localized obstacle is modelled via a repulsive Gaussian potential,

$$V_{\text{obj}}(\mathbf{r}) = V_0 \exp\left(-\frac{\varepsilon^2(x-x_0)^2}{d^2} - \frac{(y-y_0)^2}{d^2} - \frac{(z-z_0)^2}{d^2}\right), \tag{2.44}$$

where V_0 is its amplitude, d its width in the y and z directions, and (x_0, y_0, z_0) its coordinates. ε parametrises the ellipticity of the obstacle, a value of $\varepsilon = 1$ corresponds to a

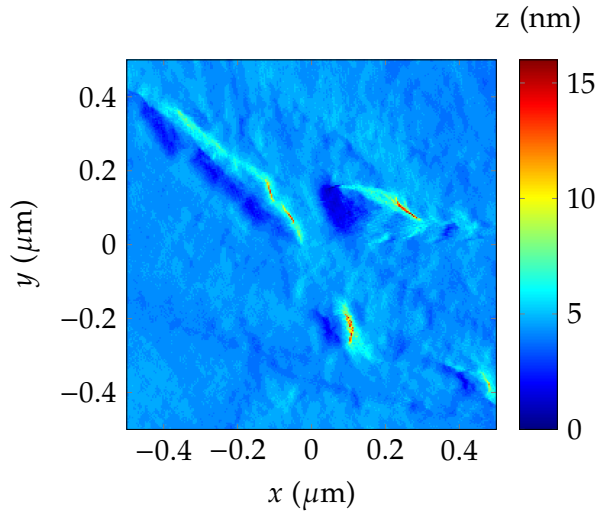

Figure 2.9: An atomic force microscope (AFM) image showing the microscopic detail on the surface of a single–core NbTi 'floppy' wire used for generating superfluid turbulence (data provided by R. P. Haley and C. Lawson [168]).

spherical obstacle, a higher value of ε 'squashes' the obstacle along x, forming a pancake shape.

2.15.2 Two and three-dimensional cylindrical Gaussian

In addition to spheres, we model cylindrical potentials as a Gaussian,

$$V_{\text{obj}}(\mathbf{r}) = V_0 \exp\left(-\frac{\varepsilon^2(x-x_0)^2}{d^2} - \frac{(y-y_0)^2}{d^2}\right), \tag{2.45}$$

where V_0 is its amplitude, d its width in the y direction, and (x_0, y_0) its coordinates. ε parametrises the ellipticity of the Gaussian (experimentally feasible with laser beam focusing or masking), so that a value of $\varepsilon = 1$ corresponds to a circular shaped hole. In 3D the Gaussian hole is extended across the entire z dimension forming a cylindrical shaped barrier.

2.15.3 Three-dimensional 'realistic' rough-surface

In many superfluid helium experiments [162] turbulence is generated by moving obstacles, the surfaces of which are rough on the length scale of the superfluid vortex core, which is of the order of 10^{-10} m in ^{4}He and 10^{-8} m in ^{3}He. As an example, Figure 2.9 is an atomic force microscope (AFM) image showing the microscopic detail on the surface of a single–core NbTi 'floppy' wire used for generating superfluid turbulence [155]. Note the appearance of an elongated scratch, believed to be typical of such wires.

We can simulate the microscopic detail through the use of a potential derived from sample AFM height-map data. We define the external potential to be,

$$V_{\text{obj}}(\mathbf{r}) = \begin{cases} V_0 & \text{if } z < (h(\alpha x, \alpha y) - z_0) \\ 0 & \text{if } z > (h(\alpha x, \alpha y) - z_0), \end{cases} \tag{2.46}$$

where V_0 is its amplitude, z_0 is a shift in height and α is a lateral scaling factor. Scaling $h(x, y)$ acts as a crude way of varying the roughness of simulated boundaries. Finally, a Gaussian blur is applied to the raw AFM data so that $V(x, y, z)$ is smooth.

Chapter 3

Numerical Methods and Procedures

Throughout Part II of this thesis the focus will be on numerical simulation of superfluidity and Bose Einstein condensates. For accurate and robust conclusions, not only must relevant models be used (such as those described in Chapter 2), but high quality numerical simulation and data processing techniques are required. A collection of numerical methods that are used throughout Part II are described in detail in this chapter, with algorithmic implementations of the methods discussed also given in Appendix C.

3.1 Numerical procedures for 2D and 3D solutions

3.1.1 Fourth order Runge-Kutta scheme

The classical fourth-order Runge-Kutta formula (RK4) is described equivalently in many texts. We follow the description in [176]. Let an initial value problem be specified as

$$\frac{\partial \psi}{\partial t} = f(\psi, t), \qquad \psi(t_0) = \psi_0.$$

A step-size, $h > 0$, is chosen as the parameter controlling how the solution is advanced over t. The scheme for estimating $\psi(t_n) = \psi_n$ is then written

$$\begin{aligned}
k_1 &= hf(t_n, \psi_n), \\
k_2 &= hf(t_n + \frac{h}{2}, \psi_n + \frac{k_1}{2}), \\
k_3 &= hf(t_n + \frac{h}{2}, \psi_n + \frac{k_2}{2}), \\
k_4 &= hf(t_n + h, \psi_n + k_3), \\
\psi_{n+1} &= \psi_n + \frac{k_1}{6} + \frac{k_2}{3} + \frac{k_3}{3} + \frac{k_4}{6} + O(h^5), \\
t_{n+1} &= t_n + h.
\end{aligned} \tag{3.1}$$

An outline derivation of the Runge-Kutta scheme is shown in Appendix A.2. In all of our relevant calculations the value of f is set as the right hand side of the homogeneous or trapped GPE. The basic structure of our time stepping loop surrounding the RK4 method is shown in Algorithm 2 and can be repeated indefinitely to reach any $t > t_0$. The step size for a given set of parameters should be chosen small enough that smaller choices make no quantitative changes to the resulting solution. The following section outlines the methods we have implemented to ensure numerical solutions are converged.

3.1.2 Numerical stability and convergence

We now investigate numerical parameters which affect the stability of simulated superfluid systems. Our direct aim is to find a suitable discretisation of space and time so that, while simulations complete swiftly, our numerical quantities are converged (they are not sensitive to small changes in computational parameters) and that quantities conserved by the equations of motion are indeed conserved in the computed numerical solutions.

We begin by estimating Δ_x, the required spatial grid spacing, by considering the width of the vortex core in a homogeneous system, a feature we would like well and accurately visualised in our numerical solutions. Through observation of a singly quantised vortex core solution of Equation 2.35 (demonstrated in Figure 2.7) we observe a core radius of approximately 5ξ. To ensure the vortex core structure is well resolved we decide to dedicate 10 grid points for a vortex core radius, suggesting a value of $\Delta_x = \xi/2$.

In the harmonically trapped case we can use the same idea. It is shown in Section B.3 that $\xi = \hbar/\sqrt{mgn}$. However, as a consequence of the trapping potential, n and ξ will vary over space. The healing length will reach its minimum in the centre of the condensate, where the density is approximately homogeneous taking the value ρ. We can write the healing length in terms of the harmonic oscillator length by first setting the value of n to $\rho = \mu/g$, then eliminating m by rearranging $l_r = \sqrt{\hbar/(m\omega)}$ for m and substituting into ξ. Following the procedure we find that $\xi = \omega\sqrt{\hbar/(\mu\omega)}l_r$ in the centre of the trap. The approximate grid spacing to adequately resolve the vortex core (at its smallest) is therefore $\Delta_x = 0.5\xi = 0.5\omega\sqrt{\hbar/(\mu\omega)}l_r$. As an example, for a trapped condensate with interaction energy $\tilde{g} = 2000$, chemical potential $\tilde{\mu} = 25.27$ and trap frequency $\omega = 8.75$ Hz we find that a value of $\Delta_x = 0.1l_r$ should be adequate.

Similar arguments (concerned with time rather than space) can be used to approximate a suitable time step h. We define a time period that we would like to be well resolved by considering by the smallest possible element moving at the fastest reasonable speed. If we define this period as $\Delta_x/5\ c$ and allocate to it 10 time steps, we find that $h = 0.5\xi/50\ c = 0.01\tau$ in natural units ($h = 0.0004\ \omega^{-1}$ in trapped units).

In addition to this process, for each set of simulation parameters it is recommended to confirm the suitability of the chosen Δ_x and h by testing the convergence and conservation

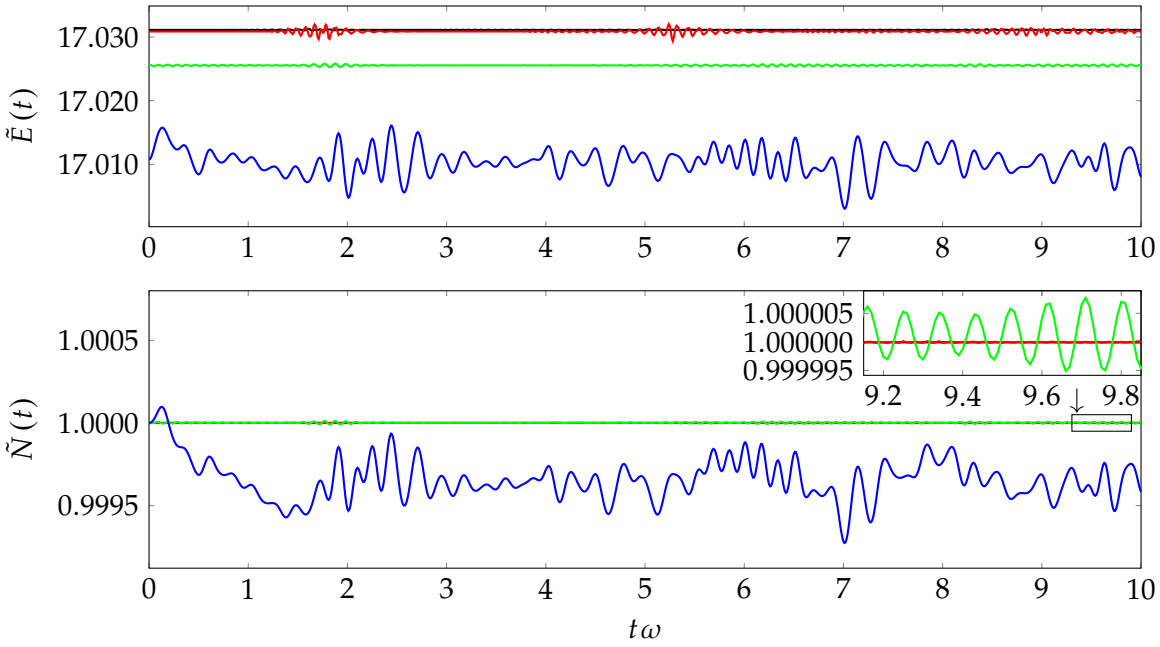

Figure 3.1: Dimensionless energy, $\tilde{E}$, and particle number, $\tilde{N}$, throughout numerical propagation of a trapped condensate containing a singly quantised vortex in its center, with interaction energy $\tilde{g} = 2000$ and chemical potential $\tilde{\mu} = 25.27$. The numerical grid width varies with each line; $\Delta_x = 0.05 l_r$ (black), $\Delta_x = 0.1 l_r$ (red), $\Delta_x = 0.2 l_r$ (green) and $\Delta_x = 0.4 l_r$ (blue). (Inset) Zoomed view of $\tilde{N}$.

in the numerical methods. The total condensate energy and particle number are good measures for this as they should both be well conserved by the GPE with a dissipation of $\gamma = 0$. An example of this process (confirming the suitability of a chosen Δ_x) is shown in Figure 3.1. For a large $\Delta_x = 0.4 l_r$ both the condensate energy and particle number fluctuate wildly. For $\Delta_x = 0.1 l_r$ the particle number is extremely well conserved to within $2 \times 10^{-5}\%$ and the energy is conserved within $5 \times 10^{-3}\%$. The smallest tested value of $\Delta_x = 0.05 l_r$ finally confirms that the energy has converged. We conclude that for the chosen system parameters that $\Delta_x = 0.1 l_r$ (the value suggested by the above analysis) is numerically sufficient and there is little reason to use $\Delta_x < 0.1 l_r$.

3.2 Identifying vortices

Large portions of this thesis are dedicated to the study of 2D vortex dynamics. As such, accurate detection of the location and charge of densely packed quantised 2D vortices is required. Methods for detecting quantum vortices by analysis of the phase are seen throughout the literature [192–199], and we have developed our own robust numerical methods for vortex identification inspired by these methods.

Recently, other authors have defined a "pseudo-vorticity" field [200, 201] in 2D and

3D. It is possible to fairly easily implement a method for vortex locating and tracking in the GPE using this field. However, the numerical schemes described in this section were devised and implemented before the pseudo-vorticity field was well known, and so below we describe the alternative scheme that was originally used in our numerical simulations. Our alternative scheme defines a "vortex field", which can be thought of as a similar to the pseudo-vorticity field described in [200, 201]. The fields are similar enough that the pseudo-vorticity could simply replace it in our 2D algorithms. For the more sophisticated case of 3D vortex line tracking an accurate and robust algorithm has recently been described by Villois *et. al.* [201].

The basic idea of vortex detection is fairly simple, with arguments similar to those used to demonstrate the quantised nature of the circulation. As shown in Section 2.7, the integrated change of phase along any closed curve C is,

$$\Delta\theta(C) = \oint_C \nabla\theta \cdot \mathrm{d}\mathbf{l} = 2\pi q, \tag{3.2}$$

where $\mathrm{d}\mathbf{l}$ is the line element and $q \in \mathbb{Z}$. Further, the fundamental theorem of calculus for line integrals [202] implies that $\Delta\theta(C) = 0$, providing that C is continuous and does not encompass a phase singularity. This result is crucial; it allows us to directly state that a vortex lies within C if and only if $\Delta\theta(C) \neq 0$.

3.2.1 Basic vortex detection method

First define a set of curves C_k with each curve lying on points of our numerical grid, so that a single C_k encompasses only a small region of the fluid (ideally, C_k should encompass a region at most the diameter of a vortex core). $\Delta\theta(C_k)$ is then approximated for each k using numerical differentiation (2nd order finite differences) and numerical line integration (trapezium or Simpson rule). If $\Delta\theta(C_k) = 0$ to within numerical accuracy then we determine that the region inside C_k contains no vortices. Otherwise the sign of $\Delta\theta(C_k)$ tells us the polarity of the encompassed vortex. Figure 3.2 demonstrates the method by detection of a single vortex.

In principle the result also allows us to calculate the exact charge of a vortex in terms of the quantum of circulation. However, for accurate determination of vortex location the curves C_k must encompass a very small area, contain few grid points, and so accuracy is low. We use only the sign of the $\Delta\theta(C_k)$ so that the integration error makes minimal difference and results in an accurate detection of vortex polarity and location. As multiply charged ($|q| > 1$) vortices are unstable (rapidly decaying into several singly charged vortices) there is no significant loss of information in practise.

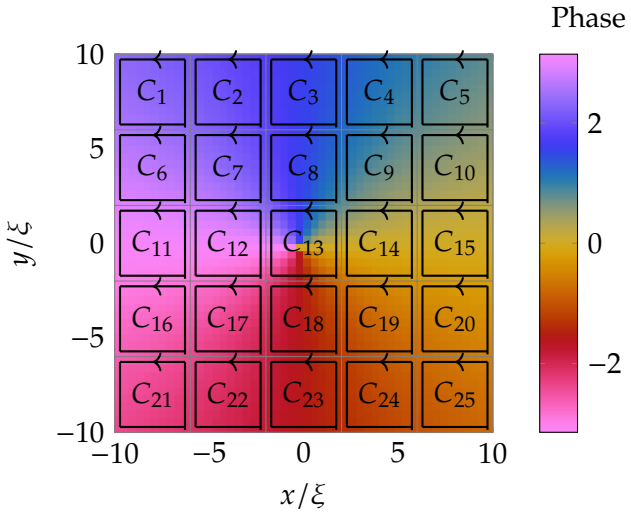

Figure 3.2: The phase for a homogeneous system with a vortex located at (0,0). Also shown is an example set of curves C_k for vortex identification. All $\Delta\theta(C_{k\neq 13}) \approx 0$, and $\Delta\theta(C_{13}) > 0$. The conclusion is that a positive vortex lies in the region defined by C_{13}.

3.2.2 Visualising vortex location with a vortex field

The basic vortex identification method set out in Section 3.2.1 is quick to implement and useful when there are few well separated vortices, but one can easily imagine a situation where the method fails. One such case would be two vortices both lying within a single C_k curve; in the case of two similarly charged vortices only a single vortex would be detected or in the case of two oppositely charged vortices potentially none at all! The solution is not always as simple as reducing the size of C_k, vortices can be densely packed and there are often too little grid points to make this reasonable.

We again define a set of curves with a width around the diameter of a vortex core, but for every grid point (taking into account boundary conditions) the curve $C_{[i,j]}$ is defined surrounding and centred on the numerical grid point $[i, j]$. A "vortex field" is then defined by the value of $\Delta\theta(C_{[i,j]})$ at every grid point. Algorithm 3 describes the process in detail. As before, areas where $\Delta\theta(C_{[i,j]}) \neq 0$ (to within numerical accuracy) signify the presence of a vortex. Figure 3.3 demonstrates a vortex field obtained from a homogeneous system with a negative vortex located at $(-\xi, 0)$ and a positive vortex located at $(\xi, 0)$. It can be easily seen where the two vortices are located in the wavefunction by direct observation of the 2D vortex field.

For every vortex detected by this algorithm, the corresponding area in the vortex field is composed of several adjoined points in the numerical grid. For correct vortex counting, these multiple points must be classified as a single vortex. The bwlabel algorithm described in Algorithm 4 is used to obtain this required classification. The algorithm takes the vortex field as input and assigns each set of connected grid points (where $\Delta\theta(C_{[i,j]}) \neq 0$) a label.

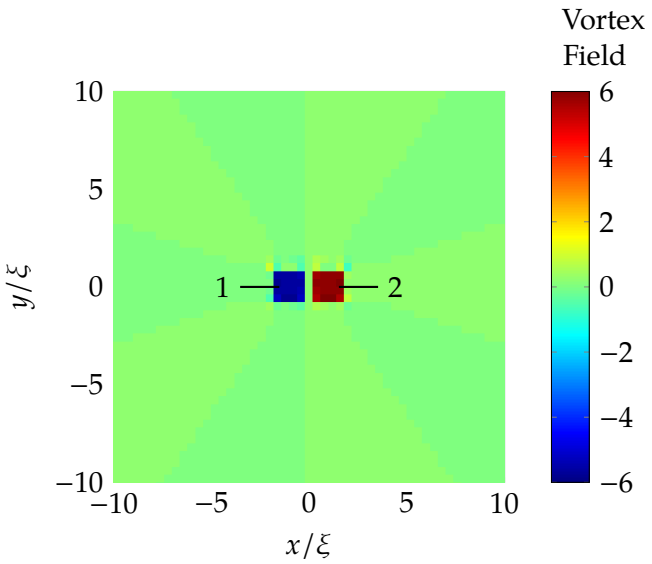

Figure 3.3: Vortex field for two oppositely charged vortices located at $(-\xi,0)$ and $(\xi,0)$ in a homogeneous system. The positive (negative) vortex leads to a positive (negative) quantity in the vortex field. In addition, the output of the bwlabel algorithm is labelled.

An example output of bwlabel is shown in Figure 3.3. To find the vortex location for a given label, we simply take the mean of all the x and y locations of points with the same label (the procedure is shown rigorously in Algorithm 5).

The algorithm described in this section leads to more accurate vortex counts when vortices are densely packed. As a bonus the accuracy of detected vortex location is improved; the final output is a average of information from several curves $C_{[i,j]}$, and so in good conditions the result can be improved by a factor of 2 when the phase singularity corresponding to a vortex lies between grid points.

3.2.3 Further improving accuracy with a Gaussian blur

When using Algorithm 3 in 'messy' wavefunctions (containing many vortices and waves), artefacts of the incorrect sign can be introduced by the numerical discretisation, differentiation and integration errors. Faint examples of these artefacts can be seen in Figure 3.3 surrounding the two labelled regions. These artefacts are spatially small (on the scale of Δ_x) and so can be corrected by removing all high frequency spatial waves from the vortex field using low-pass filtering (the filter parameters should be chosen to remove waves with wavelength smaller than the size of a vortex core). A common low-pass filter is the Gaussian blur [203], applied using a convolution. The Gaussian blur algorithm is described in Algorithm 6 and the result of applying the algorithm to the vortex field is shown in Figure 3.4. Note how the incorrectly signed artefacts surrounding the detected vortex regions are now removed.

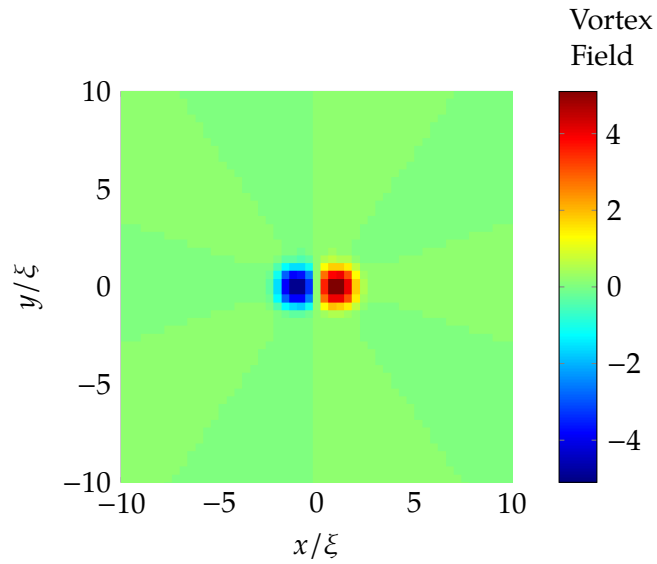

Figure 3.4: Smoothed vortex field for two oppositely charged vortices located at (−ξ,0) and (ξ,0) in a homogeneous system. The high frequency noisy artefacts in the vortex field are removed by the low-pass filtering.

A by-product of applying a low-pass filter to the vortex field is that sharp edges in structures are blurred and spread out. To identify vortex locations a threshold function is therefore used before performing the bwlabel algorithm, i.e vortices are identified when $|\Delta\theta(C_{[i,j]})| > \Delta_{\text{th}}$, where $\Delta_{\text{th}} > 0$ is some threshold. Δ_{th} can be tweaked to make the vortex detection more or less sensitive (for either detecting vortices more easily in messy systems, or to ignore weak spurious signals in the vortex field) and in general will vary for each system.

3.2.4 Avoiding 'ghost vortices'

A common problem when detecting vortices is the prevalence of invalid or uninteresting phase defects inside obstacles or when considering trapped condensates. In areas where the density is exactly zero the system phase becomes undefined. Depending on how the simulation is implemented these areas may fill with small numerical noise and cause many singularities to be detected. A similar phenomenon occurs in areas of near-zero density; well-defined singularities in the phase form but with an ill-defined vortex core in the density [180]. Examples of these vortices are shown in the low density regions of Figure 3.5. As these singularities carry negligible angular momentum and energy they are of no interest and are termed 'ghost vortices'.

A simple way to remove ghost vortices is to use a mask to hide vortices found in low-density regions in trapped systems and inside obstacles. While on the one hand it is easy to define a mask using the TF radius or considering where $V_{\text{trap}} + V_{\text{obj}} > \mu$, masks are

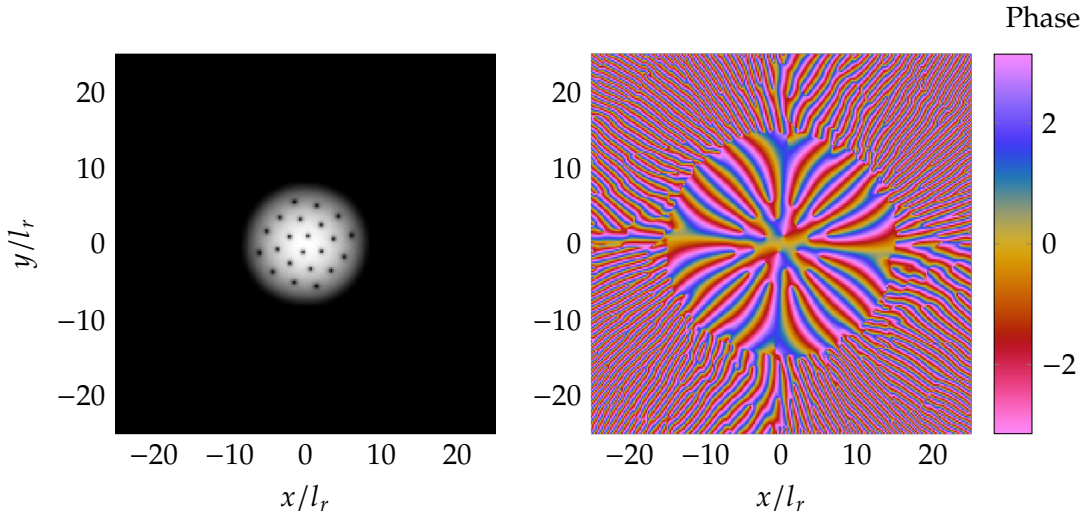

Figure 3.5: A trapped rotating condensate with $\Omega = 0.7$, $\tilde{g} = 2000$ and $\tilde{\mu} = 25.27$. Ghost vortices can be seen in the phase as singularities where the corresponding density is near-zero.

quite arbitrary in nature and an overzealous mask may hide details. Additionally, any condensate with certain excitations such a breathing mode or centre of mass oscillation will periodically extend beyond a hard coded mask.

An alternative method to avoid identifying ghost vortices presents itself when implementing Algorithm 3. The vortex field can be multiplied by the wavefunction density at every point *before* performing the Gaussian convolution step. The result is that in low-density areas the vortex field becomes completely zero and singularities in this region are no longer identified as vortices. At the centre of vortex cores the vortex field also goes to zero. However, enough vortex information remains in the vortex field in the vicinity of the vortex cores that vortices in high-density regions are still identified accurately after the Gaussian convolution. As before, the threshold value Δ_{th} controls the sensitivity of this algorithm, in particular for detecting vortices in the low density regions of the condensate. Algorithm 7 describes this method in further detail and Figure 3.6 shows the vortex field with and without the added step of multiplying by the density, demonstrating that the ghost vortices detected when using Algorithm 3 are indeed removed when using Algorithm 7.

3.3 Quantifying vortex clustering in 2D

With the ability to detect vortex polarity and locations in 2D, we can begin to better understand vortex distribution and statistics in simulations. In this section we describe the various methods of quantifying vortex distribution, both simple and complex.

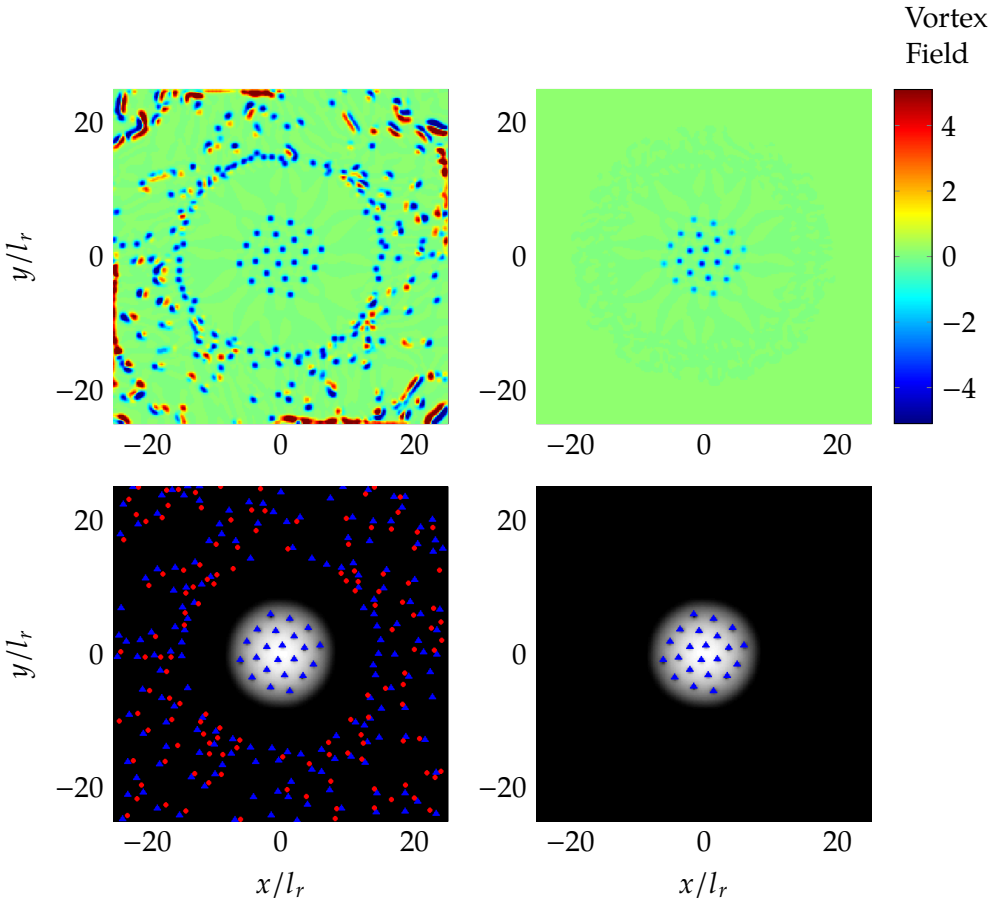

Figure 3.6: Identifying vortices within a trapped rotating condensate with $\Omega = 0.7$, $\tilde{g} = 2000$ and $\tilde{\mu} = 25.27$. (a) The smoothed vortex field using Algorithm 3, (b) the smoothed vortex field using Algorithm 7, (c) the system density with vortices identified using Algorithm 3, and (d) the system density with vortices identified using Algorithm 7. The ghost vortices seen in (a,c) are removed in (b,d).

3.3.1 Vortex counting

The simplest method of ascertaining vortex statistics is to simply count the number of vortices, N_v, in the entire system. A further obvious decomposition of this quantity is to count the number of positive and negative vortices separately, designated N_+ and N_- respectively. With this information we can define a useful property of a system's vortex distribution,

$$P_v = \frac{N_+ - N_-}{N_v}, \tag{3.3}$$

where $N_v = N_+ + N_-$ and P_v is known as the polarity of the system. This quantity takes values in the range $[-1, 1]$; when there are only positively (negatively) charged vortices in the system $P_v = 1$ ($P_v = -1$), and when there are equal quantities of positive and negatively charged vortices $P_v = 0$.

3.3.2 Ripley's K and Besag's L functions

While counting vortices as in Section 3.3.1 is a great way to gain statistics of the distribution of vortices in terms of vortex charge, the quantities tell us nothing about how vortices are located in space. The problem of spatial descriptive statistics is an old one and measures of spatial dispersion or homogeneity have in the past been applied to several datasets consisting of point locations, very similar to the results of our vortex detection algorithms. Some of these applications include spatial distribution of trees [204–206], plants [207], bird nests [208] and the spread of disease [209].

One such measure of homogeneity that has been previously applied to quantum vortices [210] is Ripley's K Function [211], defined theoretically in the following way,

$$K(s) = \lambda^{-1} E[\text{\# of points within distance } s \text{ of a randomly chosen point}], \tag{3.4}$$

where λ is the density (number per unit area) of points and $E[]$ denotes expectation. $K(s)$ can be analytically evaluated when it is known that points are distributed according to a homogeneous Poisson process, i.e. randomly placed in space. In this case each point is independent from all the other points and the resulting equation for $K(s)$ is known as complete spatial randomness (CSR),

$$K(s) = \pi s^2. \tag{3.5}$$

The simplest use of Ripley's K function is to approximate $K(s)$ from an observed set of points and test the result of CSR. Should the result be inconsistent with CSR, $K(s)$ can also tell us at what length scales the points deviate from spatial homogeneity.

For most of our simulations, $K(s)$ can be easily estimated by using observed vortex locations.

$$\hat{K}(s) = \frac{A}{N_v^2} \sum_i \sum_{j \neq i} I\left(d_{ij} < s\right), \tag{3.6}$$

where d_{ij} is the distance between the ith and jth vortex, A is the area of the region of interest, N_v is the number of vortices, and I is the indicator function (1 if its argument is true, 0 otherwise). In homogeneous simulations A could be as simple as the numerical box area, while with a trapped condensate calculating A could involve measuring the bulk part of the condensate or calculating an area using the TF radius.

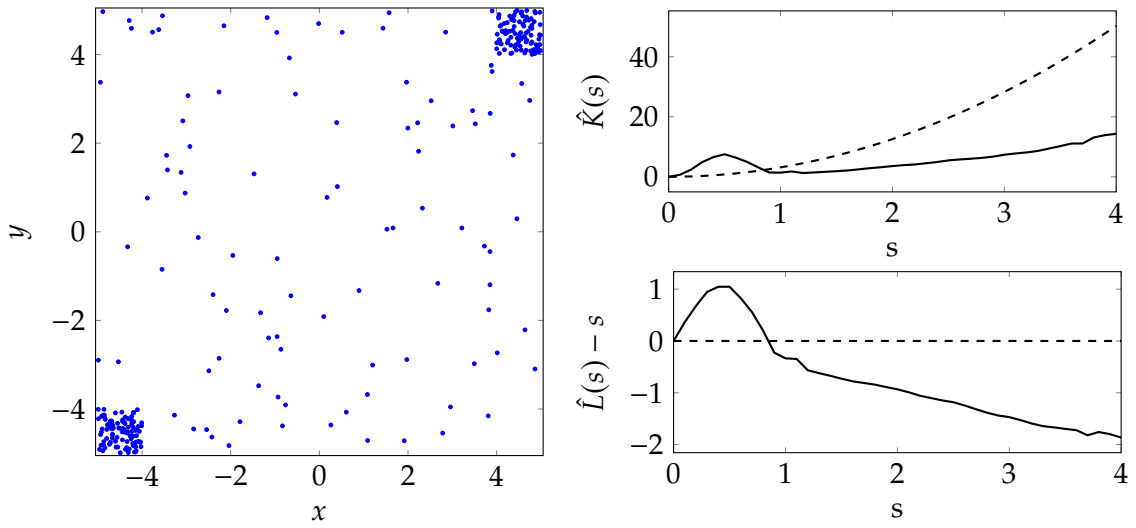

Figure 3.7: Sample points (left) used for estimating Ripley's K and Besag's L functions. Shown (right) are the estimated curves $\hat{K}(s)$ and $\hat{L}(s) - s$ (black solid lines) and the theoretical curves (dashed black lines) for points under complete spatial randomness. Here Equation 3.7 was used to calculate $\hat{K}(s)$. $\hat{L}(s) - s > 0$ for small values of s and $\hat{L}(s) - s < 0$ for larger values of s, demonstrating that the sample points are clustered at small scales and sparse at larger scales.

Equation 3.6 ignores so-called *edge effects*. These effects arise when the search radius s becomes large enough that the lack of points outside the region of interest begins to bias the estimator $\hat{K}(s)$. Ripley provides an edge-corrected estimator [212] which takes the form,

$$\hat{K}(s) = \frac{A}{N_v^2} \sum_i \sum_{j \neq i} w(\mathbf{r}_i, \mathbf{r}_j)^{-1} I\left(d_{ij} < s\right), \tag{3.7}$$

where the weight function, $w(\mathbf{r}_i, \mathbf{r}_j)$, provides edge correction. If the circle centred on the point $\mathbf{r}_i$ and passing through the point $\mathbf{r}_j$ completely lies within the region of interest, then $w(\mathbf{r}_i, \mathbf{r}_j) = 1$, otherwise $w(\mathbf{r}_i, \mathbf{r}_j)$ is equal to the proportion of the circumference of the circle that is inside the region of interest. The edge-corrected estimator provided by Equation 3.7 should be used when we are interested in large spatial scale homogeneity, i.e. when s is large, as it is on this scale edge-effects can dominate.

Visualising $\hat{K}(s)$ can be made easier by considering Besag's L function, with estimator,

$$\hat{L}(s) = \sqrt{\frac{\hat{K}(s)}{\pi}}. \tag{3.8}$$

$L(s)$ has the useful properties that under CSR the variance is approximately constant [213], which can be used as a secondary check, and $L(s) - s$ should be approximately zero for all s. Deviations from zero allow us to immediately identify in what way, as well as at what scale, spatial homogeneity is broken in the dataset.

The power of the K and L curves is demonstrated in Figure 3.7, wherein $K(s)$ and $L(s)$ were estimated (taking edge-effects into account) from inhomogeneous sample points. Inhomogeneity was enforced by randomly placing 100 sample points within the region $x, y \in (-5, 5)$, with two further randomly placed 'clusters' of 100 points in the regions $x, y \in (-5, -4)$ and $x, y \in (4, 5)$. The number of sample points and the region definitions used here are arbitrary, chosen simply for demonstration of the K and L curves. The curve $\hat{L}(s) - s$ clearly shows a positive region (suggesting clustering) on the scale of the cluster size, and a negative region (suggesting dispersion) on the scale of the box size, detecting from the point data alone exactly the spatial pattern used to generate the points.

3.3.3 Recursive Cluster Algorithm

The limit of the K and L curves is quickly reached when we want to describe statistics of both the charge and spatial features of a collection of vortices. The K and L curves operate solely on location and are not easily modified to capture the charge of a vortex an so for detailed analysis of charged vortex clusters another algorithm must be used.

The algorithm we use is the Recursive Cluster Algorithm (RCA) developed by Reeves *et. al.* [195, 196]. The algorithm allows for detailed spatial-temporal statistics regarding like-signed vortex clustering. The algorithm works in a recursive manner, by removing dipole-like structures first, and then decomposing the remaining vortices into positive or negatively signed clusters. To perform the algorithm the following two rules are applied to a collection of vortices:

- *Opposite sign vortices that are mutual nearest-neighbours are removed from the algorithm's consideration.*
- *Same-sign vortices that are closer to each other than either is to an opposite-sign vortex are placed in the same cluster.*

The rules are applied repeatedly in order until no more vortices can be added to the dipole or cluster groups. Any remaining vortices are labelled as "free vortices". An implementation of the algorithm, compatible with the output of the vortex detection algorithms in Section 3.2, is described in detail in Algorithm 8. A sample RCA decomposition of 200 randomly placed points with random polarity is demonstrated in Figure 3.8. It can be seen that the algorithm picks out the chance clusters of like-signed points.

With the decomposed points, one can begin to obtain the statistical properties of the clusters. The physical location of the cluster can be estimated using its 'center of mass',

$$\mathbf{R}_C = \frac{1}{N_C} \sum_{i \in C} \mathbf{r}_i, \tag{3.9}$$

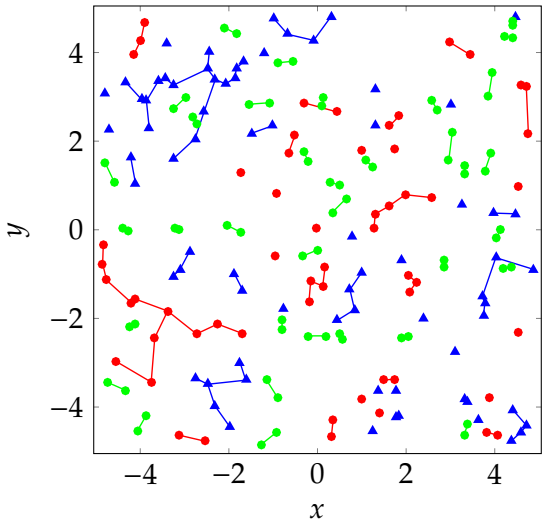

Figure 3.8: A sample RCA decomposition into clusters, free vortices and dipoles. Positive (negative) clusters and vortices are shown as blue triangles (red circles), dipoles are shown as green circles.

where C is the a set of vortices in a particular cluster, N_C is the number of vortices in the set C, and r_i is the vortex location. Additionally, the size of a particular cluster can be quantified using an expression for the approximate cluster radius,

$$R_C = \frac{1}{N_C} \sum_{i \in C} |\mathrm{r}_i - \mathbf{R}_C| \,. \tag{3.10}$$

Note that while the results of the RCA are insensitive to small changes in the initial input, over time vortex distributions can radically change. This has the consequence that $\mathbf{R}_C$ and R_C vary over time, and so time based averaging should also be used to gain statistics of vortex clustering.

3.4 Building vortex trajectories

It is of interest to be able to track vortices over time, eventually leading to the building of vortex trajectories. The process of building trajectories from the location of many different points over time is known as particle linking. Note that in particle linking, although the location of particles is known, their identity is unknown (that is, the particles are not labelled) and so it is not immediately obvious what particle at one point in time corresponds to another at different times and so methods for particle linking are therefore often built through minimisation algorithms.

The first step in the particle linking method described here is to perform frame-to-frame particle linking. Links are built by moving from one time point to the next and pairing vortices that are close together (taking into account both Euclidean distance and vortex

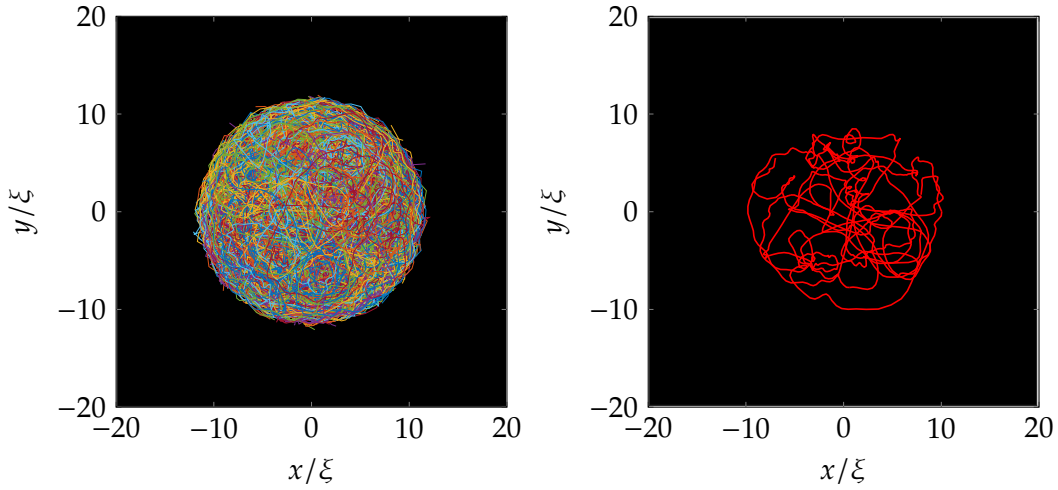

Figure 3.9: An example of building vortex trajectories for a trapped condensate with interaction energy $\tilde{g}$ = 2000 and $\tilde{\mu}$ = 25.27 filled with vortices of both polarity. (Left) 353 vortex trajectories clearly showing the movement of vortices within the boundary of the condensate. (Right) The single longest vortex trajectory, over the time period 648.5 ω^{-1}.

charge), as these are likely to be the same vortex. This step is performed efficiently using the Hungarian algorithm [214], an algorithm that is able to pair together many particles at two different time points while minimising the sum of all the pair distances.

As the simulation develops, the number of vortices will change and so trajectories will necessary end early or begin at later times. A threshold value, Δ_v, used in conjunction with the Hungarian algorithm controls if a track ends. If the Euclidean distance between a pair of vortices exceeds Δ_v, it is assumed they cannot possibly be the same vortex, and they are not linked. The algorithm continues in fashion, linking pairs of vortices frame-to-frame until the end of the simulation is reached.

Sometimes, due to numerical error or simulation dynamics, a vortex will not be detected for one or more time points before reappearing. The particle linking algorithm must take this into account, aiming to assign each vortex only a single trajectory. The second step in the method is to iterate once more through the data and investigate the ends of the trajectories. If a trajectory beginning is found close (once again taking into account euclidean distance and vortex charge) to the end of a previous trajectory within a certain number of time points, a link is made joining the two trajectories. Once again a threshold value compared to the distance between points in space and time. Should the trajectory ends be too far apart, it is assumed they are not the same vortex and remain unlinked. Figure 3.9 demonstrates the building of vortex trajectories in a trapped condensate.

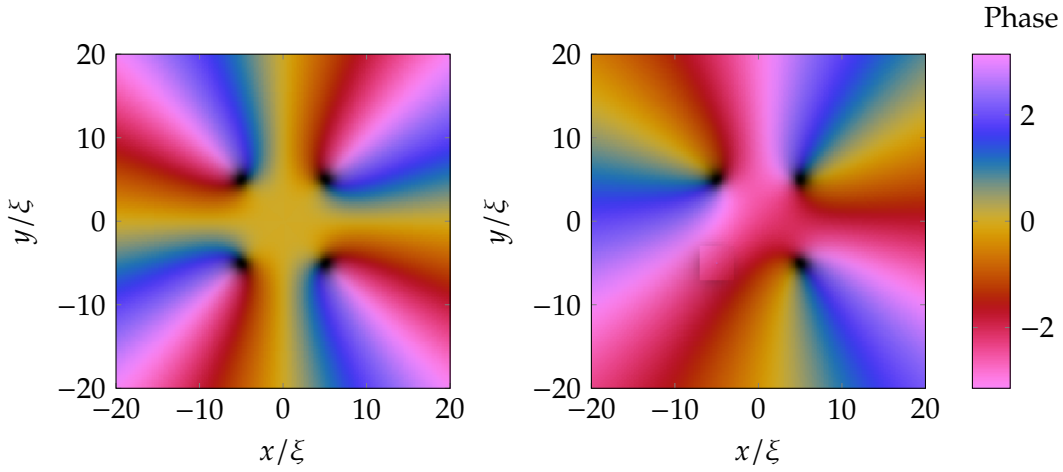

Figure 3.10: An example of the unwinding of a vortex. (Left) A homogeneous condensate containing 4 positively charged vortices located at $(\pm 5\xi, \pm 5\xi)$. (Right) The vortex at $(-5\xi, -5\xi)$ has been removed using Algorithm 9.

3.5 Removing vortices with phase unwinding

A problem with long-time numerical simulations is the effects of the finite boundaries on the results. In some cases large boxes or periodic boundary conditions are an adequate way of avoiding spurious results introduced by boundary effects. However, in some cases, the "wrapping" of vortices around the numerical domain is unfavourable as they may interfere with regions of interest and increasing the numerical grid can be infeasible due to computational constraints.

A particularly problematic example of this kind of situation is encountered often in the latter sections of this thesis: a simulation working in the moving frame with vortices nucleated via a potential obstacle. This system is of particular note because vortices that have fallen downstream wrap around the domain and re-approach the potential obstacle, modifying the nucleation dynamics and the drag force felt by the obstacle.

The ideal solution would be to implement so-called *absorbing* boundary conditions. These boundaries allow waves and vortices to pass by, without any reflections, as if they had travelled through the boundary to infinity. An approximation for absorbing boundary conditions in a homogeneous GPE has been used to study flows patterns behind an obstacle [199]. Thin fringe areas are added near the outer edges of the numerical domain. A small dissipation $\gamma \approx 0.1$ is applied in this region, ramping up smoothly from $\gamma = 0$ in the bulk to its maximal value in the fringe area. Inside the fringe region, waves and vortex pairs lose energy; the amplitude of waves decay and opposite-signed vortices move towards one-another so as to annihilate.

To facilitate the process and allow the fringe region to remain as small as possible,

vortices in the region are "unwound" using Algorithm 9. In practice this is performed by simply imprinting a vortex of opposite charge directly at a vortex's location (and so accurate vortex detection methods as described in Section 3.2 are required). A demonstration of the vortex unwinding process is shown in Figure 3.10. The vortex located at $(-5\xi, -5\xi)$ is unwound and so its phase singularity is removed. Note that around the outer side of the domain the phase winds by 8π before the process, and only by 6π after, indicating a vortex has indeed been removed.

Also demonstrated in Figure 3.10 is the result of an additional routine. At the same time as unwinding the phase, the density profile of the vortex core is replaced with the value of the density at infinity. This reduces a vortex core (which then must decay as the singularity is removed) into a collection of smaller waves, which decay much quicker.

The final result of these routines is that fluid wrapping around the numerical domain is clean (free of any vortices and waves), and the resulting in-flowing fluid does not affect any part of the simulation. This allows for simulations to be run for much longer in time, allowing for better measurement of quantities such as drag force or nucleation frequency.

3.6 Quasi-Condensate Visualisation

When simulating a finite temperature Bose gas, the raw numerical wavefunction is too noisy to allow direct visualization of vortical structures. This can be overcome by defining a quasi-condensate wavefunction $\hat{\psi}$, as established in [184]. This wavefunction is constructed by filtering out high-frequency spatial modes from the classical field wavefunction, by transforming the complex amplitudes via $\hat{a}_{\mathbf{k}} = a_{\mathbf{k}} \times \max\{1 - k^2/k_c^2, 0\}$. $\hat{\psi}$ then represents the long-wavelength component of the classical field. By forcing the vortical structures to be described by a relatively low number of modes, the vortex lines can be clearly visualised.

We find the procedure produces satisfactory visualisation of the vortical structures in the quasi-condensate, and the numerical procedures involved are relatively simple and efficient. For these reasons we use the filtering method over more computationally complex methods of defining the quasi-condensate wavefunction, such as calculating the macroscopically occupied Penrose-Onsager eigenstate of the single-particle density matrix [2].

The choice of k_c is facilitated by the the bimodal distribution of occupation numbers in the wavefunction, a distribution which develops naturally through propagation of the GPE. The high-k part of the distribution is associated with the thermal excitations and low mode occupations. The low-k part of the field is the quasi-condensate, characterised by macroscopic mode populations and superfluid ordering. k_c is chosen as the boundary in k-space between the quasi-condensate and the thermal gas. Figure 3.11 demonstrates

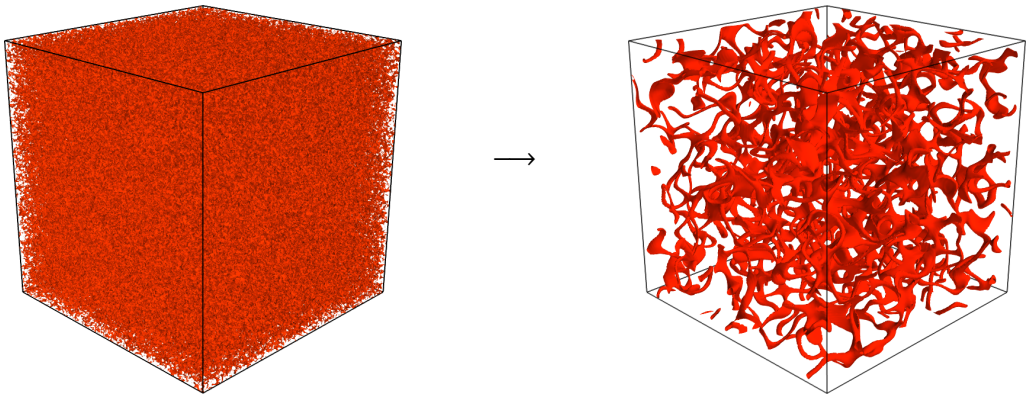

Figure 3.11: (Left) Unfiltered wavefunction density isosurface, $|\psi|^2$, from a classical-field simulation with condensate fraction $\rho_0/\rho = 0.22$ during equilibration. A vortex tangle is present but not visible by direct density visualisation. (Right) Filtered wavefunction density isosurface, $|\hat{\psi}|^2$, clearly showing the vortical structures in the gas.

the filtering technique in action.

3.7 Evaluation of vortex line-length in 3D

For a given 3D wavefunction, ψ, featuring a vortex distribution, the vortex volume V_t (the total volume associated with the vortex cores) is evaluated by numerical integration of the inside of the vortex isosurface tubes obtained from the filtered density $|\hat{\psi}|^2$, with an integration region of the whole numerical box. Note that the isosurface level Δ_i should be low enough to pick out vortex cores only (and not, e.g. fluctuations and waves), while large enough to contain sufficient grid points to allow a reasonable numerical evaluation of volume. The volume calculation at time t can be written $V_t = \int \Theta(\Delta_i - |\psi(\mathbf{r})|^2)\, \mathrm{d}V$, where Θ is the Heaviside step function. In practice the calculation of the vortex core volume can be efficiently performed by assigning a value of unity/zero to grid points located within/outside the isosurface tubes and directly integrating the result using the trapezium or Simpson's rule.

The total line length is then deduced by dividing V_t by the cross-sectional area of a vortex core, A_t (in effect, the average cross-sectional area of the isosurface tubes). The measured values of V_t and A_t will depend on the chosen isosurface level but, providing the vortex tubes are well-separated, their ratio (and hence the evaluated line length) will remain constant. For closely-positioned vortex tubes, the isosurface level can affect whether the tubes appear as two separate tubes, or start to merge, and so will lead to deviations in this ratio.

Care must be taken, however, when considering systems where the vortex core radius is varying over time, such as during quasi-condensate growth in a classical field simulation. As the condensate fraction grows, the healing length will decrease and so vortex core

radius will decrease over time. In these cases the vortex core cross-sectional area must be carefully calculated over time, by taking the varying healing length into account.

Part II

Numerical Studies

Chapter 4

Classical-like wakes behind elliptical obstacles in Bose-Einstein condensates

4.1 Introduction

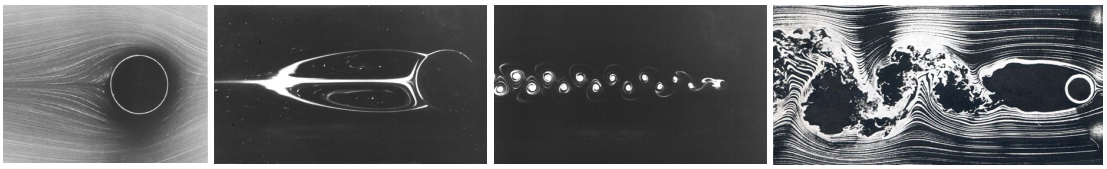

Figure 4.1: Classical viscous flow past a cylinder. From left to right: laminar flow ($Re = 3.64$) [215]; steady symmetric wake behind the cylinder ($Re = 41$) [215]; time-dependent Bénard–von Kármán vortex street ($Re = 112$) [216]; and chaotic downstream wake ($Re > 10^5$) [217].

Recent experimental [191, 161], numerical [143, 144, 218] and theoretical studies [219] have highlighted similarities between turbulence in quantum fluids and turbulence in ordinary (classical) fluids [220]. In particular, it is found that, in the idealized case of homogeneous isotropic conditions away from boundaries, the distribution of kinetic energy over the length scales obeys the celebrated Kolmogorov scaling of classical turbulence [221]. This similarity is remarkable, because a superfluid has zero viscosity and vorticity is not a continuous field. In the more realistic presence of boundaries such as an obstacle or confining channel walls, superfluid hydrodynamics is less understood, despite the large number of experiments in such scenarios.

In a classical viscous fluid [220], the prototype problem with a boundary is the flow around a cylinder or a sphere (or, changing the frame of reference, the motion of a cylinder or a sphere in a fluid at rest). The nature of such flow is determined by the Reynolds number

$Re = vd/\nu$, where v is the (assumed uniform) flow's velocity away from the obstacle, d is the obstacle's size, and ν is the fluid's kinematic viscosity. If $Re \lesssim 50$, a steady symmetric wake forms behind the obstacle; if $10^2 \lesssim Re \lesssim 10^5$ the wake becomes asymmetric and time dependent, forming the famous Bénard–von Kármán vortex street structure. For even higher values of Re, the flow becomes turbulent. These cases are depicted in Figure 4.1.

What happens in a superfluid is not clear. Firstly, the superfluid has zero viscosity ($\nu = 0$) and hence Re cannot be defined. Secondly, experiments performed in superfluid helium confirm that the flow is affected by the boundaries [222, 223]; unfortunately what is observed is not the flow pattern itself, but rather the trajectories of tracer particles, whose relation with the flow is still the subject of investigations [224]. Numerical simulations of three-dimensional (3D) superfluid flow around an oscillating sphere performed using the vortex filament model were not conclusive - quantum vortices did not appear to organise themselves into a visible classical–like wake near the obstacle [225–227].

Recent studies of the two-dimensional (2D) system have considered vortex emission and drag [228, 229, 102, 230, 231], the critical velocity [232–236], the effect of inhomogeneous potentials [230, 237, 238], the role of the obstacle parameters [231, 102, 239], and supersonic effects such as oblique dark solitons [240] and Cerenkov radiation [241]. In this chapter we discuss the rich variety of quantum wake regimes, often in close analogue to the classical counterparts, which can be obtained via the simple modification of the obstacle to an *elliptical* shape. We explore these dynamics in a homogeneous system, which serves to demonstrate the salient behaviour of superfluid flow past an elliptical obstacle, away from boundaries and density inhomogeneities which influence the vortex dynamics.

4.2 Model

We consider an atomic Bose-Einstein condensate (BEC) moving relative to a laser-induced obstacle (imposed through an external potential), as realized experimentally in 3D [242, 243, 104, 69] and quasi-2D condensates [69]. This scenario closely resembles that of the classical wake-problem [215, 216]. On a much larger scale, a similar 3D configuration has been experimentally realized in liquid helium [222, 223].

The BEC, parametrised by the wavefunction $\psi(\mathbf{r}, t)$ and assumed to be weakly-interacting and at ultracold temperature, is modelled through the GPE as described in Section 2.8.1, transformed into the moving frame as in Section 2.10.1. The external potential acting on the system $V(\mathbf{r}, t)$ is taken to be zero everywhere, apart from a localized repulsive potential which represents the obstacle with the Gaussian shape described in Section 2.15.2. A key feature of this work is that the obstacle is modified so that it has ellipticity ε, modifying the obstacle along the x axis, parallel to the flow. Such a potential can be generated via the repulsive optical dipole force from an incident blue-detuned laser beam which is moved

relative to the condensate either by deflection of the beam [242, 243, 104] or motion of the condensate itself when offset in a harmonic trap [69, 106, 167]. While laser-induced obstacles generated to date have had a circular profile, elliptical modification of the Gaussian potential can be achieved via cylindrical focussing of the laser beam.

The 2D (3D) system is simulated using the fourth-order Runge-Kutta method described in Section 3.1.1 under periodic boundary conditions on a 2048×512 ($400 \times 150 \times 150$) grid with uniform spacing $\Delta_x = 0.4\xi$. Phase unwinding (described in Section 3.5) is used in combination with a sufficiently large computational box so that the boundary conditions and nucleated vortices do not play a role in further vortex shedding. The initial condition is the stationary state of the GPE (including obstacle potential) with $v = 0$ as determined by the imaginary time convergence method described in Section 2.9. Setting $V_0 = 100\,\mu$ throughout, the external potential closely approximates an impenetrable obstacle. A small amount of noise is added to the initial condition to break symmetry: Both the real and imaginary parts of the initial wavefunction are perturbed at every grid point by random numbers of size 0.1%. To minimize initial generation of waves, v is ramped up in time along a hyperbolic tangent curve, from $v = 0$ at $t = 0$ to its terminal value at $t \approx 200\,(\xi/c)$.

4.3 Two-Dimensional Wakes

4.3.1 Vortex emission from circular obstacles

The 2D scenario of an obstacle moving through a superfluid offers a simplified platform to consolidate analogues and disparities between classical and quantum fluids. In their pioneering simulations of the 2D nonlinear Schrödinger equation, Frisch *et al.* [148] observed the formation of vortex pairs in the flow past a circular obstacle. Although Frisch *et al.* considered a "hard" cylinder, it is also natural to employ a "soft" Gaussian potential (usually used in the context of atomic condensates). In practice this changes the quantitative, but not the qualitative, behaviour. Sasaki *et al.* [193] recently provided an extensive picture of 2D superflow past such a Gaussian obstacle. The flow regimes are depicted in Figure 4.2, based on simulations of the 2D GPE using similar parameters to [193]. At low flow velocity (a), the fluid undergoes smooth laminar flow around the obstacle. The streamlines of this flow are symmetric about $x = 0$, as in perfect potential flow. At a critical flow velocity, the local fluid velocity (which is highest at the poles of the obstacle) exceeds the speed of sound, c, breaking Landau's criterion. Vortex pairs of opposite sign are nucleated periodically and drift downstream, forming a collimated wake of vortex pairs which are widely separated from each other (b). For higher velocities (c), alternating pairs of like-signed vortices are nucleated. At even higher velocities, vortex nucleation becomes highly irregular (d), forming a chaotic downstream distribution of vortices and sound (density) waves. These quantum fluid flow patterns bear some analogy to the classical flow patterns of Figure 4.1,

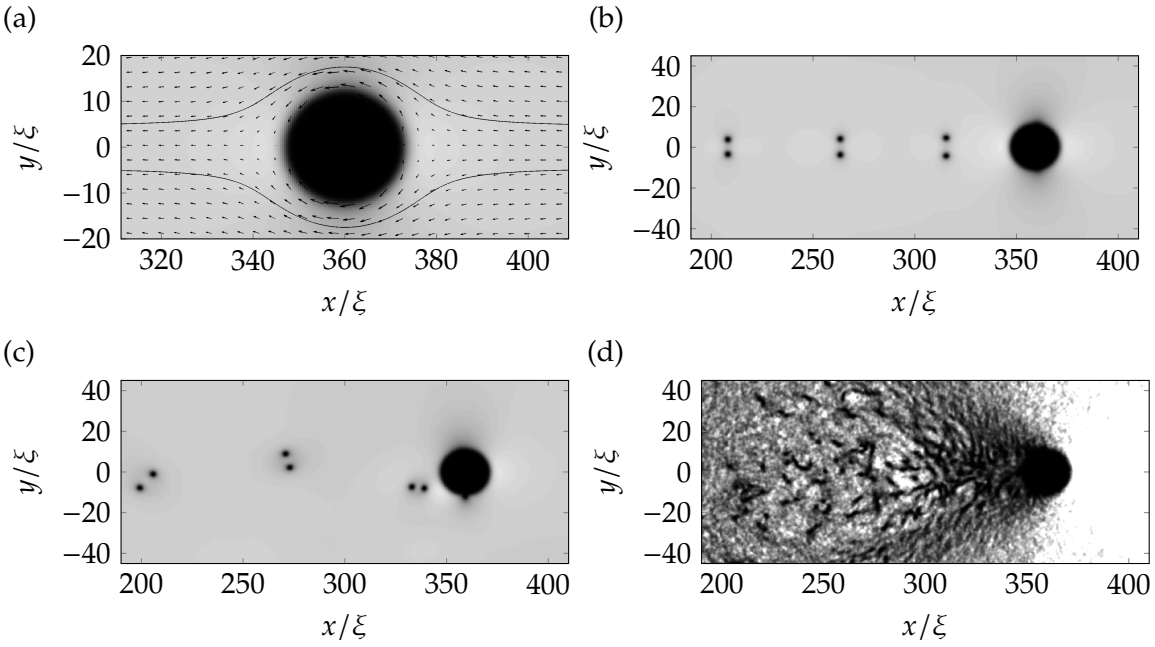

Figure 4.2: Condensate density during flow past a circular obstacle ($d = 5\xi$) at various flow speeds. For reference the critical velocity here is $v_c \approx 0.36\ c$, where c is the speed of sound. (a) Laminar flow at a sub-critical flow speed ($v = 0.3\ c$). The fluid velocity vector field and two streamlines illustrate the flow pattern. (b) Nucleation of vortex-antivortex pairs ($v = 0.365\ c$). (c) Nucleation of like-signed vortex pairs ($v = 0.37\ c$). (d) Chaotic vortex nucleation and generation of strong sound waves, forming a turbulent wake ($v = 0.9\ c$).

particularly for the laminar flow and chaotic regimes. The alternating like-signed vortices form a somewhat primitive analogue of the Bénard–von Kármán vortex street, while the vortex-antivortex pairs have no obvious classical analogue.

4.3.2 Vortex emission from elliptical obstacles

Consider, for illustration, an elliptical obstacle of size $d = 5\xi$ and ellipticity $\varepsilon = 3$ moving at speed $v = 0.365\ c$. This speed exceeds the critical velocity for the obstacle at that ellipticity, and so quantum vortices nucleate and trail behind the obstacle to form a wake [Figure 4.3(a)]. Sound waves generated by the obstacle have little effect on the vortex dynamics. At early times [Figure 4.3(a)(i)], the vortex shedding occurs through the symmetric generation of vortex-antivortex pairs, leading to a collimated and symmetric wake behind the obstacle. This is in qualitative agreement with observations for circular obstacles [148, 228, 230, 231] shown in Section 4.3.1, although for the same obstacle velocity and size, the elliptical obstacle induces a higher frequency of vortex emission and thus a denser wake.

At later times [Figure 4.3(a)(ii)], the flow becomes asymmetric due to the known instability of symmetric wakes [228]. A striking pattern emerges whereby distinct clusters of

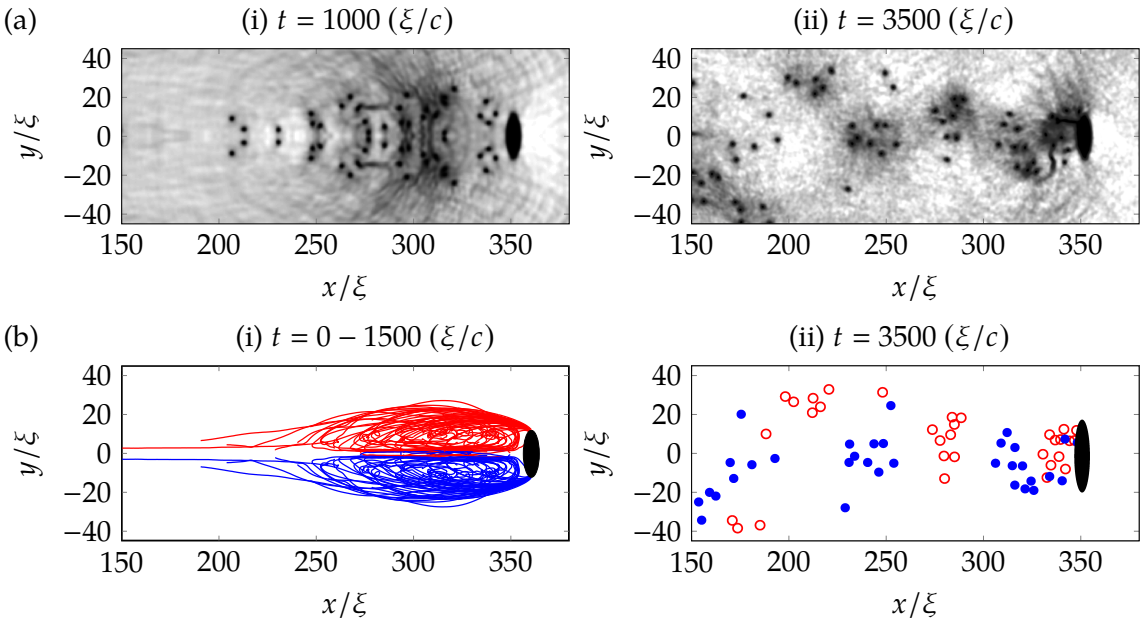

Figure 4.3: Snapshots showing the (a) density profile and (b) vortex trajectories during vortex shedding from an elliptical object ($\varepsilon = 3$) at (i) early times and (ii) later times. The obstacle has speed $v = 0.52c$ and size $d = 5\xi$. Red and blue lines represent vortices of oppositely quantized circulation. At early t, a symmetric wake similar to a classical fluid with low Re forms. Symmetry breaks at $t \approx 1500\ (\xi/c)$ at which point vortex motion becomes disordered. In this case the initial condition is noise-free.

co-rotating vortices (of the order of 8 vortices in each cluster) develop downstream of the obstacle. Each cluster contains vortices of the same sign and adjacent clusters have alternating sign. These clusters form a Bénard–von Kármán vortex street downstream from the obstacle, confirming the intuition that a sufficiently large number of quanta of circulation reproduce classical physics. Here, the ellipticity of the obstacle facilitates the formation of this street; the relatively high rate of vortex emission leads to a greater interaction between vortices in the wake which in turn promotes clustering. This is in contrast to Section 4.3.1 where vortex pairs (clusters of only 2) are produced; the vortex emission rate and hence their subsequent interaction is insufficient to induce large scale clustering.

The vortex trajectories shown in Figure 4.3(b) provide visualisation of the time-integrated nature of the wake. At early times (i), we see that the vortex trajectories are symmetric, forming a flow pattern in striking analogy to the classical wake at low Re. The generic development of vortex trajectories is as follows. Pairs of singly-quantized vortices of opposite sign peel off from the poles of the obstacle and interact with each other as vortex-antivortex pairs. Each pair propagates in the positive x direction with approximate velocity $\hbar/(md_p)$ [193], where d_p is the pair separation [18]; the pair's velocity is less than the obstacle's velocity and so it drifts behind the obstacle. As the pair moves further away from the obstacle the velocity field of surrounding nucleated vortices causes its separation to decrease

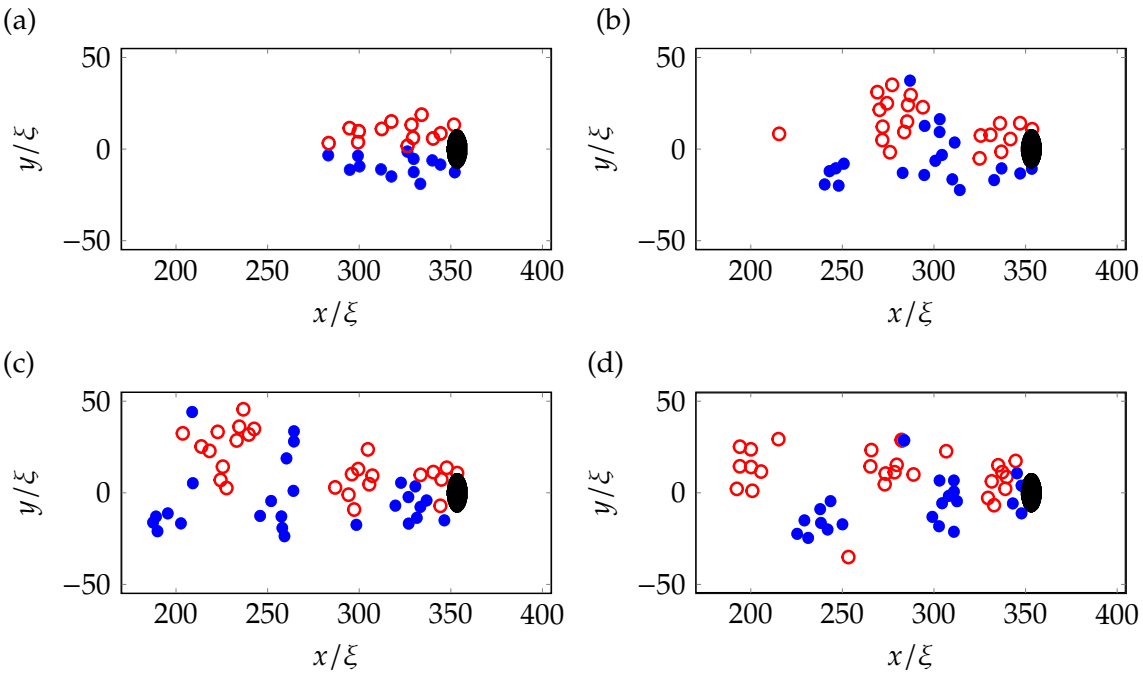

Figure 4.4: Snapshots of vortex locations during the motion of an elliptical object ($d = 5\xi$ and $\varepsilon = 3$) at speed $v = 0.52\ c$ in the presence of small-amplitude noise at $t = 0$. The snapshots are at times (a) $t = 450$, (b) 900, (c) 1000 and (d) 1100 (ξ/c). Red/blue circles represent vortices with quanta of circulation $+1/-1$. The wake forms into clusters of like-circulation that continue to be produced, in analogy to the classical Bénard–von Kármán vortex street from a cylinder.

and its velocity to increase, such that it begins to catch the obstacle up. Once the pair is sufficiently close to the obstacle, it again separates and slows down, then the cycle repeats. As more vortices are nucleated, two distinct clusters of like-circulation form. Nucleated pairs then travel around the outside of the existing cluster before contracting, speeding up and travelling through the middle of the clusters towards the obstacle. The clusters grow until they reach a maximum size depending on the obstacle's size and speed. Hereafter, nucleated vortex pairs travel around the outside of the two clusters and continue travelling downstream, becoming lost from the main wake.

4.3.3 Formation of the Bénard–von Kármán vortex street

Once the symmetry of the wake is broken, vortices no longer separate into two distinct clusters of like-circulation. Existing vortices and newly-nucleated vortices mix together behind the obstacle. To accelerate the formation of the asymmetric wake, we subsequently seed the initial condition with noise. Figure 4.4 shows the vortex locations at various stages of the evolution. The initial symmetry of the wake [Figure 4.4(a)] breaks at $t \approx 450(\xi/c)$, with the wake splitting into several clusters. The velocity field around the obstacle is affected: it depends on time and the distance of the nearest cluster of vortices. The obstacle

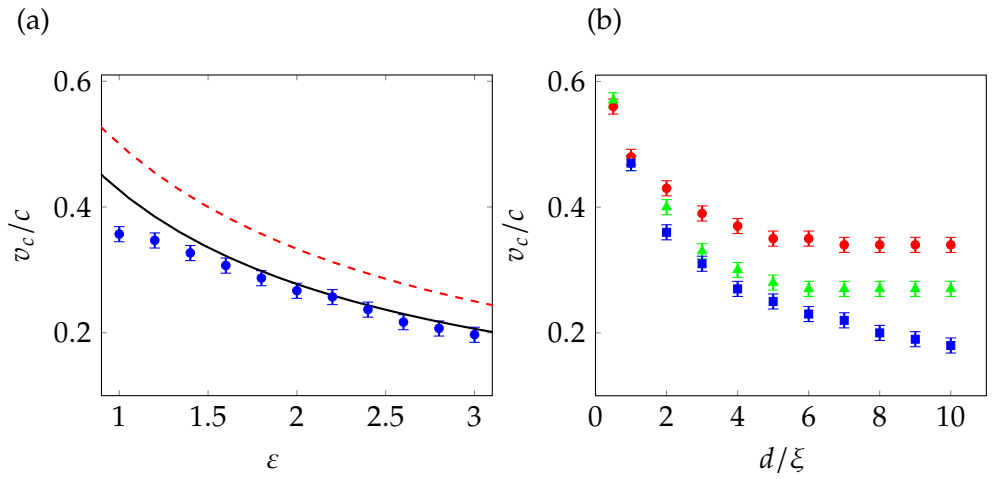

Figure 4.5: (a) Critical velocity against obstacle ellipticity ε, for $d = 10\xi$. Shown are the results of the numerical simulations (blue bars), Equation (4.1) (dashed red line) and Equation (4.3) (solid black line). (b) Critical velocity (obtained numerically) versus the obstacle width d, for ellipticity $\varepsilon = 1$ (red circles), $\varepsilon = 2$ (green triangles) and $\varepsilon = 3$ (blue squares).

no longer simultaneously produces vortex-antivortex pairs, but now generates a series of like-signed vortices. Since like-signed vortices are known to co-rotate, these vortices group into clusters which slowly rotate. This cluster affects the velocity field once more, causing a cluster of opposite signed vortices to be produced. This process then repeats such that clusters of like signed vortices are then produced behind the obstacle, much like vorticity in the classical vortex street behind a cylinder. While some positive clusters contain negative vortices and vice versa, the overall pattern is still a time-dependent Bénard–von Kármán vortex street.

For clusters consisting of pairs of vortices, it has been shown that they can survive downstream for a very long time [193]. However, for regimes with larger numbers of vortices in each cluster, the chaotic nature of vortex motion can cause originally tightly packed and circular clusters to easily stretch over large areas, form strange shapes, or even split into smaller clusters.

4.3.4 Critical Velocity past an Elliptical Obstacle

We now investigate in what ways the ellipticity of the obstacle affects the critical velocity for vortex nucleation and nucleation frequency. Figure 4.5(a) shows the critical velocity for flow past the obstacle as a function of its ellipticity, taking the obstacle to have fixed width in the y-direction of $d = 10\xi$. We determine the critical velocity numerically by performing simulations with flow velocities increasing in steps of $\Delta_v = 0.01\,c$ until vortices nucleate. For a circular object, we find that the critical velocity is $v_c = 0.355 \pm 0.005\,c$, consistent with predictions in the Eulerian ($d \gg \xi$) limit [234–236].

Studies on circular objects show that v_c depends on the obstacle's shape at small diameters, where boundary effects are significant; v_c approaches the "Eulerian" value only for large diameters $d \gg \xi$ [231, 235]. The variation of v_c with the obstacle width d is shown in Figure 4.5 (b). For $d = 10\xi$, the critical velocity effectively reaches its asymptotic value, while at smaller widths, it is much larger. As the ellipticity is increased (i.e. the obstacle becomes narrower in x), the critical velocity decreases. The modification of the critical velocity is significant: if $\varepsilon = 3$, v_c is more than 40% smaller than that for a circular obstacle.

The rough dependence of v_c on ε can be derived as follows. According to Landau's criterion [95], superfluidity breaks down when the fluid velocity exceeds the critical velocity $v_{\text{Lan}} = \min\left[E(p_e)/p_e\right]$, where p_e is the momentum of elementary excitations and $E(p_e)$ their energy. The weakly-interacting Bose gas has the dispersion relation $E(p_e) = [ngp_e^2/m + p_e^4/(4m^2)]^{1/2}$, and so the Landau critical velocity is the local speed of sound, $v_{\text{Lan}} = c_{\text{local}}$, where $c_{\text{local}} = \sqrt{ng/m}$. In a homogeneous system, however, the density is uniform and the Landau critical velocity becomes $v_{\text{Lan}} = c$, where $c = \sqrt{\rho g/m}$.

If an obstacle moves through the fluid with speed v, the local fluid velocity is enhanced near the obstacle so that the maximum local velocity, v_{max}, exceeds v. By approximating the BEC as an inviscid Euler fluid, the local velocity around the obstacle can be calculated using the complex variable framework of potential flow. The maximum local velocity is found to be at the poles with $v_{\text{max}} = (1 + \varepsilon)v$ [244], and the first estimated critical velocity, which we denote v_{c1}, is written,

$$\frac{v_{c1}}{c} = \frac{1}{1+\varepsilon}. \tag{4.1}$$

This estimate is shown as dashed red line in Figure 4.5(a), capturing the general shape of the relationship, but not the exact values for v_c.

Equation (4.1) is derived for incompressible potential flow, however, the GPE describes a compressible fluid and so the local density, $n(\mathbf{r}) = |\psi|^2$, in regions of high velocity is reduced. Ignoring the quantum pressure, the density (and therefore speed of sound) is reduced according to Bernoulli's equation [245],

$$1 + \frac{v^2}{2c^2} = \frac{n(v_{\text{loc}})}{\rho} + \frac{v_{\text{loc}}^2}{2c^2}, \tag{4.2}$$

where $v_{\text{loc}}(\mathbf{r})$ is the local velocity. We substitute the maximum local velocity, $v_{\text{max}} = (1+\varepsilon)v$, into Equation (4.2) to find the local density at that point,

$$\frac{n(v_{\text{max}})}{\rho} = 1 + \frac{v^2}{2c^2}[1 - (1+\varepsilon)^2].$$

The local speed of sound is $c_{\text{local}} = c\sqrt{n/\rho}$ and so at the point of maximal velocity,

$$c_{\text{local}} = c\sqrt{1 + \frac{v^2}{2c^2}\left[1 - (1+\varepsilon)^2\right]}.$$

We use the resulting local speed of sound and the Landau criterion to find a corrected estimate of the critical velocity, which we denote v_{c2}, for the break down of superfluidity,

$$\frac{v_{c2}}{c} = \left[\frac{3}{2}(1+\varepsilon)^2 - \frac{1}{2}\right]^{-\frac{1}{2}}. \tag{4.3}$$

This relation [solid black line in Figure 4.5(a)] gives good agreement with the computed values of v_c. The deviation for $\varepsilon \sim 1$ has been noted elsewhere [235], and can be remedied using higher order corrections taking into account the quantum pressure term.

4.3.5 Role of Obstacle Size and Ellipticity on the Wake

During the initial symmetric phase of vortex nucleation, the wakes generated by the obstacle have the same qualitative structure shown in Figure 4.3(b) (i). However, once the wake becomes asymmetric, the nature of the clusters that form are highly dependent on the velocity and shape of the obstacle. Figure 4.6 shows wakes generated for various obstacle parameters, all captured at the same time $t = 2000\ (\xi/c)$. As predicted in the previous section, for an increased ε, the critical velocity for vortex nucleation is reduced. Conversely, reducing $\varepsilon < 1$ causes the critical velocity to increase to the point of no vortices being produced for any of the tested velocities. By visual inspection of the clusters that form in Figure 4.6, it can be seen that any increase of size, ellipticity or velocity of the obstacle increases the number of vortices in the wake's clusters. We further explore this clustering behaviour and explain its roots in Section 4.3.6.

4.3.6 Vortex Clustering

We have shown that the Bénard–von Kármán vortex street forms through the clustering of like-signed vortices. Methods of quantifying the clustering of vortices in quantum fluids have been explored in the literature [194, 195, 210] and are described in detail in Section 3.3.

We begin by quantifying the effect of ellipticity on vortex clustering using Ripley's K and Besag's L functions defined in Section 3.3.2. To interpret the results, the curve

$$L_\varepsilon(s) = \langle \hat{L}(\varepsilon, s) - s \rangle, \tag{4.4}$$

is calculated. Here s characterises the radius of the clustering and $\hat{L}(\varepsilon, s)$ is the estimate of Besag's L curve given by Equation (3.8), measured at the time $t = 2500\ (\xi/c)$ for the

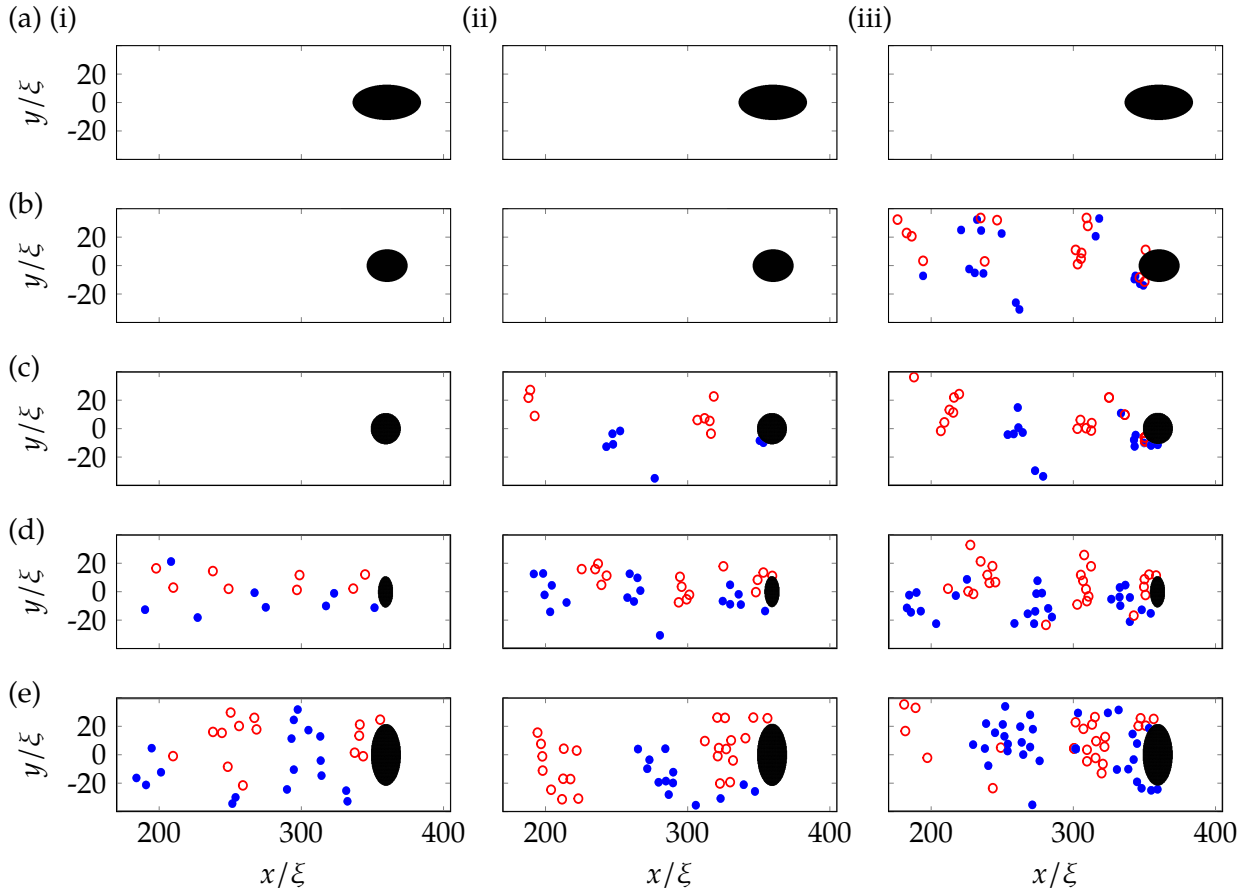

Figure 4.6: Snapshots of the vortex positions for various obstacle parameters, at $t = 2000\ (\xi/c)$. Shown are obstacles corresponding to (a) $\varepsilon = 0.5$ and $d = 5\xi$, (b) $\varepsilon = 0.75$ and $d = 5\xi$, (c) $\varepsilon = 1$ and $d = 5\xi$, (d) $\varepsilon = 2$ and $d = 5\xi$, and (e) $\varepsilon = 2$ and $d = 10\xi$, at the velocities (i) $v = 0.32c$, (ii) $v = 0.40c$, and (iii) $v = 0.48c$. Red/blue circles represent vortices with quanta of circulation $+1/-1$.

three ellipticities $\varepsilon = 1, 2, 3$. The averaging is performed for each value of ε, over 5 simulations with external flow velocities $v = 0.4, 0.425, 0.450, 0.475, 0.5\ c$. When $L_\varepsilon(s) > 0$, it is interpreted as evidence of clustering on the scale of s for ellipticity ε. Conversely when $L_\varepsilon(s) < 0$, it is interpreted as evidence of a sparsity of vortices (as compared to randomly placed points in space) on the scale of s for ellipticity ε. The resulting curves are shown in Figure 4.7.

All three curves show pronounced evidence of clustering at scales of $5\xi \lesssim s \lesssim 150\xi$ with a peak at around 50ξ, which is indeed the typical size of the largest clusters visible in Figure 4.7. Lack of clustering is evident at $s \lesssim 5\xi$, this is to be expected: multiply charged vortices are unstable, preferring to decay into several vortices distinct in space, and so clustering is not expected on scales smaller than the radius of a vortex core (approximately 5ξ). The lack of clustering at scales of $s \gtrsim 150\xi$ can be explained by the lack of vortices far from the obstacle in the $\pm y$ directions. As ε increases, the peak value of $L_\varepsilon(s)$ also increases, showing evidence that an increase of ellipticity causes an increase of the spatial

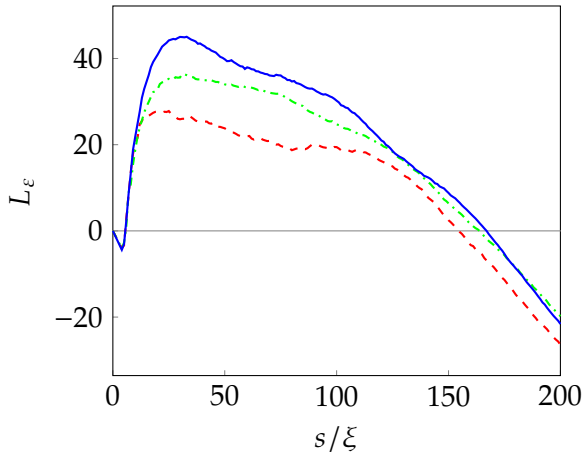

Figure 4.7: The clustering measurement $L_\varepsilon(s)$ for the three ellipticities $\varepsilon = 1$ (red dashed line), $\varepsilon = 2$ (green dot-dashed line), and $\varepsilon = 3$ (blue solid line) (with obstacle size $d = 5\xi$) averaged over 5 simulations for each ε with external flow velocities $v = 0.4, 0.425, 0.450, 0.475, 0.5\ c$.

clustering of vortices in the fluid.

The $L_\varepsilon(s)$ measurement of clustering is entirely based on the K and L functions. These functions quantify the average spatial statistics of vortex clustering, but do not tell us the number of vortices present in clusters. We now utilize the more sophisticated Recursive Cluster Algorithm (RCA) of Reeves *et. al.* [195] (described in Section 3.3.3) to identify the number of vortices contained in clusters for different ellipticities and velocities. The use of RCA allows us to investigate how both velocity and ellipticity each affect vortex clustering. We record the number of clusters N_c and the number of vortices in each cluster N_i, where i is the cluster index. Then we determine the average number of vortices in the clusters, $\langle N \rangle = (1/N_c) \sum_{i=1}^{i=N_c} N_i$ as a function of obstacle velocity v for three ellipticities $\varepsilon = 1, 2$ and 3, at times $t = 500, 510, \ldots, 2500\ (\xi/c)$. The results, plotted in Figure 4.8, show that increasing v (above the critical velocity) causes $\langle N \rangle$ to increase and that, at fixed v, $\langle N \rangle$ increases with ε.

The behaviour of the quantities explored in this section, and therefore the reason that elliptical obstacles are efficient at producing classical-like wakes, can be explained by considering the shedding frequency of vortices. It is known that the shedding frequency increases with the velocity of the flow [229] and for an elliptical obstacle, the combination of a reduced critical velocity and increased local velocity around the obstacle has the effect of increasing the shedding frequency with ε and d. The overall result is that, when increasing any of v, ε or d, vortex shedding frequency is increased and so more vortices are nucleated in a given time period, causing the cluster size to increase (explaining the behaviour of L_ε, $\langle N \rangle$, and the vortex clustering variation in Figure 4.6). By further simulation at large obstacle velocity ($v \gtrsim 0.6$), we also find that for all values of ε, the large velocity causes

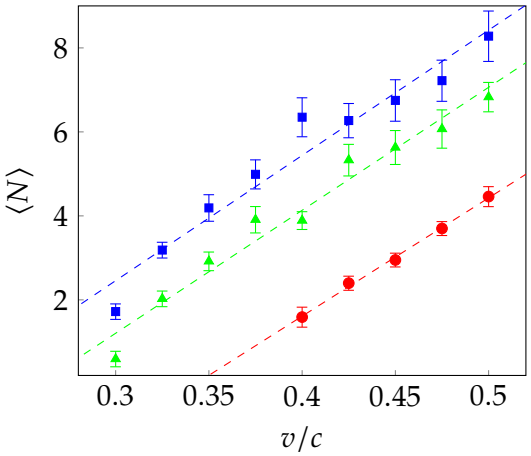

Figure 4.8: Average number of vortices in the clusters as a function of the obstacle velocity v. Shown are cases with $\varepsilon = 1$ (red squares), $\varepsilon = 2$ (green triangles) and $\varepsilon = 3$ (blue squares) with $d = 5\xi$. Also shown are linear fits to the data for each value of ε.

vortices to nucleate non-periodically, inducing an irregular flow without a visible Bénard–von Kármán vortex street configuration, in agreement with previous simulations with circular obstacles of smaller diameter [193].

4.4 Three-Dimensional Wakes

We now generalize our results to 3D by considering quantum wakes in three-dimensional flow past a localized obstacle, as simulated via the 3D GPE with the 3D obstacle potential of Equation (2.44). Our results will confirm that the features observed in 2D wakes also arise in the 3D setting. A comprehensive study of the parameter space is, however, not tractable in 3D due to the computational intensity of large scale 3D simulations.

4.4.1 Symmetric Wakes

For a spherical ($\varepsilon = 1$) object with $d = 5\xi$, we find that the critical velocity is $v_c = 0.455 \pm 0.05\,c$, consistent with $v_c = 0.55\,c$ reported in the Eulerian limit ($d \gg \xi$) [245, 246]. Making the obstacle ellipsoidal, with the short direction parallel to the flow, reduces the critical velocity, in parallel with our 2D observations. For example, for $\varepsilon = 5$, the critical velocity is reduced to $v_c = 0.315 \pm 0.05\,c$. Figure 4.9(a) shows the 3D wake generated past this ellipsoidal obstacle ($d = 5\xi$ and $\varepsilon = 5$) when moving at super-critical speed $v = 0.6\,c$. Vortex rings, the 3D analogue of vortex-antivortex pairs, are ejected at high frequency (due to the obstacles high ellipticity) in the direction of the flow. At early times ($t = 450\,(\xi/c)$ in this case) the vortex configuration maintains cylindrical symmetry about the obstacle's axis, as is clearly visible in the xy and xz planes in Figure 4.9(b) and (c). As the vortex rings move

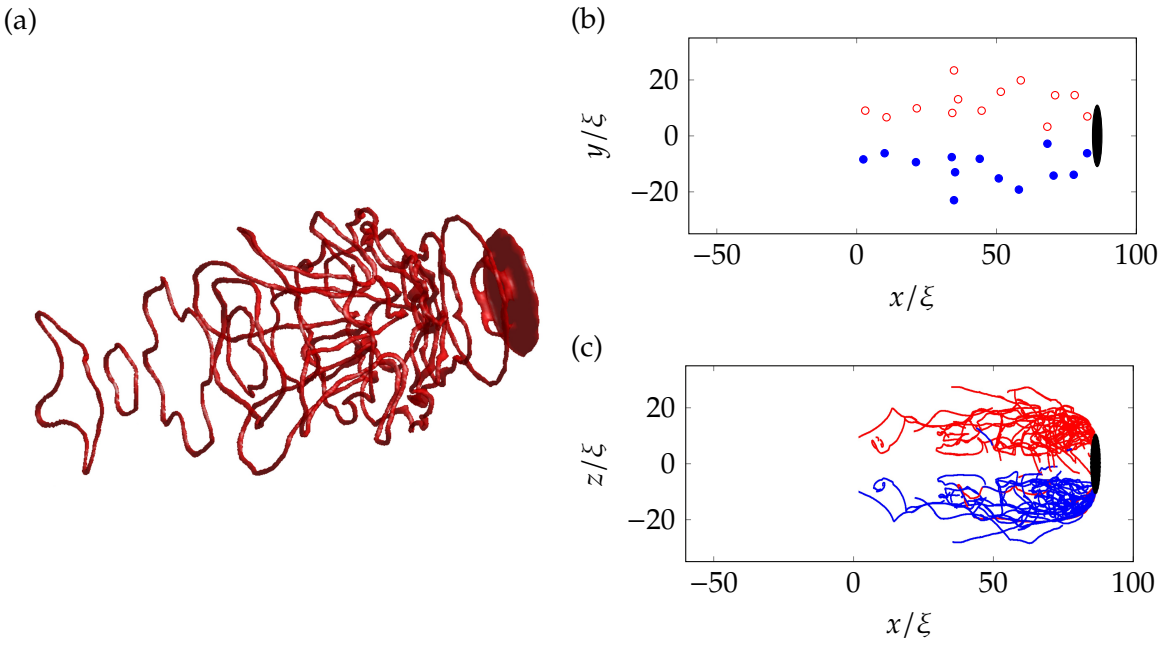

Figure 4.9: Symmetric wake in 3D at $t = 450\,(\xi/c)$ for an elliptical obstacle ($d = 5\xi$ and $\varepsilon = 5$) moving at $v = 0.6\,c$. (a) Isosurface plot of low density, over a range $[0, 100]$ in x and $[-25, 25]$ in y and z. (b) Vortex locations in the xy plane. (c) Vortex trajectories in the xz plane. In (b) and (c) red/blue denotes vortex lines with quanta of circulation $+1/-1$.

downstream they shrink and speed up, returning to the object, sometimes passing through other vortex rings. A similar behaviour is observed [247] in the evolution of toroidal bundles of many coaxial vortex rings which leapfrog around each other. Occasionally a ring will escape this cycle and fall downstream. These behaviours lead to the formation of an organized symmetric wake behind the obstacle, the 3D analogue of our 2D observations.

4.4.2 Asymmetric Wakes

We break the cylindrical symmetry of the system by tilting the obstacle by a small angle in the xz plane. The vortex rings, illustrated in Figure 4.10, now eject and evolve asymmetrically; Kelvin waves and reconnections occur, forming an apparently disordered tangle of vortices behind the obstacle. Due to the manner in which symmetry is broken, the wake remains approximately symmetric in the xy plane, as evident in Figure 4.10 (b). However, unlike in Figure 4.9, the vortices do not self organise into two clusters of alternate circulation. This is due to the vortex rings interacting, reconnecting and shifting out of the plane (which manifests in 2D as two alternate-sign vortices approaching one another).

However, in the xz plane (Figure 4.10 (c)), symmetry is broken. Due to the relatively high frequency of vortex nucleation and relatively low flow speed, like signed vortices cluster together as they are ejected by the obstacle, much like the 2D solutions seen in

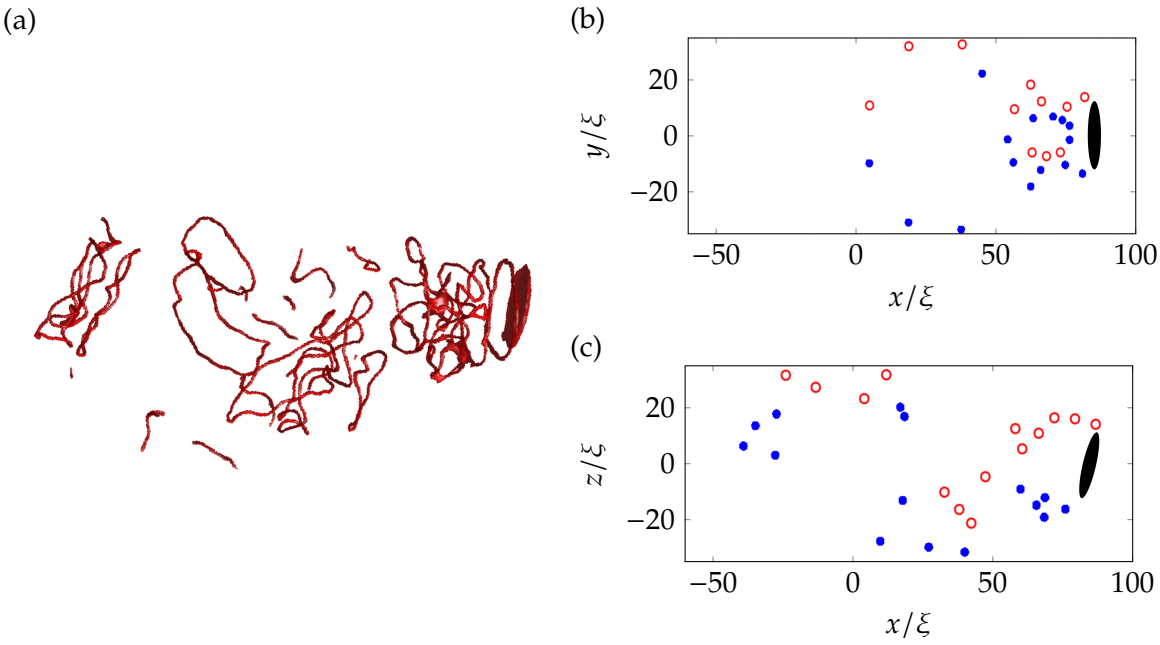

Figure 4.10: Asymmetric wake in 3D at $t = 340\,(\xi/c)$ for an elliptical obstacle ($d = 5\xi$ and $\varepsilon = 5$) moving at $v = 0.6\,c$. (a) Isosurface plot of low density, over a range $[-60, 100]$ in x and $[-25, 25]$ in y and z. (b) Vortex locations in the xy plane. (c) Vortex locations in the xz plane. In (b) and (c) red/blue denotes vortex lines with quanta of circulation $+1/-1$.

earlier sections. Downstream the tangle may shift both across or out of the plane. In 2D, although this manifests as a shift in location of the vortex clusters, the clusters largely remain rather than forming dipoles.

4.5 Conclusions

We have shown that the motion of an obstacle in a Bose-Einstein condensate produces classical-like wakes consisting of quantum vortices of the same polarity. This is consistently observed in both 2D and 3D scenarios. By modifying the obstacle so that it is elliptical, which reduces the critical velocity for vortex nucleation, vortices are generated at a sufficiently high rate that they undergo strong interactions with their neighbours (rather than being swept away). This leads to the production of classical-like wakes. Symmetric wakes resemble those observed in classical flow at low *Re*. These are unstable, forming time-dependent asymmetric structures similar to the Bénard–von Kármán vortex street of classical fluid dynamics. Vortex singularities in the inviscid superfluid thus mimic classical vortex patterns typical of viscous flows. The effects which we describe (dependence of the critical velocity and cluster size on the obstacle's size, velocity and ellipticity) can be experimentally studied in atomic Bose-Einstein condensates using moving laser-induced potentials. They are also relevant to the motion of objects (such as vibrating wires, grids

v/c	Re_s	$f\tau$	St	Predicted St
0.500	3.004	3.053×10^{-3}	0.1310	0.1353
0.450	1.931	3.187×10^{-3}	0.1519	0.1343
0.400	0.8584	2.700×10^{-3}	0.1363	0.1259
0.365	0.1073	1.329×10^{-3}	0.0781	0.0955

Table 4.1: Measurements of quantities related to the calculation of the superfluid Reynolds number, Re_s, from a selection of our simulations with $\varepsilon = 1$ and $d = 5\xi$. Our measurements of St agree well with the best fit $\mathrm{St} - \mathrm{Re}_s$ curve calculated in [199].

and forks) in superfluid helium, as the obstacle's ellipticity plays a role which is analogous to rough boundaries [248, 190]. This idea is explored in detail in Chapter 7.

4.5.1 A 'superfluid Reynolds number'

The work in this chapter has been built upon by Reeves *et. al.* [199]. The group performed 2D simulations using circular ($\varepsilon = 1$) obstacles over a large parameter space of d and v. The group performed many GPE simulations using a high speed CUDA code running on a cluster of graphics cards. The large number of simulations enabled Reeves *et. al.* to identify a superfluid Reynolds number, via dynamical similarity of a hard cylinder in classical viscous flow and a soft Gaussian obstacle in superfluid flow.

Reeves *et. al.* define the superfluid Reynolds number as, $\mathrm{Re}_s = (v - v_c)D/\kappa$, where $D = 2d[\log(V_0/\mu)]^{1/2}$ is the effective cylinder width and $\kappa = \hbar/m$. For circular obstacles, Re_s characterises the transition to quantum turbulence, with the predicted development of an irregular wake at $\mathrm{Re}_s \approx 0.7$, irrespective of cylinder size. The authors go on to measure the Strouhal number, $\mathrm{St} = fD/v$, where f is the dominant frequency in the power spectrum of F_y, the transverse force on the obstacle (defined in Appendix B.2). It was found that the Strouhal and superfluid Reynolds numbers lie on a classical-like $\mathrm{St} - \mathrm{Re}_s$ curve of the form $\mathrm{St} = \mathrm{St}_\infty[1 - \alpha/(\mathrm{Re}_s + \beta)]$. We have confirmed that our simulations with circular obstacles agree with this observation and are reasonably consistent with the best fitting $\mathrm{St} - \mathrm{Re}_s$ curve obtained by Reeves *et. al.*, $\mathrm{St} = 0.1402[1 - 0.1126/(\mathrm{Re}_s + 0.2456)]$. A selection of our measurements are listed, along with the predicted values of St, in Table 4.1.

Chapter 5

Decay of 2D quantum turbulence in a highly oblate Bose-Einstein condensate

5.1 Introduction

Ultracold gaseous Bose-Einstein condensates (BECs) provide a unique testbed with which to investigate the phenomenon of quantum turbulence and the more rudimentary realm of superfluid vortex dynamics [197, 141]. These systems provide an impressive degree of parameter manipulation unavailable in superfluid helium, the traditional context for studying quantum turbulence [147], with scope to control the particle interactions and potential landscape in both time and space. The typical size of these systems is only one or two orders of magnitude larger than the vortex core size. These compact length scales mean that the collective behaviour of vortices and their interaction with the background condensate is significant. The emergence of turbulent-like behaviour in the form of a vortex tangle was observed by Henn *et al.* in 2009 by oscillating a three-dimensional condensate [105]. What's more, the experimentalist's handle over the confining potential enables crossover to two-dimensional quantum turbulence [249]: by tightly confining the trap geometry along one axis, such that the vortices closely embody point vortices [250], states of two-dimensional quantum turbulence have been recently reported [251, 106].

In the recent experiment of Kwon *et al.* [106], a trapped, oblate BEC was translated past a stationary, laser-induced obstacle. As investigated in Chapter 4, vortices and anti-vortices were nucleated into the condensate once the relative speed exceeded a critical value [148], characteristic of superfluids. A state of two-dimensional quantum turbulence emerged, characterized by a disordered distribution of vortices. The authors monitored the number of vortices, revealing the dependence on the relative speed and the thermal

relaxation of the vortices. They directly observed vortex collision events, characterized by a crescent-shaped depletion in the condensate density. Furthermore, some vortex cores were seen to coalesce, evidence of vortex pair annihilation.

In this chapter we elucidate these experimental findings through mean-field simulations of the two–dimensional Gross-Pitaevskii equation (GPE), both at zero-temperature and in the presence of thermal dissipation, modelled through a phenomenological dissipation term. Notably, our simulations provide insight into the sign of the circulation of the vortices and the early-stage evolution, not accessible experimentally. We establish the key stages of the dynamics, from the initial nucleation of vortices and formation of a quasi-classical wake, through the rapid symmetry breaking and disorganization of the vortices, to the decay of the vortices by annihilation or passage out of the condensate.

5.2 Model

In the experiment, a ^{23}Na condensate with $N = 1.8 \times 10^6$ atoms was confined within a highly-oblate cylindrically symmetric harmonic trap $V_{\text{trap}}(x, y, z) = \frac{1}{2}m[\omega_r^2(x^2+y^2)+\omega_z^2 z^2]$, with axial frequency $\omega_z = 2\pi\times350$ Hz and radial frequency $\omega_r = 2\pi\times15$ Hz (corresponding to an aspect ratio parameter $\omega_z/\omega_r \approx 23$) and where m denotes the atomic mass. A 2D mean-field description is strictly valid when the condition $Na_s l_z^3/l_r^4 \ll 1$ is satisfied, where $l_z = \sqrt{\hbar/m\omega_z}$ and $l_r = \sqrt{\hbar/m\omega_r}$ are the axial and radial harmonic oscillator lengths and a_s is the s-wave scattering length [252, 253]. For this experiment, $Na_s l_z^3/l_r^4 = 8.3$, i.e. the system remains 3D in nature. Nonetheless, the energy required to induce an excitation in the axial direction is much larger than in the radial direction, and so Kelvin waves in the z-direction are suppressed [254] and the dynamics of the vortices is essentially 2D. Therefore, we will adopt a 2D description throughout this chapter and show that it is sufficient to capture the experimental observations. It is worth noting that in the xy plane the condensate closely approximates a Thomas-Fermi (inverted parabola) density profile with radius $R_{\text{TF}} \approx 70\mu m$.

We parametrise the condensate by the 2D wavefunction $\psi(\mathbf{r}, t)$; the condensate density distribution follows as $n(\mathbf{r}, t) = |\psi(\mathbf{r}, t)|^2$. The wavefunction satisfies the GPE, Equation (2.1), as described in Section 2.2. For computational efficiency, the numerical simulations are performed using dimensionless quantities as described in Section 2.8.2. Quantities are made dimensionless by writing them in terms of the harmonic oscillator units: length in terms of the radial harmonic oscillator length l_r, energy in terms of $\hbar\omega_r$, and time in terms of inverse radial trapping frequency ω_r^{-1}. However, to remain relevant to the experimental work of Kwon *et al.*, in this chapter we report all quantities in their full dimensional form.

We solve the GPE on a 1024×1024 grid, with grid spacing 0.27μm in both x and y, using the fourth-order Runge-Kutta method described in Section 3.1.1. We have verified that

reducing the grid spacing has no effect on our results. The vortex core size is characterized by the healing length $\xi = \hbar/\sqrt{mng}$; at the condensate centre this has the value $\xi \approx 0.6\mu$m.

Following the experiment, the total potential acting on the condensate, $V(\mathbf{r}, t)$, is the above harmonic trap plus a static Gaussian-shaped circular obstacle potential of the form described in Section 2.15.2,

$$V_{\text{obj}}(\mathbf{r}) = V_0 \exp\left(-\frac{(x - x_0)^2}{d^2} - \frac{y^2}{d^2}\right), \tag{5.1}$$

with $V_0 = 15\mu$ and $d = 11.31\mu$m, so as to match the experimental parameters. The initial ground-state BEC is obtained by solving the GPE using the imaginary time method shown in Section 2.9, with an enforced norm of $N = 1.8 \times 10^6$ to match the experimental value. At $t = 0$ the harmonic trap is centred at $x_0 = 18.5\mu$m. The trap is translated towards the left, at speed v, over a distance of 37μm; to smooth this speed curve we additionally include a linear acceleration/deceleration over 3.75ms at the start/end, which is included as part of the 37μm translation. Once the trap is at rest, the obstacle amplitude V_0 is ramped down to zero over 0.4s.

5.3 Number of Vortices Generated

Following removal of the obstacle, we determine the number of vortices in the system N_v using the methods described in Section 3.2. We limit our search to 75 percent of the Thomas-Fermi radius (centred on the centre-of-mass to account for sloshing motion); by avoiding the low density periphery we avoid artefacts from ghost vortices and match closely what is performed experimentally (since vortices close to the edge are not detected due to low signal-to-noise [255]).

In Figure 5.1 we plot N_v versus the translation speed v. We see the same *qualitative* form between our simulations (red squares) and the experiment (black diamonds): above a critical speed $v_c \approx 0.45$mm/s vortices enter the system, nucleated by the relative motion between the obstacle and the superfluid, and for $v > v_c$ the growth in N_v is initially rapid but tails off for $v \gg v_c$. Quantitatively, however, the GPE overestimates N_v. One can expect that thermal dissipation, not accounted for in the GPE, will act to reduce the number of vortices in the system. Experimental limitations in resolving and counting vortices may also contribute to the over-estimate of N_v from the GPE.

We include the effects of dissipation via the addition of phenomenological dissipation [179, 180], γ, which enters the GPE by replacing i on the left hand side by $(i - \gamma)$, a process formally derived in Section 2.11. This term induces the decay of excitations; for single vortices this manifests in them spiralling out of the trapped condensate [181, 254, 256, 257]. The system is sensitive to the exact value of γ used; for larger γ, less vortices are nucleated

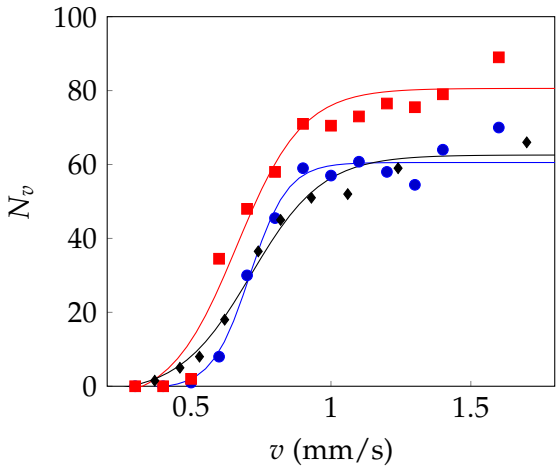

Figure 5.1: Number of vortices N_v in the condensate after removal of the obstacle. Shown are simulations of the GPE without dissipation (red squares), with dissipation $\gamma = 0.0003$ (blue circles) and experimental results extracted from Figure 1 of [106] (black diamonds). Sigmoid fits are also shown as lines. Each point is averaged over 20 ms once the obstacle amplitude reaches $V_0 = 0$. For comparison, the speed of sound in the centre of the BEC is $c_{\text{local}} \approx 4.6$ mm/s.

by the obstacle at early times and vortices spiral out of the system faster. We choose the value $\gamma = 0.0003$ so that the number of vortices produced by the obstacle is in agreement with the experimental observations at temperature $T \sim 130$nK. We enforce the atom number throughout the dissipative simulations so as to emulate the experiment (for which no significant loss of atom number was observed). With this dissipation the data for N_v becomes reduced (blue circles), bringing it closely in line with the experimental data.

5.4 Stages of the Condensate Evolution

We now examine in detail the evolution of the condensate, charting its dynamics from the initial stage (when the harmonic trap translation begins) to the intermediate and final stages (randomization and decay of the vortices). We see the same qualitative evolution with and without dissipation, and for all velocities exceeding v_c. For the purposes of illustration, we focus on an example with dissipation and a translation speed $v = 1.4$mm/s.

Figure 5.2 shows the condensate density at various times. At the start of the simulation ($t = 0$) the condensate has a smooth circular density profile, with a density depression due to the obstacle. Later vortices appear as small dots of low density; superimposed red/blue markers identify vortices of positive/negative circulation.

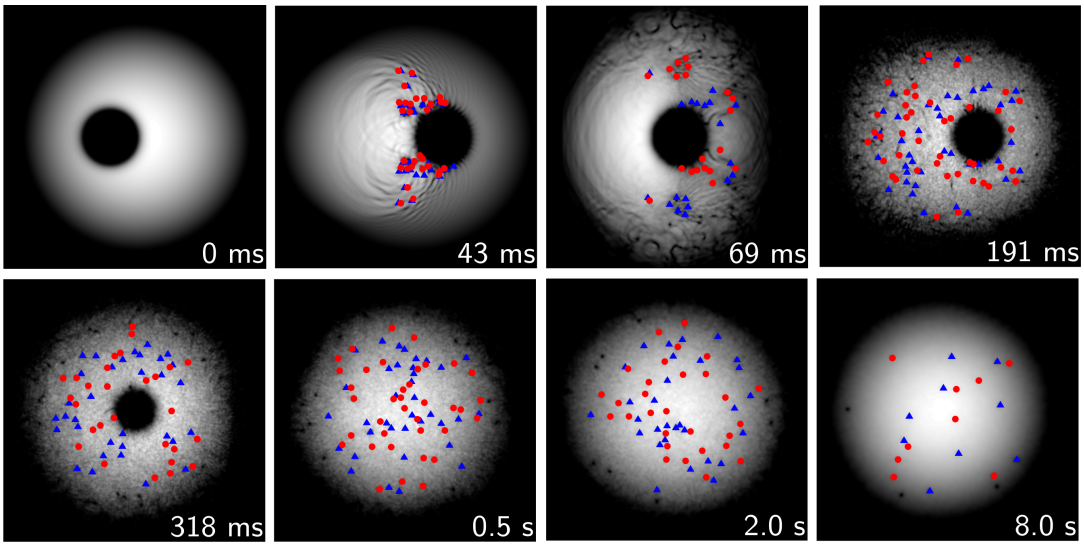

Figure 5.2: Snapshots of the condensate density, for a translational speed $v = 1.4$mm/s and in the presence of dissipation ($\gamma = 0.0003$). The obstacle is completely removed at 0.43s. The field of view in each subfigure is of size $[170\mu\text{m}]^2$ and shifted along the x-axis so as to best display the condensate. Vortices with positive (negative) circulation are highlighted by red circles (blue triangles).

5.4.1 Vortex Nucleation and Wake Formation

To initiate the dynamics, the harmonic trap is translated to the left. This is performed sufficiently rapidly that the condensate does not adiabatically follow the trap minimum, but rather begins a sloshing motion in the trap; the centre-of-mass of the BEC oscillates at the trap frequency and the BEC undergoes a quadrupolar shape oscillation. As the BEC sloshes first to the left, its speed increases. When the local fluid velocity exceeds the speed of sound, vortices nucleate [148] at the poles of the obstacle (where the local fluid velocity is the greatest) and are washed downstream (to the left). As seen in Chapter 4, the pattern of vortices nucleated by a moving obstacle in a superfluid depends, in general, on the speed, shape and size of the obstacle [102, 193, 258]. During the initial evolution vortices of negative and positive circulation are created near each pole in an irregular manner, sometimes with alternating circulation; other times several vortices of the same circulation appear. During this early stage ($t = 43$ms), vortices of opposite circulation may become very close and annihilate (i.e. undergo a 2D reconnection), leaving behind density (sound) waves. The condensate then sloshes to the right; this motion not only carries the existing vortices to the opposite (right) side of the obstacle but nucleates further vortices. As the condensate's sloshing mode is damped by the dissipation, the relative speed of the obstacle decreases and the vortex nucleation pattern changes: like-signed vortices are generated near each pole. In our case, the rate of vortex nucleation is sufficiently high that the like-sign vortices interact strongly with each other, collectively forming macroscopic

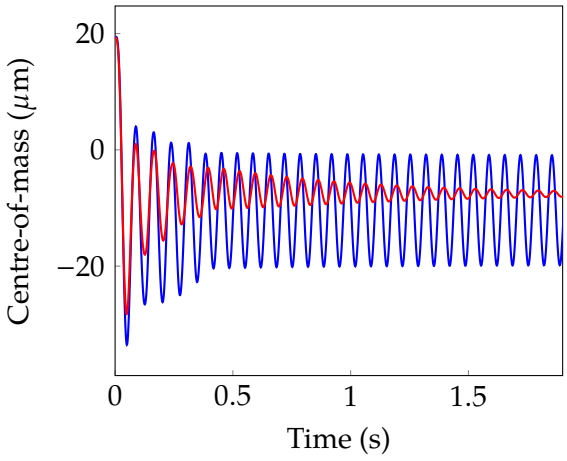

Figure 5.3: Centre-of-mass oscillations during condensate evolution for the BEC without the dissipation term (blue), and with a dissipation of $\gamma = 0.0003$ (red).

clusters of negative and positive vortices near the object ($t = 69$ms). This is reminiscent of the wakes in classical viscous fluids past cylindrical obstacles [258]. As the condensate continues to slosh, more vortices nucleate into the system. It must be stressed that, up to these early times ($t = 191$ms), the vortex distribution remains symmetric about the x axis.

Without the dissipation term in the GPE, the sloshing mode initially decays while the obstacle is present but then persists with constant amplitude once the obstacle is removed. If dissipation is included then the sloshing mode continues to decay. Figure 5.3 shows the centre-of-mass oscillation over time, demonstrating the decay and that in either case, the sloshing mode is produced at the trap frequency.

5.4.2 Vortex Randomization

In the presence of the obstacle and the sloshing mode, vortices continually nucleate and their spatial distribution remains approximately symmetric about the x axis. At later times ($t > 318$ms) this symmetry breaks and the vortices evolve into a completely disorganised, apparently random configuration with no significant clustering of like-signed vortices. This random distribution of vortices is consistent with the experimental observations [106]; following this we also classify the system as one of quantum turbulence. Besides vortices, the condensate contains also collective modes and an energetic, disordered sound field, with this spatial range of excitations further indicative of two-dimensional quantum turbulence [249, 251]. (Note that the typical characteristic diagnostics of steady-state 2D quantum turbulence, e.g. steady state energy spectra and the inverse energy cascade, are not appropriate here since the system is not continuously driven.)

The vortex randomization is driven by the growth of numerical noise. We have re-

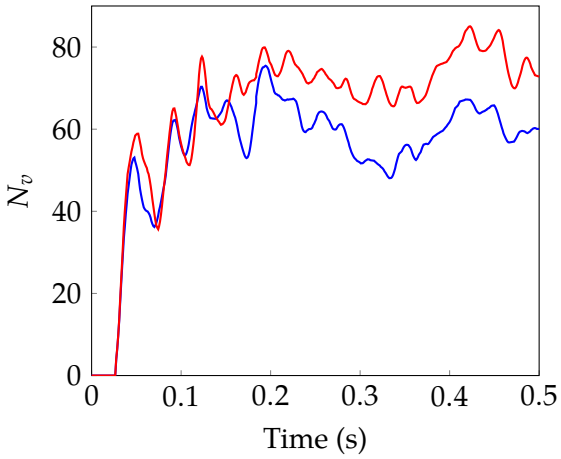

Figure 5.4: Growth of vortex number (in a single realization) at early times for a translational speed of v = 1.4mm/s. Shown are the results with no dissipation (blue) and with dissipation γ = 0.0003 (red).

peated our results in the presence of imposed noise (amplitude 5%, as described elsewhere [258]) and find the qualitative dynamics to be unchanged (although, as one would expect, the vortex randomization occurs at a slightly earlier time). This noise serves to model the natural fluctuations that arises in a realistic experimental scenario, e.g. due to thermal and quantum atomic fluctuations, electromagnetic noise, vibrations, etc.

It is interesting to note the obstacle is still in the system at this point, nucleating vortices in a symmetrical manner. The disorganised vortices already in the system create a velocity field which quickly mixes newly created vortices nucleated at the poles of the obstacle. Visual inspection, confirmed by the RCA clustering-detection algorithm [194, 195] described in Section 3.3.3, shows no significant clusters beyond this stage of the evolution. By the time the obstacle is removed the vortex configuration is essentially random, but the number of positive and negative vortices stays approximately equal. It is important to remark that, without detecting the sign of the vortex circulation, we could not reach these conclusions.

5.4.3 Vortex Decay

It is clear from Figure 5.2 that, following the removal of the obstacle, the number of vortices, N_v, depletes. Indeed, one expects that the condensate will decay towards its vortex–free, time–independent ground state. To quantify the vortex generation and decay, Figure 5.4 plots the growth of N_v at early times, and Figure 5.5 (a, b) plots the decay of vortices over the remaining experimental time period. The onset of vortex nucleation is at around t = 0.02ms; this is the time taken for accelerating condensate to exceed the speed of sound at the poles of the object. At first N_v grows steeply, as vortices (around 40-60) are rapidly

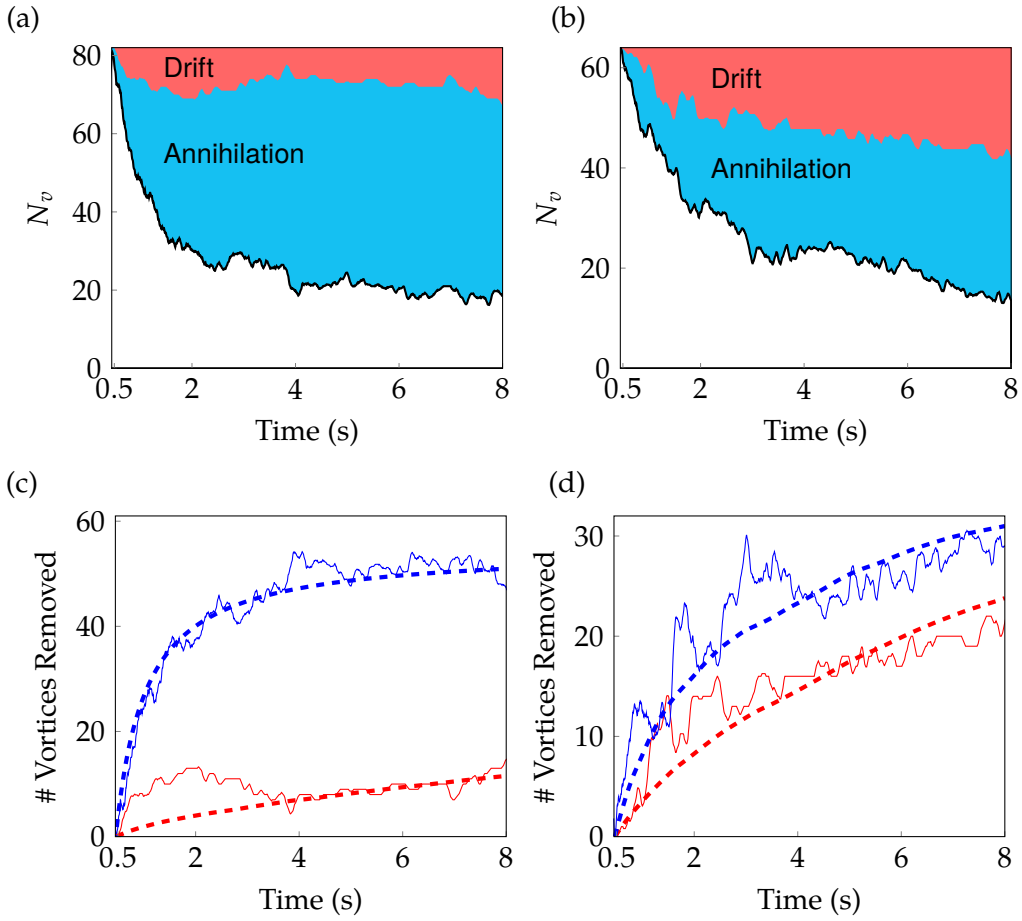

Figure 5.5: Vortex decay in the absence of dissipation (a, c) and with dissipation $\gamma = 0.0003$ (b, d) for a translational speed of $v = 1.4$mm/s. The upper figures show the decay of the total vortex number $N_v(t)$, with the contribution of drifting and annihilation depicted by the shaded regions. The lower figures show the drift number $N_d(t)$ (blue solid lines) and annihilation number $N_a(t)$ (red solid lines), plus their respective fits (dashed lines).

driven into the system. Subsequently, N_v grows more slowly; vortices continue to be nucleated from the obstacle but vortices undergo annihilation or move into low density regions where they are not detected. The fluctuations in N_v are amplified, particularly at early times, by the shape oscillations of the condensate, which carry vortices in and out of the detection radius. As the obstacle is removed, the surrounding condensate fills the low density area. Vortices (including some outside of the detection radius) move inwards with the condensate, causing N_v to peak at $t \approx 0.4$s. Following removal of the obstacle, the vortex number N_v decays with time. This is shown in Figure 5.5(a) and (b) for the absence and presence of dissipation, respectively.

Kwon's decay model

Kwon *et al.* [106] argued that there are two mechanisms by which vortices decay: (i) thermal dissipation (resulting in drifting of vortices to the edge of the condensate), and (ii) vortex-antivortex annihilation events, and proposed that the vortex decay takes the form:

$$\frac{\mathrm{d}N_v}{\mathrm{d}t} = -\Gamma_1 N_v - \Gamma_2 {N_v}^2. \tag{5.2}$$

Here the linear and nonlinear terms, parametrised by the positive coefficients Γ_1 and Γ_2, respectively, model these two decay processes. From our simulations we are able to independently count the number of vortices which drift out and the number which annihilate. We decompose the number of vortices according to

$$N_v(t) = N_i - N_d(t) - N_a(t), \tag{5.3}$$

where N_i is the initial number of vortices (when the obstacle is removed), $N_d(t)$ is the cumulative number of vortices which have drifted out of the condensate and $N_a(t)$ is the cumulative number which have undergone pair annihilation. The contribution of both vortex drifting and annihilation to the overall decay of N_v is depicted by the coloured regions in Figure 5.5(a) and (b). In the absence of dissipation the vortex decay is dominated by annihilation. Indeed, apart from at early times (where internal condensate dynamics carry vortices out to high radii), no vortices drift out. In contrast, in the presence of dissipation, vortices continue to drift out over time, consistent with dissipative dynamics of single vortices [256].

Unfortunately, fitting $N_v(t)$ directly to Equation (5.2) leads to inconclusive results. While we find that the best-fitting solutions fit the data well, the resulting values for Γ_1 are found to be negative, corresponding to a positive growth. Considering that Γ_1 is a term associated to thermal dissipation there is no reason to expect a growth here. We interpret this inconsistency as resulting from fitting Equation (5.2) directly; the meaning of the rates Γ_1 and Γ_2 (i.e as characterising rates of vortex loss through drifting and vortex-antivortex annihilation) are not enforced, and so the best-fit parameters cannot be used to infer anything about the physical processes.

Our solution is to enforce the meaning of Γ_1 and Γ_2 while performing the fitting process. The decomposition of N_v as Equation (5.3) enables us to independently fit the drift and annihilation decay processes as two coupled ODEs for N_d and N_a,

$$\frac{\mathrm{d}N_d}{\mathrm{d}t} = \Gamma_1 N_v, \qquad \frac{\mathrm{d}N_a}{\mathrm{d}t} = \Gamma_2 {N_v}^2. \tag{5.4}$$

By taking the time derivative of Equation (5.3) and substituting in Equation (5.4), Equation

(5.2) can be recovered. As a consequence of fitting the coupled ODEs independently, the physical meaning of each rate term is enforced. To further fix the physical meaning, the fitted value of both Γ_1 and Γ_2 are forced to be positive (corresponding to a vortex decay over time). The vortex decomposition along with the each independent fit is shown in Figure 5.5(c) and (d) for the absence and presence of dissipation, respectively. We find that the rate equation fits fairly well most cases, although finds difficulty in fitting the lack of vortex decay via drifting when $\gamma = 0$.

In the absence of dissipation we find a value of $\Gamma_1 = 5.5 \times 10^{-2}$. However, it is not appropriate to discuss the physical meaning of Γ_1 in this case, since $\gamma = 0$ and so N_d is not of a decaying form. Note that in general, for a trapped zero temperature condensate vortices decay via phonon emission, however in the specific case of a *harmonic* trap it has been shown that due to reabsorption of phonons no net decay occurs [259]. This explains the less successful fit for N_d in the absence of dissipation. We also find the corresponding $\Gamma_2 = 9.7 \times 10^{-3}$. While the experimental observations [106] suggest Γ_2 is proportional to T^2 and thus approaches 0 as $T \to 0$, our results demonstrate a finite Γ_2 in this limit.

With the inclusion of a dissipation of $\gamma = 0.0003$ we obtain $\Gamma_1 = 12.3 \times 10^{-2}$, this corresponds to an increase to the rate of vortex decay via the drifting out mechanism, as expected when introducing dissipation into the system [256]. We also find $\Gamma_2 = 5.3 \times 10^{-3}$. These values are in good agreement with the values obtained by Kwon *et al.* when fitting to their coldest experiments.

Modified decay model

We have shown that the rate equation proposed by Kwon *et al.* [106], Equation (5.2), can be used to characterise the decay of vortices via two mechanisms: a rate of decay due to drifting, and a rate of decay due to annihilation. However, to obtain physically realistic fits, we were forced to enforce the meaning of the two decay terms as part of the fitting mechanism, a process which is not ideal.

Post publication [260] of the results in this chapter, several authors [261, 262] independently investigated vortex interactions in the context of quantum turbulence, providing arguments and evidence to support modified rate equations for the decay of vortex number in atomic BEC experiments. Recently, Cidrim *et al.* [261] proposed a scheme for generating two-dimensional quantum turbulence with the novelty of controlling the *polarisation* of the resulting turbulence by the addition of small localised repulsive potentials. Similarly to our findings in Section 5.4.3, fitting to Equation (5.2) without enforcing the meaning of the terms provided physically unrealistic decay rates. Cidrim *et al.* proposed a simple argument that takes into account the polarised nature of the turbulence and early-time steeper-than-quadratic effects, providing the following phenomenological model of vortex

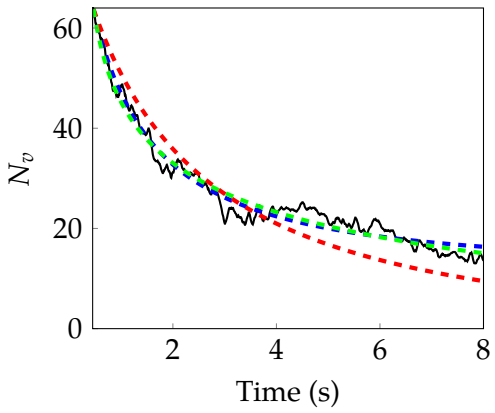

Figure 5.6: Comparison of the three vortex decay models introduced in this chapter. Shown is the decay of vortex number for our GPE simulation with dissipation $\gamma = 0.0003$ and a translational speed of $v = 1.4$mm/s. (black solid line). Also shown is fits to the data using Kwon's rate equation (blue dashed line), Kwon's rate equation while enforcing the meaning of the decay rates (red dashed line) and Cidrim's equation (green dashed line).

decay,

$$\frac{dN_+}{dt} = -\Gamma_3 {N_+}^{3/2} - \Gamma_4 (N_+ N_-)^2,$$
$$\frac{dN_-}{dt} = -\Gamma_3 {N_-}^{3/2} - \Gamma_4 (N_+ N_-)^2, \tag{5.5}$$

where N_+/N_- are the number of vortices of positive/negative circulation, so that $N_v = N_+ + N_-$. Fitting to this model gave physically realistic values for both decay rates in all of their simulated cases. For the unpolarised turbulence that we investigate, Equation (5.5) can be equivalently written as

$$\frac{dN_v}{dt} = -\Gamma_3 {N_v}^{3/2} - \frac{\Gamma_4}{8} {N_v}^4. \tag{5.6}$$

Groszek *et al.* independently provided evidence [262] that vortex annihilation events are in fact a four-body loss mechanism, leading to an annihilation decay rate of the form $dN_v/dt \sim -N_v^4$, supporting the findings of Cidrim *et al.* The argument for four-body loss is based on a two step annihilation process involving a vortex-antivortex pair and two so called *catalyst* vortices. In the first step a vortex-antivortex pair interacts with a catalyst vortex, so as to produce a solitary wave structure which travels at near the speed of sound. In the second step the structure scatters off another catalyst vortex, leading to its destruction and the emission of sound.

As a further test of Cidrim's modified decay law we have fitted Γ_3 and Γ_4 to our simulation with dissipation $\gamma = 0.0003$ and trap speed $v = 1.4$mm/s. A comparison of the

Decay rate	*Kwon's equation*	*Decomposed Kwon's equation*	*Cidrim's equation*
Drift	$\Gamma_1 = -1.8 \times 10^{-1}$	$\Gamma_1 = 12.3 \times 10^{-2}$	$\Gamma_3 = 2.0 \times 10^{-2}$
Annihilation	$\Gamma_2 = 1.4 \times 10^{-2}$	$\Gamma_2 = 5.3 \times 10^{-3}$	$\Gamma_4 = 3.3 \times 10^{-6}$

Table 5.1: Comparison of the resulting decay rates when fitting Kwon's equation [Equation (5.2)], decomposed Kwon's equation [Equation (5.4)] and Cidrim's equation [Equation (5.6)] to the decay of vortex number for our GPE simulation with dissipation $\gamma = 0.0003$ and a translational speed of $v = 1.4$mm/s.

resulting decay rates is shown in Table 5.1, and the fits are visually compared in Figure 5.6. Kwon's equation [Equation (5.2)] provides a good qualitative fit to the decay rate overall, but physical processes cannot be inferred from the resulting values of the decay rates Γ_1 and Γ_2. Enforcing the meaning of the terms in Kwon's equation by fitting $N_d(t)$ and $N_a(t)$ independently [Equation (5.4)] performs the least favourably overall, but provides physically realistic decay rates. Finally, Cidrim's equation [Equation (5.6)] qualitatively fits *at least* as well as Kwon's equation, while having the advantage of physically realistic values for the decay rates and the ability to handle non-zero turbulence polarity. We note that our resulting values for Γ_3 and Γ_4 when fitted to Cidrim's equation compare well to values obtained by Cidrim *et al.* when fitting to decaying 2D turbulence with zero polarisation and $N_v(0) \sim 150$. These results suggest that of the fitting methods described, Cidrim's Equation is the best performing phenomenological model of vortex decay.

5.5 Crescent-Shaped Density Structures

In the experiment, Kwon *et al.* observed the occasional appearance of crescent-shaped waves of depleted density. Lacking direct access to the vortex signs, they suggested that these structures result from annihilation events of vortices of opposite circulation [263–265]: a vortex reconnection is predicted to induce an intense, localised, rarefaction sound pulse [151, 266]. Numerical studies featuring vortex annihilation in 2D [267, 261, 262] also predict the formation of a dark solitonic wave during vortex annihilation events.

Figure 5.7 shows snapshots of the condensate density and phase during a reconnection event in one of our simulations. Vortices show up as localized dips in the density (upper row) and 2π-defects in the phase (lower row). Figure 5.7 (a) shows a vortex (A) and antivortex (B) close to each other, and a third vortex (C) in the vicinity. Note that the individual vortices are not spatially resolvable through their density alone (the vortex cores merge into a deep, elongated crescent-shaped depression), but they are clearly identified by the phase plot. A short time later (b), vortices A and B annihilate, as confirmed by the disappearance of their phase singularities, leaving behind a dark solitonic wave (S) with a linear phase step. This solitonic wave rapidly evolves into a shallow, crescent-shaped

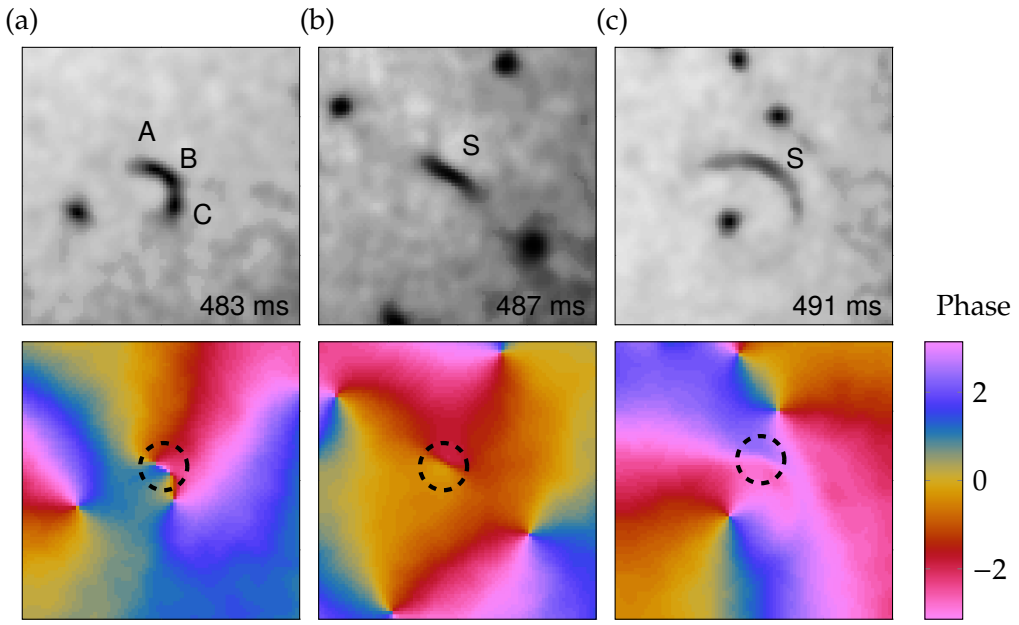

Figure 5.7: Density (upper) and phase (lower) just before (a), immediately following (b) and a later time after (c) a vortex-antivortex annihilation event. The field of view is $[23.5\mu\text{m}]^2$, surrounding the vortex pair/sound pulse (highlighted by a circle in the phase).

sound wave [Figure 5.7 (c)].

In other words, our simulations yield the formation of the dark solitonic waves observed by other authors [267, 261, 262] and the crescent shaped density depletions seen in experiments. However, we find that these features are not uniquely formed by annihilation events - they may also result from from two (or more) vortices in close proximity. Information about the condensate phase is thus crucial to distinguish the nature of these observed structures. In this direction, an approach has recently been proposed for the experimental detection of quantized vortices and their circulation in a 2D BEC [166].

5.6 Vortex Generation via an Elliptical Obstacle

It is evident from the snapshots in Figure 5.2 that the initial translation of the condensate past the obstacle generates not just vortices but also shape excitations, sound waves (low-amplitude density waves), and high-amplitude density waves. These additional excitations will heat the condensate and modify the subsequent turbulent dynamics in a highly nonlinear and complicated manner. While reducing the translational speed reduces this disruption, this also reduces the number of vortices. A less disruptive and more efficient (higher rate of vortex nucleation) means to generate vortices may be provided by employing a laser-induced obstacle of a form similar to that used in Chapter 4, with an

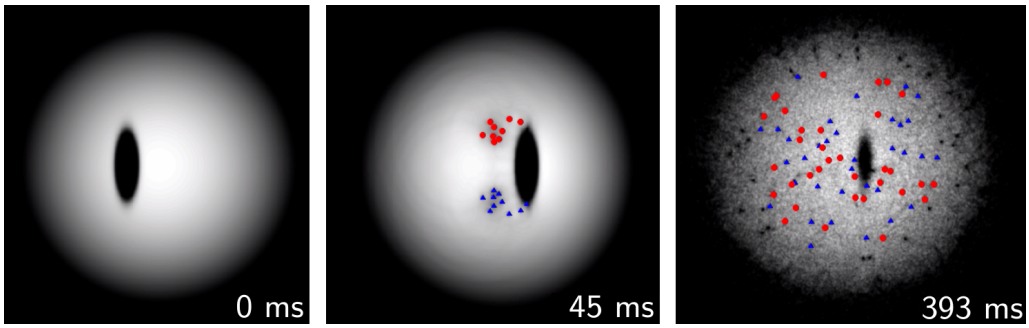

Figure 5.8: Snapshots of the condensate density for a translational of speed $v = 0.8\text{mm/s}$ past an elliptical obstacle (ellipticity $\varepsilon = 3$). The field of view in each subfigure is of size $[170\mu\text{m}]^2$ and shifted along the x-axis so as to best display the condensate. Compared to the corresponding snapshots in Figure 5.2, the elliptical obstacle generates as many final vortices but at a lower translational speed and with reduced condensate disruption.

elliptical rather than circular cross-section (experimentally attainable through cylindrical beam focusing).

Repeating our simulations with such an elliptical obstacle, whose shape is defined by Equation (2.45), with arbitrary ellipticity $\varepsilon = 3$ (the short/long axis being parallel/perpendicular to the flow) confirms the same qualitative behaviour as in Chapter 4 for homogeneous systems [258]: the ellipticity acts to reduce the critical superfluid velocity and, for a given flow speed, increase the rate of vortex nucleation. To illustrate the merits of the elliptical obstacle, in Figure 5.8 we depict snapshots of the condensate dynamics for ellipticity $\varepsilon = 3$ and a translational speed of $v = 0.8\text{mm/s}$. Despite a lower translational speed, the number of vortices generated by the time the obstacle is removed is almost identical to the circular example of Figure 5.4. As a consequence of the reduced translational speed, the condensate disruption is visibly reduced. This reduction is quantified by measurement of the compressible kinetic energy in the system over time, shown in Figure 5.9. It is also worth noting that the elliptical obstacle promotes the formation of clusters of like-signed vortices (see intermediate time), and thus may facilitate future exploration of coherent vortex structures.

5.7 Conclusions

In conclusion, we have shown that the recent experimental creation and decay of vortices within a BEC [106] is well described by simulations of the 2D GPE with phenomenological dissipation (despite the 3D nature of the system). Theoretical access to the condensate phase, and thus the circulation of the vortices, promotes our understanding of the dynamics. In the early stages of translation of the obstacle, a quasi-classical wake of vortices forms behind it, before symmetry breaking causes disorganisation of the vortices. After

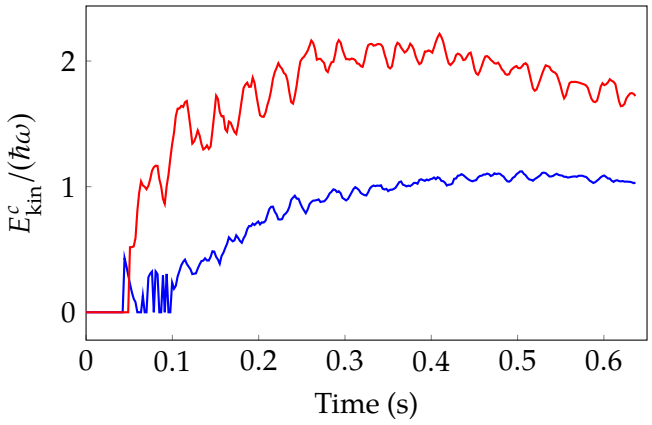

Figure 5.9: Compressible kinetic energy, E^c_{kin}, at early times for a circular obstacle ($\varepsilon = 1$) and trap translation speed $v = 1.4$mm/s (red), and an elliptical obstacle ($\varepsilon = 3$) and trap translation speed $v = 0.8$mm/s (blue).

the obstacle is removed, the vortices decay in a manner which is consistent with the two mechanisms proposed by Kwon *et al.*, i.e. loss of vortices at the condensate edge due to thermal dissipation and vortex-antivortex annihilation events within the condensate.

We fit the vortex decay the rate equations proposed by Kwon *et al.* and Cidrim *et al.* In the case of Kwon's equation we enforce the meaning of the decay rates to find values comparable to the coldest experiments of Kwon *et al.* In the case of fitting to Cidrim's modified equation, we find rates comparable to the simulations of Cidrim *et al.* without the need to enforce meaning. We conclude that Cidrim's equation fits to the data most favourably, while providing physically realistic values for the decay rates.

We confirm the occasional appearance of crescent-shaped density features, resulting either from the proximity of vortex cores or from a sound pulse which follows a vortex-antivortex reconnection. Finally, we propose that a moving *elliptical* obstacle may provide a cleaner and more efficient means to generate two-dimensional quantum turbulence.

Chapter 6

Quasi-classical turbulence and the critical velocity in a quenched Bose gas

6.1 Introduction

The experimental realisation of Bose-Einstein condensates (BEC) in weakly interacting atomic gases has stimulated great interest in the dynamics of quantum turbulence in condensates, a state dominated by an irregular tangle of quantised vortex lines, a defining feature of superfluids with circulation constrained by quantum mechanics. This is in contrast to everyday viscous fluids where eddies can have arbitrary shape, size and circulation. Despite the differences between superfluids and classical fluids, the Kolmogorov energy spectra has been observed in superfluid turbulence [143–145], suggesting a deep link between them [141].

Experimentally, quantum turbulence in atomic BECs can be generated as a result of broken symmetry after a fast quench into the BEC regime. The Kibble-Zurek mechanism [96–98] then leads to the formation of turbulent vortex tangle. Other methods such as oscillating the trapping potential [105] have also been demonstrated. The nature of a turbulent vortex tangle can be categorised based on the form of the energy spectrum, where two regimes have been identified. In Vinen or ultra-quantum turbulence, vortex tangles are random and have only a single length scale: the average inter-vortex spacing. In Kolmogorov or quasi-classical turbulence, the energy spectrum of the tangle follows the celebrated Kolmogorov $k^{-5/3}$ scaling, where k is wavenumber, as in the classical regime. Numerical studies have linked the quasi-classical regime with the presence of metastable bundles of polarized quantum vortices [210].

The link between quantum and classical fluids has also been demonstrated in quasi-2D

condensates, where it has been predicted that the wake of quantized vortices produced downstream of an obstacle can collectively mimic classical wakes, including the Bérnard-von Kármán vortex street [193, 258, 199]. Theoretical studies leading to the prediction of 2D classical-like wakes are discussed in detail in Chapters 4 and 5 for the homogeneous and trapped case, respectively.

A second defining feature of superfluids is the absence of excitations when a flow (relative to some obstacle or boundary) is slower than a critical velocity; above this velocity, the flow becomes dissipative. This can be understood in terms of the Landau criterion, which predicts excitations when the local fluid velocity exceeds $v_{\rm L} = \min[E(p)/p]$, where p is the momentum of elementary excitations and $E(p)$ their energy [95]. In weakly-interacting atomic Bose-Einstein condensates, and for infinitesimally small perturbations, one obtains $v_{\rm L} = c$, the speed of sound.

Experimentally, the breakdown of superfluidity in atomic BECs has been probed by introducing a localized repulsive obstacle, engineered via the repulsive force generated by focussed blue-detuned laser beam, and moving the condensate relative to the obstacle [69, 106, 167, 268, 242, 243, 104, 269]. This has enabled measurement of the critical velocity and the direct observation of the ensuing excitations, that is, pairs of quantized vortex lines with opposite polarity. In flattened quasi-2D condensates, this scenario currently provides a route to engineer states of two-dimensional quantum turbulence [69, 106]. The vortex dynamics of 2D quantum turbulence is studied theoretically for one specific experimental set-up [106] in Chapter 5.

The motion of an obstacle in the zero-temperature Bose gas, described by the Gross-Pitaevskii equation, is a well-studied problem, particularly for circular obstacles in 2D geometries. The pioneering simulations of the 2D nonlinear Schrödinger equation (NLSE) by Frisch *et al.* [148] demonstrated the existence of a critical velocity for a moving impenetrable circular obstacle, $v_{\rm c} \sim 0.4c$, above which vortex-antivortex pairs are nucleated. For small obstacles, boundary effects tend to suppress vortex nucleation, and, as the obstacle's size increases, the critical velocity reduces towards an asymptotic value [234–236]. The critical velocity also depends on the shape of the obstacle, for example, Chapters 4 and 5 discuss how obstacles with elliptical cross-section lead to reduced/heightened $v_{\rm c}$, depending on the orientation relative to the flow [258, 270]. Similar behaviour holds for spherical obstacles, albeit with the emission of vortex rings and increased critical speeds of circa $0.7c$ [271, 245, 258]. In current condensate experiments [69, 106, 242, 243, 104, 269, 167, 268], the obstacles are penetrable, corresponding to a Gaussian potential of finite amplitude. The same qualitative behaviour emerges as with impenetrable obstacles,although the critical velocity and vortex nucleation patterns become modified [193].

Very recently, Kwon *et al.* have undertaken a systematic experimental analysis of the critical velocity for vortex shedding, exploring the dependence of the nucleation on height

and width of the penetrable obstacle and the crossover from penetrable to impenetrable obstacles [167]. Their results, obtained in a condensate with temperature much lower than the critical temperature for condensation, are in agreement with previous zero-temperature predictions based on the Gross-Pitaesvkii equation. Their work has made a significant step in consolidating our theoretical and experimental understanding of the critical velocity in a condensate in the zero-temperature limit. At the same time, it has highlighted the need to extend the study of the critical velocity to finite temperatures.

In this chapter we model a fast quenched three-dimensional homogeneous Bose gas at finite temperature via classical field simulations. Following [184] we evolve the gas from a selection of strongly non-equilibrium initial conditions and observe the growth and formation of a dense tangle of vortex lines in the superfluid part of the gas. By using a strongly non-equilibrium initial condition, with random phase at all points in space, we model an infinitely fast quenched system. We monitor the dynamics as the turbulent vortex tangle decays and the gas reaches thermalised equilibrium. By observing the vortex tangle kinetic energy spectrum and vortex line-density over time, we find a decay characteristic of ultra-quantum turbulence.

With the resulting equilibrium states we insert a cylindrical obstacle with Gaussian profile and study the behaviour of the gas as it flows around the obstacle. We find that the critical velocity decreases with temperature and increases with condensate fraction (ratio of condensate to total density). Indeed, the critical velocity is found to be closely proportional to the speed of sound of the condensate, which scales as the square root of the condensate fraction. Above the critical velocity, vortex nucleation occurs either through pairs of vortex lines, collections of vortex rings, or direct formation of a vortex tangle, and we indicate the occurrence of these structures in the parameter space of condensate fraction and flow speed.

6.2 Classical field method

We consider a weakly-interacting Bose gas with N atoms of mass m in a periodic box of volume D^3. We approximate binary atom interactions by a contact pseudo-potential $V_{\text{int}}(\mathbf{r}-\mathbf{r}') = g\delta(\mathbf{r}-\mathbf{r}')$, where g is a coefficient which characterises the atomic interactions and δ is the Dirac delta function [1]. The approximations would lead us naturally to model the Bose gas in the zero-temperature limit, using the mean-field model described in Sections 2.1 and 2.2. Instead, however, in this chapter we will also include the thermal fraction inherent in the gas at *finite* temperature. In order to theoretically model the thermal excitations, one must progress beyond the mean-field approximation. Various methods have been proposed for this purpose, as reviewed elsewhere [272, 169, 273–276]. Among these methods, a popular one is the classical field method [277–279, 184, 280, 281, 272].

Initial conditions						
N/D^3 (ξ^{-3})	0.50	0.50	0.50	0.50	0.50	0.50
E/D^3 ($\mu\xi^{-3}$)	2.57	2.13	1.75	1.33	0.53	0.23
Equilibrium state						
ρ_0/ρ	0.05	0.25	0.35	0.50	0.75	0.90
T/T_λ	0.96	0.78	0.69	0.54	0.28	0.11

Table 6.1: Condensate fraction and temperature of the classical field equilibrium state for our chosen initial conditions. The exact measured value of ρ_0/ρ depends on the chosen value of k_c, which defines the quasi-condensate; we find only minimal variation at equilibrium.

Section 2.12 provides a brief description of the classical field method for a homogeneous Bose gas.

We parametrise the gas by the classical field $\psi(\mathbf{r}, t)$. Whereas the standard mean-field wavefunction describes the condensate only, in the classical field model $\psi(\mathbf{r}, t)$ instead describes the entire multi-mode 'classical' gas [169, 275]. The classical field method has been used to model beyond-mean-field phenomena, including thermal equilibration dynamics [184, 281–283], condensate fractions [278], critical temperatures [284], correlation functions [285], spontaneous production of vortex-antivortex pairs in quasi-2D gases [192], thermal dissipation of vortices [286], and related effects in binary condensates [287, 288, 282].

The evolution of $\psi(\mathbf{r}, t)$ is governed by Equation (2.1), the GPE. The density distribution of atoms is then $n(\mathbf{r}, t) = |\psi(\mathbf{r}, t)|^2$. The GPE conserves the total number of particles N, given by Equation (2.2), and the total energy E, given in Appendix B by Equation (B.2). In this chapter we express all quantities in terms of the natural units of the homogeneous Bose gas defined in Section 2.8.1: density in terms of a uniform value $\rho = N/D^3$, length in terms of the homogeneous healing length $\xi = \hbar/\sqrt{mg\rho}$, speed in terms of the speed of sound $c = \sqrt{\rho g/m}$, energy in terms of the chemical potential of the homogeneous condensate $\mu = \rho g$, and time in terms of $\tau = \hbar/g\rho$.

We label the modes of the system through the wavevector $\mathbf{k}$ and the occupation of mode $\mathbf{k}$ as $n_\mathbf{k} = |a_\mathbf{k}|^2$. To allow for occupation across all classical modes of the system, the initial condition is the highly non-equilibrium state defined in Section 2.14.3. The temperature of the gas is varied through a rescaling of the initial condition $\psi(\mathbf{r}, 0)$ so as to fix the number density, N/D^3, and energy density, E/D^3. The choice of number density and energy density uniquely determines the condensate fraction ρ_0/ρ, and therefore the temperature T/T_λ, for the equilibrium state of the Bose gas. Table 6.1 lists the parameters used in our simulations and the resulting condensate fractions.

The GPE is evolved numerically, in the absence of any potential ($V = 0$), using the fourth-order Runge-Kutta method described in Section 3.1.1 on a 192^3 periodic grid with time step $\Delta t = 0.01\tau$ and isotropic grid spacing $\Delta = 0.75\xi$. The spatial discretisation of

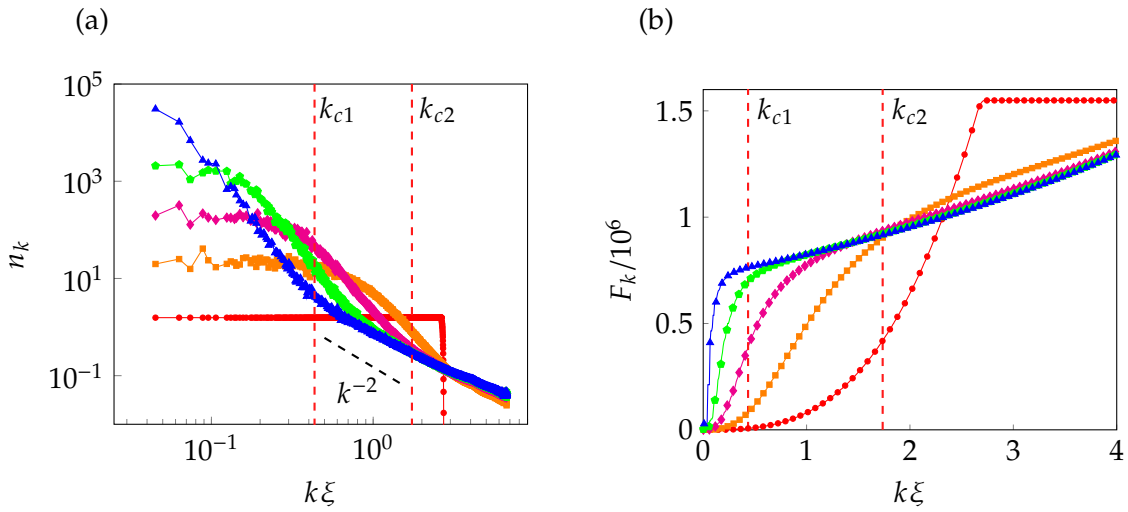

Figure 6.1: (a) Occupation numbers, n_k, of the Bose gas as it decays to equilibrium at times (red circles) $t/\tau = 0$, (orange squares) 25, (magenta diamonds) 75, (green pentagons) 200, and (blue triangles) 1000. Here the final condensate fraction at equilibrium is $\rho_0/\rho = 0.50$. (b) Integral distribution of the particles, $F_k = \sum_{k'<k} n_{\mathbf{k}'}$, at the same times. $k_{c1} = 10\,(2\pi/D)$ and $k_{c2} = 40\,(2\pi/D)$ are labelled by red dashed lines. A line proportional to the Rayleigh-Jeans distribution with $\mu = 0$, $n_k \propto k^{-2}$, is also shown by a black dashed line.

our numerical grid implies that high momenta are not described in our simulations. In effect, an ultraviolet cutoff is introduced, $n_{\mathbf{k}}(t) = 0$ for $k > k_{\max}$, where $k = |\mathbf{k}|$ and the maximum described wave vector amplitude is $k_{\max} = \sqrt{3}\pi/\Delta$.

6.3 Formation of the turbulent vortex tangle

6.3.1 Defining the quasi-condensate

The ensuing evolution from the strongly non-equilibrium initial conditions has been outlined previously [184, 282]. Initially the mode occupation numbers n_k are uniformly distributed over wavenumbers k. Theoretical studies of the relaxation of this state show that the system is in a regime that can be described in terms of weak-turbulence theory. The random-phase approximation can be used, breaking the time reversal symmetry of the GPE, to derive an irreversible kinetic equation for the averaged wave spectrum [281]. The resulting kinetic equation describes evolution of the wave spectrum towards the classically derived Rayleigh-Jeans equilibrium distribution,

$$n_k^{\mathrm{eq}} = \frac{T}{k^2 - \mu}, \tag{6.1}$$

where T is temperature and μ is the chemical potential [289].

During evolution of the Bose gas, self-ordering leads to a coherent regime where the phases of the complex amplitudes $a_{\mathbf{k}}$ become strongly correlated. This regime is marked by the rapid growth in the occupation of low-k modes [demonstrated in Figure 6.1(a)], so that the distribution evolves to a bimodal form. The high-k part of the distribution is associated with the thermal excitations and low mode occupations, the equilibrium state of which closely follows the predicted Rayleigh-Jeans spectrum, albeit modified by the nonlinear interaction with the condensed particles [281]. The low-k part of the field is associated with the condensate, characterised by macroscopic mode populations and superfluid ordering. Due to the random phases used in the initial condition, a dense tangle of quantised vortices forms in the condensed part of the gas, shown in Figure 6.2, which relaxes over very long times.

From the bimodal distribution [visible in Figure 6.1 (b)], a wavenumber k_c is chosen as the boundary in k-space between the condensate part and the thermal part of the gas. The formation of a 'shoulder' in the integral distribution indicates that a macroscopic fraction of the particles reside in the low-k modes, which facilitates the choice of k_c. In this work we focus on the value, $k_{c1} = 10\ (2\pi/D)$. However, in some cases we will also show quantities measured using a cutoff of $k_{c2} = 40\ (2\pi/D)$, so as to emphasise the effect of the choice of k_c. These cases will be clearly marked as such.

The raw wavefunction, ψ, is too noisy to allow direct visualisation of the resulting superfluid vortex tangle. This is overcome by defining a quasi-condensate wavefunction $\hat{\psi}$, as established in [184]. High-frequency modes are filtered from the classical field wavefunction by transforming the complex amplitudes via $\hat{a}_{\mathbf{k}} = a_{\mathbf{k}} \times \max\{1 - k^2/k_c^2, 0\}$. This filtering technique is demonstrated in Section 3.6 and is analogous to spatial course-grained averaging, so that $\hat{\psi}$ contains the long-wavelength component of the classical field only. The condensate fraction, ρ_0/ρ, is defined as the proportion of the entire gas within the quasi-condensate, where $\rho_0 = 1/D^3 \int |\hat{\psi}|^2 \, \mathrm{d}\mathbf{r}$. Note that while GPE dynamics conserves N for the entire gas, the quasi-condensate particle number is free to vary. As occupation of the low-k modes grows and the quasi-condensate forms, ρ_0/ρ grows significantly, but stabilises near its equilibrium value before the vortex tangle decays significantly.

Its physical properties, e.g. temperature and condensate fraction, are uniquely determined by N and the kinetic energy of the system [281]. It is interesting to note that the equilibrium condensate fraction is insensitive to the number of modes, providing that the number of modes is, or exceeds, 16^3. This suggests that this number of modes is sufficient to model the thermodynamic limit of the system. For comparison, we employ 192^3 modes.

The quasi-condensate wavefunction is used to visualise the condensed part of the Bose gas, using evolving isosurface levels of $|\hat{\psi}|^2 = 0.05\,\langle|\hat{\psi}|^2\rangle$. This level was chosen so that the resulting vortex structures are shown with approximately constant cross-sectional radius similar to the radius of a true vortex core (facilitated by the approximate quasi-condensate

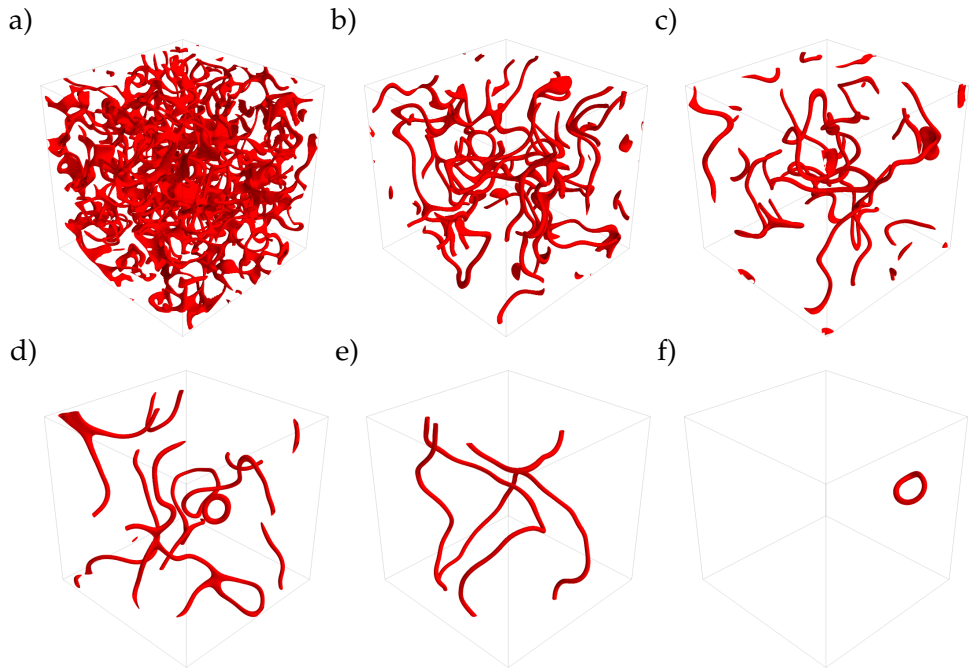

Figure 6.2: A sample evolution of the turbulent vortex tangle present in the condensed part of the Bose gas as it decays to equilibrium. Here the final condensate fraction of the gas at equilibrium is $\rho_0/\rho = 0.50$. Shown are isosurfaces of the quasi-condensate density at isosurface level $0.05\,\langle|\hat{\psi}|^2\rangle$ at times (a) $t/\tau = 0$, (b) 500, (c) 1000, (d) 2000, (e) 4000, and (f) 10 000. At later times (not shown) all vortex lines dissipate from the system. Here the quasi-condensate is visualised using a cutoff of $k_c = 10\,(2\pi/D)$.

density term $\langle|\hat{\psi}|^2\rangle$).

6.3.2 Approximate temperature of the gas

As we first saw in Section 1.1, using the statistical mechanics of bosons it can be shown that for a *non-interacting* ideal gas of bosons there exists a simple prediction for how the condensate fraction of the gas grows as temperature decreases [1],

$$N_0 = N\left[1 - \left(\frac{T}{T_\lambda}\right)^\beta\right], \tag{6.2}$$

where N_0 is the number of condensed particles, T_λ is the critical temperature for condensation and β is a parameter that depends on the geometry of the system. For particles in a 3 dimensional box, $\beta = 3/2$ [1]. By inverting this relation we could obtain a simple minded approximation for the temperature of our equilibrated Bose gas, ignoring interactions.

However, Berloff *et al.* [286] recently provided the following empirical relationship for

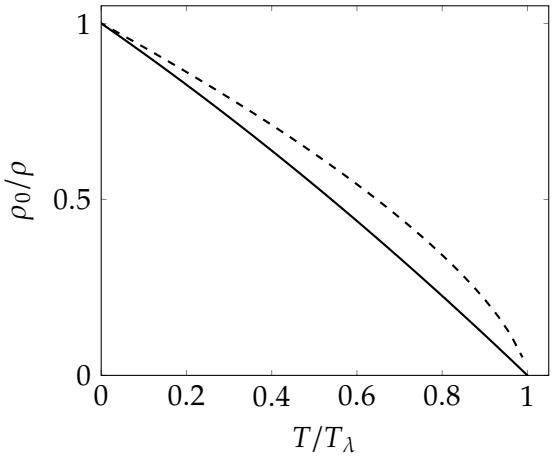

Figure 6.3: The condensate fraction and temperature relation for a weakly-interacting Bose gas for our simulation parameters (black solid line) and for an ideal non-interacting Bose gas (black dashed line).

a *weakly-interacting* Bose gas in a 3 dimensional box:

$$\frac{T}{T_\lambda} = 1 - \left(1 - \alpha\sqrt{\rho\xi^3}\right)\frac{\rho_0}{\rho} - \alpha\sqrt{\rho\xi^3}\left(\frac{\rho_0}{\rho}\right)^2, \tag{6.3}$$

where $\alpha = 0.2275$ is a fitting parameter. We will use this relation throughout the chapter to evaluate the temperature of the gas using the condensate fraction at equilibrium. The relation is compared to the relation for an ideal non-interacting Bose gas in Figure 6.3. Table 6.1 lists the resulting approximate temperatures at equilibrium for the parameters chosen in our simulations.

6.3.3 Energy scales of the vortex tangle

One method to characterise the turbulence of the vortex tangle formed in the quasi-condensate is by studying how the kinetic energy of the vortices is distributed over length scales. There are three length scales of particular interest: the length scale associated with the computational box, the length scale associated with the superfluid healing length, and the length scale associated with the inter-vortex spacing, ℓ. The corresponding wavenumbers are $k_D = 2\pi/D$, $k_\xi = 2\pi/\xi$, and $k_\ell = 2\pi/\ell$. The inter-vortex spacing can be approximated by $1/\sqrt{L}$, a relation derived through dimensional arguments where L is the vortex line-density (length of vortex line per unit volume). These length scales provide the perspective required to interpret the distribution of energy. Note that the quantities ξ and ℓ vary over time. As ℓ varies until equilibrium, we allow k_ℓ to be time dependent. On the other hand ξ varies rapidly early times, quickly reaching an approximately steady value, so we use

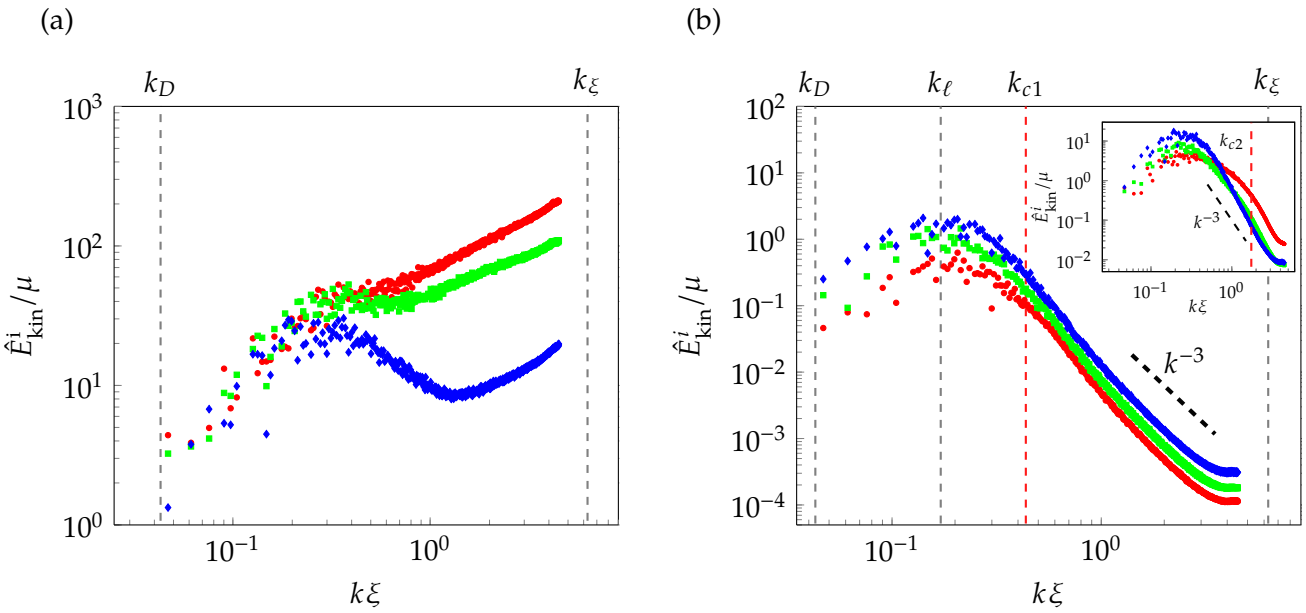

Figure 6.4: Incompressible kinetic energy spectrum for the (a) entire Bose gas and (b) quasi-condensate with $\rho_0/\rho = 0.25$ (red circles), $\rho_0/\rho = 0.50$ (green squares), and $\rho_0/\rho = 0.75$ (blue diamonds) at time $t/\tau = 300$ and with a cutoff of $k_c = 10\ (2\pi/D)$ (labelled k_{c1}). Dashed lines show the scale of the healing length, k_ξ, the length scale of inter-vortex spacing k_ℓ, and the length scale of the periodic box k_D. A guide line proportional to k^{-3} is also shown. (Inset) The same data, but with a cutoff of $k_c = 40\ (2\pi/D)$ (labelled k_{c2}).

the value of ξ at equilibrium to define a constant k_ξ.

The kinetic energy of the quasi-condensate is defined as $E_{\mathrm{kin}} = \int \frac{\hbar^2}{2m}|\nabla\hat{\psi}|^2\,\mathrm{d}\mathbf{r}$. Using Parseval's theorem, the corresponding kinetic energy spectrum, $\hat{E}_{\mathrm{kin}}(k)$, can be written in terms of the angle-average of $\left|\mathcal{F}(\sqrt{E_{\mathrm{kin}}})\right|^2$ [143], where $\mathcal{F}$ denotes the Fourier transform, so that,

$$\int E_{\mathrm{kin}}(\mathbf{r})\,\mathrm{d}^3\mathbf{r} = \int \hat{E}_{\mathrm{kin}}(k)\,\mathrm{d}k. \tag{6.4}$$

The kinetic energy can be further decomposed into compressible and incompressible parts, $E_{\mathrm{kin}} = E^i_{\mathrm{kin}} + E^c_{\mathrm{kin}}$, by using the decomposition [143] $\sqrt{n}v_j = (\sqrt{n}v_j)^c + (\sqrt{n}v_j)^i$, with $\nabla\cdot(\sqrt{n}v_j)^i = 0$, where n is the fluid density and $\mathbf{v}$ is the fluid velocity. The incompressible kinetic energy spectrum is then denoted $\hat{E}^i_{\mathrm{kin}}(k)$.

Figure 6.4 (a) shows the incompressible kinetic energy spectrum of the entire Bose gas (filtering out no modes) at various temperatures, sampled at time $t/\tau = 300$ so as to characterise the vortex tangle before significant decay, while providing enough time for the quasi-condensate to form. It can be seen in all cases that the high-k modes are sufficiently occupied that drawing conclusions is difficult. To overcome this, we calculate the incompressible kinetic energy spectrum of the quasi-condensate only, shown in Figure 6.4 (b), by filtering with a cutoff of $k_c = 10\ (2\pi/D)$.

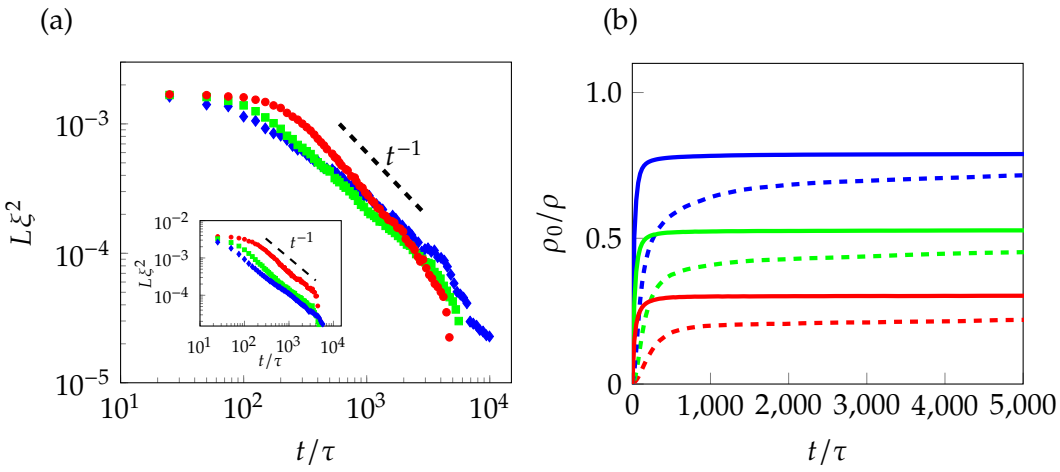

Figure 6.5: (a) Vortex line density over time for $\rho_0/\rho = 0.25$ (red circles), $\rho_0/\rho = 0.50$ (green sqaures), and $\rho_0/\rho = 0.75$ (blue diamonds) with a cutoff of $k_c = 10\ (2\pi/D)$. Each line is an average of 5 simulations. A line proportional to t^{-1}, characteristic of the decay of a ultra-quantum turbulence, is shown (dashed black line) as reference. (Inset) The same data, but with a cutoff of $k_c = 40\ (2\pi/D)$. (b) Condensate fraction over time for the quasi-condensate filtered with a cutoff of $k_c = 10\ (2\pi/D)$ (dashed lines) and $k_c = 40\ (2\pi/D)$ (solid lines), leading to equilibrium states with $\rho_0/\rho = 0.25$ (red), $\rho_0/\rho = 0.50$ (green), and $\rho_0/\rho = 0.75$ (blue). The exact value of ρ_0/ρ depends on the chosen value of k_c; we find only minimal variation at equilibrium.

Figure 6.4 (b) clearly shows that our turbulence is unlike turbulence in ordinary fluids. In classical turbulence, the energy is concentrated at the smallest wavenumber k_D, decreasing as $k^{-5/3}$ (the celebrated Kolmogorov scaling) in the region $k_D < k < k_\ell$. Figure 6.4 shows no pile-up of energy near k_D and no Kolmogorov scaling; on the contrary, the energy peaks at length scales just above k_ℓ. The visible k^{-3} dependence of the spectra in the region $k_\ell < k < k_\xi$ arises from the vortex cores [143]. Figure 6.4 (Inset) shows the same data when filtered with a cutoff of $k_c = 40\ (2\pi/D)$. We find that for all temperatures, although the exact values of $\hat{E}^i_{\rm kin}(k)$ are modified by the inclusion of higher modes, the general form of the spectrum is insensitive to the precise choice of k_c.

6.4 Relaxation of the vortex tangle

As the condensate evolves over the course of the simulation, the initially-formed dense vortex tangle remains random and isotropic throughout the decay to one or more vortex rings, which eventually also decay, leading to a vortex-free state (the “equilibrated" state). A example of such a decay is shown in Figure 6.2.

Insight into the nature of the quasi-condensate turbulence can be obtained by investigating the relaxation of the vortex tangle, obtained by monitoring the vortex line-density L. We estimate the vortex line-length from the total volume of the isosurface tubes, $V_{\rm t}$. We

ρ_0/ρ	α	β	k_c
0.25	0.35 ± 0.09	1.04 ± 0.06	10 $(2\pi/D)$
0.50	0.15 ± 0.02	0.95 ± 0.06	10 $(2\pi/D)$
0.75	0.071 ± 0.02	0.81 ± 0.08	10 $(2\pi/D)$
0.25	0.61 ± 0.10	1.05 ± 0.04	40 $(2\pi/D)$
0.50	0.18 ± 0.03	1.04 ± 0.03	40 $(2\pi/D)$
0.75	0.063 ± 0.005	0.94 ± 0.01	40 $(2\pi/D)$

Table 6.2: Best fitting power law decay of the vortex line density over time, fitted to the equation $L(t) = \alpha t^{-\beta}$ for the data demonstrated in Figure 6.5 (a). Error bounds show the 95% confidence interval.

assume that each vortex tube has uniform constant circular cross-sectional area A_t; the total vortex line-length is then V_t/A_t.

Note that this approximation is only strictly valid for vortices well separated in space and for steady condensate fraction (so that the healing length of the quasi-condensate is constant). A more sophisticated and robust algorithm for calculating and tracking vortex line length has recently been described [200, 201], however the computational requirements are higher. We find that the computationally efficient estimate we employ here is accurate enough for our analysis due to the fact that it is only at very early times where the condensate fraction changes significantly [Figure 6.5(b)], and our vortices are indeed well separated for the majority of the decay [Figure 6.2(b-f)].

We find that the temporal decay of the vortex line density, shown in Figure 6.5 (a), has power-law form, $L \sim t^{-\beta t}$ with $\beta \approx 1$ or slightly less depending on the condensate fraction (precise values are given in Table 6.2). Figure 6.5 (a) is therefore consistent with Figure 6.4 (b) and the absence of a Kolmogorov spectrum, because the decay of classical Kolmogorov turbulence, would be significantly quicker, $L \sim t^{-3/2}$ [290, 291]. Instead, the exponent $\beta \approx 1$ which we observe is consistent with the 'ultra-quantum' turbulent regime revealed by the experiments of Walmsley & Golov [292], who created the turbulence by injecting vortex rings in a sample of superfluid helium initially at rest.

To confirm the ultra-quantum interpretation of the turbulence, we compute the velocity correlation function, $f(r)$, defined at a fixed point in time as

$$f(r) = \frac{\langle v_x(\mathbf{r}) v_x(\mathbf{r} + r\hat{\mathbf{e}}_x)\rangle}{\langle v_x(\mathbf{r})^2\rangle} \tag{6.5}$$

where $\mathbf{v}$ is the quasi-condensate fluid velocity and the ensemble average is performed over positions $\mathbf{r}$. While we have used the x direction in the definition of $f(r)$, due to the isotropic nature of the turbulence using the y or z direction leads to similar results. The function is a dimensionless measure of velocity correlation at distance r, with $f(0) = 1$, and is shown in Figure 6.6 (a) for the three of our simulated parameter sets (spanning

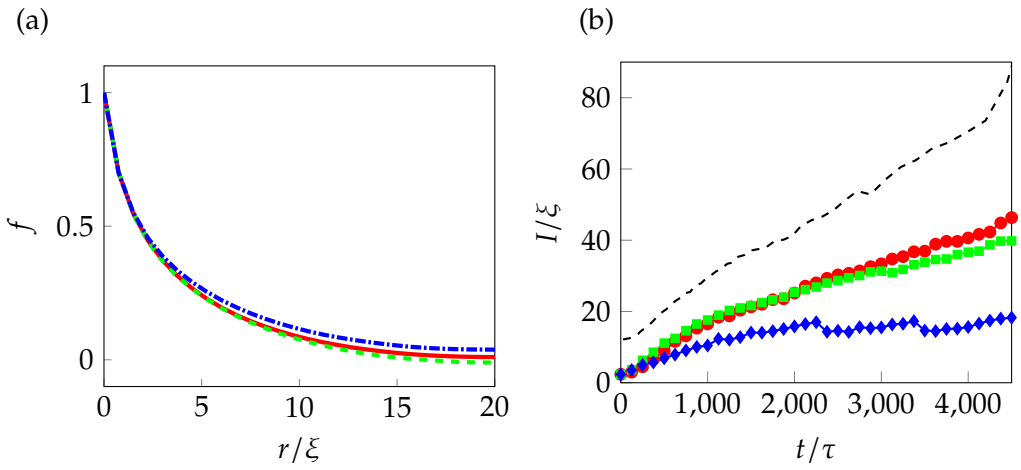

Figure 6.6: (a) Snapshots of the velocity correlation function $f(r)$ at time $t = 300\tau$ for equilibrium states with $\rho_0/\rho = 0.25$ (red solid line), $\rho_0/\rho = 0.50$ (green dashed line), and $\rho_0/\rho = 0.75$ (blue dot-dashed line). (b) The integral scale as the quasi-condensate vortex tangle decays, for equilibrium states with $\rho_0/\rho = 0.25$ (red circles), $\rho_0/\rho = 0.50$ (green squares), and $\rho_0/\rho = 0.75$ (blue diamonds). Also shown is the value of $\ell/2$ during decay for a quasi-condensate with equilibrium state $\rho_0/\rho = 0.25$ (dashed line). Here the quasi-condensate is defined using a cutoff of $k_c = 10\ (2\pi/D)$

the range of temperatures) at a time of $t/\tau = 300$. The choice of time allows us to probe the velocity correlations after the quasi-condensate has formed, but before any significant decay of the vortex tangle has taken place. For the time chosen, the velocity correlation functions are not significantly different for each of our simulation parameters. If the vortex lines are essentially randomly oriented, at distance $r \approx \ell/2$ the velocity correlation should vanish. Indeed, Figure 6.6 (a) shows that at time $t/\tau = 300$ (when we monitor the energy spectrum, and $\ell \approx 30\xi$) the correlation function has become negligible at such distances. The lack of velocity correlation at large scales suggests a lack of vortex bundles (collections of co-rotating aligned vortex lines of the same circulation), theorised to be the driving force of the large scale kinetic energy in quasi-classical turbulence.

The integral scale provides a convenient measure of the distance over which velocities are correlated by producing a scalar value from the velocity correlation function. It is defined as

$$I = \int_0^\infty f(r)\,\mathrm{d}r, \tag{6.6}$$

and is shown in Figure 6.6 (b) evolving over time during the vortex tangle evolution. In all cases, at the time of $t = 5000/\tau$ there remains only a single vortex ring in the system. Three lines corresponding to different temperatures are shown, with each line an average of 5 simulations. The value of I increases as the vortex tangle decays in all of the simulated cases, an expected result as vortices decay and so velocity becomes correlated over larger

regions of space. At early times, $I(0) \approx 0$, reflecting the random nature of the initial tangle. As the tangle decays, the value of I grows, but remains significantly less than ℓ, demonstrating that as the vortex tangle evolves over time, there is no evidence of vortex lines "bundling up" to create a large scale flow. We find that as with the incompressible kinetic energy and decay of vortex line-density, the qualitative behaviour of $f(r)$ and L is largely unchanged by the choice of cutoff. Filtering less modes only has the effect of introducing disorder into the quasi-condensate wavefunction, slightly reducing the exact quantitative values of f and I.

The results of the velocity correlation and integral scale measurements confirm the conclusions of the kinetic energy spectrum measurements, that is, there is no evidence of energy at scales larger than the inter-vortex spacing at any point during vortex decay, at all simulated temperatures. This is perhaps not such a surprising result, the initial vortex tangle is seeded and forms from random fluctuations in the phase of the 3D wavefunction, favouring the random nature of quasi-classical turbulence.

6.5 Moving obstacle at finite-temperature

6.5.1 Critical velocity for vortex nucleation

Having obtained the equilibrated finite-temperature states of the Bose gas, we now move on to consider a laser-induced obstacle moving through the gas. The obstacle, uniform in z, is translated in the x-direction at speed v. Our simulations are conducted moving with the obstacle, transformed into the moving frame as in Section 2.10.1. The obstacle is imposed through a time-independent cylindrical Gaussian potential, as described in Section 2.15.2,

$$V(\mathbf{r}) = V_0 \exp\left(-\frac{x^2 + y^2}{d^2}\right),$$

where d and V_0 parametrise the width and amplitude of the potential. The amplitude is linearly increased from $V_0 = 0$ at first introduction to its maximal value $V_0 = 5\mu$ over a period of 200τ. The frame speed is increased adiabatically to the required value according to the temporal profile $v \tanh(\hat{t}/200\tau)$, where $\hat{t}$ denotes the time from introduction of the obstacle.

Simulations are repeated (from identical initial conditions) with increasing terminal speeds (in steps of $0.057c$) until vortices are detected. Vortex detection is by visual inspection of the filtered density, up to a maximum simulation time $\hat{t} = 500\tau$ (which is long enough to ensure that the obstacle is fully introduced and at terminal speed, but otherwise arbitrary). This procedure defines the critical velocity v_c. There is a systematic uncertainty in our measurement of v_c, arising from the discrete terminal speeds employed. Note that we have repeated this process for multiple randomized initial conditions, and

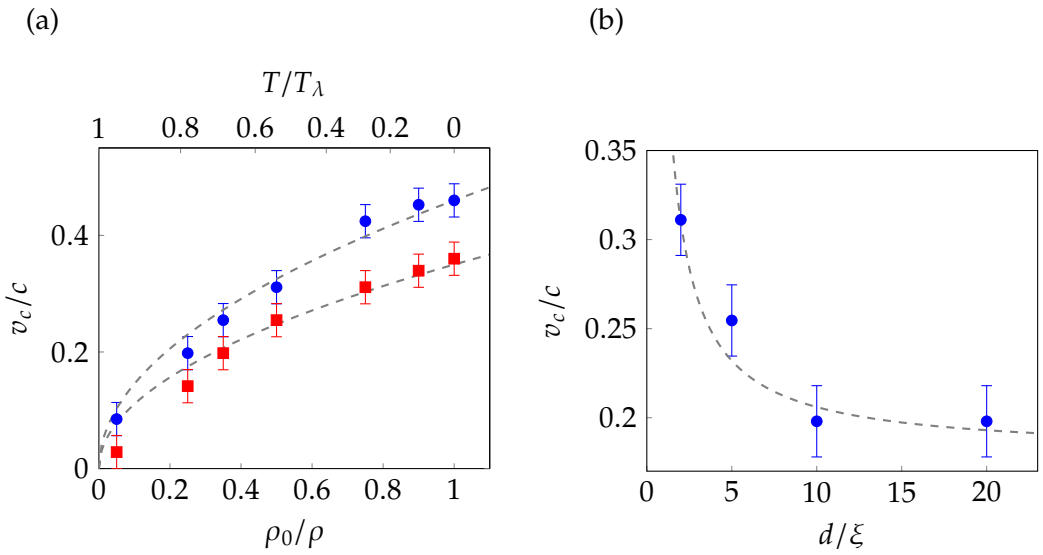

Figure 6.7: (a) Critical velocity v_c for the moving Gaussian-shaped obstacle (uniform in z) as a function of condensate fraction ρ_0/ρ and temperature T/T_λ, for obstacle widths $d = 2\xi$ (blue circles) and $d = 5\xi$ (red squares). The dotted lines show the analytic model $v_c = \beta\sqrt{\rho_0/\rho}$ with fitted coefficients $\beta = 0.46c$ and $0.35c$. (b) The critical velocity approaches an asymptotic value as the obstacle size is increased. Included is a fit of the form $v_c = \alpha/d + \gamma$ with $\alpha = 0.26$ (ξ^2/τ) and $\gamma = 0.18c$. Errors bars represent the systematic uncertainty in v_c due to the discretised values of v considered.

find no change in our measurement of v_c; that is, the systematic uncertainty due to using discretised speeds is larger than the statistical uncertainty arising from different random initial conditions.

Figure 6.7 (a) shows the variation of v_c with both condensate fraction ρ_0/ρ (lower abscissa) and temperature T/T_λ (upper abscissa), for two example obstacles widths. The critical velocity has a maximum value at zero temperature (unit condensate fraction), and decreases nonlinearly as temperature increases (condensate fraction decreases), reaching zero at the critical point for condensation.

At zero temperature, the critical velocity is of the order of the condensate speed of sound $c = \sqrt{\rho g/m}$, with a general form $v_c(T = 0) = \beta c$, where β is a parameter which depends solely on the shape of the obstacle (here d and V_0). The simulated v_c data in Figure 6.7 closely follow the simple functional form $v_c(T) = v_c(0)\sqrt{\rho_0/\rho}$, as shown by the dashed lines. An expression for the critical velocity valid at zero and non-zero temperatures is

$$v_c(T) = \beta\sqrt{\rho_0 g/m}. \tag{6.7}$$

In other words, for a given obstacle, the critical velocity is a fixed fraction of the speed of sound based on the *condensate* density rather than the total particle density [293].

Figure 6.7 (b) shows the variation of v_c with the obstacle width d at finite temperature, for the example of $T/T_\lambda = 0.56$. The qualitative behaviour is consistent with that seen in Chapter 4 at zero temperature [231, 235, 258]: for small d the critical velocity is sensitive to d (due to the prominence of boundary effects) but as d increases v_c decreases towards a limiting value (the Eulerian limit). However, the critical velocities are systematically reduced compared to the zero temperature case due to the reduced condensate speed of sound at finite temperature.

6.5.2 Vortex nucleation pattern

Finally we examine the manner in which vortices are nucleated from the obstacle. At zero temperature, one expects the nucleation of straight anti-parallel vortex lines from the obstacle, either released in unison or staggered in time [148, 193, 258], which move downstream relative to the obstacle. At finite temperature, we observe the loss of vortex symmetry along the obstacle axis, and three general regimes of vortex nucleation, with representative examples shown in Figure 6.8:

Vortex lines A pair of "wiggly" vortex lines is produced [Figure 6.8(a)]. The wiggles are driven by the thermal fluctuations, which cause the vortex elements to be nucleated at slightly different times along the obstacle; this is visible at intermediate times (snapshots (iii) and (iv)). These elements ultimately merge together along the axis of the obstacle to form a wiggly vortex/anti-vortex line. Similar vortex configurations in the form of lines which are partially attached to a thin wire were also observed in liquid helium [294].

Vortex rings Here vortices predominately form vortex rings [Figure 6.8(b)]. The vortex loops generated at the obstacle rapidly peel away from the obstacle, reconnecting with adjacent loops to form rings. Due to the way the vortex rings form initially along the obstacle, they are elliptical and polarised such that they are longer along the obstacle axis.

Vortex tangle Strong interaction between successively nucleated vortices leads to the formation of a complex tangle of vortex lines behind the obstacle [Figure 6.8(c)].

While the vortex line regime is analogous to the zero temperature case, no analogue occurs for the ring and tangle regimes. We note that even a small amount of thermal fluctuations is enough to vastly change the form of vortex nucleation, such as the vortex rings produced in Figure 6.8(c) for a condensate fraction of 0.91.

To systematically map the occurrence of these regimes, we measure the vortex line-density L and vortex polarity R (described below) at a fixed observation time of $\hat{t} = 500\tau$, throughout the parameter space of flow velocity and condensate fraction. The results

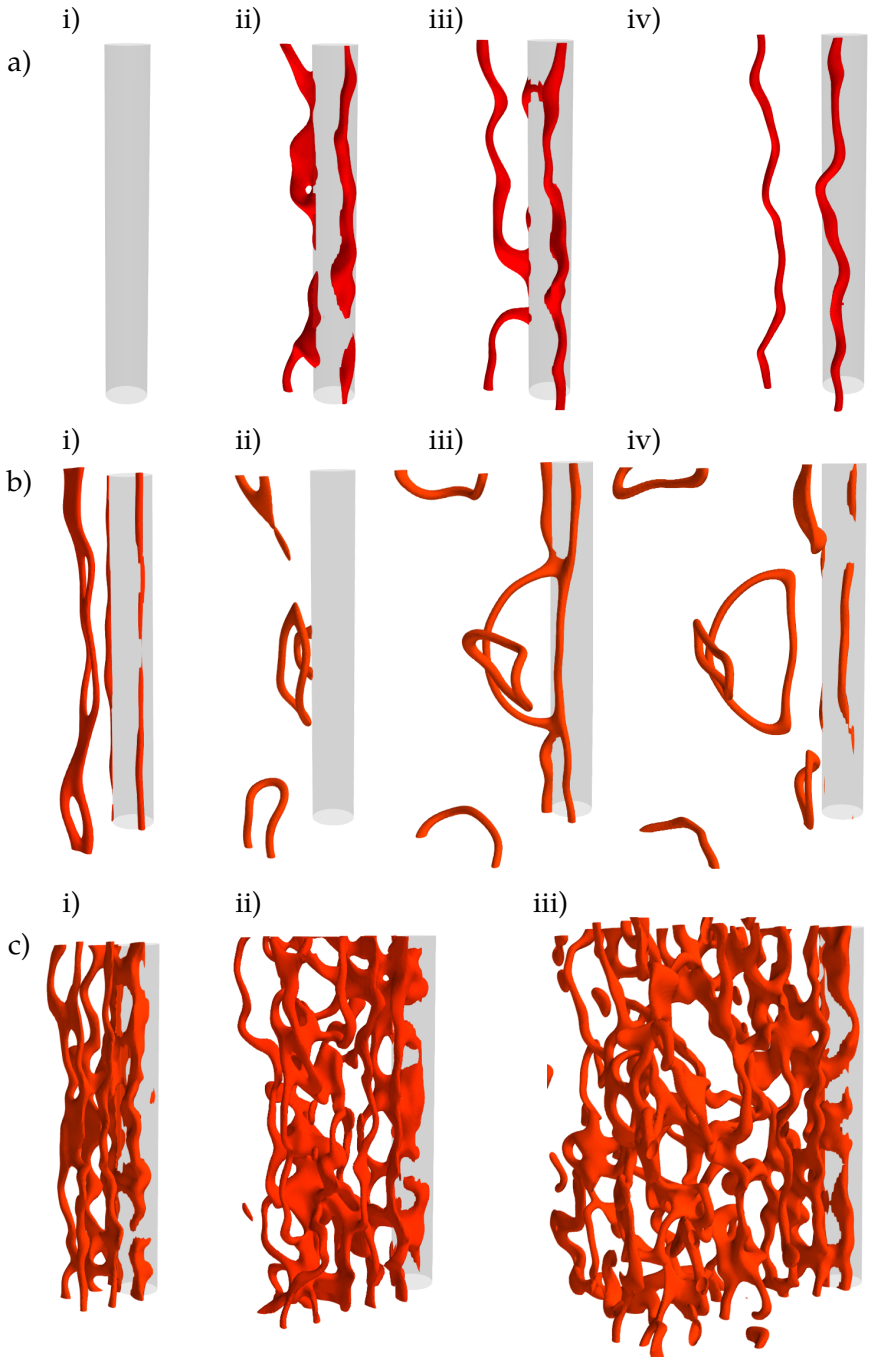

Figure 6.8: Snapshots of the typical vortex nucleation from the moving Gaussian-shaped obstacle with $d = 5\xi$ (gray) in the finite temperature Bose gas. The three cases (a-c) are representative of the behaviour across the whole parameter space. Shown are isosurfaces of the quasi-condensate density ($|\hat{\psi}|^2 = 0.05\langle|\hat{\psi}|^2\rangle$). (a) Vortices are shed as pairs of anti-parallel vortex lines. Here the system parameters are $\rho_0/\rho = 0.25$ and $v = 0.17c$, and the snapshots correspond to times (i) $\hat{t}/\tau = 210$, (ii) 460, (iii) 585 and (iv) 710. (b) Vortex rings are nucleated from the obstacle. The system parameters are $\rho_0/\rho = 0.90$ and $v = 0.42c$, and the times are (i) $\hat{t}/\tau = 500$, (ii) 700, (iii) 875 and (iv) 950. (c) A vortex tangle forms behind the obstacle. The system parameters are $\rho_0/\rho = 0.35$ and $v = 0.59c$, and the times are (i) $\hat{t}/\tau = 250$, (ii) 375 and (iii) 500.

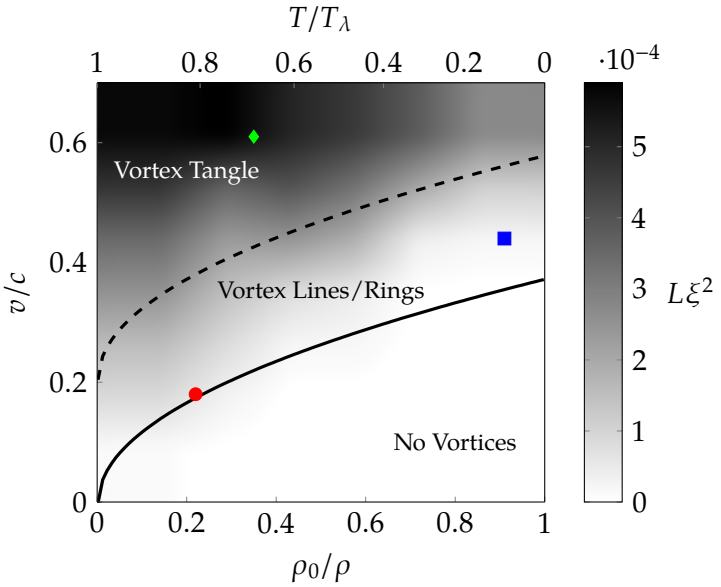

Figure 6.9: Vortex line density L (at an observation time $\hat{t} = 500\tau$) as a function of flow speed and condensate fraction, with the qualitative regimes of vortex nucleation indicated. The markers correspond to the three representative cases shown in Figure 6.8(a) [red circle], (b) [blue square] and (c) [green diamond]. This line length density data, obtained from 36 simulations, has been interpolated. The obstacle has size $d = 5\xi$.

are presented in Figure 6.9. Below the critical velocity (solid black line) no vortices are produced, and thus $L = 0$. Above the critical velocity, L increases strongly with the flow velocity. This is to be expected since the frequency of vortex nucleation increases with flow velocity [148]. L also increases with decreasing condensate fraction (increasing temperature), indicating the significant role of thermal fluctuations in enhancing vortex production.

Just above the critical velocity, where the vortex line-length density is relatively small, vortex nucleation occurs through vortex lines and rings. The low flow velocity ensures that the vortex nucleation frequency is low, thereby suppressing strong interaction or reconnection between nucleated vortices. Here, whether lines or rings are produced is sensitive to the random initial conditions, and so it is not possible to further distinguish these nucleation regimes within this parameter space. In these cases a more consistent characterisation of the vortex form is given by R, described below. At higher flow velocities, where the vortex line-length density is relatively high, the nucleation frequency becomes sufficiently high that vortices immediately undergo strong interactions with each other, reconnecting and developing into a vortex tangle. The transition in the parameter space from vortex lines/rings to tangles is indicated approximately by the dashed line, although statistical effects blur the true boundary.

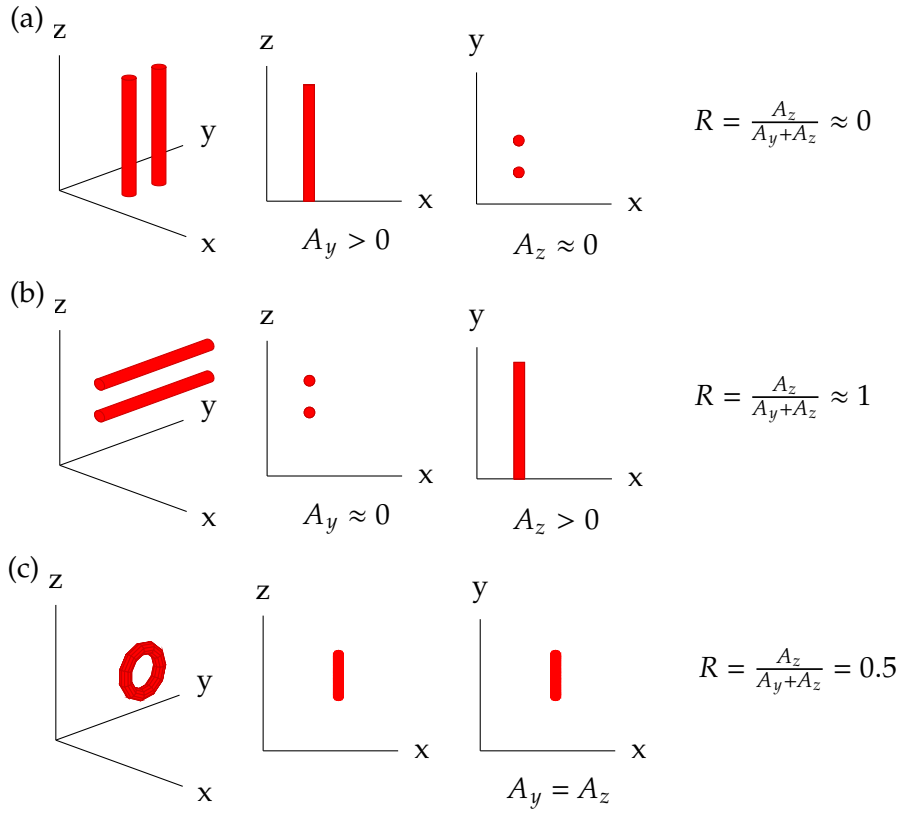

Figure 6.10: Schematic of the vortex polarisation, $R = A_z/(A_y + A_z)$, where A_y and A_z are the total area of vortices when the vortex distribution is projected along the y and z directions, respectively. (a) Vortex lines aligned predominantly along the z axis. (b) Vortex lines aligned predominantly along the y axis. (c) A vortex ring lying in the yz plane.

We further characterise the vortex distribution by its polarisation through the quantity $R = A_z/(A_y + A_z)$, where A_y and A_z are the total area of vortices when the vortex distribution is projected along the y and z directions, respectively. A value $R \approx 0$ corresponds to vortex lines aligned predominantly along the z axis, $R \approx 1$ corresponds to lines aligned predominantly along y, and $R \approx 0.5$ corresponds to an isotropic vortex distribution (in the yz plane). These three cases are demonstrated in Figure 6.10. When measured at the same fixed observation time of $\hat{t} = 500\tau$, the parameter space of R has the same qualitative form as that for L, increasing with velocity and decreasing with condensate fraction. R typically lies in the range $0.1 \lesssim R \lesssim 0.4$ for the lines/rings regime, consistent with the presence of lines which are predominantly aligned along z and rings which are elongated along z. It is worth noting that while the occurrence of lines or rings, for a given flow velocity and condensate fraction, is sensitive to the initial conditions, the value of R is highly reproducible (to within a few percent). For the vortex tangle regime, $0.4 \lesssim R \lesssim 0.5$. It is worth noting that this shows that the produced tangle can be highly isotropic, despite two-dimensional nature of the obstacle that generates it.

6.6 Conclusions

Using classical field simulations, we have modelled a finite temperature homogeneous Bose gas, studied the character of the resulting turbulent vortex tangle and analysed the nucleation of vortices past a moving cylindrical obstacle.

We evolved the classical field from highly non-equilibrium initial conditions, through vortex tangle decay, to thermalized equilibrium states with ranging temperatures and condensate fractions. We have found a kinetic energy spectrum that demonstrates a *lack* of quasi-classical turbulence, and through tracking the vortex line-density over time, we find a decay characteristic of ultra-quantum turbulence for certain system parameters. We have studied the velocity correlation function and integral scale to find no evidence of large scale coherence, again consistent with ultra-quantum turbulence. This is in contrast to previous investigations [143, 144] in which quasi-classical spectra were observed. We note that these studies differ from ours in fundamental ways. In the case of Kobayashi *et. al.* dissipation was applied at small scales dynamically throughout the simulation, as opposed to the post-processing filter we employ. In the case of Nore *et. al.* the initial condition was that of Taylor-Green flow, a state significantly different from our highly random and non-equilibrium initial conditions.

With the resulting equilibrium states we have inserted a cylindrical obstacle with Gaussian profile into the system, and imposed a flow relative to the gas. We have found that, above the critical velocity, vortices are nucleated forming wiggly anti-parallel pairs of vortex lines, vortex rings, or as a vortex tangle.

The critical velocity decreases with increasing temperature, becoming zero at the critical temperature, and scales with the speed of sound of the condensate, i.e. as the square root of the condensate fraction.

Chapter 7

Flow past a rough surface

7.1 Introduction

At sufficiently low temperatures, liquid helium has two striking properties. Firstly, it flows without viscosity, and secondly, its vorticity is constrained to thin quantised vortices, characterised by their fixed circulation h/m (the ratio of Planck's constant to the mass of the relevant boson - one atom in ^{4}He and one Cooper pair in ^{3}He-B) and microscopic core radius ξ (0.1 nm in ^{4}He and 10 nm in ^{3}He-B). This is in contrast to the eddies observed in everyday viscous fluids, which can have arbitrary shape, size and circulation.

Of ongoing experimental and theoretical study is the nature of turbulence in superfluids [295, 138, 142, 140], a state dominated by an irregular tangle of the quantised vortex lines. Despite the fundamental differences between superfluids and classical fluids, the observation of Kolmogorov energy spectra (made famous in the context of classical isotropic turbulence) in superfluid turbulence [295] are suggestive of a deep connection between them. Superfluid turbulence is at present most commonly formed by moving obstacles, including grids [153, 190], wires [154–156], forks [158, 159], propellers [160, 161], spheres [157] and other objects [162]. Despite progress in visualizing the flow of superfluid helium in the bulk [142, 296], including individual vortex reconnections [112], there is little direct experimental evidence about what happens at boundaries. Here vortices are believed to be generated by two mechanisms. Firstly, they can nucleate at the boundary of the vessel or object. When the relative flow speed is sufficiently low, the flow is laminar (potential) and dissipationless. Near curved boundaries, however, vortex nucleation occurs if the local flow velocity exceeds a critical value. Secondly, the vortices can be procreated from so-called 'remanent vortices' which are present in the system since cooling the helium through the superfluid transition. Note that remnant vortices can be avoided using judicious, slow experimental protocols [297].

The nano-scale vortex core in superfluid helium is comparable in size to the typical

roughness of the boundaries of the vessel or stirring object. Unfortunately, the lack of direct experimental information about vortex nucleation at the boundaries and the subsequent vortex-boundary interactions limit the interpretation of experiments. Theoretical progress is challenging and to date has focussed on smooth and idealised surfaces. In principle, the superfluid boundary conditions are straightforward: the superfluid velocity component which is perpendicular to the boundary must vanish at the boundary, whereas the tangential component (in the absence of viscous stresses) can slip. For the latter reason, we do not expect boundary layers, typical of viscous flows. Implementing these superfluid boundary conditions, Schwarz [298] and Tsubota [299] found that one or more vortices sliding along a smooth surface can become deflected or trapped by a small hemispherical bump. Such bumps can also serve as nucleation sites for vortices; the local superfluid velocity is raised at the pole of the bump and more readily breaks the critical velocity for vortex nucleation [245]. Moreover, simulations detailed in Chapter 4 reveal that if the bump is elliptically shaped and elongated perpendicular to the imposed flow, the superfluid velocity at the pole is enhanced, reducing the critical velocity for vortex nucleation and increasing the vortex nucleation rate (for a given super-critical imposed flow). We expect therefore that microscopically-small surface roughness may promote the nucleation of vortices at a surface. For pre-existing vortex lines in the vicinity of the surface, there is also indirect experimental evidence of a 'vortex mill' mechanism which continuously feeds vorticity into the flow by stretching the existing vortex lines. This mechanism has been shown to work when the spooling vortex, held by pinning sites at the surface, is aligned in the streamwise direction [300].

7.2 Method

To shed light on the microscopic behaviour of superflow near a rough boundary, we work with the three-dimensional profile of a real surface, shown in Figure 7.1. This corresponds to one square micron region of the surface of a thin NbTi wire used to generate quantum turbulence at Lancaster University, as profiled via atomic force microscopy (AFM) [168]. The surface is rough, with a height up to around 15 nm, and features sharp grooves and steep ridges, likely to have arisen during the etching phase of the wire preparation. We assume that such features are typical of the wires and similar objects used across other superfluid turbulence experiments.

Traditionally, the Vortex Filament Model (VFM) [301] has been used to model the motion of vortex lines in the presence of smooth spherical [302, 303], hemispherical [298, 299] and cylindrical boundaries [304, 227]. However the model is unsuitable for our purposes for several reasons. Firstly, it assumes that the vortex core is infinitesimal compared to any other length scale, which is not the case if the vortex core size and wall roughness are

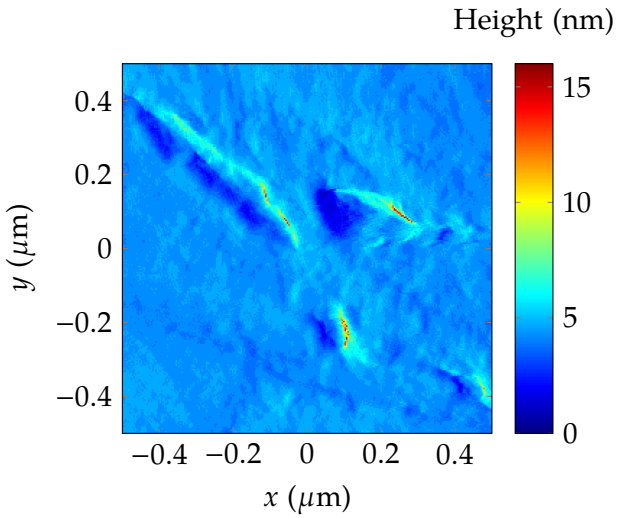

Figure 7.1: AFM image of a section of the NbTi wire used to generate turbulence in superfluid helium at Lancaster University (data provided by R. P. Haley and C. Lawson).

comparable. Secondly, microscopic behaviours such as vortex nucleation and the loss of vortex energy to sound emission are not captured in the model. For example, VFM requires the arbitrary seeding of vortex loops in order to generate turbulence, and sound emission during reconnection events and through Kelvin waves is neglected. Thirdly, it is difficult to generalise from smooth, geometrically simple (cylindrical or spherical) boundaries to the rough boundaries which interest us.

Another approach which suffers similar difficulties [305] is the Hall-Vinen-Bekarevich-Khalatnikov (HVBK) equations [306, 307]. The approach is a two fluid model, with an inviscid Euler superfluid component and a Navier-Stokes normal fluid component. The two fluids are coupled via a mutual friction which depends on a coarse-grained vorticity, defined by the local density of superfluid vortex lines. As multiple vortices contribute to the vorticity, the HVBK equations are coarse-grained over length scales larger than the average vortex separation, and so the boundary conditions require further assumptions or the introduction of unknown sliding/pinning parameters.

We instead model the flow of superfluid helium over this surface through the Gross-Pitaevskii equation (GPE) [170] for a weakly-interacting Bose superfluid, as described in Chapter 2. The GPE is equivalent to a hydrodynamic model with fluid density $n(\mathbf{r}, t) = |\psi(\mathbf{r}, t)|^2$ and local velocity $\mathbf{v}_{\mathrm{loc}}(\mathbf{r}, t) = (\hbar/m)\nabla\theta$, and embodies a classical continuity equation and a modified Euler equation (the modification being the presence of a quantum pressure term, arising from zero-point motion of the particles and is responsible for vortex nucleation). Further details of the hydrodynamic description of the GPE can be found in Section 2.6. While the GPE provides only a qualitative model of the strongly-interacting superfluid helium (for example, the excitation spectrum of the GPE lacks helium's ro-

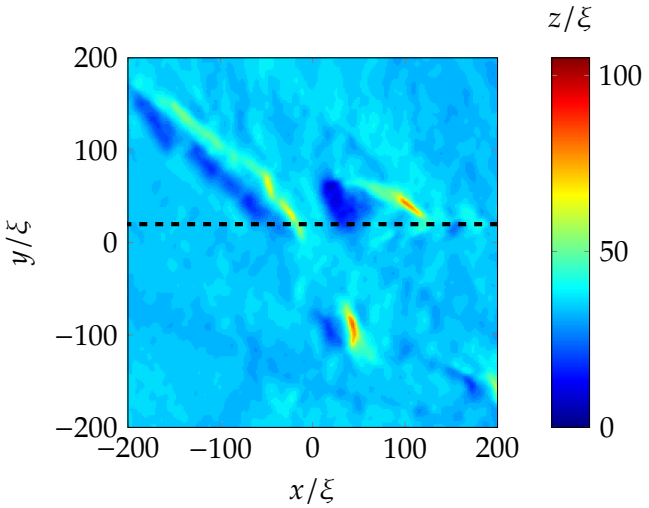

Figure 7.2: AFM image of a section of the NbTi wire rough surface, mapped into the computational coordinate system and smoothed by a Gaussian blur (standard deviation 6 nm) so as to remove discontinuities in the surface profile. The profile used in our 2D simulations ($y = 0.05\,\mu$m) is marked by a dashed line.

ton minimum), it nevertheless contains the key microscopic physical ingredients of our problem: a finite-size vortex core, vortex-boundary interactions, and vortex-vortex reconnections [170]. Furthermore, any boundary, however irregular, can be conveniently modelled through the potential term $V(\mathbf{r}, t)$ in the GPE.

The GPE model is numerically simulated in the homogeneous form as described in Section 2.8.1, and so in this chapter we report quantities scaled by the natural units: the vortex core size is characterised by the healing length $\xi = \hbar/\sqrt{m\rho g}$ and the natural speed, energy and time scales are provided by the speed of sound $c = \sqrt{\rho g/m}$, the chemical potential $\mu = \rho g$ and the unit $\tau = \xi/c$, respectively.

Our results are based on intensive simulations of the GPE over the entire AFM surface, resolved down to a sub-core scale of $\Delta = 0.4\xi$. In ^{4}He the vortex core size is $a_0 \approx 10^{-10}$ m [308], such that the AFM image has true core dimensions $(10^4 \times 10^4 \times 100)a_0^3$. It is not computationally feasible to model the corresponding range of scales directly within the GPE; as such we map the AFM image onto the largest practical healing length volume of $(400{\times}400{\times}100)\xi^3$. This is simulated in a box of size $(400{\times}400{\times}200)\xi^3$, on a $1000{\times}1000{\times}500$ spatial grid, which is periodic in x and y. The boundary condition near $z = 0$ is the profile of the surface, and a hard wall boundary is implemented at $z = 200\xi$. The numerical domain is twice as high as the highest point of the data in the third dimension. We find this domain adequate to avoid finite size effects; the region of interest is near the AFM surface, and the results of vortex lines interacting with the $z = 200\xi$ boundary do not significantly affect this region.

We smooth the original AFM data with a Gaussian blur (standard deviation 6 nm),

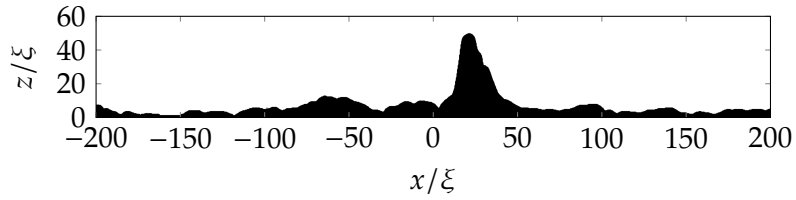

Figure 7.3: The 2D rough surface profile that we employ in our two-dimensional simulations. The surface is taken from the full AFM data so as to capture one of the 'mountain' features present on the surface. The data is mapped onto our computational coordinate system as described in Section 7.2 and the exact mapping is shown here.

so as to remove discontinuities in the surface profile, with the result shown in Figure 7.2. The rough surface is then incorporated into the GPE by setting a potential barrier $V = 5\mu$ below the surface, heavily prohibiting density there; above the surface (where $V = 0$) the density recovers to the bulk value ρ over a length scale of the order of ξ. Section 2.15.3 describes the form of V we use in further detail. Additionally, in all our simulations the zero level of the z dimension is arbitrarily shifted so that the minimum height of the two or three-dimensional surface profile is at the level $z = 0$, so as to optimise use of the computational box. The time evolution algorithm is the 4th order Runge-Kutta scheme described in Section 3.1.1 with time step $\Delta_t = 0.01\tau$, and is performed across 256 (2.6 GHz) cores of a high-performance computer cluster.

Our three-dimensional simulations model the entire rough surface by using the entire AFM data provided to us, imposed as a potential. However, in the interests of effective exploration of the parameter space, we also perform some simulations in reduced dimensionality. Here we simulate only a single row of the AFM data (marked in Figure 7.2 and shown in detail in Figure 7.3) using the 2D-GPE, ignoring the y dimension. The selected row was chosen so as to contain a two-dimensional analogue of the steep prominences found along the wire's surface.

We first obtain the stationary solution of the GPE in the presence of the rough boundary, with bulk density ρ. The GPE is then transformed into the frame moving at speed v in the x-direction (equivalent to an imposed flow in the opposite direction) by the addition of a Galilean boost term $i\hbar v\partial\Psi/\partial x$ to the right-hand side of the GPE, as described in Section 2.10.1. The flow speed is ramped up smoothly from zero to the final value of v.

7.3 Two-dimensional results

We begin by focusing on our two-dimensional simulations. For the surface depicted in Figure 7.3, we find the critical velocity for vortex nucleation to be $v_c = (0.125 \pm 0.025)\, c$. This is significantly less than the critical velocity for a circular obstacle (which has a critical velocity of $v_c \approx 0.36\, c$ [230, 258, 270] in the Eulerian limit (obstacle diameter $d \gg \xi$). This

result shows that the effect described throughout Chapter 4 is also occurring for the sharp feature protruding from the rough surface. The location acts as a nucleation site due to the high curvature, which induces a high local fluid velocity, and so Landau's criterion is broken here before anywhere else in the system. We will refer to such structures that induce this property as 'mountains'.

7.3.1 Vortex nucleation

Early-time vortex nucleation

At early times the resulting flow depends on the velocity of the imposed fluid flow. Below the critical velocity, the fluid undergoes smooth potential flow around the surface. The instantaneous streamlines of this flow, demonstrated in Figure 7.4(a), vary smoothly around the surface with streamlines far away from the surface straight and unaffected by the roughness, and streamlines near the surface showing high curvature.

At velocities above the the critical velocity, a series of vortices nucleate from the peak of the highest mountain. The circulation of the vortices produced in the wake of the mountain will depend on the direction of the imposed flow. In our simulations the flow is in the negative x direction and so the produced vortices have positive circulation.

The strength of the imposed flow affects the vortex nucleation frequency, so that for larger flow velocities more vortices are produced in a given time period. This is confirmed by measurement of N_v at different flow velocities, shown in Table 7.1 for this and modified surfaces. For velocities just higher than the critical velocity, vortices nucleate from the mountain at low enough frequency that they fall downstream and do not interact significantly. For high velocities, however, many vortices nucleate in close proximity and interact strongly with one another. Vortex co-rotation is induced and this leads to the vortices combining into a larger-scale cluster of positive circulation. Figure 7.4 shows the early vortex configuration for different imposed flow speeds.

		v					
		0.15	0.25	0.35	0.45	0.55	0.65
β	1	3	19	42	69	120	176
	0.7	0	4	21	54	85	107
	0.5	0	0	13	32	60	94
	0.4	0	0	0	18	43	53

Table 7.1: Number of vortices, N_v, measured in the fluid at $t = 3000\tau$ over the 2D parameter space. A blue (red) shading labels the existence (lack of) a boundary layer in the resulting system.

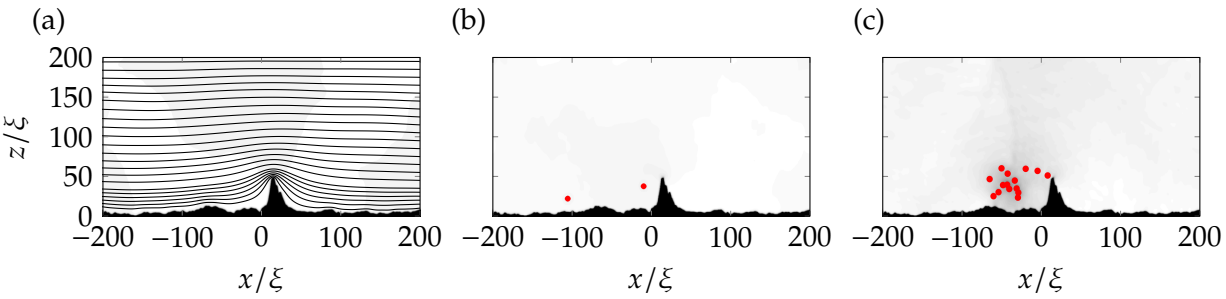

Figure 7.4: Early time evolution of 2D flow past the rough surface for flow speeds (from left to right) of $v = 0.10, 0.15, 0.35\,c$. Depicted are snapshots of density and vortex locations at time $t = 500\tau$. Red (blue) symbols represent vortices of positive (negative) circulation. Instantaneous streamlines of the system velocity are also shown in (a).

Secondary clusters

For the case where vortices combine into a larger-scale cluster, an interesting effect occurs. Close to the surface, the combined velocity field of the cluster induces a relatively large local velocity in the opposite direction to the imposed flow. This induces a secondary generation of vortices from smaller-scale surface prominences. The secondary vortices are of opposite circulation to the cluster that induced them (in our case, negative circulation) and also form a new vortex cluster. As this cluster grows, the velocity field that caused the effect is cancelled out, leading to a cessation of secondary vortex production. Figure 7.5 demonstrates the production of a secondary cluster of negative circulation vortices in a simulation with $v = 0.35\,c$. Note that the generation of secondary clusters is significantly enhanced if the surface is rough downstream of the mountain; if the surface is perfectly smooth downstream, the local velocity must exceed the speed of sound to generate new vortices. With surface roughness the local curvature vastly reduces the velocity requirement so that the velocity generated by a vortex cluster can induce further nucleation. We also note that it is possible to generate tertiary vortices/clusters; these arise when the secondary cluster induces a sufficiently high flow speed to generate even further vortices from the local surface roughness. Secondary and tertiary vortex nucleation is shown in detail in Figure 7.6, with a schematic overlay describing the process.

Truncated surfaces

It is evident by the snapshots shown in Figure 7.4 that the vortex generation is dominated by the large single mountain in the surface. Tall surface prominences lead to a large local curvature and so induce a large local velocity, in analogy to the elliptical obstacles featured in Chapter 4. For this reason it can be reasoned that even if the imposed flow v has a high enough velocity that the smaller provinces also act as vortex nucleation sites, the mountains that lead to the largest curvature will induce the highest local velocity and

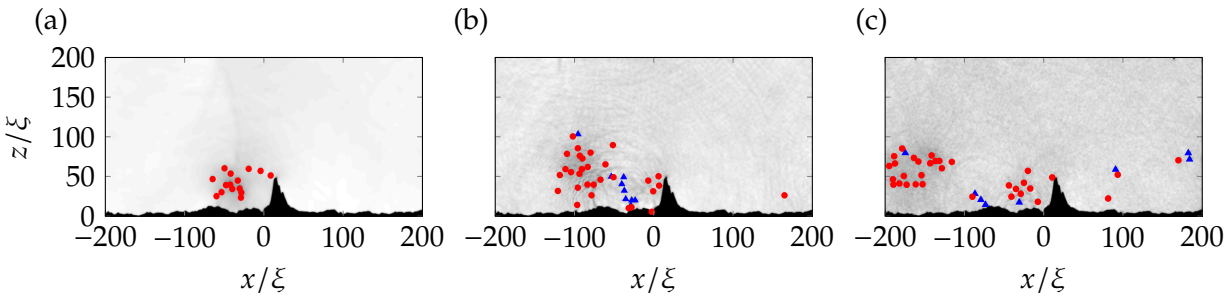

Figure 7.5: Evolution of 2D flow past the rough surface for a flow speed of $v = 0.35c$. Depicted are snapshots of density and vortex locations at times (from left to right) $t = 500$, 1580, and 2100 τ. Red (blue) symbols represent vortices of positive (negative) circulation.

vortex nucleation frequency, and so will always be the main producer of vorticity.

To further analyse how the height of the mountains affects fluid flow in the vicinity of a surface, we now describe how the situation changes with truncation of the mountain height, to a percentage β of the maximum height h_0, i.e. $h(x, y) \to h(x, y)H(z/h_0 = \beta)$, where $H(z)$ is the Heaviside step function ($\beta = 1$ corresponds to no truncation, $\beta = 0$ corresponds to complete truncation). For the AFM image we use, this truncation can be thought of as a way of varying surface roughness by removing the sharpest features.

Figure 7.7 shows snapshots (at fixed time) for various levels of truncation β, with all cases having the same flow speed $v = 0.35\,c$. We are immediately able to see that the height of the mountain plays a critical role in both the critical velocity and vortex nucleation frequency, as expected. Even when the mountain is capped as little as to 0.7 of its maximal height, the number of vortices produced is visibly reduced. The vortices are generated at a sufficient frequency that secondary vortices are still formed, but in a lower quantity. For $\beta = 0.5$ even fewer vortices are produced, and for this case no clustering takes place and in turn no secondary vortices are formed. For $\beta = 0.4$ no vortices are generated at all; the

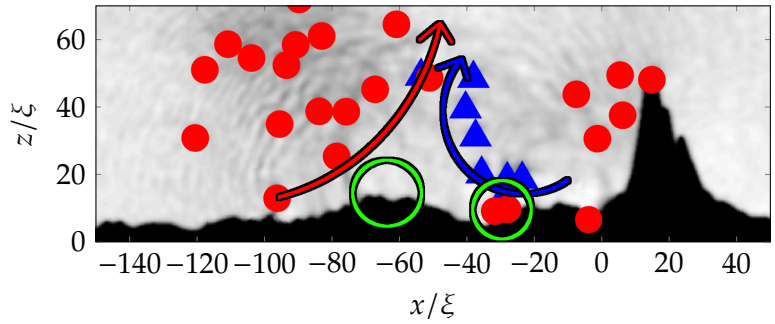

Figure 7.6: Snapshot of fluid density and vortex locations at time $t = 1580\,\tau$ with $v = 0.35\,c$, demonstrating secondary and tertiary vortex nucleation. Red (blue) symbols represent vortices of positive (negative) circulation. The direction of the vortex cluster velocity field is labelled with red and blue arrows, with the secondary and tertiary nucleation sites circled in green.

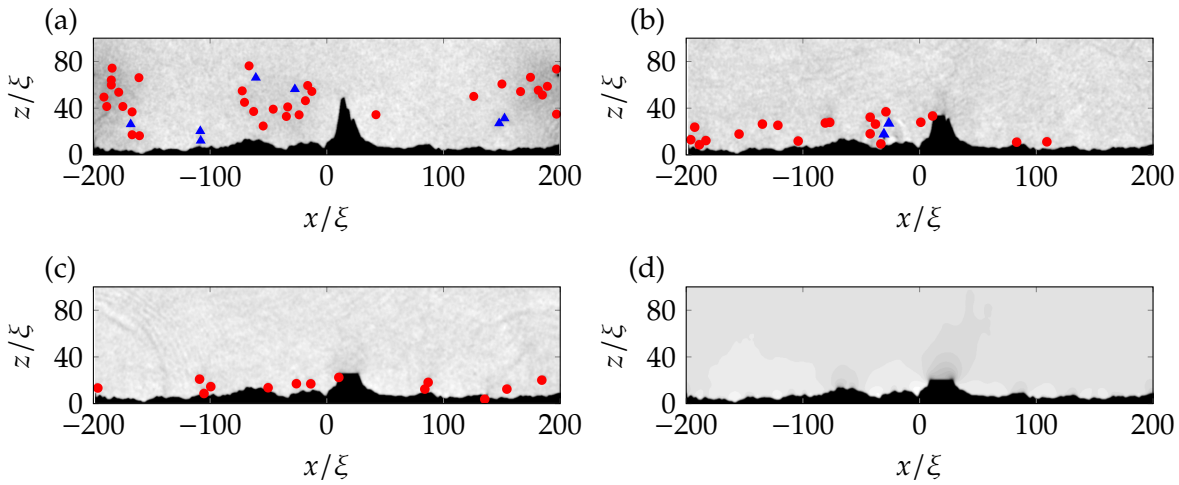

Figure 7.7: Same-time density snapshots for flow speed is $v = 0.35\,c$, time $t = 2440\tau$ and various levels of surface truncation: (a) $\beta = 1$, (b) $\beta = 0.7$, (c) $\beta = 0.5$ and (d) $\beta = 0.4$, where β represents the truncation height relative to the highest point in the surface. Vortices with positive (negative) circulation are labelled with red (blue) markers.

reduction in height has increased the critical velocity so that $v_c > v$.

7.3.2 Two-dimensional boundary layer

Consider Figures 7.4, 7.5 and 7.7. Notice that in all depicted cases the average height of the vortices is of the order of the highest mountain in the surface of the wire. We find for many cases throughout the parameter space that the vortices, whether as single points or as clusters, self organise in the vicinity of the surface, forming a primitive two-dimensional boundary layer with thickness on the scale of the height of the highest mountain.

In addition to the collection of vortices near the surface, for the cases where secondary clusters are formed vortex-antivortex pairs are able to pair together. In this case, they are two-dimensional analogue of vortex rings and so travel in the positive z direction, away from the boundary layer and into the bulk.

We now quantify the prevalence of the boundary layer throughout the parameter space of the system by studying the vortex distribution at late times. We define whether a boundary layer has formed in the following way. At $t = 3000\tau$ (our maximum 2D simulation time) we measure the vortex distribution. If the median vortex height is less than the height of the tallest mountain, we say the vortices have formed a boundary layer (we employ the median here as the distribution of vortex height is skewed in the positive z direction by the relatively small number of escaping vortex rings). If the median vortex height is larger than the height of the tallest mountain, we say a boundary layer has not formed. Figure 7.8 shows both cases, as well as a histogram of vortex height with the resulting median vortex height indicated for each case.

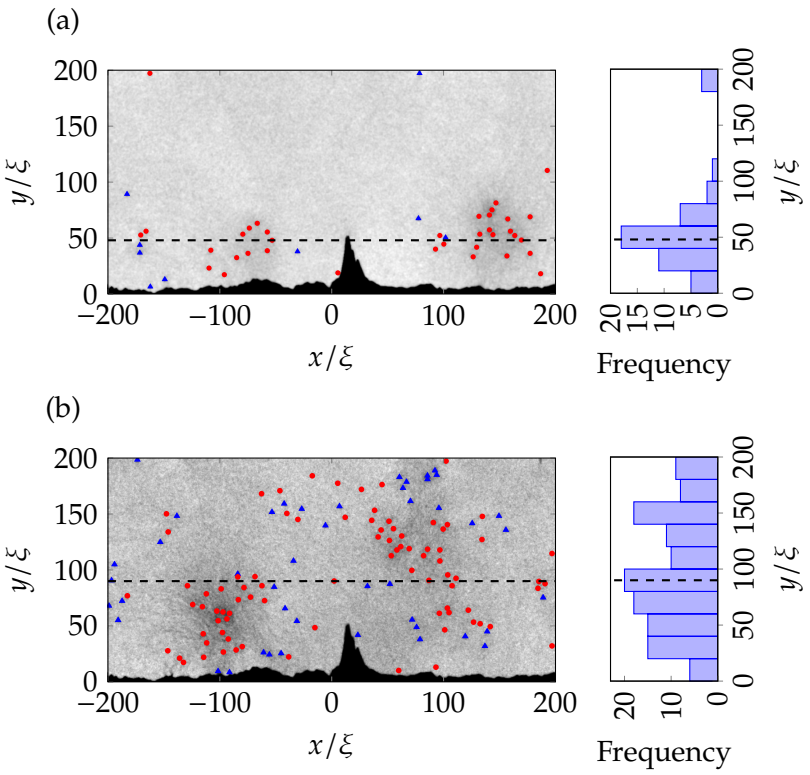

Figure 7.8: (Left) Density snapshots for flow speeds (a) $v = 0.35\,c$ and (b) $v = 0.55\,c$, at time $t = 3000\tau$. Vortices with positive (negative) circulation are labelled with red (blue) markers. (Right) Histogram of vortex height with the median height shown as a black dashed line. If the median height is less than the height of the highest point of the surface, we say a boundary layer has formed.

We perform simulations for a variety of truncation heights and flow velocities with the results shown in Table 7.1. Note that the boundary layer effect is not universal, for higher velocities the vortex distribution instead fills the computational box. For low (but still super-critical) velocities, the vortices are distributed in agreement with a boundary layer, but with a reduced density of vortices.

7.4 Three-dimensional results

We now move on to focus on the three-dimensional case, modelling the 3D surface by utilising the entire AFM data set. Due to the large computational requirements of a fully 3D numerical simulation of the scale required, only the full height surface (no truncation) for only a few velocities is performed.

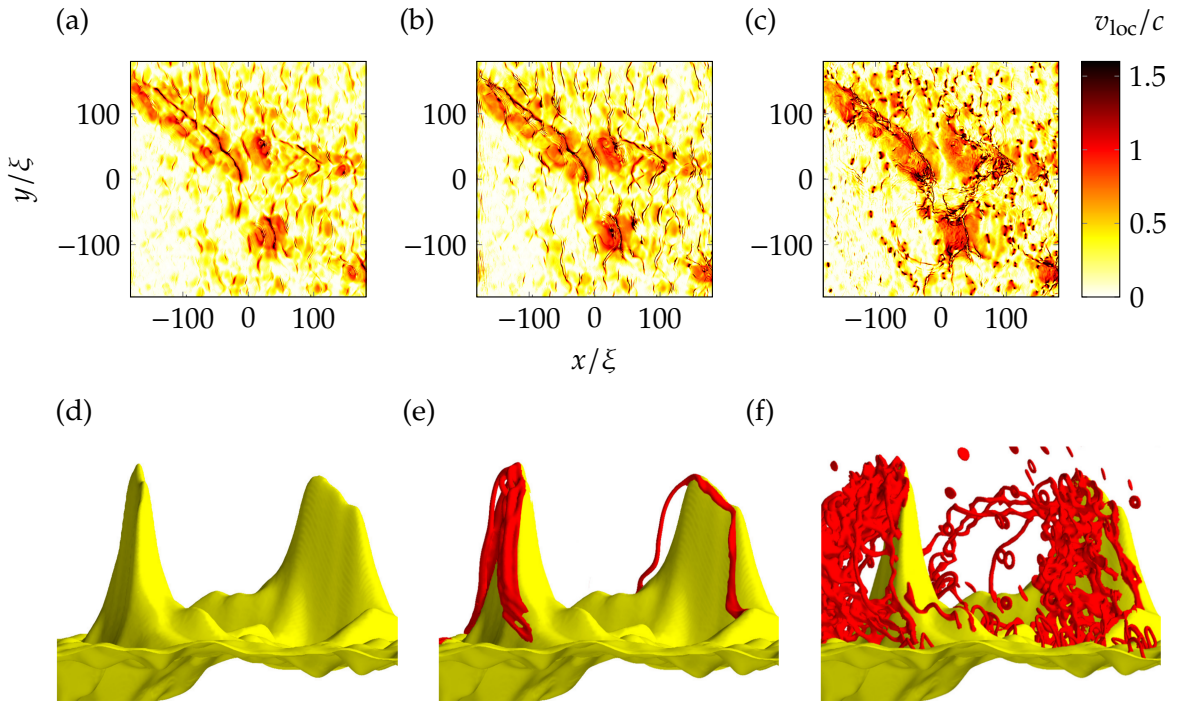

Figure 7.9: (a-c) Magnitude of the local fluid speed, $v_{\mathrm{loc}} = |\mathbf{v}_{\mathrm{loc}}|$, shown in the xy-plane and computed just above the surface (where the density drops to 10% of the bulk density), at three times $t = 20, 30, 100\,\tau$ with $v = 0.6\,c$. (d-f) Zoomed isosurface plots of density $n(\mathbf{r}, t)$ (plotted at 25% of the bulk density), showing the surface (yellow) and vortices (red) in the vicinity of the two tallest mountains (view taken along y over the x-range $15\xi \leq x \leq 125\xi$) at the same times.

7.4.1 Vortex nucleation from the surface

In similarity to the two-dimensional case, in the vicinity of the surface the local fluid speed, $v_{\mathrm{loc}} = |\mathbf{v}_{\mathrm{loc}}|$, is enhanced considerably by the surface roughness, with maximum speeds occurring near the tallest mountain. This can be seen through inspection of the local velocities near the surface, shown for several points in time in Figure 7.9 (a-c). Throughtout the simulation the areas of highest velocity occur near the surface prominences seen in Figure 7.2.

As expected, up to a critical imposed velocity, the flow remains laminar and free of vortices. The critical velocity for vortex nucleation across this particular surface occurs for an imposed flow of $v_c \approx 0.2c$; this is considerably smaller than, say a hemispherical bump for which $v_c \approx 0.5c$ [245], indicating the significant role of the surface roughness in enhancing the breakdown of laminar flow, similarly to the two-dimensional case. For an increased imposed flow velocity of $v = 0.6\,c$, the critical velocity is first exceeded at the highest mountain, leading to nucleation of vortex lines, shown in Figure 7.9 (e), and then by other high mountains on the surface.

Nucleated vortices either peel off the boundary, or, more frequently, slide down the

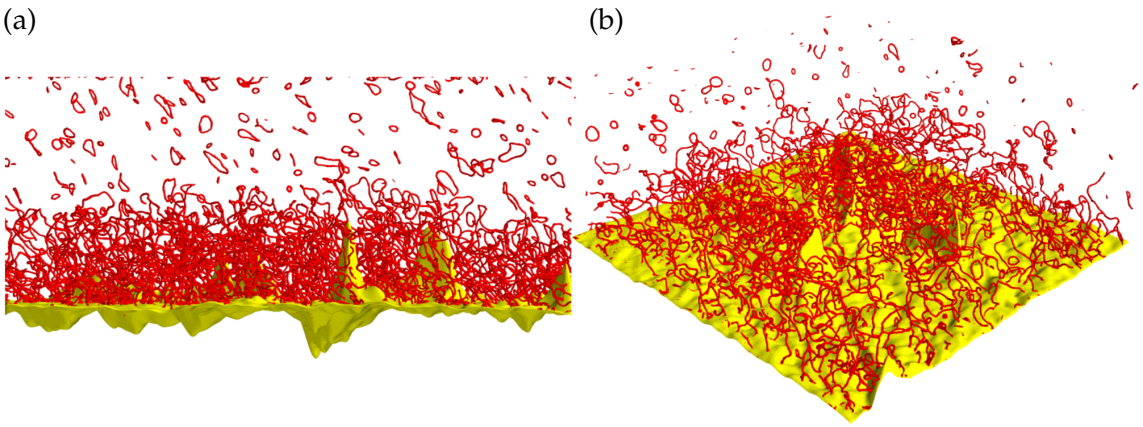

Figure 7.10: Instantaneous isosurfaces of density $n(\mathbf{r}, t)$ (plotted at 25% of the bulk density) showing the surface (yellow) and vortices (red) for a super-critical flow ($v = 0.6c$) in the saturated turbulent regime reached at long times ($t = 1220\tau$). Notice the turbulent boundary layer up to approximately the height of the highest mountains and the region of small vortex rings above it.

slopes of the mountains in the form of partially attached vortex loops (carried by the imposed flow). Nucleated vortex loops are of the same orientation and so form clusters (manifesting as partially attached vortex bundles) on the leeward side of the mountains.

The combined velocity field of the vortex bundles along with nucleation of small vortex loops throughout the surface causes an increase and spreading of areas with high local velocity near the surface, visible in Figures 7.9(b, c). The velocity field causes vortex stretching and further vortex nucleation, distorting the organised bundles of vortices and small rings into a complex tangle downstream of the mountains. The resulting tangle is continuously fed by further vortices nucleated from the surface. Vortex bundles and the beginnings of such a tangle can be seen in Figure 7.9(f). The fully developed vortex tangle in the vicinity of the surface is demonstrated in Figure 7.10.

7.4.2 Three-dimensional boundary layer

We focus on our 3D simulation with an imposed flow speed of $v = 0.6\,c$. For this combination of surface and flow speed, as the number of vortices increases the complex turbulent region of vortex lines remains strongly localised to the vicinity of the surface, up to approximately the height of the highest mountain. The distribution of vortices can be seen to form a distinct layer, visible in the lower half of Figure 7.10 (a). In addition to the visible layer, reconnections due to the interaction of neighbouring vortex lines causes a continuous ejection of vortex rings which spread into the bulk, visible in the upper part of Figure 7.10 (a-b).

The turbulent layer and ejected vortex rings are not isotropic: on average, vortex lines are flattened parallel to plane of the surface and the ejected vortex rings lie more in the

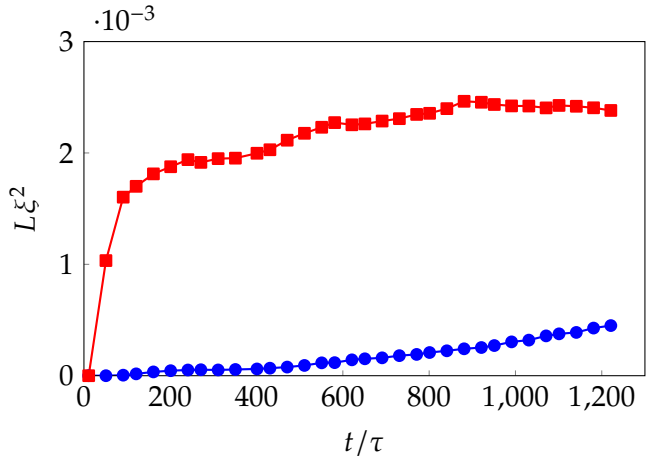

Figure 7.11: Vortex line-density below (L_0, red squares) and above (L_1, blue circles) the height of $z = 100\xi$, approximately the height of the tallest mountain, for a 3D simulation with imposed flow speed of $v = 0.6\,c$.

xy plane (so that they travel vertically away from the layer). For the slower, but still supercritical, imposed flow with speed $v = 0.2\,c$ the turbulent layer still forms with the same height, albeit with reduced density of vortices, generalising the behaviour of the boundary layers that formed in our 2D simulations.

Vortex line-length density

As the layer of vortices forms, the vortex line-length in the vicinity of the boundary increases with time at a much faster rate than in the bulk. However, once the layer has covered the entire computational surface, the vortex line-length within the boundary layer approximately saturates. Vortex rings continue to be ejected from the layer, and so the vortex line length in the bulk continues to slowly grow.

We quantify this behaviour by monitoring vortex line-density below and above the height of the highest mountain, L_0 and L_1 respectively. By measuring line-density in this way we are able to ascertain two things. Firstly, we will be able to measure the boundary layer's vortex line-density over time, so as we can say when the layer has saturated. Secondly, we can compare values in the region of the surface and away from the surface, as a measure of the density of the boundary layer compared to the bulk.

We split the computational box in half, with $z < 100\xi$ and $z \geq 100\xi$. We first estimate the vortex line-length in each half using the method described in Section 3.7, obtaining the vortex line-lengths for the lower and upper half of the box, $V_0(t)/A$ and $V_1(t)/A$ respectively. Finally the two quantities are used to compute the vortex line-densities L_0 and L_1 throughout the simulation, shown in Figure 7.11.

We find that both L_0 and L_1 grow over time as vortex lines are nucleated into the

superfluid. L_0 quickly grows at early times, and then saturates at a value around 2.4×10^{-3} at around $t \approx 800$. On the other hand, L_1 grows much slower than L_0 and shows significantly less vortex line-density throughout the simulation, and does not saturate but instead exhibits a steady growth of vortex line-density throughout, even after L_0 has saturated at $t \approx 800$.

These measurements confirm a transient period of fast vortex line-density growth at early times which saturates in the lower half of the computational box, corresponding to the region in the vicinity of the rough surface. In addition, we observe a continuous growth of vortex line-density in the bulk, due to vortex ring formation and emission into the upper half of the computational box. This process is further investigated in Section 7.4.3.

7.4.3 Vortex ring generation through the vortex mill mechanism

At early times, nucleated vortex lines can form aligned along the flow direction, twisted due to the bundling of vortex lines nucleated at high-frequency. An example of this structure can be seen in the background of Figure 7.9 (f). The twisted vortex lines generate more vorticity which feed into the boundary layer tangle, by spooling small vortex loops though the vortex-mill mechanism envisaged by Schwarz [300]. This confirms that, for the AFM surface and an imposed flow of $v = 0.6\,c$, the vortex tangle which develops can be interpreted as generated either intrinsically or extrinsically: in both cases vortices nucleate at the highest mountains before filling the layer below.

At later times (due to the modified velocity field by the saturated boundary layer) and for higher imposed flow velocities, the critical velocity is exceeded across greater areas of the surface. However, even after the generation of a considerable vortex tangle, the highest mountains continue to dominate vortex nucleation; here the fluid velocity is always the highest and vortex shedding occurs at the fastest rate. Despite this, we have already seen that the vortex line-density in the vicinity of the surface saturates at late times. To maintain equilibrium, vortex line-length is continuously ejected from the boundary layer by the process of vortex twisting, reconnections, and the formation of vortex rings that detach and travel in the positive z direction; a demonstration of this process is seen in Figure 7.12. This process provides further evidence of the presence of a vortex mill mechanism in the system, where vortex line-length is injected into the bulk of the superfluid in the form of small rings escaping the boundary layer tangle.

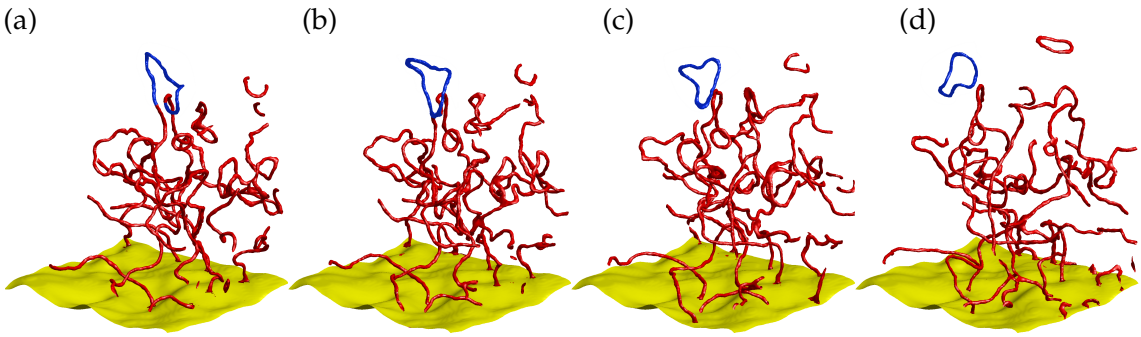

Figure 7.12: Instantaneous isosurfaces of density $n(\mathbf{r}, t)$ (plotted at 25% of the bulk density) showing the rough surface (yellow) and vortex lines (red) in the saturated regime at times $t = 730, 740, 750, 770\,\tau$ and with $v = 0.6\,c$. The view is of the region $120\xi < x < 196\xi$, $48\xi < y < 124\xi$, $20\xi < z < 160\xi$. Highlighted in blue is an escaping vortex ring (originating from the tangle) that later travels in the positive z direction and into the bulk of the fluid.

Velocity profile

We further explore the turbulent boundary layer by measuring the local velocity, $\mathbf{v}_{\rm loc} = \hbar\nabla\theta/m$, as a function of distance, so as to obtain a velocity profile. We define the quantity

$$v_{\rm xy}(z) = \langle v_{\rm loc}(\mathbf{r})\rangle_{\rm xy}, \tag{7.1}$$

where $\langle v_{\rm loc}(\mathbf{r})\rangle_{\rm xy}$ denotes averaging of the local fluid speed in the xy plane. We measure $v_{\rm xy}(z)$ for all z using an average of 10 snapshots at times $1130 < t/\tau < 1220$ (so that we measure the turbulent saturated regime). The resulting quantity $v_{\rm xy}(z)$ is a measurement of the typical local speed of the fluid flow at the height of z. For our simulation with $v = 0.6\,c$, we find three regions in the profile of $v_{\rm xy}(z)$ (shown in Figure 7.13).

In the region $100\xi \lesssim z \lesssim 200\xi$, the local flow speed is $v_{\rm xy}(z) \approx 0.6$, showing that the fluid velocity is unaffected by the rough surface at heights of more than the height of the tallest mountain. The small vortex rings in this region, after spatial averaging, are observed to have no effect on the mean speed of the flow. We also note that the effect of the finite hard wall boundary at $x = 200\xi$ is minimal.

In the region $40 \lesssim z \lesssim 100\xi$ the presence of vortices near the surface creates a velocity field that on the average counteracts the imposed flow velocity. The overall effect is to slow the typical flow speed the closer to the surface it is measured, in analogy to a viscous boundary layer in classical fluids.

In the region $0 \lesssim z \lesssim 40\xi$ most of the computational volume is below the surface, and so only the fluid in the valleys is computed as part of the average. In this region the typical speed of the flow rapidly drops to almost zero.

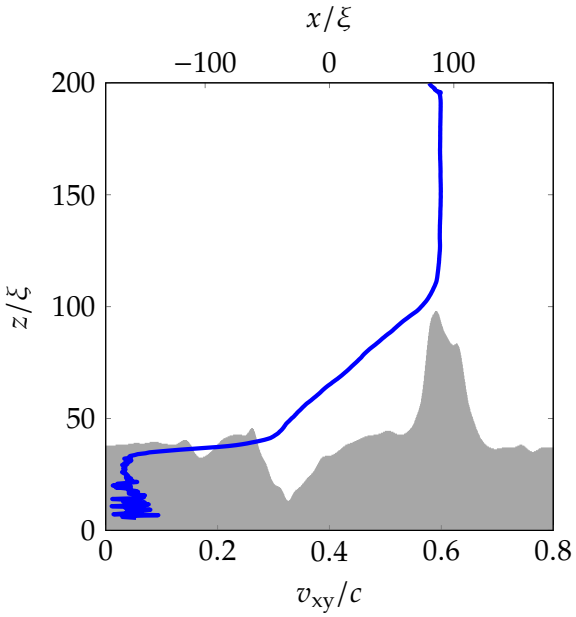

Figure 7.13: Typical local flow speed (lower abscissa) at various heights above the surface of the wire, averaged over 10 points in time, at $1130 < t/\tau < 1220$ and with $v = 0.6\,c$. For comparison, a 2D sample of the 3D surface ($y = 0.1\,\mu$m, demonstrating one of the tallest surface features) is shown in grey (upper abscissa).

7.5 Conclusions

In conclusion, we have modelled superflow over a real surface region of a thin NbTi "floppy wire" used in helium II experiments and imaged via Atomic Force Microscopy. We have used the zero temperature GPE to numerically simulate a superfluid flow with the profile of the wire inserted using a potential term, obtaining numerical results in both 2D and in 3D.

We have performed 2D simulations and explored the parameter space of surface roughness (modified by truncation of the 'roughest' features in the wire) and flow velocity (imposed via a frame shift in the governing equation). For all roughness we have observed the formation of a 2D 'boundary layer' at certain velocities exceeding the critical velocity, consisting of a collection of quantum vortices that remain in the vicinity of the surface. We find that imposing an even higher velocity destroys the boundary layer behaviour. Our large scale 3D simulations also confirm that, for at least one set of parameters, the formation of the boundary layer generalises to three dimensions. We have shown that the vortex line-density saturates over time in the layer, and have demonstrated a qualitatively similar boundary layer velocity profile as those seen in classical viscous fluids.

Our findings are a surprising result because in fluid dynamics boundary layers arise from viscous forces, which in superflow at absolute zero operate through a fundamentally

different mechanism. These findings further illustrate the deep analogies between classical and quantum fluids.

Our results suggest that in current helium II experiments the walls of channels which confine the flow of superfluid liquid helium and the surfaces of moving objects such as wires, grids, propellers, spheres may be covered by a thin 'superfluid boundary layer' consisting of vortex loops and rings. The experimental implications of 'superfluid boundary layers' on macroscopic observables need to be investigated. This should particularly stimulate experiments in ^{3}He-B, where, due to relative large healing length, it is possible to study flows with controlled surface height roughness. Our results could also be interpreted and potentially observable in the context of quasi-two-dimensional atomic BEC experiments, where recent work has enabled dynamic arbitrarily shaped obstacles, 'painted' with blue-detuned laser light [58].

Chapter 8

Conclusions and future work

8.1 Conclusions

In this chapter, we summarise the conclusions of the work presented throughout the thesis, and suggest relevant directions in which the work can be extended in the future.

In Part I we introduced the mean-field theory that allows for accurate modelling of a dilute, weakly interacting Bose-Einstein condensate. We described the GPE, a non-linear Schrödinger equation used to model condensates at zero temperature, along with extensions to model finite temperatures through phenomenological damping and the classical-field method. We also described the theory and practice of various numerical procedures we have used throughout the thesis.

Classical-like wakes behind elliptical obstacles in Bose-Einstein condensates

In Chapter 4 we showed that a 2D or 3D obstacle in the presence of superfluid flow in a Bose-Einstein condensate generates wakes of quantum vortices which resemble those of classical viscous flow past a cylinder or sphere.

We demonstrated a key ingredient to produce classical-like wakes: high vortex nucleation rate so that vortices undergo strong interactions with their neighbours, rather than being swept away. The role of ellipticity in this chapter was to reduce the critical velocity for vortex nucleation and increase vortex nucleation frequency and density, to facilitate strong interaction between vortices.

The symmetric wakes produced are similar to those observed in classical flow at low *Re*. We showed that they are unstable, forming time-dependent asymmetric structures similar to the Bénard–von Kármán vortex street of classical fluid dynamics.

The effects we described are relevant to the motion of objects such as vibrating wires, grids and forks in superfluid helium, where the obstacle's ellipticity plays a role which is analogous to rough boundaries [248, 190], and described patterns in the density distribu-

tion that could be potentially observed in experimental atomic Bose-Einstein condensates, with moving laser-induced potentials.

Decay of 2D quantum turbulence in a highly oblate Bose-Einstein condensate

In Chapter 5 , we modelled the experimental set up of Kwon *et al.* in which the creation and decay of vortices within a BEC [106] was observed. We showed that the system is well described by simulations of the 2D-GPE with phenomenological dissipation (despite the system's technically 3D nature). We elucidated the system's experimentally unobserved early stages, showing that vortex clusters form behind a laser-induced obstacle. We demonstrated that early time symmetry breaking causes disorganisation of the vortices and that by the time the obstacle is removed, the vortices are well randomised. We confirmed the occasional appearance of crescent-shaped density features, resulting either from the proximity of vortex cores or from a sound pulse which follows a vortex-antivortex reconnection.

We showed that the vortices decay in a manner which is consistent with the two mechanisms proposed by Kwon *et al.* (loss of vortices at the condensate edge due to thermal dissipation and vortex-antivortex annihilation events within the condensate) and fitted the rate equations proposed by Kwon *et al.* and Cidrim *et al.* to the vortex decay that we observed in our numerical simulations. We concluded that Cidrim's equation fits to the data most favourably, while providing physically realistic values for the decay rates.

Quasi-classical turbulence and the critical velocity in a quenched Bose gas

In Chapter 6, we modelled a finite temperature homogeneous Bose gas. We evolved the classical field from highly non-equilibrium initial conditions, through decay of a vortex tangle, to thermalised equilibrium states with a range of temperatures and condensate fractions.

We characterised the turbulent vortex tangle by finding a kinetic energy spectrum that demonstrates a *lack* of quasi-classical turbulence, and through tracking the vortex line-density over time, we found a decay rate characteristic of ultra-quantum turbulence. We confirmed the result by calculating the velocity correlation function and integral scale, finding them to be consistent with ultra-quantum turbulence.

With the resulting equilibrium states we inserted a cylindrical obstacle with Gaussian profile, and imposed a fluid flow. We found that above the critical velocity, vortices are nucleated as wiggly vortex lines, vortex rings, or as a vortex tangle. We demonstrated that the critical velocity decreases with increasing temperature (becoming zero at the critical temperature for condensation) and scales with the the speed of sound of the condensate, which can be written as the square root of the condensate fraction.

Simulating the rough surface of a "Floppy Wire"

In Chapter 7, we modelled the rough surface of a real "floppy wire" used in helium II experiments through a potential term in the zero temperature GPE and by imposing a flow. The surface of the wire was provided via atomic force microscopy. We performed two-dimensional simulations of the surface at various levels of truncation and at various flow speeds to probe the parameter space.

We observed for various truncations of the 2D profile and for several flow velocities in excess of the critical velocity, the formation of a 'boundary layer' of quantum vortices. In each case, for a high enough imposed flow velocity the boundary layer effect breaks down and quantum vortices instead fill the computational box.

We performed large scale 3D simulations, showing that the boundary layer effect generalises to three dimensions. We showed evidence of a "vortex mill" mechanism leading to escaping vortex rings formed from the boundary layer. We measured the velocity profile of the fluid flow and demonstrated a qualitatively similar profile to those seen for boundary layers in classical viscous fluids.

Our results suggest that in superfluids the surfaces of moving objects may be covered by a thin 'superfluid boundary layer' consisting of vortex loops and rings. This is a surprising effect: boundary layers usually arise from viscous forces, which in zero temperature superfluids are completely absent.

8.2 Future work

Other quantum analogues of classical-like wakes

Many studies of viscous flow in classical fluids have been performed over the years. Collections such as Van Dyke's *Album of Fluid Motion* [217] demonstrate the wide range of flows possible with various obstacle shapes and sizes in both 2D and 3D regimes. As an example, the wakes of rectangular (rather than circular) obstacles and recesses are shown in Figure 8.1. Chapter 4 investigated the classical-like wakes in the simplest case of a cylinder in quantum flow. It would be an extremely interesting direction for future work to attempt to experiment with the more complicated examples of classical flow patterns that exist in the literature. The idea that the behaviour of many quantum vortices collectively reproduces classical physics would suggest that perhaps other analogies of classical fluid wakes exist in the quantum fluid realm.

Finite temperature trapped Bose gas

While the work set our in Chapter 6 is based on a homogeneous system, in reality Bose-Einstein condensates are experimentally confined in traps, rendering the gas inhomoge-

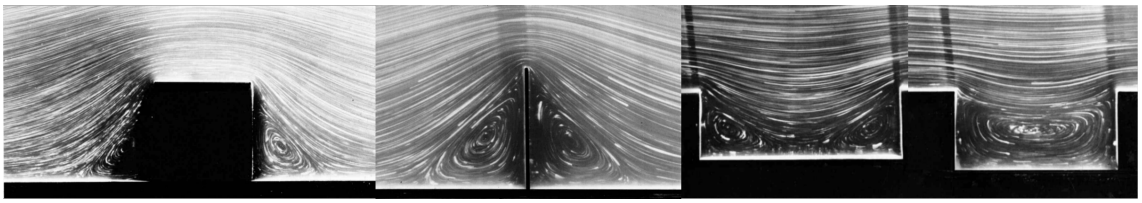

Figure 8.1: Various examples of classical viscous fluid flow around square obstacles and recesses [217].

neous. One can expect significant corrections to the critical velocity and resulting vortex nucleation regime due to density gradients. It would be interesting to see these higher order effects studied in future works, in particular in the common case of a harmonic trapping potential.

On the other hand, recent advances have led to the formation of quasi-homogeneous condensates in box-like traps [61, 62]. Here, the higher order corrections associated with trapping inhomogeneity should have minimal effect. An interesting direction for future experimental work would be to compare our experimentally measurable numerical predictions, such as critical velocity or the vortex line-density decay rate, to experimental data incorporating quasi-homogeneous box-like traps.

Exploring the superfluid boundary layer

The experimental implications of possible 'superfluid boundary layers', demonstrated in Chapter 7, on macroscopic observables need to be investigated. The results we have shown in 3D should particularly stimulate experiments in ^{3}He-B, where, due to relative large healing length, it is possible to observe vortex core structure and study flows with controlled surface height roughness.

An alternative experimental application of the 2D boundary layers observed in Chapter 7 can be found in the context of atomic BECs. Recently, the path has opened towards the realisation of dynamic and arbitrarily shaped obstacles [58]. By utilizing arbitrary potentials, a moving rough surface could be implemented in a quasi-two-dimensional atomic BEC.

Numerically there is also much work to still be done, particularly in 3D. While current computational limits are reached quickly with our simulations, the potential future increase in power of high performance clusters or even desktop computers could allow for quicker numerical simulation and easier visualisation of results. Along these lines, a potential extension to the work in Chapter 7 is the undertaking of a significant exploration of the 3D parameter space. It would be interesting to explore the response to changes to the imposed superfluid flow speed and surface roughness through truncation, and if the behaviour generalises from our two-dimensional results to the three-dimensional case.

Part III

Appendix

Appendix A

Detailed Derivations

A.1 Critical temperature and condensate fraction for a non-interacting Bose gas

Consider a three-dimensional non-interacting Bose gas of volume D^3 confined by hard walls. The critical temperature, T_λ, is defined as the highest temperature at which macroscopic occupation of the ground state takes place. For a large number of particles, N, the zero-point energy in the system can be neglected, so that the energy of the ground state is $\epsilon_0 = 0$, and the energy levels can be considered as a continuous variable, ϵ. The number of particles in excited states is then written,

$$N_{\text{ex}}(T, \mu) = \int_0^\infty g(\epsilon) f(\epsilon)\, \mathrm{d}\epsilon = \int_0^\infty \frac{g(\epsilon)}{e^{(\epsilon-\mu)/k_\text{B}T} - 1}\, \mathrm{d}\epsilon, \tag{A.1}$$

where $g(\epsilon)$ is the density of states and $f(\epsilon)$ is the Bose-Einstein distribution. Note that equation A.1 will achieve its greatest value when $\mu = 0$. We now consider the critical temperature, T_λ. At this temperature, it is possible for the total number of particles to be accommodated in excited states,

$$N = N_{\text{ex}}(T_\lambda, 0) = \int_0^\infty \frac{g(\epsilon)}{e^{\epsilon/k_\text{B}T_\lambda} - 1}\, \mathrm{d}\epsilon. \tag{A.2}$$

The density of states for a three-dimensional gas confined by hard walls can be written as

$$g(\epsilon) = \frac{D^3 m^{3/2} \epsilon^{3/2-1}}{\sqrt{2}\pi^2\hbar^3}, \tag{A.3}$$

where m is the mass of a single particle [1]. Using this equation for $g(\epsilon)$ with Equation A.2, the expression for the number of particles becomes

$$N = \frac{D^3 m^{3/2}}{\sqrt{2}\pi^2\hbar^3} \int_0^\infty \frac{\epsilon^{3/2-1}}{e^{\epsilon/k_B T_\lambda} - 1} \, \mathrm{d}\epsilon. \tag{A.4}$$

We now introduce a change of variable, $w = \epsilon/k_B T_\lambda$, so that

$$N = \frac{D^3 (m k_B T_\lambda)^{3/2}}{\sqrt{2}\pi^2\hbar^3} \int_0^\infty \frac{w^{3/2-1}}{e^w - 1} \, \mathrm{d}w = \frac{D^3 (m k_B T_\lambda)^{3/2}}{\sqrt{2}\pi^2\hbar^3} \Gamma(3/2)\zeta(3/2), \tag{A.5}$$

where $\Gamma(x)$ is the Gamma function, $\zeta(x) = \sum_{n=1}^\infty n^{-x}$ is the Riemann-zeta function, and using the relation $\int_0^\infty w^{x-1}/(e^w - 1)\, \mathrm{d}w = \Gamma(x)\zeta(x)$. Rearranging A.5 for T_λ, and using $\Gamma(3/2) = \sqrt{\pi}/2$, leads to the expression,

$$T_\lambda = \frac{2\pi\hbar^2}{m k_B} \left(\frac{\rho}{\zeta(3/2)} \right)^{2/3}, \tag{A.6}$$

where $\rho = N/D^3$ is the uniform number density.

Now consider Equation A.2 with an arbitrary temperature $T < T_\lambda$. We can use the same procedure as above to write,

$$N_{ex}(T, 0) = \frac{D^3 (m k_B T)^{3/2}}{\sqrt{2}\pi^2\hbar^3} \Gamma(3/2)\zeta(3/2). \tag{A.7}$$

By making use of both Equation A.5 and A.7, we find

$$N_{ex}(T, 0) = N \left(\frac{T}{T_\lambda} \right)^{3/2}. \tag{A.8}$$

The number of particles in the ground state is $N_0(T) = N - N_{ex}(T, 0)$, and so we can equivalently write Equation A.8 as,

$$\frac{N_0}{N} = 1 - \left(\frac{T}{T_\lambda} \right)^{3/2}. \tag{A.9}$$

A.2 Derivation of the Runge-Kutta scheme

Presented here is the derivation of the explicit second-order Runge-Kutta scheme. The ideas and methods easily extend to the forth-order scheme used in this thesis, but in the interests of brevity the entire proof will be given to second order, with the relevant forth

order extensions clearly noted. Let an initial value problem be specified as

$$\psi'(t) = f(\psi(t), t), \qquad \psi(t_0) = \psi_0,$$

where $t_n = nh$, h is a chosen step size, and $f(\psi(t), t)$ is known. The aim of the scheme is to estimate some $\psi(t_m)$ from the known $\psi(t_0)$ through the application of a single numerical step of size h, m times.

For a single application of the numerical step we attempt to find the unknown value of $\psi(t_{n+1})$, which can be written,

$$\begin{aligned}\psi(t_{n+1}) &= \psi(t_n) + \left[\psi(t_{n+1}) - \psi(t_n)\right] \\ &= \psi(t_n) + \int_{t_n}^{t_{n+1}} f\left(\psi(\tau), \tau\right) \mathrm{d}\tau.\end{aligned}$$

We now decide to approximate the (difficult to calculate) integral $\int_{t_n}^{t_{n+1}} f\left(\psi(\tau), \tau\right) \mathrm{d}\tau$ using quadrature, leading to the modified expression,

$$\psi(t_{n+1}) \approx \psi(t_n) + h \sum_{i=1}^{N} \omega_i f(t_n + h\nu_i, \psi(t_n + h\nu_i)),$$

where N is the order of the numerical scheme, ω_i are weights and ν_i are locations in time positioned between t_n and t_{n+1} inclusive. In this second-order derivation we take $N = 2$, a forth-order scheme would alternatively require $N = 4$.

We take the first temporal point to be $\nu_1 = 0$, so that the first term in the sum is

$$k_1 = h f(t_n, \psi(t_n)).$$

We can then easily calculate the value of k_1. A single step in Euler's method tells us that $\psi(t_n + h\nu_2) \approx \psi(t_n) + h\nu_2 f(t_n, \psi(t_n))$ and so we write k_2 in a form containing k_1,

$$k_2 = h f(t_n + h\nu_2, \psi(t_n + h\nu_2)) \approx h f(t_n + \nu_2 h, \psi(t_n) + \nu_2 k_1).$$

For a forth order scheme we would then introduce k_3 and k_4, following the same methods of writing k_i in previous terms up to k_{i-1}. To second order, the quadrature formula becomes

$$\psi(t_{n+1}) \approx \psi(t_n) + \omega_1 k_1 + \omega_1 k_2. \tag{A.10}$$

However, note that we still must derive values for the quantities $\nu_{i>1}$ and ω_i.

Consider the Taylor expansion,

$$\psi(t+h) = \psi(t) + h\psi'(t) + \frac{h^2}{2}\psi''(t) + \cdots,$$

where for the full forth-order derivation, further higher order terms are also considered. We substitute this expansion into the left hand side of Equation A.2, which leads to

$$\psi(t_n) + h\psi'(t_n) + \frac{h^2}{2!}\psi''(t_n) + O(h^3) \approx \psi(t_n) + \omega_1 k_1 + \omega_2 k_2. \tag{A.11}$$

Note that

$$\psi'(t_n) = f,$$
$$\psi''(t_n) = \frac{\partial f}{\partial t} + f\frac{\partial f}{\partial \psi},$$

by the definition of $\psi'(t)$ and the total derivative, and where the arguments of $f(t_n, \psi(t_n))$ have been suppressed for notational ease. We then substitute the expressions for $\psi'(t_n)$, $\psi''(t_n)$, k_1 and k_2 into Equation A.2,

$$hf + \frac{h^2}{2}\left(\frac{\partial f}{\partial t} + f\frac{\partial f}{\partial \psi}\right) + O(h^3) = \omega_1 hf + \omega_2 hf(t_n + \nu_2 h, \psi(t) + \nu_2 k_1). \tag{A.12}$$

Now consider the Taylor expansion,

$$f(t+h, \psi+g) = f(t,\psi) + h\frac{\partial f(t,\psi)}{\partial t} + g\frac{\partial f(t,\psi)}{\partial \psi} + \cdots,$$

where for the full forth-order derivation, further higher-order terms are also considered. We substitute this expansion into Equation A.2, including terms up to the required order, and find

$$hf + \frac{h^2}{2!}\left(\frac{\partial f}{\partial t} + f\frac{\partial f}{\partial \psi}\right) + O(h^3) = \omega_1 hf + \omega_2\left(hf + \nu_2 h^2\frac{\partial f}{\partial t} + \nu_2 h^2 f\frac{\partial f}{\partial \psi}\right) + O(h^3). \tag{A.13}$$

By equating terms on both the right hand side and left hand side of Equation A.2, we find that for the second-order Runge-Kutta scheme the following equivalences are required for consistency,

$$\omega_1 + \omega_2 = 1,$$
$$\nu_2\omega_2 = \frac{1}{2}.$$

For the forth-order scheme, more but similar equivalences are required for consistency. The canonical choice for the second-order Runge-Kutta methods is $\nu_2 = 1$ and $\omega_1 = \omega_2 = 1/2$. The scheme can then be directly written down,

$$\psi(t_{n+1}) = \psi(t_n) + \frac{k_1}{2} + \frac{k_2}{2} + O(h^3), \tag{A.14}$$

where $k_1 = hf(t_n, \psi(t_n))$ and $k_2 = hf(t_n + h, \psi(t_n) + k_1)$.

When this proof outline is followed with $N = 4$, the forth-order Runge-Kutta scheme can be found,

$$\psi(t_{n+1}) = \psi(t_n) + \frac{k_1}{6} + \frac{k_2}{3} + \frac{k_3}{3} + \frac{k_4}{6} + O(h^5), \tag{A.15}$$

where

$$\begin{aligned} k_1 &= hf(t_n, \psi(t_n)), \\ k_2 &= hf(t_n + \frac{h}{2}, \psi(t_n) + \frac{k_1}{2}), \\ k_3 &= hf(t_n + \frac{h}{2}, \psi(t_n) + \frac{k_2}{2}), \\ k_4 &= hf(t_n + h, \psi(t_n) + k_3). \end{aligned}$$

A.3 Derivation of the Gross-Pitaevskii Equation

This section derives the GPE following the methodology outlined in [309]. We begin by revisiting the quantum field theory formalism used to describe a many-body quantum system [310]. Such a system is described by an N-body wavefunction, $\tilde{\Psi}(\mathbf{r}_1 ... \mathbf{r}_N, t)$ which obeys the famous Schrödinger equation

$$i\hbar \frac{\partial}{\partial t} \tilde{\Psi}(\mathbf{r}_1 ... \mathbf{r}_N, t) = \hat{H} \tilde{\Psi}(\mathbf{r}_1 ... \mathbf{r}_N, t), \tag{A.16}$$

where $\mathbf{r}_i$ describes the coordinates of the ith body. Consider a closed system containing a dilute, weakly interacting Bose gas of N atoms. Such a system would be described by $\tilde{\Psi}(\mathbf{r}_1 ... \mathbf{r}_N, t)$, with a Hamiltonian of the form

$$\hat{H} = \sum_{k=1}^{N} \hat{h}_0(\mathbf{r}_k, t) + \frac{1}{2} \sum_{k,l=1}^{N} \hat{V}(\mathbf{r}_k, \mathbf{r}_l). \tag{A.17}$$

Here $\hat{h}_0(\mathbf{r}, t) = -\frac{\hbar^2}{2m}\nabla^2 + V_{\text{ext}}(\mathbf{r}, t)$ is a contribution arising from the effects of a single particle in an external potential. We assume in the dilute gas all interactions are binary, and so the second term arises from collisions between 2 atoms. The factor of $\frac{1}{2}$ ensures the effects are only counted once over the entire sum.

We now reformulate this system in a different representation, using the so called 'occupation number' orthonormal basis $|n_1...n_\infty\rangle$. This basis arises from the observation that multiple particles sharing an energetically accessible state are indistinguishable. Instead we consider only the number of particles in each state i and denote this n_i. Such states often correspond to states with fixed energy ε_i. While the number of states is infinite, our system contains a fixed number of bosons, N, implying that there are at most N states occupied.

The wavefunction is mapped into the 'occupation number' basis via

$$\tilde{\Psi}(\mathbf{r}_1...\mathbf{r}_N, t) \rightarrow |\tilde{\Psi}(t)\rangle = \sum_{n_1...n_\infty} c(n_1...n_\infty, t)\,|n_1...n_\infty\rangle\,,$$

with appropriately chosen complex coefficients, $c(n_1...n_\infty, t)$. The values c must follow the particle statistics rules (e.g. for bosons, must be symmetric under swapping of quantum numbers) and be normalised so that the probabilities correctly sum to one. We find that for our bosons,

$$\int |\tilde{\Psi}|^2\, d\mathbf{r} = 1 \Rightarrow \sum_{n_1...n_\infty} |c(n_1...n_\infty, t)|^2 \frac{N!}{n_1!...n_\infty!} = 1.$$

As particles are indistinguishable, some sets of occupation numbers correspond to multiple N-particle states. The term $N!/n_1!...n_\infty!$ has been introduced in the sum, so as to take this into account.

In this formulation, note that the state vectors $|n_1...n_\infty\rangle$ are time-independent, and the evolution of the system is entirely encoded in the values of $c(n_1...n_\infty, t)$. As part of the overall picture, we also must describe the movement of bosons between different states or energy levels. It is convenient to visualise this as the simultaneous destruction of a particle in state j and creation of a particle in state i, described mathematically using the single particle annihilation and creation operators [311],

$$\hat{a}_j\,|n_1...n_i...n_j...n_\infty\rangle = \sqrt{n_j}\,|n_1...n_i...n_j - 1...n_\infty\rangle\,,$$
$$\hat{a}_i^\dagger\,|n_1...n_i...n_j...n_\infty\rangle = \sqrt{n_i + 1}\,|n_1...n_i + 1...n_j...n_\infty\rangle\,,$$

which satisfy the bosonic commutation relations,

$$[\hat{a}_i, \hat{a}_j^\dagger] = \delta_{ij} \qquad [\hat{a}_i, \hat{a}_j] = [\hat{a}_i^\dagger, \hat{a}_j^\dagger] = 0.$$

Any single particle changing states can now be described through these operators; a particle moving from state j to state i is described using a single annihilation operator and a single creation operator through the product $\hat{a}_i^\dagger \hat{a}_j$. Similarly, as we decided to simplify the system by considering a dilute gas where all interactions are binary collisions, all interac-

tions can be described by two particles changing state, using the product $\hat{a}_i^\dagger \hat{a}_k^\dagger \hat{a}_j \hat{a}_l$. Using these tools and ideas, the original description in Equations A.16 and A.17 is now written

$$i\hbar \frac{\partial}{\partial t} |\tilde{\Psi}\rangle = \hat{H} |\tilde{\Psi}\rangle ,$$

with the Hamiltonian

$$\hat{H} = \sum_{ij} \langle i| \hat{h}_0 |j\rangle \hat{a}_i^\dagger \hat{a}_j + \frac{1}{2} \sum_{ijkl} \langle ik| \hat{V} |jl\rangle \hat{a}_i^\dagger \hat{a}_k^\dagger \hat{a}_j \hat{a}_l, \tag{A.18}$$

where

$$\begin{aligned}
\langle i| \hat{h}_0 |j\rangle &= \int \phi_i^*(\mathbf{r}) \hat{h}_0 \phi_j(\mathbf{r})\, d\mathbf{r}, \\
\langle ik| \hat{V} |jl\rangle &= \frac{1}{2} \left[(ik|\hat{V}|jl) + (ik|\hat{V}|lj) \right], \\
(ik|\hat{V}|jl) &= \iint \phi_i^*(\mathbf{r}) \phi_k^*(\mathbf{r}') \hat{V}(\mathbf{r} - \mathbf{r}') \phi_l(\mathbf{r}') \phi_j(\mathbf{r})\, d\mathbf{r}' d\mathbf{r},
\end{aligned}$$

and $\phi_i(\mathbf{r})$ are the single-particle eigenstates: solutions of the Schrödinger equation without the interaction term. For further convenience we introduce the so-called Bose field operators

$$\begin{aligned}
\hat{\Psi}(\mathbf{r}, t) &= \sum_i \hat{a}_i(t) \phi_i(\mathbf{r}), \\
\hat{\Psi}^\dagger(\mathbf{r}, t) &= \sum_i \hat{a}_i^\dagger(t) \phi_i^*(\mathbf{r}),
\end{aligned}$$

which can be thought of as operators that represent the addition or removal of a particle at time t and location $\mathbf{r}$. As with the annihilation and creation operators, the Bose field operators also satisfy the commutation relations,

$$[\hat{\Psi}(\mathbf{r}, t), \hat{\Psi}^\dagger(\mathbf{r}', t)] = \delta(\mathbf{r} - \mathbf{r}') \qquad [\hat{\Psi}(\mathbf{r}, t), \hat{\Psi}(\mathbf{r}', t)] = [\hat{\Psi}^\dagger(\mathbf{r}, t), \hat{\Psi}^\dagger(\mathbf{r}', t)] = 0. \tag{A.19}$$

Using these operators, the Hamiltonian in Equation A.18 can be again rewritten as

$$\begin{aligned}
\hat{H} = &\int \hat{\Psi}^\dagger(\mathbf{r}, t)\, \hat{h}_0 \hat{\Psi}(\mathbf{r}, t)\, d\mathbf{r} \\
&+ \frac{1}{2} \iint \hat{\Psi}^\dagger(\mathbf{r}, t) \hat{\Psi}^\dagger(\mathbf{r}', t) V(\mathbf{r} - \mathbf{r}') \hat{\Psi}(\mathbf{r}', t) \hat{\Psi}(\mathbf{r}, t)\, d\mathbf{r}' d\mathbf{r},
\end{aligned} \tag{A.20}$$

where, as before, $\hat{h}_0(\mathbf{r}, t) = -\frac{\hbar^2}{2m}\nabla^2 + V_{\text{ext}}(\mathbf{r}, t)$ and $V(\mathbf{r} - \mathbf{r}')$ is the two-body interaction potential.

We now turn our attention to the particle interactions. We first note that in this deriva-

tion, a perturbation approach is taken, with the the single-particle eigenstates, $\phi_i(\mathbf{r})$, used as a basis. As the functions $\phi_i(\mathbf{r})$ are defined as solutions of the Schrödinger equation without interactions, strictly speaking, the resulting approach is applicable only when inter-particle interactions are weak. We further add to our approximations a simplification of the interaction potential, by considering all interactions as totally elastic contact collisions. Through scattering theory, the resulting strength of the interactions, g, can be related to the s-wave scattering length, a_s, which is measurable for a particular atom in the lab. This approach leads to a leading order approximation of $g = 4\pi\hbar^2 a_s/m$. Our two-body interaction potential then becomes,

$$V(\mathbf{r} - \mathbf{r}') = g\delta(\mathbf{r} - \mathbf{r}'),$$

which when inserted into Equation A.20 gives the Hamiltonian,

$$\hat{H} = \int \hat{\Psi}^\dagger(\mathbf{r}, t)\, \hat{h}_0 \hat{\Psi}(\mathbf{r}, t)\, d\mathbf{r} + \frac{g}{2} \int \hat{\Psi}^\dagger(\mathbf{r}, t)\hat{\Psi}^\dagger(\mathbf{r}, t)\hat{\Psi}(\mathbf{r}, t)\hat{\Psi}(\mathbf{r}, t)\, d\mathbf{r}.$$

The Bose field operator $\hat{\Psi}(\mathbf{r}, t)$ evolves over time according to the Heisenberg equation of motion

$$i\hbar \frac{\partial}{\partial t}\hat{\Psi}(\mathbf{r}, t) = [\hat{\Psi}(\mathbf{r}, t), \hat{H}].$$

By expanding out the commutator, using standard commutator identities along with the relations in Equation A.19 and integrating out resulting delta functions we find

$$\begin{aligned} i\hbar \frac{\partial}{\partial t}\hat{\Psi}(\mathbf{r}, t) &= \int [\hat{\Psi}, \hat{\Psi}^\dagger \hat{h}_0 \hat{\Psi}]\, d\mathbf{r} + \frac{g}{2} \int [\hat{\Psi}, \hat{\Psi}^\dagger \hat{\Psi}^\dagger \hat{\Psi}\hat{\Psi}]\, d\mathbf{r} \\ &= \int [\hat{\Psi}, \hat{\Psi}^\dagger]\hat{h}_0\hat{\Psi} + \hat{\Psi}^\dagger[\hat{\Psi}, \hat{h}_0\hat{\Psi}]\, d\mathbf{r} \\ &\qquad + \frac{g}{2} \int [\hat{\Psi}, \hat{\Psi}^\dagger]\hat{\Psi}^\dagger\hat{\Psi}\hat{\Psi} + \hat{\Psi}^\dagger[\hat{\Psi}, \hat{\Psi}^\dagger]\hat{\Psi}\hat{\Psi} + \hat{\Psi}^\dagger\hat{\Psi}^\dagger[\hat{\Psi}, \hat{\Psi}\hat{\Psi}]\, d\mathbf{r} \\ &= \hat{h}_0\hat{\Psi}(\mathbf{r}, t) + g\hat{\Psi}^\dagger(\mathbf{r}, t)\hat{\Psi}(\mathbf{r}, t)\hat{\Psi}(\mathbf{r}, t). \end{aligned} \tag{A.21}$$

We can continue to simplify the equation of motion by considering a mean-field approach for a single macroscopically occupied state. In the case of Bose-Einstein condensation the lowest energy level is macroscopically occupied and so we decompose the field operator via

$$\hat{\Psi}(\mathbf{r}, t) = \hat{\psi}(\mathbf{r}, t) + \hat{\delta}(\mathbf{r}, t),$$

where $\psi(\mathbf{r}, t)$ is a field operator for the condensate and $\hat{\delta}(\mathbf{r}, t)$ is a field operator for the non-condensed atoms, whether that be atoms in higher states, atoms residing in the thermal cloud, or atoms influenced by quantum mechanical fluctuations.

We now make the Bogoliubov approximation [15], a somewhat violent symmetry break-

ing approximation in which the condensate field operator is replaced by a classical field,

$$\hat{\psi}(\mathbf{r}, t) = \psi(\mathbf{r}, t) = \sqrt{N_0}\phi_0(\mathbf{r}, t),$$

where N_0 is the number of particles in the condensate. Written in this way, it is then possible to approximate the condensate density using $n(\mathbf{r}, t) = |\psi(\mathbf{r}, t)|^2$. Unfortunately a direct consequence of the action is that the physical state described by $\hat{\Psi}(\mathbf{r}, t)$ no longer satisfies the same symmetries as before. In particular, the total number of particles is not conserved. This approximation is justified by the understanding that as the condensate forms, it takes on a single phase, and all the particles in the condensate can be described by a single wavefunction. In addition, it is assumed that if there are many particles in the condensate, the exact value of N_0 does not affect the system state significantly, that is, $N_0 \approx N_0 + 1$. This approximation is essentially equivalent to the statement $\langle\hat{\Psi}(\mathbf{r}, t)\rangle = \psi(\mathbf{r}, t) \neq 0$, where $\langle\ldots\rangle$ denotes the ensemble average. The non-condensed field operator $\hat{\delta}(\mathbf{r}, t)$ remains as an operator in the decomposition, and captures all the fluctuations around $\psi(\mathbf{r}, t)$. It is generally assumed that $\langle\hat{\delta}(\mathbf{r}, t)\rangle = 0$.

In principle, the classical field $\psi(\mathbf{r}, t)$ is interpreted as the condensed atoms, however it can also be interpreted as the condensate atoms along with excitations of the system, as long as the occupation at high energy states and the size of quantum fluctuations are both negligible. The classical field, or c-field, approaches can be used to model finite temperature effects by modelling part of the thermal cloud with highly populated modes below a certain momentum cutoff, explored in Section 2.12.

In the limit of $T \to 0$, all of the particles become part of the condensate, so that $N = N_0$. The contribution from the non-condensate atoms can be neglected, $\hat{\delta}(\mathbf{r}, t) = 0$, and the field operator is written $\hat{\Psi}(\mathbf{r}, t) = \psi(\mathbf{r}, t)$. In this case, the Heisenberg equation of motion in Equation A.21 reduces to

$$\begin{aligned} i\hbar\frac{\partial}{\partial t}\psi(\mathbf{r}, t) &= \hat{h}_0\psi(\mathbf{r}, t) + g\psi^*(\mathbf{r}, t)\psi(\mathbf{r}, t)\psi(\mathbf{r}, t) \\ &= \left(-\frac{\hbar^2}{2m}\nabla^2 + V_{\text{ext}}(\mathbf{r}, t) + g|\psi(\mathbf{r}, t)|^2\right)\psi(\mathbf{r}, t), \end{aligned}$$

the so-called Gross-Pitaevskii equation (GPE), also known as the non-linear Schrödinger equation (NLSE).

Finally, note that as the particle number is no longer strictly conserved, calculations should be performed within the grand canonical ensemble [7]. This approach leads to the modified Hamiltonian $\hat{H} \to \hat{H} - \mu\hat{N}$, where μ is the chemical potential and $\hat{N}$ is the total number operator. The above derivations can be easily repeated with the modified Hamiltonian to obtain a physically equivalent version of the GPE with a chemical potential

term,

$$i\hbar\frac{\partial}{\partial t}\psi(\mathbf{r},t)=\left(-\frac{\hbar^2}{2m}\nabla^2+V_{\text{ext}}(\mathbf{r},t)+g|\psi(\mathbf{r},t)|^2-\mu\right)\psi(\mathbf{r},t). \tag{A.22}$$

A.4 Derivation of the Hydrodynamic Equations via the Madelung Transformation

Inserting the Madelung transformation (Section 2.6) into the GPE and writing the result in tensor notation yields

$$\mathrm{i}\hbar\left(\frac{\partial R}{\partial t}+\mathrm{i}\frac{\partial\theta}{\partial t}R\right)e^{\mathrm{i}\theta}=-\frac{\hbar^2}{2m}e^{\mathrm{i}\theta}\left(\frac{\partial^2 R}{\partial x_j^2}+2\mathrm{i}\frac{\partial\theta}{\partial x_j}\frac{\partial R}{\partial x_j}+\mathrm{i}\frac{\partial^2\theta}{\partial x_j^2}R-\frac{\partial\theta}{\partial x_j}\frac{\partial\theta}{\partial x_j}R\right)+gR^3e^{\mathrm{i}\theta}+VRe^{\mathrm{i}\theta}.$$

The real and imaginary parts of the GPE, once divided by $\exp(\mathrm{i}\theta)$, then take the form

$$-\hbar R\frac{\partial\theta}{\partial t}=-\frac{\hbar^2}{2m}\left(\frac{\partial^2 R}{\partial x_j\partial x_j}-R\frac{\partial\theta}{\partial x_j}\frac{\partial\theta}{\partial x_j}\right)+gR^3+VR, \tag{A.23}$$

$$\hbar\frac{\partial R}{\partial t}=-\frac{\hbar^2}{2m}\left(2\frac{\partial\theta}{\partial x_j}\frac{\partial R}{\partial x_j}+R\frac{\partial^2\theta}{\partial x_j\partial x_j}\right). \tag{A.24}$$

Consider Equation (A.24) and note that $n=mR^2\Rightarrow\frac{\partial n}{\partial t}=2mR\frac{\partial R}{\partial t}$, allowing us to rewrite the equation in terms of n,

$$\begin{aligned}\frac{\partial n}{\partial t}&=-\hbar R\left(2\frac{\partial\theta}{\partial x_j}\frac{\partial R}{\partial x_j}+R\frac{\partial^2\theta}{\partial x_j\partial x_j}\right)\\&=-2mR\frac{\partial R}{\partial x_j}\frac{\partial}{\partial x_j}\left(\frac{\hbar}{m}\theta\right)-mR^2\frac{\partial^2}{\partial x_j\partial x_j}\left(\frac{\hbar}{m}\theta\right)\\&=-\frac{\partial n}{\partial x_j}\frac{\partial}{\partial x_j}\left(\frac{\hbar}{m}\theta\right)-n\frac{\partial^2}{\partial x_j\partial x_j}\left(\frac{\hbar}{m}\theta\right).\end{aligned}$$

The terms containing the phase can then be directly replaced with the fluid velocity, $v_j=\frac{\partial}{\partial x_j}\left(\frac{\hbar}{m}\theta\right)$.

$$\begin{aligned}\frac{\partial n}{\partial t}&=-\frac{\partial n}{\partial x_j}v_j-n\frac{\partial}{\partial x_j}v_j\\&=-\frac{\partial}{\partial x_j}\left(nv_j\right).\end{aligned}$$

Rewritten in vector form the result is a continuity equation,

$$\frac{\partial n}{\partial t}+\nabla(n\mathbf{v})=0. \tag{A.25}$$

Now consider Equation (A.23), written in the form

$$\frac{\hbar}{m}\frac{\partial\theta}{\partial t} = \frac{\hbar^2}{2m^2}\left(\frac{1}{R}\frac{\partial^2 R}{\partial x_j \partial x_j} - \frac{\partial\theta}{\partial x_j}\frac{\partial\theta}{\partial x_j}\right) - \frac{gR^2}{m} - \frac{V}{m}.$$

Note that it can easily be shown $\frac{1}{R}\frac{\partial^2 R}{\partial x_j \partial x_j} = \frac{1}{\sqrt{n}}\nabla^2\sqrt{n}$ and $\frac{\hbar^2}{2m^2}\frac{\partial\theta}{\partial x_j}\frac{\partial\theta}{\partial x_j} = \frac{v^2}{2}$. It follows that Equation (A.23) can be written,

$$\begin{aligned}
&\frac{\hbar}{m}\frac{\partial\theta}{\partial t} = \frac{\hbar^2}{2m^2}\frac{1}{\sqrt{n}}\nabla^2\sqrt{n} - \frac{v^2}{2} - \frac{gR^2}{m} - \frac{V}{m} \\
&\Rightarrow \frac{\partial}{\partial t}\left(\frac{\hbar}{m}\frac{\partial\theta}{\partial x_k}\right) = \frac{\partial}{\partial x_k}\left(\frac{\hbar^2}{2m^2}\frac{1}{\sqrt{n}}\nabla^2\sqrt{n}\right) - \frac{\partial}{\partial x_k}\left(\frac{v^2}{2}\right) - \frac{2gR}{m}\frac{\partial R}{\partial x_k} - \frac{1}{m}\frac{\partial V}{\partial x_k} \\
&\Rightarrow n\frac{\partial v_k}{\partial t} = n\frac{\partial}{\partial x_k}\left(\frac{\hbar^2}{2m^2}\frac{1}{\sqrt{n}}\nabla^2\sqrt{n}\right) - n\frac{\partial}{\partial x_k}\left(\frac{v^2}{2}\right) - 2gR^3\frac{\partial R}{\partial x_k} - n\frac{1}{m}\frac{\partial V}{\partial x_k}.
\end{aligned}$$

Introduce the pressure, defined as $p = \frac{1}{2}g\left(\frac{n}{m}\right)^2 = \frac{gR^4}{2}$, and then using $\frac{\partial p}{\partial x_k} = 2gR^3\frac{\partial R}{\partial x_k}$ we can write,

$$n\frac{\partial v_k}{\partial t} + n\frac{\partial}{\partial x_k}\left(\frac{v^2}{2}\right) = n\frac{\partial}{\partial x_k}\left(\frac{\hbar^2}{2m^2}\frac{1}{\sqrt{n}}\nabla^2\sqrt{n}\right) - \frac{\partial p}{\partial x_k} - mR^2\frac{\partial}{\partial x_k}\left(\frac{V}{m}\right).$$

We now now use the following two results,

$$\begin{aligned}
v_j\frac{\partial}{\partial x_j}v_k &= \frac{\partial}{\partial x_k}\left(\frac{v_j v_j}{2}\right) \\
2\frac{\partial}{\partial x_k}\left(\frac{1}{\sqrt{n}}\frac{\partial^2}{\partial x_j \partial x_j}\sqrt{n}\right) &= \frac{1}{n}\frac{\partial}{\partial x_j}n\frac{\partial}{\partial x_j}\frac{\partial}{\partial x_k}\ln n,
\end{aligned}$$

and find,

$$n\left(\frac{\partial}{\partial t}v_k v_j\frac{\partial v_k}{\partial x_j}\right) = -\frac{\partial p}{\partial x_k} - \frac{\partial}{\partial x_j}P_{jk} - n\frac{\partial}{\partial x_k}\left(\frac{V}{m}\right),$$

where $P_{jk} = -\frac{\hbar^2}{4m^2}n\frac{\partial^2 \ln n}{\partial x_j \partial x_k}$ is the quantum pressure. Writing this in vector notation, we obtain an equation similar to the Euler equation for an inviscid fluid,

$$n\left(\frac{\partial \mathbf{v}}{\partial t} + (\mathbf{v}\cdot\nabla)\,\mathbf{v}\right) = -\nabla p - \nabla\mathbf{P} - n\nabla\left(\frac{V}{m}\right). \tag{A.26}$$

Appendix B

Important Quantities

B.1 Energy

The energy functional of the GPE is written

$$\varepsilon(\psi) = \frac{\hbar^2}{2m}|\nabla\psi|^2 + \frac{g}{2}|\psi|^4 + V|\psi|^2, \tag{B.1}$$

where the first term is the kinetic energy, the second term is the energy arising from atom-atom interactions, and the final term is the energy associated with the external potential. This functional can be integrated over space to find a value for the condensate energy,

$$E = \int \varepsilon(\psi)\, \mathrm{d}\mathbf{r} \tag{B.2}$$

Equivalently, the energy of the system can be decomposed into a sum of the contributions from various types of energy in the system,

$$E = E_{\mathrm{kin}} + E_{\mathrm{int}} + E_{\mathrm{pot}},$$

so that,

$$E_{\mathrm{kin}} = \int \frac{\hbar^2}{2m}|\nabla\psi|^2\, \mathrm{d}\mathbf{r},\ E_{\mathrm{int}} = \int \frac{g}{2}|\psi|^4\, \mathrm{d}\mathbf{r},\ E_{\mathrm{pot}} = \int V|\psi|^2\, \mathrm{d}\mathbf{r}, \tag{B.3}$$

the kinetic, interaction, and potential energies respectively.

Also of interest is the kinetic energy spectrum $\hat{E}_{\mathrm{kin}}(k)$. Using Parseval's theorem, the kinetic energy spectrum can be defined using the angle-average of $\left|\mathcal{F}\left(\sqrt{E_{\mathrm{kin}}}\right)\right|^2$ [143], where $\mathcal{F}$ denotes the Fourier transform, so that

$$E_{\mathrm{kin}} = \frac{1}{(2\pi)^3}\int_0^\infty \hat{E}_{\mathrm{kin}}(k)\, \mathrm{d}k. \tag{B.4}$$

The kinetic energy can be further decomposed into compressible and incompressible parts,

$$E_{\text{kin}} = E^i_{\text{kin}} + E^c_{\text{kin}},$$

by using $\sqrt{n}v_j = (\sqrt{n}v_j)^c + (\sqrt{n}v_j)^i$, with $\nabla(\sqrt{n}v_j)^i = 0$, where $\mathbf{v}$ is the fluid velocity [143]. The spectrum of E^i_{kin} can be defined so that a similar relation to Equation B.4 holds.

B.2 Force

A useful quantity to know for the study of superflow around a obstacle is the force exerted by the fluid on the obstacle, also known as the drag force. Let

$$\begin{aligned} J_k &= nv_k, \\ p &= \frac{g}{2}\left(\frac{n}{m}\right)^2, \\ P_{jk} &= -\frac{\hbar^2}{4m^2} n \frac{\partial}{\partial x_j}\frac{\partial}{\partial x_k}\ln(n), \\ T_{jk} &= nv_jv_k + p\delta_{jk} + P_{jk}, \end{aligned}$$

where J_k is momentum, p is pressure, P_{jk} is the quantum pressure, and T_{jk} is the energy-momentum flux tensor. Then it can be shown that the two equations,

$$\frac{\partial}{\partial t}n + \frac{\partial}{\partial x_k}J_k = 0 \tag{B.5}$$

$$\frac{\partial}{\partial t}J_k + \frac{\partial}{\partial x_j}T_{jk} + n\frac{\partial}{\partial x_k}\left(\frac{V}{m}\right) = 0, \tag{B.6}$$

are equivalent to the continuity equation and modified Euler equation derived from the GPE in Section A.4. Now, using Equation B.6, the kth component of the force can be written,

$$F_k = \frac{\partial}{\partial t}\int_V nv_k \,\mathrm{d}V = -\int_V \frac{\partial}{\partial x_j}T_{jk}\,\mathrm{d}V - \int_V n\frac{\partial}{\partial x_k}\left(\frac{V}{m}\right)\mathrm{d}V. \tag{B.7}$$

B.3 Healing Length

The characteristic length scale of a GPE based system is the healing length, ξ. We can directly find a expression for ξ by considering the minimum length needed for a large perturbation to return to the equilibrium value. Consider only the kinetic and interaction terms in Equation 2.1,

$$\frac{\hbar^2}{2m}\nabla^2\psi = g|\psi(\mathbf{r},t)|^2\psi. \tag{B.8}$$

Dimensionally we can balance these terms by replacing $\nabla^2\psi$ with $2\psi/\xi^2$, leading to

$$\frac{\hbar^2}{m\xi^2} = gn, \tag{B.9}$$

where $n(\mathbf{r}, t) = |\psi(\mathbf{r}, t)|^2$. Rearranging for ξ, we find

$$\xi = \frac{\hbar}{\sqrt{mgn}}. \tag{B.10}$$

Note that, in general, the healing length depends on the condensate density n. However, in a homogeneous system $n(\mathbf{r}, t) = \rho$ is the uniform density, and so we can write the homogeneous healing length as

$$\xi = \frac{\hbar}{\sqrt{mg\rho}}. \tag{B.11}$$

B.4 Speed of sound

The weakly-interacting Bose gas has the dispersion relation,

$$E(p_e) = \sqrt{\frac{ngp_e^2}{m} + \frac{p_e^4}{4m^2}}, \tag{B.12}$$

where $n(\mathbf{r}, t) = |\psi(\mathbf{r}, t)|^2$ is the local condensate density, p_e is the momentum of elementary excitations and $E(p_e)$ their energy [95]. Consider excitations with a small momentum p_e. Here the dispersion relation is linear and sound-like,

$$E(p_e) \approx \sqrt{\frac{ng}{m}}p_e, \tag{B.13}$$

with a speed of sound, $c_{\text{local}} = \sqrt{ng/m}$, dependent on the local condensate density $n(\mathbf{r}, t)$. In a homogeneous system $n(\mathbf{r}, t) = \rho$ is the uniform density, and so the speed of sound in a homogeneous system is

$$c = \sqrt{\frac{\rho g}{m}}. \tag{B.14}$$

Appendix C

Algorithms

C.1 Density/Phase Visualisation Technique

We describe here a technique to visualise both the wavefunction phase and density often used in this thesis. The advantage of the method is that it allows for an easy way to visualise the state of the phase of the system, while also retaining information about what areas of phase are unimportant due to the non-existence of fluid density in that region. Common problems with phase visualisation include the prevalence of ghost vortices[180] when considering a trapped condensate; with this method the discontinuities introduced by ghost vortices are entirely unseen. Previously, this has been attained through the use of masks to hide the unimportant phase regions in trapped systems. These masks are quite arbitrary in nature and an overzealous mask may hide details. Additionally, any condensate with a breathing mode or centre of mass oscillation will periodically extend beyond a hard coded mask. The method outlined in this section instead smoothly hides the unwanted areas of phase by using the density information in the system, disregarding the need for masks completely.

Plotting Algorithm

Initially, the phase plotting is performed as normal, a process involving a conversion of a set of values in the region $[-\pi, \pi)$ to an image (defined as a 2D grid of pixels of size $n \times m$). Examples include MATLAB's image/pcolor commands or gnuplot's splot command. It is recommended, but not required, that a periodic colourmap (such as MATLAB's 'hsv') of equal lightness is used. The $n \times m$ pixels obtained from this procedure will most commonly be stored in the `rgb` format, a triad of values (r, g, b) corresponding to the values of the red, green and blue intensities of the pixel respectively. For a maximum intensity of 255 (a common format for `rgb` pixels), a pixel with value $(0, 0, 0)$ is black, and a pixel of $(255, 255, 255)$ is white.

Each pixel must be instead represented in the `hsl` format, a triad of values (h, s, l) corresponding to the values of the hue, saturation and lightness of the pixel respectively. `hsl` is most commonly represented such that $h \in [0, 360)$ and $s, l \in [0, 1]$. Any pixel of the form $(h, s, 0)$ is black, and any pixel of the form $(h, s, 1)$ is white.

For each pixel, the lightness is then modified so that for a pixel at location (x, y), $l = |\psi(x, y)|^2 / \max(|\psi|^2)$. Once complete, conversion back to `rgb` format must presumably be performed, before finally re-plotting in one's software of choice. Areas of low density will appear in black, while areas of high density will show hues corresponding to the fluid phase at that location.

Colour space conversion - `rgb` to `hsl`

Given an `rgb` format pixel (r, g, b), rescale so that $r, g, b \in [0, 1]$. The brightness of the pixel is described by l. Compute $m = \max(r, g, b)$, $n = \min(r, g, b)$ and set $l = (m+n)/2$. The hue of the pixel is described by h and the strength of that hue is given by s. These quantities depend on the previously calculated m and n. If $m = n$ then the pixel is achromatic and $h = s = 0$, otherwise,

$$s = \begin{cases} \frac{m-n}{2-m-n} & \text{if } l \leq 0.5 \\ \frac{m-n}{m+n} & \text{if } l > 0.5, \end{cases} \tag{C.1}$$

$$h = \begin{cases} 60(\frac{g-b}{m-n}) & \text{if } m = r \\ 60(\frac{b-r}{m-n} + 2) & \text{if } m = g \\ 60(\frac{r-g}{m-n} + 4) & \text{if } m = b. \end{cases} \tag{C.2}$$

The resulting triad (h, s, l) then describes the required pixel in `hsl` format.

Colour space conversion - `hsl` to `rgb`

Given a `hsl` format pixel (h, s, l), compute $c = (1 - |2l - 1|) \times s$ and $h' = h/60$. Using these quantities, calculate $x = c(1 - |h' \mod 2 - 1|)$. To obtain values for r', g' and b', substitute c and x into

$$(r', g', b') = \begin{cases} (c, x, 0) & \text{if } 0 \leq h' < 1 \\ (x, c, 0) & \text{if } 1 \leq h' < 2 \\ (0, c, x) & \text{if } 2 \leq h' < 3 \\ (0, x, c) & \text{if } 3 \leq h' < 4 \\ (x, 0, c) & \text{if } 4 \leq h' < 5 \\ (c, 0, x) & \text{if } 5 \leq h' < 6. \end{cases} \tag{C.3}$$

Compute $m = l - c/2$ and substitute m into $(r, g, b) = (r' + m, g' + m, b' + m)$. The resulting triad (r, g, b) is then the required pixel described in `rgb` format.

C.2 Other Numerical Algorithms

Algorithm 1: An optimisation algorithm to find a chemical potential, μ (to within $\pm\Delta$), so that the equilibrium state approached by the DGPE has the correct atom number. c is a small constant, used to allow for a trade-off between convergence and running time (similar to gradient decent methods).

input : Threshold value Δ, step size c, interaction strength g, initial chemical potential μ_0
output: Chemical potential μ

repeat
  $\mu_1 = \mu_0$;
  $\psi \leftarrow$ Numerically find the ground state for g and μ_0 using imaginary time propagation;
  $n_0 \leftarrow \text{norm}(\psi)$;
  $\psi \leftarrow$ Propagate in real time with dissipation $\gamma = 0.1$;
  $n_1 \leftarrow \text{norm}(\psi)$;
  if $n_1 > n_0$ **then**
    $\mu_0 = \mu_0 - c \times \texttt{abs}(n_1 - n_0)$;
  end
  if $n_1 < n_0$ **then**
    $\mu_0 = \mu_0 + c \times \texttt{abs}(n_1 - n_0)$;
  end
until $\text{abs}(\mu_1 - \mu_0) < \Delta$;
$\mu \leftarrow \mu_0$;

Algorithm 2: RK4 algorithm for advancing a ODE/PDE in time with optional re-normalisation.

input : An initial field ψ, a step size h, optional phase profile Θ

$t \leftarrow 0$, $dt \leftarrow -ih$;
repeat
  Perform a single step of the RK4 Scheme;
  $t = t + dt$;
  $n \leftarrow \text{norm}(\psi)$;
  for all points i **in** ψ **do**
    $\psi[i] \leftarrow \psi[i]/\sqrt{n}$;
  end
  if *we want a phase profile imprinted into the ground state* **then**
    for all points i **in** ψ **do**
      $\psi[i] \leftarrow \Theta[i].|\psi[i]|$;
    end
  end
until *a suitable ground state is found*;
$dt = h$;
repeat
  Perform a single step of the RK4 Scheme;
  $t = t + dt$;
  if *real time normalisation is enabled* **then**
    $n \leftarrow \text{norm}(\psi)$;
    for all points i **in** ψ **do**
      $\psi[i] \leftarrow \psi[i]/\sqrt{n}$;
    end
  end
until *satisfied*;

Algorithm 3: Vortex detection. Outputs a field with positive values near a vortex with circulation 1, negative values near a vortex with circulation -1 and zero valued otherwise. This algorithm will detect ghost vortices.

input : A $n_x \times n_y$ phase profile θ. A line integral width l.
output: A 'vortex field' Q.

for $i \leftarrow 1 + l/2$ **to** $n_x - l/2$ **do**
  for $i \leftarrow 1 + l/2$ **to** $n_y - l/2$ **do**
    $Q[i, j] \leftarrow \oint_{C_{[i,j]}} \nabla\theta \, ds$, where $C_{[i,j]}$ is a square loop of width l centred on point $[i, j]$;
  end
end

Algorithm 4: The B/W Label algorithm. Outputs a field with the same non-zero regions of the input binary field, but with each connected region labeled with a unique value.

input : A $n_x \times n_y$ binary field P.
output: A $n_x \times n_y$ field Q.

Let L be a $4 \times (n_x.n_y)$ field;
Let A be a vector length 4;
for all points i, j **in** L **do** $L[i, j] \leftarrow -1$;
for all points i, j **in** Q **do** $Q[i, j] \leftarrow -1$;
$l_c \leftarrow 1, r_c \leftarrow 0$;
for $i \leftarrow 2$ **to** $n_x - 1$ **do**
  for $j \leftarrow 2$ **to** $n_y - 1$ **do**
    if $P[i, j] = 0$ **then continue**;
    $A \leftarrow (Q[i + 1, j - 1], Q[i, j - 1], Q[i - 1, j - 1], Q[i - 1, j])$;
    for $c \leftarrow 1$ **to** 4 **do**
      if $A[c] \geq 0$ **then**
        $Q[i, j] \leftarrow A[c]$;
        $L[c, l_c] \leftarrow A[c]$;
      end
    end
    if $Q[i, j] \geq 0$ **then** $l_c \leftarrow lc + 1$;
    else
      $Q[i, j] \leftarrow r_c$;
      $rc \leftarrow r_c + 1$;
    end
  end
end
for $r \leftarrow 1$ **to** $(n_x.n_y)$ **do**
  if `max`(*elements of L in row r*)$= -1$ **then continue**;
  $m \leftarrow$ `min`(*elements of L in row r with value* ≥ 0);
  for $c \leftarrow 1$ **to** 4 **do**
    if $L[c, r] \neq m$ **and** $L[c, r] \geq 0$ **then**
      for all points i **in** Q **do**
        if $Q[i] = L[c, r]$ **then** $Q[i] \leftarrow m$;
      end
    end
  end
end

Algorithm 5: Calculate vortex locations and polarity.

input : A $n_x \times n_y$ field θ. A $n_x \times n_y$ field P. A threshold value t.
output: Number of vortices found, n_v. Vortex location, a $2 \times n_v$ field V_l. Vortex polarity, a vector V_p of length n_v.

$Q \leftarrow$ Algorithm 6 $\leftarrow$ Algorithm 3 $\leftarrow (\theta, P)$;
for all points i, j **in** R **do** $R[i, j] \leftarrow 0$;
for all points i, j **in** S **do** $S[i, j] \leftarrow 0$;
$n_v \leftarrow 0$;
for $i \leftarrow 1$ **to** n_x **do**
  for $j \leftarrow 1$ **to** n_y **do**
    if $Q[i, j] > t$ **then** $R[i, j] = 1$;
    if $Q[i, j] < t$ **then** $S[i, j] = 1$;
  end
end
foreach $C \in (R, S)$ **do**
  $D \leftarrow$ Algorithm 4 $\leftarrow C$;
  for $i \leftarrow 1$ **to** `max` (D) **do**
    $V[1, n_v] \leftarrow$ mean row of the points where $D = i$;
    $V[2, n_v] \leftarrow$ mean column of the points where $D = i$;
    if $C = R$ **then** $V[3, n_v] \leftarrow 1$;
    if $C = S$ **then** $V[3, n_v] \leftarrow -1$;
    $n_v \leftarrow n_v + 1$;
  end
end

Algorithm 6: Gaussian convolution. Filters out features with structures of size less than the input filter width. The output is analogous to a 'blurring' of the input field. This allows high frequency noise to be removed.

input : A $n_x \times n_y$ field Q, a Gaussian filter width g.
output: A $n_x \times n_y$ field G.

for $k \leftarrow 1$ **to** n_x **do**
  for $l \leftarrow 1$ **to** n_y **do**
    for $i \leftarrow 1$ **to** n_x **do**
      for $j \leftarrow 1$ **to** n_y **do**
        $G[k, l] \leftarrow G[k, l] + Q[i, j] \times \exp\left(-[(k - i)^2 + (l - j)^2]/g^2\right)$;
      end
    end
    $G[k, l] \leftarrow G[k, l]/(n_x.n_y)$;
  end
end

Algorithm 7: Improved vortex detection. Outputs a field with positive values near a vortex with circulation 1, negative values near a vortex with circulation -1 and zero valued otherwise. This method ignores ghost vortices.

input : A $n_x \times n_y$ density profile R, A $n_x \times n_y$ phase profile θ. A line integral width l.

output : A 'vortex field' Q.

for $i \leftarrow 1 + l/2$ **to** $n_x - l/2$ **do**
  for $i \leftarrow 1 + l/2$ **to** $n_y - l/2$ **do**
    $S \leftarrow R(i, j)/\texttt{max}(R)$;
    $Q[i, j] \leftarrow S \times \oint_{C_{[i,j]}} \nabla\theta \, ds$, where $C_{[i,j]}$ is a square loop of width l centred on point $[i, j]$;
  end
end

Algorithm 8: The Recursive Cluster Algorithm. Decomposes a list of vortices into vortex dipoles or clusters. Vortices are labelled with a cluster number, with vortex dipoles labelled with −1.

```
input  : Vortex locations and polarity. Number of vortices, n_v.
output : A group number for each vortex
n_rca ← 0;
while dipoles continue to be identified do
    for i ← 1 to n_v do
        if vortex i is mutual nearest neighbours with some other vortex j then
            if vortex i is of opposite polarity to j then
                Set both vortices as group -1;
            end
        end
    end
end
while the vortex group configuration continues to change do
    for i ← 1 to n_v do
        for j ← 1 to n_v do
            if either vortex i or j is in group -1 then continue;
            if vortex i and j are closer than either is to a vortex of opposite polarity then
                if one of the two vortices i and j is in a group n then
                    Set both vortices as group n;
                else if both vortices i and j are in groups n and m then
                    Set all vortices in groups n and m as group min(n,m);
                else
                    n_rca ← n_rca + 1;
                    Set both vortices as group n_rca;
                end
            end
        end
    end
end
```

Algorithm 9: The vortex unwinding algorithm. By accurately imprinting a vortex, this algorithm removes vortices from the input wavefunction non-destructively.

input : A $n_x \times n_y$ complex field ψ. A 'safe' distance d. Vortex core radius c.
output: A $n_x \times n_y$ complex field ϕ.

$\phi \leftarrow \psi$;
$(n_v, V_l, V_p) \leftarrow$ Algorithm 5 $\leftarrow \psi$;
for $i \leftarrow 1$ **to** n_v **do**
  if $|V_l[i]| > d$ **then**
    Imprint a vortex of polarity $V_p[i]$ at location $V_l[i]$ in ϕ;
    for $j \leftarrow -c$ **to** c **do**
      for $k \leftarrow -c$ **to** c **do**
        $x \leftarrow V_l[1, i] + j$;
        $y \leftarrow V_l[2, i] + k$;
        $\phi(x, y) \leftarrow \psi_{\text{inf}} \times \texttt{phase}(\psi(x, y))$;
      end
    end
  end
end

Bibliography

[1] C. Pethick and H. Smith, *Bose-Einstein Condensation in Dilute Gases* (Cambridge University Press, 2002), ISBN 9781139811781.

[2] L. P. Pitaevskii and S. Stringari, *Bose-Einstein Condensation* (Oxford University Press, Oxford, 2003), ISBN 9780198507192.

[3] A. Griffin, D. Snoke, and S. Stringari, *Bose-Einstein Condensation* (Cambridge University Press, 1996), ISBN 9780521589901.

[4] D. Tilley and J. Tilley, *Superfluidity and Superconductivity*, Graduate Student Series in Physics (Taylor & Francis, 1990), ISBN 9780750300339.

[5] S. N. Bose, Zeitschrift für Physik **26**, 178 (1924).

[6] A. Einstein, Sitzber. Kgl. Preuss. Akad. Wiss. **23**, 3 (1925).

[7] K. Huang, *Statistical Mechanics* (Wiley, 1987), ISBN 9780471815181.

[8] W. H. Keesom and M. Wolfke, Communications from the Physical Laboratory at the University of Leiden **190**, 17 (1927).

[9] W. Keesom and A. Keesom, Physica **2**, 557 (1935).

[10] P. Kapitza, Nature **141**, 74 (1938).

[11] J. F. Allen and A. D. Misener, Nature **141**, 75 (1938).

[12] F. London, Nature **141**, 643 (1938).

[13] F. London, Phys. Rev. **54**, 947 (1938).

[14] L. D. Landau, J. Phys. (USSR) **5**, 71 (1941).

[15] N. N. Bogoliubov, J. Phys. (USSR) **11**, 23 (1947).

[16] L. Onsager, Nuovo Cimento **6**, 249 (1949).

[17] R. P. Feynman, Progress in Low Temperature Physics, Vol. 1. (Amsterdam: North-Holland) pp. 17–53 (1955).

[18] R. J. Donnelly, *Quantized Vortices in Helium II* (Cambridge University Press, Cambridge, 1991).

[19] L. D. Landau, J. Phys. (USSR) **11**, 91 (1947).

[20] H. Palevsky, K. Otnes, K. E. Larsson, R. Pauli, and R. Stedman, Phys. Rev. **108**, 1346 (1957).

[21] J. L. Yarnell, G. P. Arnold, P. J. Bendt, and E. C. Kerr, Phys. Rev. Lett. **1**, 9 (1958).

[22] D. G. Henshaw, Phys. Rev. Lett. **1**, 127 (1958).

[23] H. Palevsky, K. Otnes, and K. E. Larsson, Phys. Rev. **112**, 11 (1958).

[24] W. D. Phillips, Rev. Mod. Phys. **70**, 721 (1998).

[25] S. Chu, Rev. Mod. Phys. **70**, 685 (1998).

[26] C. N. Cohen-Tannoudji, Rev. Mod. Phys. **70**, 707 (1998).

[27] M. H. Anderson, J. R. Ensher, M. R. Matthews, C. E. Wieman, and E. A. Cornell, Science **269**, 198 (1995).

[28] K. B. Davis, M. O. Mewes, M. R. Andrews, N. J. van Druten, D. S. Durfee, D. M. Kurn, and W. Ketterle, Phys. Rev. Lett. **75**, 3969 (1995).

[29] *"The Nobel Prize in Physics 2001"* (The Royal Swedish Academy of Sciences, 2001).

[30] H. F. Hess, Phys. Rev. B **34**, 3476 (1986).

[31] C. E. Hecht, Physica **25**, 1159 (1959).

[32] I. F. Silvera and J. T. M. Walraven, Phys. Rev. Lett. **44**, 164 (1980).

[33] I. F. Silvera and J. T. M. Walraven, Progress in Low Temperature Physics X (Elsevier, Amsterdam) p. 139 (1986).

[34] W. Ketterle, Rev. Mod. Phys. **74**, 1131 (2002).

[35] E. A. Cornell and C. E. Wieman, Rev. Mod. Phys. **74**, 875 (2002).

[36] C. C. Bradley, C. A. Sackett, J. J. Tollett, and R. G. Hulet, Phys. Rev. Lett. **75**, 1687 (1995).

[37] C. C. Bradley, C. A. Sackett, and R. G. Hulet, Phys. Rev. Lett. **78**, 985 (1997).

[38] S. L. Cornish, N. R. Claussen, J. L. Roberts, E. A. Cornell, and C. E. Wieman, Phys. Rev. Lett. **85**, 1795 (2000).

[39] G. Modugno, G. Ferrari, G. Roati, R. J. Brecha, A. Simoni, and M. Inguscio, Science **294**, 1320 (2001).

[40] A. Robert, O. Sirjean, A. Browaeys, J. Poupard, S. Nowak, D. Boiron, C. I. Westbrook, and A. Aspect, Science **292**, 461 (2001).

[41] T. Weber, J. Herbig, M. Mark, H.-C. Nägerl, and R. Grimm, Science **299**, 232 (2003).

[42] S. Kraft, F. Vogt, O. Appel, F. Riehle, and U. Sterr, Phys. Rev. Lett. **103**, 130401 (2009).

[43] M. Lu, N. Q. Burdick, S. H. Youn, and B. L. Lev, Phys. Rev. Lett. **107**, 190401 (2011).

[44] S. Stellmer, M. K. Tey, B. Huang, R. Grimm, and F. Schreck, Phys. Rev. Lett. **103**, 200401 (2009).

[45] Y. N. M. de Escobar, P. G. Mickelson, M. Yan, B. J. DeSalvo, S. B. Nagel, and T. C. Killian, Phys. Rev. Lett. **103**, 200402 (2009).

[46] S. Stellmer, M. K. Tey, R. Grimm, and F. Schreck, Phys. Rev. A **82**, 041602 (2010).

[47] P. G. Mickelson, Y. N. Martinez de Escobar, M. Yan, B. J. DeSalvo, and T. C. Killian, Phys. Rev. A **81**, 051601 (2010).

[48] Y. Takasu, K. Maki, K. Komori, T. Takano, K. Honda, M. Kumakura, T. Yabuzaki, and Y. Takahashi, Phys. Rev. Lett. **91**, 040404 (2003).

[49] A. Griesmaier, J. Werner, S. Hensler, J. Stuhler, and T. Pfau, Phys. Rev. Lett. **94**, 160401 (2005).

[50] D. G. Fried, T. C. Killian, L. Willmann, D. Landhuis, S. C. Moss, D. Kleppner, and T. J. Greytak, Phys. Rev. Lett. **81**, 3811 (1998).

[51] F. Pereira Dos Santos, J. Léonard, J. Wang, C. J. Barrelet, F. Perales, E. Rasel, C. S. Unnikrishnan, M. Leduc, and C. Cohen-Tannoudji, Phys. Rev. Lett. **86**, 3459 (2001).

[52] S. P. Mathew and S. N. Kaul, Journal of Physics: Condensed Matter **23**, 266003 (2011).

[53] J. Kasprzak, M. Richard, S. Kundermann, A. Baas, P. Jeambrun, J. M. J. Keeling, F. M. Marchetti, M. H. Szymanska, R. Andre, J. L. Staehli, et al., Nature **443**, 409 (2006).

[54] G. Ferrari, M. Inguscio, W. Jastrzebski, G. Modugno, G. Roati, and A. Simoni, Phys. Rev. Lett. **89**, 053202 (2002).

[55] G. Modugno, M. Modugno, F. Riboli, G. Roati, and M. Inguscio, Phys. Rev. Lett. **89**, 190404 (2002).

[56] G. Thalhammer, G. Barontini, L. De Sarlo, J. Catani, F. Minardi, and M. Inguscio, Phys. Rev. Lett. **100**, 210402 (2008).

[57] D. J. McCarron, H. W. Cho, D. L. Jenkin, M. P. Köppinger, and S. L. Cornish, Phys. Rev. A **84**, 011603 (2011).

[58] K. Henderson, C. Ryu, C. MacCormick, and M. G. Boshier, New Journal of Physics **11**, 043030 (2009).

[59] C. Ryu, M. F. Andersen, P. Cladé, V. Natarajan, K. Helmerson, and W. D. Phillips, Phys. Rev. Lett. **99**, 260401 (2007).

[60] A. Ramanathan, K. C. Wright, S. R. Muniz, M. Zelan, W. T. Hill, C. J. Lobb, K. Helmerson, W. D. Phillips, and G. K. Campbell, Phys. Rev. Lett. **106**, 130401 (2011).

[61] A. L. Gaunt, T. F. Schmidutz, I. Gotlibovych, R. P. Smith, and Z. Hadzibabic, Phys. Rev. Lett. **110**, 200406 (2013).

[62] L. Chomaz, L. Corman, T. Bienaimé, R. Desbuquois, C. Weitenberg, S. Nascimbéne, J. Beugnon, and J. Dalibard, Nat. Comm. **6**, 6162 (2015).

[63] M. Greiner, O. Mandel, T. Esslinger, T. W. Hänsch, and I. Bloch, Nature **415**, 39 (2002).

[64] L. J. LeBlanc, A. B. Bardon, J. McKeever, M. H. T. Extavour, D. Jervis, J. H. Thywissen, F. Piazza, and A. Smerzi, Phys. Rev. Lett. **106**, 025302 (2011).

[65] A. Görlitz, J. M. Vogels, A. E. Leanhardt, C. Raman, T. L. Gustavson, J. R. Abo-Shaeer, A. P. Chikkatur, S. Gupta, S. Inouye, T. Rosenband, et al., Phys. Rev. Lett. **87**, 130402 (2001).

[66] F. Schreck, L. Khaykovich, K. L. Corwin, G. Ferrari, T. Bourdel, J. Cubizolles, and C. Salomon, Phys. Rev. Lett. **87**, 080403 (2001).

[67] H. Moritz, T. Stöferle, M. Köhl, and T. Esslinger, Phys. Rev. Lett. **91**, 250402 (2003).

[68] D. Rychtarik, B. Engeser, H.-C. Nägerl, and R. Grimm, Phys. Rev. Lett. **92**, 173003 (2004).

[69] T. W. Neely, E. C. Samson, A. S. Bradley, M. J. Davis, and B. P. Anderson, Phys. Rev. Lett. **104**, 160401 (2010).

[70] D. V. Freilich, D. M. Bianchi, A. M. Kaufman, T. K. Langin, and D. S. Hall, Science **329**, 1182 (2010).

[71] P. Drazin and R. Johnson, *Solitons: An Introduction*, Cambridge Computer Science Texts (Cambridge University Press, 1989), ISBN 9780521336550.

[72] S. Stellmer, C. Becker, P. Soltan-Panahi, E.-M. Richter, S. Dörscher, M. Baumert, J. Kronjäger, K. Bongs, and K. Sengstock, Phys. Rev. Lett. **101**, 120406 (2008).

[73] J. Weiner, *Cold and Ultracold Collisions in Quantum Microscopic and Mesoscopic Systems* (Cambridge University Press, 2003), ISBN 9781139439497.

[74] S. Inouye, M. R. Andrews, J. Stenger, H.-J. Miesner, D. M. Stamper-Kurn, and W. Ketterle, Nature **392**, 151 (1998), ISSN 0028-0836.

[75] J. Stenger, S. Inouye, M. R. Andrews, H.-J. Miesner, D. M. Stamper-Kurn, and W. Ketterle, Phys. Rev. Lett. **82**, 2422 (1999).

[76] L. P. Pitaevskii, Zh. Eksp. Teor. Fiz. **40**, 646 (1961).

[77] E. Gross, Nuovo Cimento **20**, 454 (1961).

[78] F. Dalfovo, S. Giorgini, L. P. Pitaevskii, and S. Stringari, Rev. Mod. Phys. **71**, 463 (1999).

[79] H.-H. Chen and C.-S. Liu, Phys. Rev. Lett. **37**, 693 (1976).

[80] D. Schumayer and B. Apagyi, Phys. Rev. A **65**, 053614 (2002).

[81] B. Malomed, in *Encyclopedia of Nonlinear Science*, edited by A. Scott (Routledge, New York, 2005), pp. 639–643.

[82] J. Denschlag, J. E. Simsarian, D. L. Feder, C. W. Clark, L. A. Collins, J. Cubizolles, L. Deng, E. W. Hagley, K. Helmerson, W. P. Reinhardt, et al., Science **287**, 97 (2000).

[83] S. Burger, K. Bongs, S. Dettmer, W. Ertmer, K. Sengstock, A. Sanpera, G. V. Shlyapnikov, and M. Lewenstein, Phys. Rev. Lett. **83**, 5198 (1999).

[84] B. P. Anderson, P. C. Haljan, C. A. Regal, D. L. Feder, L. A. Collins, C. W. Clark, and E. A. Cornell, Phys. Rev. Lett. **86**, 2926 (2001).

[85] Z. Dutton, M. Budde, C. Slowe, and L. V. Hau, Science **293**, 663 (2001).

[86] A. Fetter, Journal of Low Temperature Physics **161**, 445 (2010), ISSN 0022-2291.

[87] C. Lobo, A. Sinatra, and Y. Castin, Phys. Rev. Lett. **92**, 020403 (2004).

[88] B. P. Anderson, P. C. Haljan, C. E. Wieman, and E. A. Cornell, Phys. Rev. Lett. **85**, 2857 (2000).

[89] E. J. Yarmchuk, M. J. V. Gordon, and R. E. Packard, Phys. Rev. Lett. **43**, 214 (1979).

[90] K. W. Madison, F. Chevy, W. Wohlleben, and J. Dalibard, Phys. Rev. Lett. **84**, 806 (2000).

[91] E. Hodby, G. Hechenblaikner, S. A. Hopkins, O. M. Maragò, and C. J. Foot, Phys. Rev. Lett. **88**, 010405 (2002).

[92] J. R. Abo-Shaeer, C. Raman, J. M. Vogels, and W. Ketterle, Science **292**, 476 (2001).

[93] P. C. Haljan, I. Coddington, P. Engels, and E. A. Cornell, Phys. Rev. Lett. **87**, 210403 (2001).

[94] A. L. Fetter and A. A. Svidzinsky, Journal of Physics: Condensed Matter **13**, R135 (2001).

[95] P. Nozières and D. Pines, *The Theory of Quantum Liquids II* (Addison-Wesley, Redwood City, 1990).

[96] T. W. B. Kibble, Journal of Physics A: Mathematical and General **9**, 1387 (1976).

[97] W. H. Zurek, Nature **317**, 505 (1985).

[98] J. R. Anglin and W. H. Zurek, Phys. Rev. Lett. **83**, 1707 (1999).

[99] M. R. Matthews, B. P. Anderson, P. C. Haljan, D. S. Hall, C. E. Wieman, and E. A. Cornell, Phys. Rev. Lett. **83**, 2498 (1999).

[100] L. Dobrek, M. Gajda, M. Lewenstein, K. Sengstock, G. Birkl, and W. Ertmer, Phys. Rev. A. **60**, 3381(R) (1999).

[101] A. E. Leanhardt, A. Görlitz, A. P. Chikkatur, D. Kielpinski, Y. Shin, D. E. Pritchard, and W. Ketterle, Phys. Rev. Lett. **89**, 190403 (2002).

[102] B. Jackson, J. F. McCann, and C. S. Adams, Phys. Rev. A **61**, 051603 (2000).

[103] C. Raman, J. R. Abo-Shaeer, J. M. Vogels, K. Xu, and W. Ketterle, Phys. Rev. Lett. **87**, 210402 (2001).

[104] S. Inouye, S. Gupta, T. Rosenband, A. P. Chikkatur, A. Görlitz, T. L. Gustavson, A. E. Leanhardt, D. E. Pritchard, and W. Ketterle, Phys. Rev. Lett. **87**, 080402 (2001).

[105] E. A. L. Henn, J. A. Seman, G. Roati, K. M. F. Magalhães, and V. S. Bagnato, Phys. Rev. Lett. **103**, 045301 (2009).

[106] W. J. Kwon, G. Moon, J.-Y. Choi, S. W. Seo, and Y.-I. Shin, Phys. Rev. A **90**, 063627 (2014).

[107] J. R. Abo-Shaeer, C. Raman, and W. Ketterle, Phys. Rev. Lett. **88**, 070409 (2002).

[108] K. W. Madison, F. Chevy, V. Bretin, and J. Dalibard, Phys. Rev. Lett. **86**, 4443 (2001).

[109] P. Engels, I. Coddington, P. C. Haljan, V. Schweikhard, and E. A. Cornell, Phys. Rev. Lett. **90**, 170405 (2003).

[110] Y. Shin, M. Saba, M. Vengalattore, T. A. Pasquini, C. Sanner, A. E. Leanhardt, M. Prentiss, D. E. Pritchard, and W. Ketterle, Phys. Rev. Lett. **93**, 160406 (2004).

[111] W. F. Vinen, Proceedings of the Royal Society of London A: Mathematical, Physical and Engineering Sciences **260**, 218 (1961).

[112] G. P. Bewley, D. P. Lathrop, and K. R. Sreenivasan, Nature **441**, 588 (2006).

[113] L. D. Carr, C. W. Clark, and W. P. Reinhardt, Phys. Rev. A **62**, 063611 (2000).

[114] L. D. Carr, C. W. Clark, and W. P. Reinhardt, Phys. Rev. A **62**, 063610 (2000).

[115] M. Remoissenet, *Waves Called Solitons: Concepts and Experiments*, Advanced Texts in Physics (Springer Berlin Heidelberg, 2013), ISBN 9783662037904.

[116] Y. S. Kivshar and B. Luther-Davies, Phys. Rep. **298**, 81 (1998).

[117] P. Kevrekidis, D. Frantzeskakis, and R. Carretero-González, *Emergent Nonlinear Phenomena in Bose-Einstein Condensates: Theory and Experiment*, Springer Series on Atomic, Optical, and Plasma Physics (Springer Berlin Heidelberg, 2007), ISBN 9783540735915.

[118] D. J. Frantzeskakis, Journal of Physics A: Mathematical and Theoretical **43**, 213001 (2010).

[119] D. L. Feder, M. S. Pindzola, L. A. Collins, B. I. Schneider, and C. W. Clark, Phys. Rev. A **62**, 053606 (2000).

[120] J. Brand and W. P. Reinhardt, Phys. Rev. A **65**, 043612 (2002).

[121] V. Tikhonenko, J. Christou, B. Luther-Davies, and Y. S. Kivshar, Opt. Lett. **21**, 1129 (1996).

[122] J. S. Russell, Report of the fourteenth meeting of the British Association for the Advancement of Science **311**, Plates XLVII (1845).

[123] H. C. Kim, R. L. Stenzel, and A. Y. Wong, Phys. Rev. Lett. **33**, 886 (1974).

[124] K. Naugolnykh and L. Ostrovsky, *Nonlinear Wave Processes in Acoustics*, Cambridge Texts in Applied Mathematics (Cambridge University Press, 1998), ISBN 9780521399845.

[125] G. Agrawal, *Nonlinear Fiber Optics*, Optics and Photonics (Elsevier Science, 2001), ISBN 9780080479743.

[126] A. Hasegawa and Y. Kodama, *Solitons in optical communications*, Oxford series in optical and imaging sciences (Clarendon Press, 1995), ISBN 9780198565079.

[127] K. E. Strecker, G. B. Partridge, A. G. Truscott, and R. G. Hulet, Nature **417**, 150 (2002).

[128] L. Khaykovich, F. Schreck, G. Ferrari, T. Bourdel, J. Cubizolles, L. D. Carr, Y. Castin, and C. Salomon, Science **296**, 1290 (2002).

[129] R. Dodd, *Solitons and nonlinear wave equations* (Academic Press, 1982), ISBN 9780122191206.

[130] P. Emplit, J. P. Hamaide, F. Reynaud, G. Froehly, and A. Barthelemy, Opt. Commun. **62**, 374 (1987).

[131] B. Denardo, W. Wright, S. Putterman, and A. Larraza, Phys. Rev. Lett. **64**, 1518 (1990).

[132] B. Denardo, B. Galvin, A. Greenfield, A. Larraza, S. Putterman, and W. Wright, Phys. Rev. Lett. **68**, 1730 (1992).

[133] M. Chen, M. A. Tsankov, J. M. Nash, and C. E. Patton, Phys. Rev. Lett. **70**, 1707 (1993).

[134] A. Weller, J. P. Ronzheimer, C. Gross, J. Esteve, M. K. Oberthaler, D. J. Frantzeskakis, G. Theocharis, and P. G. Kevrekidis, Phys. Rev. Lett. **101**, 130401 (2008).

[135] P. Engels and C. Atherton, Phys. Rev. Lett. **99**, 160405 (2007).

[136] I. Shomroni, E. Lahoud, S. Levy, and J. Steinhauer, Nat. Phys. **5**, 193 (2009).

[137] P. Davidson, *Turbulence: An Introduction for Scientists and Engineers* (OUP Oxford, 2004), ISBN 9780191589850.

[138] D. I. Bradley, S. N. Fisher, A. M. Guenault, R. P. Haley, G. R. Pickett, D. Potts, and V. Tsepelin, Nat. Phys. **7**, 473 (2011).

[139] L. Skrbek and K. R. Sreenivasan, Physics of Fluids **24**, 011301 (2012).

[140] L. Boué, V. L'vov, A. Pomyalov, and I. Procaccia, Phys. Rev. Lett. **110**, 014502 (2013).

[141] C. F. Barenghi, L. Skrbek, and K. R. Sreenivasan, Proceedings of the National Academy of Sciences **111**, 4647 (2014).

[142] D. E. Zmeev, P. M. Walmsley, A. I. Golov, P. V. E. McClintock, S. N. Fisher, and W. F. Vinen, Phys. Rev. Lett. **115**, 155303 (2015).

[143] C. Nore, M. Abid, and M. E. Brachet, Phys. Rev. Lett. **78**, 3896 (1997).

[144] M. Kobayashi and M. Tsubota, Phys. Rev. Lett. **94**, 065302 (2005).

[145] J. Yepez, G. Vahala, L. Vahala, and M. Soe, Phys. Rev. Lett. **103**, 084501 (2009).

[146] E. Fonda, D. P. Meichle, N. T. Ouellette, S. Hormoz, K. R. Sreenivasan, and D. P. Lathrop, *Visualization of kelvin waves on quantum vortices* (2012), `arXiv:1210.5194`.

[147] C. F. Barenghi, R. Donnelly, and W. Vinen, *Quantized Vortex Dynamics and Superfluid Turbulence* (Springer, Berlin, 2001).

[148] T. Frisch, Y. Pomeau, and S. Rica, Phys. Rev. Lett. **69**, 1644 (1992).

[149] J. Koplik and H. Levine, Phys. Rev. Lett. **71**, 1375 (1993).

[150] J. Koplik and H. Levine, Phys. Rev. Lett. **76**, 4745 (1996).

[151] M. Leadbeater, T. Winiecki, D. C. Samuels, C. F. Barenghi, and C. S. Adams, Phys. Rev. Lett. **86**, 1410 (2001).

[152] N. G. Berloff, Phys. Rev. A **69**, 053601 (2004).

[153] S. Davis, P. Hendry, and P. McClintock, Physica B: Condensed Matter **280**, 43 (2000).

[154] A. Guénault, V. Keith, C. Kennedy, S. Mussett, and G. Pickett, Journal of Low Temperature Physics **62**, 511 (1986).

[155] D. Bradley, M. Človečko, M. Fear, S. Fisher, A. Guénault, R. Haley, C. Lawson, G. Pickett, R. Schanen, V. Tsepelin, et al., Journal of Low Temperature Physics **165**, 114 (2011).

[156] S. N. Fisher, A. J. Hale, A. M. Guénault, and G. R. Pickett, Phys. Rev. Lett. **86**, 244 (2001).

[157] J. Jäger, B. Schuderer, and W. Schoepe, Phys. Rev. Lett. **74**, 566 (1995).

[158] R. Blaauwgeers, M. Blazkova, M. Človečko, V. Eltsov, R. de Graaf, J. Hosio, M. Krusius, D. Schmoranzer, W. Schoepe, L. Skrbek, et al., Journal of Low Temperature Physics **146**, 537 (2007).

[159] D. I. Bradley, M. Človečko, S. N. Fisher, D. Garg, E. Guise, R. P. Haley, O. Kolosov, G. R. Pickett, V. Tsepelin, D. Schmoranzer, et al., Phys. Rev. B **85**, 014501 (2012).

[160] J. Maurer and P. Tabeling, EPL (Europhysics Letters) **43**, 29 (1998).

[161] J. Salort, C. Baudet, B. Castaing, B. Chabaud, F. Daviaud, T. Didelot, P. Diribarne, B. Dubrulle, Y. Gagne, F. Gauthier, et al., Physics of Fluids **22**, 125102 (2010).

[162] L. Skrbek and W. Vinen, in *Quantum Turbulence*, edited by M. Tsubota and W. Halperin (Elsevier, 2009), vol. 16 of *Progress in Low Temperature Physics*, pp. 195 – 246.

[163] W. F. Vinen, Proceedings of the Royal Society of London A: Mathematical, Physical and Engineering Sciences **240**, 114 (1957), ISSN 0080-4630.

[164] P. M. Walmsley, A. I. Golov, H. E. Hall, A. A. Levchenko, and W. F. Vinen, Phys. Rev. Lett. **99**, 265302 (2007).

[165] W. F. Vinen, Phys. Rev. B **61**, 1410 (2000).

[166] A. T. Powis, S. J. Sammut, and T. P. Simula, Phys. Rev. Lett. **113**, 165303 (2014).

[167] W. J. Kwon, G. Moon, S. W. Seo, and Y. Shin, Phys. Rev. A **91**, 053615 (2015).

[168] C. Lawson, Ph.D. thesis, Lancaster University (2013).

[169] N. P. Proukakis and B. Jackson, Journal of Physics B: Atomic, Molecular and Optical Physics **41**, 203002 (2008).

[170] P. Roberts and N. Berloff, in *Quantized Vortex Dynamics and Superfluid Turbulence*, edited by C. Barenghi, R. Donnelly, and W. Vinen (Springer Berlin Heidelberg, 2001), vol. 571 of *Lecture Notes in Physics*, pp. 235–257, ISBN 978-3-540-42226-6.

[171] L. Warszawski and A. Melatos, Monthly Notices of the Royal Astronomical Society **415**, 1611 (2011).

[172] N. G. Parker, Ph.D. thesis, The University of Durham (2004).

[173] J. Thijssen, *Computational Physics* (Cambridge University Press, 1999), ISBN 9780521575881.

[174] W. Bao and W. Tang, Journal of Computational Physics **187**, 230 (2003).

[175] M. Edwards and K. Burnett, Phys. Rev. A **51**, 1382 (1995).

[176] W. H. Press, S. A. Teukolsky, W. T. Vetterling, and B. P. Flannery, *Numerical Recipes in FORTRAN; The Art of Scientific Computing* (Cambridge University Press, New York, NY, USA, 1993), 2nd ed., ISBN 0521437164.

[177] M. L. Chiofalo, S. Succi, and M. P. Tosi, Phys. Rev. E **62**, 7438 (2000).

[178] L. Pitaevskii and E. Lifshitz, *Physical Kinetics: Volume 10 (Course of Theoretical Physics)* (Butterworth-Heinemann, 1981), ISBN 0750626356.

[179] S. Choi, S. A. Morgan, and K. Burnett, Phys. Rev. A **57**, 4057 (1998).

[180] M. Tsubota, K. Kasamatsu, and M. Ueda, Phys. Rev. A **65**, 023603 (2002).

[181] E. Madarassy and C. F. Barenghi, Journal of Low Temperature Physics **152**, 122 (2008).

[182] A. A. Penckwitt, R. J. Ballagh, and C. W. Gardiner, Phys. Rev. Lett. **89**, 260402 (2002).

[183] C. W. Gardiner, P. Zoller, R. J. Ballagh, and M. J. Davis, Phys. Rev. Lett. **79**, 1793 (1997).

[184] N. G. Berloff and B. V. Svistunov, Phys. Rev. A **66**, 013603 (2002).

[185] P. Carruthers and K. S. Dy, Phys. Rev. **147**, 214 (1966).

[186] V. E. Zakharov and A. B. Shabat, Sov. Phys. JETP **34**, 62 (1972).

[187] V. E. Zakharov and A. B. Shabat, Sov. Phys. JETP **37**, 823 (1973).

[188] N. G. Berloff, Journal of Physics A: Mathematical and General **37**, 1617 (2004).

[189] M. J. Davis, S. A. Morgan, and K. Burnett, Phys. Rev. Lett. **87**, 160402 (2001).

[190] D. I. Bradley, D. O. Clubb, S. N. Fisher, A. M. Guénault, R. P. Haley, C. J. Matthews, G. R. Pickett, V. Tsepelin, and K. Zaki, Phys. Rev. Lett. **95**, 035302 (2005).

[191] J. Maurer and P. Tabeling, EPL (Europhysics Letters) **43**, 29 (1998).

[192] T. P. Simula and P. B. Blakie, Phys. Rev. Lett. **96**, 020404 (2006).

[193] K. Sasaki, N. Suzuki, and H. Saito, Phys. Rev. Lett. **104**, 150404 (2010).

[194] A. C. White, C. F. Barenghi, and N. P. Proukakis, Phys. Rev. A **86**, 013635 (2012).

[195] M. T. Reeves, T. P. Billam, B. P. Anderson, and A. S. Bradley, Phys. Rev. Lett. **110**, 104501 (2013).

[196] M. T. Reeves, T. P. Billam, B. P. Anderson, and A. S. Bradley, Phys. Rev. A **89**, 053631 (2014).

[197] A. C. White, B. P. Anderson, and V. S. Bagnato, Proceedings of the National Academy of Sciences **111**, 4719 (2014).

[198] T. Simula, M. J. Davis, and K. Helmerson, Phys. Rev. Lett. **113**, 165302 (2014).

[199] M. T. Reeves, T. P. Billam, B. P. Anderson, and A. S. Bradley, Phys. Rev. Lett. **114**, 155302 (2015).

[200] C. Rorai, J. Skipper, R. M. Kerr, and K. R. Sreenivasan, *Approach and separation of quantum vortices with balanced cores* (2014), `arXiv:1410.1259`.

[201] A. Villois, G. Krstulovic, D. Proment, and H. Salman, *Vortex filament tracking method in the Gross-Pitaevskii model* (2016), `arXiv:1604.03595`.

[202] R. Larson and B. Edwards, *Multivariable Calculus* (Cengage Learning, 2013), ISBN 9781285060293.

[203] L. Shapiro and G. Stockman, *Computer Vision* (Prentice Hall, 2001).

[204] R. P. Duncan, Journal of Ecology **81**, 403 (1993).

[205] C. J. Peterson and E. R. Squiers, Journal of Ecology **83**, 847 (1995).

[206] D. Stoyan and A. Penttinen, Statistical Science **15**, 61 (2000).

[207] N. E. Stamp and J. R. Lucas, Journal of Ecology **78**, 589 (1990).

[208] K. F. Gaines, A. L. Bryan, and P. M. Dixon, Waterbirds **23**, 64 (2000).

[209] P. J. Diggle and A. G. Chetwynd, Biometrics **47**, 1155 (1991).

[210] A. W. Baggaley, C. F. Barenghi, A. Shukurov, and Y. A. Sergeev, EPL (Europhysics Letters) **98**, 26002 (2012).

[211] P. M. Dixon, Encyclopaedia of Environments **3**, 1796 (2002).

[212] B. D. Ripley, Journal of Applied Probability **13**, 255 (1976).

[213] B. D. Ripley, Journal of the Royal Statistical Society **41**, 368 (1979).

[214] H. W. Kuhn, Naval Research Logistics Quarterly **2**, 83 (1955).

[215] S. Taneda, J. Phys. Soc. Jpn. **11**, 302 (1956).

[216] S. Taneda, J. Phys. Soc. Jpn. **50**, 1398 (1981).

[217] M. Van Dyke, *An Album of Fluid Motion* (Parabolic Press, Stanford, CA, 1982).

[218] A. W. Baggaley, J. Laurie, and C. F. Barenghi, Phys. Rev. Lett. **109**, 205304 (2012).

[219] V. S. L'vov, V. Nazarenko, and G. E. Volovik, Journal of Experimental and Theoretical Physics Letters **80**, 479 (2004).

[220] U. Frisch, *Turbulence. The legacy of A .N. Kolmogorov* (Cambridge University Press, Cambridge, 1995).

[221] C. F. Barenghi, V. L'vov, and P.-E. Roche, *Velocity spectra of quantum turbulence: experiments, numerics and models* (2013), `arXiv:1306.6248`.

[222] M. R. Smith, D. K. Hilton, and S. Van Sciver, Phys. Fluids **11**, 1 (1999).

[223] T. Zhang and S. Van Sciver, Nature Physics **1**, 36 (2005).

[224] Y. Sergeev and C. Barenghi, J. Low Temp. Phys. **157**, 429 (2009).

[225] R. Hänninen, M. Tsubota, and W. F. Vinen, Phys. Rev. B **75**, 064502 (2007).

[226] S. Fujiyama and M. Tsubota, Phys. Rev. B **79**, 094513 (2009).

[227] R. Goto, S. Fujiyama, H. Yano, Y. Nago, N. Hashimoto, K. Obara, O. Ishikawa, M. Tsubota, and T. Hata, Phys. Rev. Lett. **100**, 045301 (2008).

[228] C. Nore, M. E. Brachet, and S. Fauve, Physica D **65**, 154 (1993).

[229] T. Winiecki, J. F. McCann, and C. S. Adams, Phys. Rev. Lett. **82**, 5186 (1999).

[230] T. Winiecki, B. Jackson, J. F. McCann, and C. S. Adams, Journal of Physics B: Atomic, Molecular and Optical Physics **33**, 4069 (2000).

[231] C. Huepe and M. E. Brachet, Physica D **140**, 126 (2000).

[232] J. S. Stießberger and W. Zwerger, Phys. Rev. A **62**, 061601 (2000).

[233] M. Crescimanno, C. G. Koay, R. Peterson, and R. Walsworth, Phys. Rev. A **62**, 063612 (2000).

[234] N. G. Berloff and P. H. Roberts, J. Phys. A **33**, 4025 (2000).

[235] S. Rica, Physica D **148**, 221 (2001).

[236] C. T. Pham, C. Nore, and M. E. Brachet, Comptes Rendus Physique **5**, 3 (2004).

[237] B. Jackson, J. F. McCann, and C. S. Adams, Phys. Rev. Lett. **80**, 3903 (1998).

[238] K. Fujimoto and M. Tsubota, Phys. Rev. A **83**, 053609 (2011).

[239] T. Aioi, T. Kadokura, T. Kishimoto, and H. Saito, Phys. Rev. X **1**, 021003 (2011).

[240] G. A. El, A. Gammal, and A. M. Kamchatnov, Phys. Rev. Lett. **97**, 180405 (2006).

[241] I. Carusotto, S. X. Hu, L. A. Collins, and A. Smerzi, Phys. Rev. Lett. **97**, 260403 (2006).

[242] C. Raman, M. Köhl, R. Onofrio, D. S. Durfee, C. E. Kuklewicz, Z. Hadzibabic, and W. Ketterle, Phys. Rev. Lett. **83**, 2502 (1999).

[243] R. Onofrio, C. Raman, J. M. Vogels, J. R. Abo-Shaeer, A. P. Chikkatur, and W. Ketterle, Phys. Rev. Lett. **85**, 2228 (2000).

[244] H. Schlichting and A. Ulrich, Jb. dt. Luftfahrtforschung I **1**, 8 (1942).

[245] T. Winiecki, Ph.D. thesis, The University of Durham (2001).

[246] T. Winiecki, J. F. McCann, and C. S. Adams, EPL (Europhysics Letters) **48**, 475 (1999).

[247] D. H. Wacks, A. W. Baggaley, and C. F. Barenghi, Physics of Fluids **26**, 027102 (2014).

[248] M. Blažková, D. Schmoranzer, L. Skrbek, and W. F. Vinen, Phys. Rev. B **79**, 054522 (2009).

[249] N. G. Parker and C. S. Adams, Phys. Rev. Lett. **95**, 145301 (2005).

[250] S. Middelkamp, P. J. Torres, P. G. Kevrekidis, D. J. Frantzeskakis, R. Carretero-González, P. Schmelcher, D. V. Freilich, and D. S. Hall, Phys. Rev. A **84**, 011605 (2011).

[251] T. W. Neely, A. S. Bradley, E. C. Samson, S. J. Rooney, E. M. Wright, K. J. H. Law, R. Carretero-González, P. G. Kevrekidis, M. J. Davis, and B. P. Anderson, Phys. Rev. Lett. **111**, 235301 (2013).

[252] A. M. Mateo and V. Delgado, Phys. Rev. A **74**, 065602 (2006).

[253] N. G. Parker and D. H. J. O'Dell, Phys. Rev. A **78**, 041601 (2008).

[254] B. Jackson, N. P. Proukakis, C. F. Barenghi, and E. Zaremba, Phys. Rev. A **79**, 053615 (2009).

[255] Y. Shin, private communication.

[256] A. J. Allen, E. Zaremba, C. F. Barenghi, and N. P. Proukakis, Phys. Rev. A **87**, 013630 (2013).

[257] D. Yan, R. Carretero-González, D. J. Frantzeskakis, P. G. Kevrekidis, N. P. Proukakis, and D. Spirn, Phys. Rev. A **89**, 043613 (2014).

[258] G. W. Stagg, N. G. Parker, and C. F. Barenghi, Journal of Physics B: Atomic, Molecular and Optical Physics **47**, 095304 (2014).

[259] N. G. Parker, N. P. Proukakis, C. F. Barenghi, and C. S. Adams, Phys. Rev. Lett. **92**, 160403 (2004).

[260] G. W. Stagg, A. J. Allen, N. G. Parker, and C. F. Barenghi, Phys. Rev. A **91**, 013612 (2015).

[261] A. Cidrim, F. E. A. dos Santos, L. Galantucci, V. S. Bagnato, and C. F. Barenghi, Phys. Rev. A **93**, 033651 (2016).

[262] A. J. Groszek, T. P. Simula, D. M. Paganin, and K. Helmerson, *Onsager vortex formation in bose-einstein condensates in two-dimensional power-law traps* (2015), `arXiv:1511.06552`.

[263] S. Nazarenko and M. Onorato, Journal of Low Temperature Physics **146**, 31 (2007).

[264] C. Rorai, K. R. Sreenivasan, and M. E. Fisher, Phys. Rev. B **88**, 134522 (2013).

[265] S. Prabhakar, R. P. Singh, S. Gautam, and D. Angom, Journal of Physics B: Atomic, Molecular and Optical Physics **46**, 125302 (2013).

[266] S. Zuccher, M. Caliari, A. Baggaley, and C. Barenghi, Physics of Fluids **24**, 125108 (2012).

[267] S. Nazarenko and M. Onorato, Journal of Low Temperature Physics **146**, 31 (2007).

[268] W. J. Kwon, S. W. Seo, and Y.-I. Shin, Phys. Rev. A **92**, 033613 (2015).

[269] R. Desbuquois, L. Chomaz, T. Yefsah, J. Léonard, J. Beugnon, C. Weitenberg, and J. Dalibard, Nature Physics **8**, 645 (2012).

[270] G. W. Stagg, A. J. Allen, C. F. Barenghi, and N. G. Parker, Journal of Physics: Conference Series **594**, 012044 (2015).

[271] T. Winiecki and C. S. Adams, EPL (Europhysics Letters) **52**, 257 (2000).

[272] M. Brewczyk, M. Gajda, and K. Rzażewski, Journal of Physics B: Atomic, Molecular and Optical Physics **40**, R1 (2007).

[273] A. Griffin, T. Nikuni, and E. Zaremba, *Bose-Condensed Gases at Finite Temperatures* (Cambridge University Press, 2009), ISBN 9780521837026.

[274] N. Proukakis, S. Gardiner, M. Davis, and M. Szymanska, *Quantum Gases: Finite Temperatures and Non-equilibrium Dynamics*, Cold atoms (Imperial College Press, 2013), ISBN 9781848168107.

[275] P. Blakie, A. Bradley, M. Davis, R. Ballagh, and C. Gardiner, Advances in Physics **57**, 363 (2008).

[276] N. G. Berloff, M. Brachet, and N. P. Proukakis, Proceedings of the National Academy of Sciences **111**, 4675 (2014).

[277] Y. Kagan and B. V. Svistunov, Phys. Rev. Lett. **79**, 3331 (1997).

[278] M. J. Davis, S. A. Morgan, and K. Burnett, Phys. Rev. Lett. **87**, 160402 (2001).

[279] A. Sinatra, C. Lobo, and Y. Castin, Phys. Rev. Lett. **87**, 210404 (2001).

[280] M. J. Davis, S. A. Morgan, and K. Burnett, Phys. Rev. A **66**, 053618 (2002).

[281] C. Connaughton, C. Josserand, A. Picozzi, Y. Pomeau, and S. Rica, Phys. Rev. Lett. **95**, 263901 (2005).

[282] R. W. Pattinson, N. P. Proukakis, and N. G. Parker, Phys. Rev. A **90**, 033625 (2014).

[283] S. Nazarenko, M. Onorato, and D. Proment, Phys. Rev. A **90**, 013624 (2014).

[284] M. J. Davis and P. B. Blakie, Phys. Rev. Lett. **96**, 060404 (2006).

[285] T. M. Wright, N. P. Proukakis, and M. J. Davis, Phys. Rev. A **84**, 023608 (2011).

[286] N. G. Berloff and A. J. Youd, Phys. Rev. Lett. **99**, 145301 (2007).

[287] N. Berloff and C. Yin, Journal of Low Temperature Physics **145**, 187 (2006).

[288] H. Salman and N. G. Berloff, Physica D **238**, 1482 (2009).

[289] A. C. Newell, S. Nazarenko, and L. Biven, Physica D **152**, 520 (2001).

[290] M. R. Smith, R. J. Donnelly, N. Goldenfeld, and W. F. Vinen, Phys. Rev. Lett. **71**, 2583 (1993).

[291] S. R. Stalp, L. Skrbek, and R. J. Donnelly, Phys. Rev. Lett. **82**, 4831 (1999).

[292] P. M. Walmsley and A. I. Golov, Phys. Rev. Lett. **100**, 245301 (2008).

[293] M. Leadbeater, T. Winiecki, and C. S. Adams, Journal of Physics B: Atomic, Molecular and Optical Physics **36**, L143 (2003).

[294] L. Hough, L. A. K. Donev, and R. J. Zieve, Phys. Rev. B **65**, 024511 (2001).

[295] C. F. Barenghi, V. S. L'vov, and P.-E. Roche, Proceedings of the National Academy of Sciences **111**, 4683 (2014).

[296] D. Duda, P. Švančara, M. La Mantia, M. Rotter, and L. Skrbek, Phys. Rev. B **92**, 064519 (2015).

[297] N. Hashimoto, R. Goto, H. Yano, K. Obara, O. Ishikawa, and T. Hata, Phys. Rev. B **76**, 020504 (2007).

[298] K. W. Schwarz, Phys. Rev. Lett. **47**, 251 (1981).

[299] M. Tsubota, Phys. Rev. B **50**, 579 (1994).

[300] K. W. Schwarz, Phys. Rev. Lett. **64**, 1130 (1990).

[301] K. W. Schwarz, Phys. Rev. B **38**, 2398 (1988).

[302] R. Hänninen, M. Tsubota, and W. F. Vinen, Phys. Rev. B **75**, 064502 (2007).

[303] D. Kivotides, C. F. Barenghi, and Y. A. Sergeev, Phys. Rev. B **77**, 014527 (2008).

[304] R. Hänninen and A. W. Baggaley, Proceedings of the National Academy of Sciences **111**, 4667 (2014).

[305] K. Henderson and C. Barenghi, Czechoslovak Journal of Physics **46**, 75 (1996).

[306] J. Salort, P.-E. Roche, and E. Lévêque, EPL (Europhysics Letters) **94**, 24001 (2011).

[307] J. Salort, B. Chabaud, E. Lévêque, and P.-E. Roche, EPL (Europhysics Letters) **97**, 34006 (2012).

[308] G. W. Rayfield and F. Reif, Phys. Rev. **136**, A1194 (1964).

[309] N. P. Proukakis and B. Jackson, Journal of Physics B: Atomic, Molecular and Optical Physics **41**, 203002 (2008).

[310] A. Fetter and J. Walecka, *Quantum Theory of Many-particle Systems*, International series in pure and applied physics (McGraw-Hill, 1971).

[311] L. Schiff, *Quantum Mechanics*, International series in pure and applied physics (McGraw-Hill, 1968).